Photonic nano materials: anisotropic transport and optical Bloch oscillations

Riccardo Sapienza

Photonic nanomaterials, anisotropic transport and optical Bloch oscillations

Ph.D. Thesis

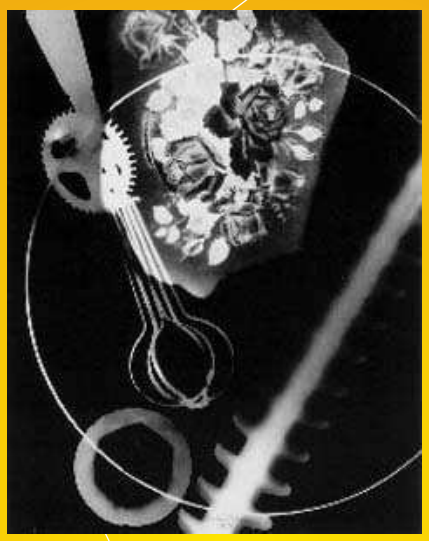

RICCARDO SAPIENZA


Photonic nano materials: anisotropic transport and optical Bloch oscillations

Ph.D. Thesis in - Tesi di dottorato in - Thèse de doctorat en
Atomic and molecular spectroscopy and quantum optics,
European Ph.D. school, XVII ciclo

Riccardo Sapienza

To obtain the degree of
Docteur de l'Université Paris VI
and
Dottore dell'Università di Firenze

Defended on February 7th 2005

Dr. Dominique Delande . . . . . Ph.D. Advisor
Dr. Diederik Wiersma . . . . . Ph.D. Advisor
Prof. Robert Pick . . . . . Commission member
Prof. Vincenzo Schettino . . . . . Commission member
Prof. Valentin Freilikher . . . . . Referee
Prof. Costas Soukoulis . . . . . Referee

Institutions

This Ph.D. thesis is the result of the collaboration between

European Laboratory for Non-linear Spectroscopy (LENS)
Polo Scientifico di Sesto Fiorentino
Via Nello Carrara 1 50019 Sesto Fiorentino - Firenze, Italy

Università degli studi di Firenze, Dipartimento di Fisica
Polo Scientifico di Sesto Fiorentino
Via G. Sansone 1 50019 Sesto Fiorentino - Firenze, Italy

Laboratoire Kastler-Brossel (LKB)
École Normale Supérieure et Université Pierre et Marie Curie
4 place Jussieu, F-75252 paris Cedex 05 France

Research projects

The research work described in this thesis is financially supported by:

Istituto Nazionale di Fisica della Materia (INFM),
Project PAIS-Randlas 2002

Ministero dell'Istruzione, dell'Università e della Ricerca (MIUR), Project Coffin-Silicon Photonic Crystals 2002

European Community, Marie Curie Fellowship Contract nr HPMT-CT-2000-00102

Fondazione Ing. Aldo Gini, Padova, Italy.

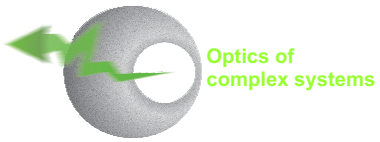

Contacts: sapienza@lens.unifi.it
http://www.complexphotonics.org/

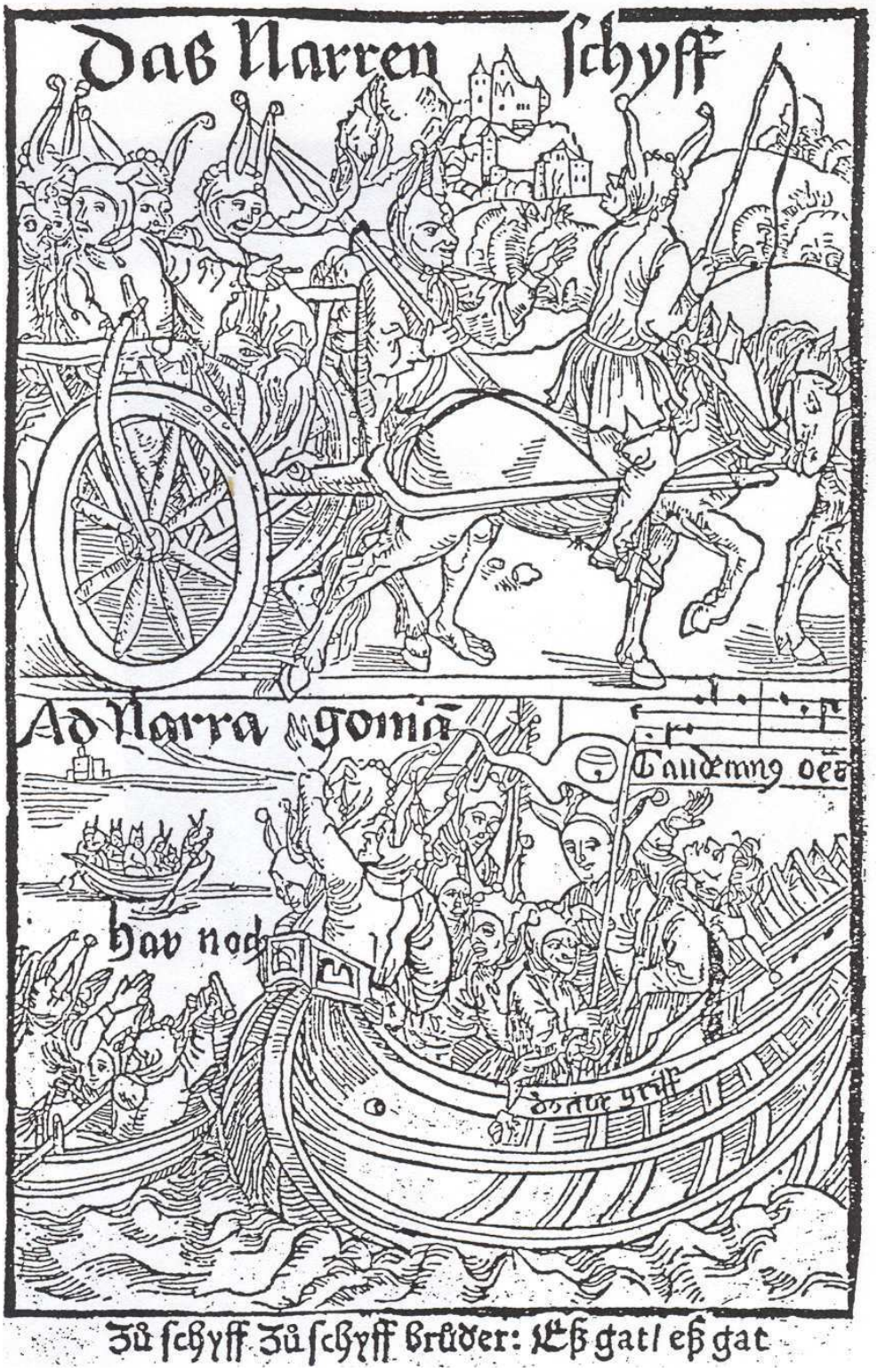

Figura 1: Exlibris: **Fools On A Cart And A Boatload Of Fools** The fools are setting out for their destination, the land of fools. They call out *har noch* i.e. follow us! and All aboard, Brothers: it's leaving, it's leaving [1]. (see also the notes at the end of the thesis)

Abstract

Nowadays, propagation of light in complex dielectric nano-materials is a rich and fascinating area of research, both for its fundamental implications and for its practical technological impact. In this thesis we investigate the effects of interference in quasi-ordered photonic systems.

Light in random dielectric media is described through a random walk from scatterer to scatterer. Interference effects do survive the multiple scattering and give rise to fascinating phenomena. In the strong scattering regime light could even become localized and propagation is no longer possible. In ordered media, the periodicity leads to cooperative scattering and interference. In this case the transport becomes strongly frequency-dependent; it can be inhibited (destructive interference) or substantially improved (constructive interference).

Whereas the knowledge on the propagation of light waves in completely ordered and disordered structures is now rapidly increasing, little is known about the behavior of optical waves in the huge intermediate regime between complete order and disorder.

Quasi-ordered systems show breaking of rotational or translational symmetry and exhibit novel and unusual forms of light transport. Anisotropic scattering random media and nematic liquid crystals, or specially tailored photonic crystals and Fibonacci quasi-crystals are examples of quasi-ordered systems that we will investigate in this thesis.

- *What would happen if a preferential scattering direction or a preferential polarizability axis were to be introduced in an isotropic random scattering system?*
- *How would light propagation be in a periodic dielectric media if a linear optical potential was superimposed to the crystalline structure?*

In this thesis we will try to address these questions, based on theoretical arguments, numerical simulations and experimental evidences.

Riassunto

Al giorno d'oggi, la propagazione della luce in nano-materiali dielettrici complessi è un soggetto di ricerca ricco ed affascinante. In questa tesi studiamo gli effetti dell'interferenza della luce nei sistemi fotonici quasi-ordinati.

La luce nei mezzi dielettrici disordinati è descritta tramite un modello di cammino casuale da diffusore a diffusore: gli effetti di interferenza sopravvivono la diffusione multipla e producono fenomeni interessanti ed inaspettati. Nelle strutture che diffondono molto fortemente, la luce potrebbe persino essere localizzata e il trasporto inibito. In quelle ordinate, la periodicità della struttura induce una forma di diffusione e d'interferenza cooperativa: il trasporto diventa fortemente dipendente dalla frequenza, può essere inibito (interferenza distruttiva) o favorito sostanzialmente (interferenza costruttiva).

Mentre la nostra comprensione della propagazione di luce in strutture completamente ordinate o disordinate sta, negli ultimi anni, crescendo considerevolmente, poco è conosciuto circa il comportamento delle onde luminose nell'enorme regime intermedio fra ordine e disordine totali. I sistemi quasi-ordinati mostrano la rottura della simmetria di rotazione o di traslazione e forme nuove e non convenzionali di trasporto della luce. Da un lato i mezzi disordinati che presentano diffusione anisotropa ed i cristalli liquidi nematici, e dall'altro i cristalli fotonici appositamente modificati ed i quasi-cristalli fotonici di Fibonacci sono esempi di sistemi quasi-ordinati che studieremo in questa tesi.

- *Quali conseguenze potrebbe portare l'introduzione di una direzione preferenziale di diffusione o di un asse preferenziale di polarizabilità, in un sistema disordinato a diffusione isotropa?*
- *Come potrebbe essere alterata la propagazione della luce in una struttura periodica se una un potenziale ottico lineare fosse aggiunto alla struttura cristallina?*

In questa tesi proveremo a rispondere a entrambe queste domande, con argomentazioni teoriche, simulazioni numeriche e prove sperimentali.

Résumé

Aujourd'hui, la propagation de la lumière dans les nano-matériaux diélectriques complexes est un sujet de recherche riche et fascinant, tant pour ses implications fondamentales que pour son impact technologique. Dans cette thèse, nous étudions les effets d'interférence de la lumière dans les systèmes photoniques quasi-ordonnés.

Dans des milieux diélectriques aléatoires, on peut décrire le mouvement des photons mutiplement diffusés par une marche aléatoire de diffuseur en diffuseur: la plupart des effets d'interférence se moyennent alors à zéro, mais certains survivent quand même au désordre et induisent des phénomènes non-triviaux. Dans des milieux qui diffusent très fortement, la lumière pourrait même devenir localisée et aucun transport ne serait possible. Dans les milieux ordonnés, la périodicité conduit à des lois de dispersion inhabituelles où les effect collectifs d'interférence dominent: le transport est fortement dépendant de la fréquence, il peut être sensiblement augmenté (interférences constructives) ou complètement inhibé (interférences destructives).

Notre compréhension de la propagation des ondes lumineuses dans les milieux ordonnés et désordonnés augmente rapidement, mais le comportement dans le régime intermédiaire entre les deux extrèmes – ordre parfait et désordre complet – est mal compris. Les systèmes quasi-ordonnés brisent la symétrie de rotation ou de translation et présentent des formes nouvelles et non-conventionnelles de transport de la lumière. Les milieux aléatoires qui diffusent anisotropiquement et les cristaux liquides nématiques, les formes spéciales de cristaux photoniques et les quasi-cristaux photoniques de Fibonacci sont des exemples de systèmes quasi-ordonnés que nous étudions dans cette thèse.

- *Que se passe-t-il si une direction préférentielle de diffusion ou un axe préférentiel de polarisabilité est présent dans un milieu aléatoire ?*

- *Comment la propagation de la lumière est elle modifiée dans une structure périodique si un potential optique est superposé à la structure cristalline ?*

Dans cette thèse nous essayerons de répondre à ces questions, avec des arguments théoriques, des simulations numériques et des résultats expérimentaux.

Summary

This thesis is the result of a three-year international doctorate on *Atomic and Molecular Spectroscopy and Quantum Optics*, done in collaboration between LENS, the *European Laboratory for Non-Linear Spectroscopy*, University of Florence, and the University of Paris VI.

I have carried on the first two years of experimental research at LENS, European Laboratory for Non-Linear Spectroscopy, in Firenze, under the supervision of Diederik Wiersma. In the last year I have completed a theoretical and computational project at *Laboratoire Kastler-Brossel*, École Normale Supérieure et Université Pierre et Marie Curie, in Paris, under the supervision of Dominique Delande.

The experiment for the measurement of the anisotropic weak localization from ordered nematics has been done together with Sushil Mujumdar, at present in the University of Alberta (Canada), and in collaboration with Arjon G. Yodh and Cecil Cheung, from the Department of Physics and Astronomy of the University of Pennsylvania, Philadelphia (USA).

The measurement of the optical analogue of electronic Bloch oscillations has been done together with Paola Costantino from the University of Florence (Italy), and in collaborations with Lorenzo Pavesi and Mher Ghulinyan from the University of Trento (Italy), and Claudio J. Oton from the Department of Fundamental Physics, University of La Laguna, Tenerife (Spain).

During these three years I have been affiliated to INFM, the Istituto Nazionale di Fisica della Materia, which kindly supported my work.

The work described in this thesis has been published in the following papers:

- R. Sapienza, S. Mujumdar, C. Cheung, A. Yodh, and D. Wiersma, *Anisotropic weak localization of light*, Physics Review Letters **92**, 033903 (2004)

- R. Sapienza, D. Delande, and D. Wiersma, *Anisotropic weak localization of light: from isotropic scattering to ordered nematic liquid crystals*, Molecular Crystal and Liquid Crystal (2004) (in press).

- R. Sapienza, P. Costantino, D. Wiersma, and M. Ghulinyan, C. Oton, L. Pavesi, *Optical Analogue of Electronic Bloch Oscillations*, Physics Review Letters **91**, 263902 (2003) [cover story].

- D. Wiersma, R. Sapienza, S. Mujumdar, M. Colocci, M. Ghulinyan, L. Pavesi, *Optics of nanostructured dielectrics*, Journal of optics. A, Pure and applied optics **7**, 190-197 (2005).

- M. Ghulinyan, C. J. Oton, L. Dal Negro, L. Pavesi, R. Sapienza, M. Colocci, and D. Wiersma, *Light pulse propagation in Fibonacci quasicrystals*, Physics Review B. (2004) (in press).

- D. Wiersma, S. Gottardo, R. Sapienza, S. Mujumdar, S. Cavalieri, M. Colocci, R. Righini, L. Dal Negro, C. Oton, M. Ghulinyan, Z. Gaburro, L. Pavesi, F. Aliev, P. Johnson, A. Lagendijk, W. Vos, *Light transport in complex photonic systems*, in Waves scattering in Complex Media: from theory to applications, Kluwer Academic Publisher, Dordrecht 2003.

Contents

Chapter 1

Introduction to light transport in complex dielectrics

In the last decades a new frontier has emerged, with the goal of understanding the role of light interference within light propagation and of exploiting it to control and mould the flow of light. In the last decades, this fundamental speculation has met the growing interest of the photonic nano-material world. Recent technological developments make possible to design and assembly novel photonic structures, and the mesoscopic theories of light are powerful tools to interpret, understand and engineer them. Nowadays, propagation of light in complex dielectric nano-materials is a rich and fascinating area of research and one of the fastest growing subject in modern physics.

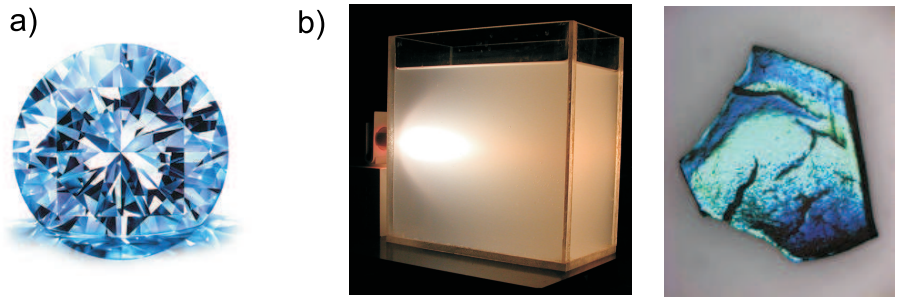

Figure 1.1: a) Light passing through a diamond, which is an homogenous dielectric. b) Examples of complex dielectrics. On the left, diffusion of light in a turbid liquid (courtesy of Francesco lo Bue). On the right, light reflected from a photonic crystal, titania inverse opal (courtesy of Willem Vos, from [2]).

With complex dielectrics, we intend dielectric structures with an index of refraction that has variations on a length scale that is roughly comparable to the incident wavelength. Such structures strongly scatter light. An homogeneous, non-absorbing medium is transparent and ordinary refraction and reflections can be observed. A sample with random dielectric constant is opaque, and typically white, when absorption is absent, while a periodically modulated one is iridescent and exhibits wavelength dependent reflection. A glass of milk, white paint or the iridescent wings of some butterflies are

examples of complex dielectrics. A possible building block for constructing a complex

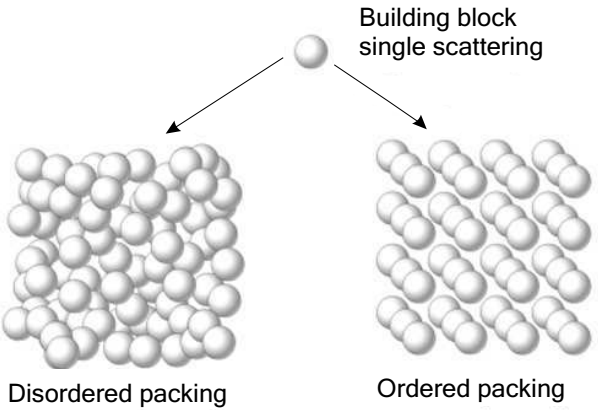

Figure 1.2: Ordered and disordered packing of a single-scattering unit.

dielectric is a micro sphere of diameter comparable to the wavelength, and of a certain refractive index that is different from its surrounding medium. The single scattering from such a sphere has a rich structure due to internal resonances in the sphere, but its behavior is well-understood and can be calculated using the formalism of Mie-scattering [3]. A complex dielectric material can then be realized by micro-assembly of several micro spheres. The spheres can be assembled in various ways with two opposite possibilities: a completely disordered packing and a fully ordered assembly (see Fig. 1.2). The cumulative behavior after assembly will depend heavily on the way the spheres as packed together. This is due to the interference between the scattered waves, and the way the waves are multiply scattered from one sphere to another. If the spheres are packed according to a crystal-like structure then the interference will be constructive only in certain well defined directions, giving rise to Bragg refraction and reflection. In the disordered case, the photons will perform a random walk from one sphere to the other. The occurrence of interference effects is now less obvious to understand, however also in random systems, interference effects turn out to be very important.

1.1 Disordered photonics

Disordered photonic systems are media in which the dielectric constant varies randomly in space, as for example a suspension of scattering micro-particles in a liquid, as it is the case for ordinary milk, or a grind crystal powder. The phase of the scattered waves is random, and thus one can model light propagation with a *random walk* which leads to a multiple scattering process (see Fig. 1.3). A diffusion model which considers the transport of photons like hard balls with no internal degree of freedom can be appropriate. But this simple picture is not complete as some interference effects can survive the multiple scattering.

When one shines coherent light on a system with fixed disorder, the scattered light has a "grainy" random intensity pattern with very bright and dark spots. This is a signature of preserved phase coherence upon multiple scattering. At the bright spots

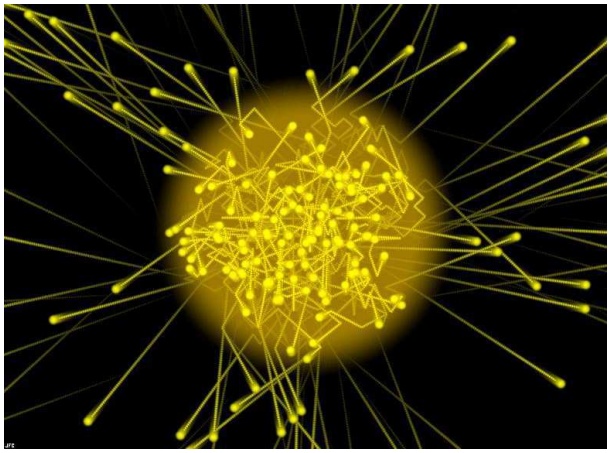

Figure 1.3: Illustration of multiple scattering in a disordered dielectric medium. Many photons random walks are shown. (courtesy of Jean-Francois Colonna, http://www.lactamme.polytechnique.fr/.)

many scattered waves interfere constructively while at the dark spots they cancel out. This effect is called *speckle* and can be observed with bulk systems and surfaces (see Fig. 1.4). If we average over many system configurations, as for example in a turbid liquid, we smooth out the profile and wash out the interference pattern. But some coherent effects can survive the ensemble averaging. One of the most evident is *coherent backscattering*, a two-waves interference responsible for up to a doubling of the backscattered intensity and which thus decreases the optical conduction of the medium.

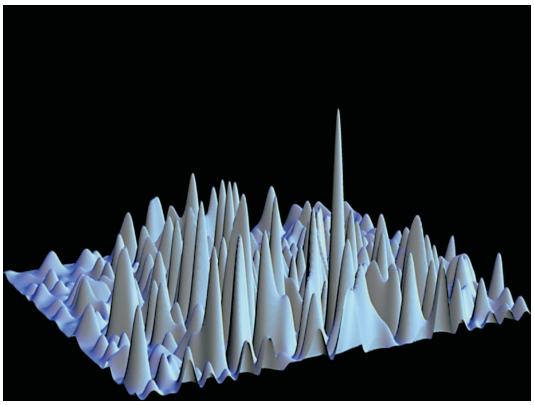

Figure 1.4: Simulated speckle pattern from light incident on a disordered medium. (From [4])

If the disorder is so strong that the light is scattered before completing an optical cycle, then *Anderson localization* can occur, a phase transition which brings the system into a regime where diffusive transport is inhibited (see Fig. 1.5). P. Anderson won the Nobel prize in 1977 for his investigations into this very important issue [5, 6].

There exist fascinating analogies between electron transport and transport of optical waves in dielectric structures [7]. Interference of light in random dielectric systems

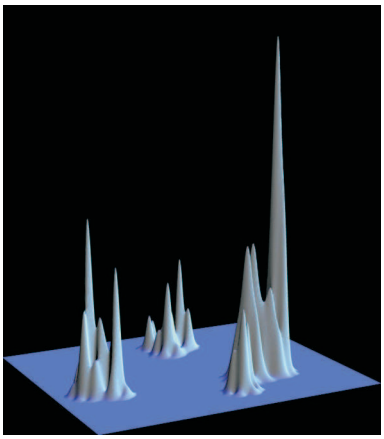

Figure 1.5: Illustration of the light intensity distribution in the regime of Anderson localization. Light is confined in small regions of the medium, the localized states, which are exponentially confined. (From [4])

influences the transport of light in a way that is similar to the interference that occurs for electrons when they propagate in disordered conducting materials. In disordered systems the optical counterpart of weak localization [8, 9, 10, 11], Anderson localization [12, 13, 14], short and long range correlations [15, 16, 17], and universal conductance fluctuations [18] have all been observed. These are various examples of wave phenomena where interference effects play a crucial role both in the optical and the electronic case. Often these processes are easier to study with light because the coherence length of an optical wave packet is usually much longer than that of an electronic wavepacket, photon-photon interaction are extremely weak, and pure wave effects can be singled out.

1.2 Ordered photonics

On the other hand one can think of ordered photonic media as a set of systems which can be modelled directly starting from the interference and without a random walk picture, as the correlation in the position of the scatterers cannot be neglected. The periodicity allows for a cooperative scattering with important contributions from all points of the sample. Artificially engineered ordered (periodic) photonic materials are well known as *photonic crystals* as in them light behaves as electronic waves in ordinary crystals [20]. Interference effects in this case cannot be regarded as a correction to a diffusive picture, but are instead the main process ruling light propagation.

One of the most important technological advances of the last century has been the control of electron transport in "electronic devices". In contrast with the centrality of electronic devices and their fast development, such a technology, which is based on electrons, is reaching its limits. The limits of electron systems can be overcome naturally in equivalent photon systems, which are not subject to decoherence and unwanted interactions.

If the scattering of the spheres that constitute a photonic crystal is strong enough (that is the refractive index contrast between the spheres and their surrounding medium

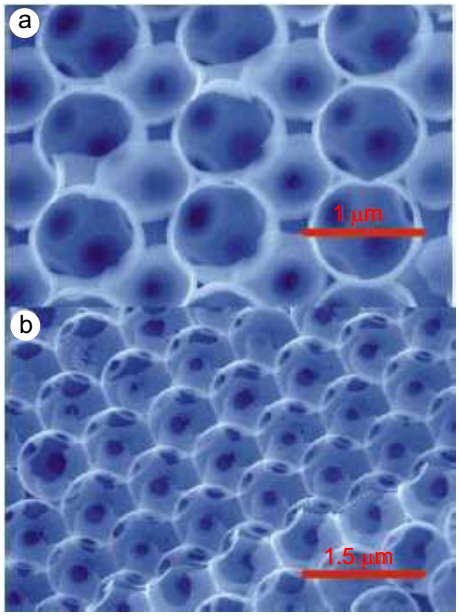

Figure 1.6: SEM images of internal facets of silicon inverse opal: a, (110) facet. b, (111) facet (courtesy of A. Blanco, [19]).

is large and their diameter is resonant with the wavelength) the interference can become destructive in all directions, for a certain range of frequencies. In analogy with the behavior of electrons in semiconductors, this range of optical frequencies is referred to as a photonic band gap. Inside a photonic band gap, the density of light modes becomes zero, which means that spontaneous light emission is inhibited [21]. A defect in the structure opens up a state in the middle of a bandgap, localized at the defect. In this way defect lines and circuits can be written on a photonic crystal, which could allow to control the flow of light.

1.3 Optical anisotropy

In transparent materials with anisotropic dielectric permittivity, important optical effects can be observed. *Birefringency* and *dichroism* are the most common, but also anisotropic light transport and interference can take place. It is very interesting to speculate how their microscopic counterpart can affect light scattering in ordered and disordered structures.

Liquid crystals in the nematic phase are opaque and therefore also give rise to multiple light scattering. They are strongly scattering materials that differ fundamentally from common isotropic random media. The nematic phase of a liquid crystal is characterized by a local alignment of the molecules in a direction called the nematic director, and an otherwise translational disorder [22, 23, 24]. The partial ordering of the nematic phase leads to an anisotropic scattering function. With an external magnetic field, the whole sample can be oriented in a common direction (monodomain regime), making the director a *global* property of the system. In this case the anisotropy in the scattering cross section leads, for large enough samples, to an anisotropic multiple scattering

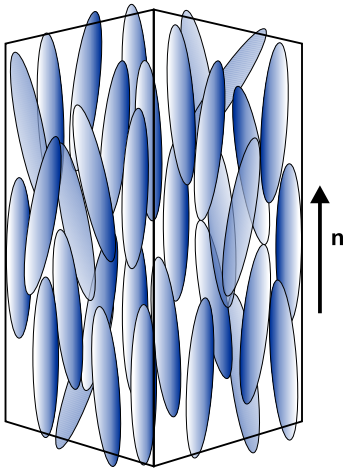

Figure 1.7: Nematic liquid crystals have a degree of order, as the molecules tend to be parallel to the nematic director.

process, and monodomain nematics are therefore ideal systems to study anisotropic multiple light scattering.

Anisotropic diffusion has recently arisen considerable interest as it can allow the control of the optical properties of materials, and achieve, for example, switching as in ordinary liquid crystal displays. Moreover, increasing the degree of anisotropy, a three dimensional type of transport can be brought into a quasi-two dimensional one, where the diffusion occurs mainly in a plane [25]. In addition the role of transport anisotropy in Anderson localization is not yet known and tunable anisotropy could be exploited to bring the system in and out the phase transition.

1.4 In between these extremes

The possibility of exploiting interference effects to control the flow of light has recently arisen a considerable interest. For this reason the attention is focussed on *mesoscopic samples*, in which phase-coherence is preserved. They are of a size intermediate between the microscopic molecular one, and the averaged bulk. We will investigate samples whose size does not exceed the coherence length of the wave, which for light waves can be as long as kilometers, whereas, in electron systems, it is usually smaller than micrometers [7].

Whereas the laws of light propagation in completely ordered and disordered structures are well understood, little is known about the behavior of optical waves in the intermediate regime between total order and disorder.

The breaking of fundamental symmetries of nature manifests itself in various optical phenomena and can be important for our understanding of the interaction between light and complex matter. Ordered and disordered systems are characterized by a different degree of symmetry: disordered systems by the rotational and the translational invariance of the isotropic random medium, ordered ones by the axial and the translational symmetry of the periodic potential.

From the disordered side we will focus on anisotropic random scattering systems.

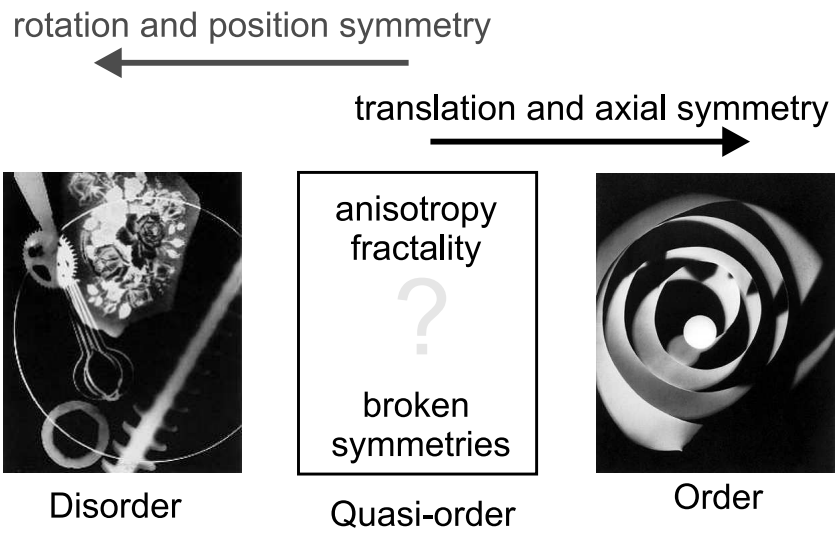

Figure 1.8: Ordered and disordered systems are characterized by a different degree of symmetry. Little is known of the regimes which lie in between these extremes (from Man Ray, rayograph 1926).

The novelties in anisotropic systems lie in the presence of preferential directions, whose varying degrees of anisotropy break one or more of the *symmetries* (rotational and translational, or polarization independence) typical of the isotropic random medium. A simple average of all the microscopic details is not any more justified. One of the most robust two-waves interference phenomena, called coherent backscattering, will be measured and simulated in this thesis, for an ensemble of Rayleigh scatterers and ordered nematic liquid crystals. We will show that anisotropy survives the multiple scattering averaging and is still present in the interference pattern.

On the ordered side, we will investigate photonic crystals whose translational symmetry is gradually lifted. If a periodic dielectric constant is altered with a linear variation along a direction, the light propagation is less and less appropriately described with delocalized Bloch waves. In analogy with electronic systems, when a linear gradient is introduced in the optical potential (proportional to the dielectric function), the Bloch states turn into localized Wannier-Stark modes, and the photons perform the optical analogue of *Bloch oscillations* between the band-edges of the resulting tilted bandgap [26].

The class of *quasicrystals* belongs to the intermediate regime between periodic and random [27]. In these deterministic non-periodic structures, translational symmetry is absent. Among the various 1D quasicrystals, the Fibonacci binary quasicrystal has been the subject of an extensive theoretical and experimental effort in the last two decades. The Fibonacci structure is realized by stacking two different dielectric layers accordingly to a non-periodic but deterministic generation rule: the Fibonacci sequence, each number in the sequence is generated from the sum of the preceding two. Many electronic quasicrystals follow an analogous construction rule in three dimensions to produce long-range atomic order without conventional periodicity [28]. Transmission spectra of quasi-periodic structures possess a rich fractal nature and very narrow resonance peaks which are separated by forbidden frequency regions, called "pseudo-band

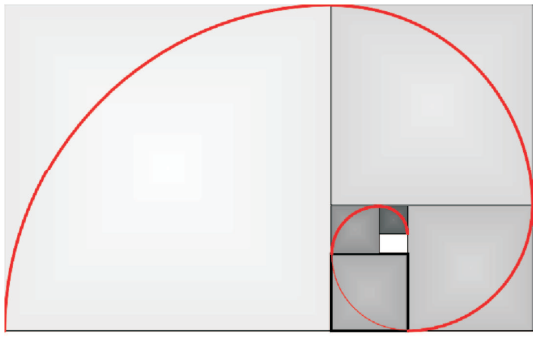

Figure 1.9: Fibonacci spiral where each new square has a side which is as long as the sum of the latest two square's sides (which is the Fibonacci sequence).

gaps", although the global structure is not periodic [29, 30]. Time-resolved measurements on 1D Fibonacci quasi-crystals show strong pulse delays and pulse stretching for excitation in the proximity of these pseudo-bandgaps, at the bandedges.

First in *chapter 2*, the isotropic coherent backscattering model will be presented, then in *chapter 3* an extension to anisotropic scattering will be presented. Anisotropic weak localization of light in ordered nematic liquid crystals has been measured and will be discussed in *chapter 4*. In *chapter 5*, a Monte Carlo simulation of light propagation in an ensemble of Rayleigh scatterers will be performed and the anisotropy of the cone of backscattering enhancement be shown. Then the attention will focus on ordered and quasi-ordered systems, in *chapter 6*. The first experimental evidence of the analogue of electronic Bloch oscillations in photonic crystals with broken translational invariance will be shown. Then time-resolved experiments on light transport at the band-edges of Fibonacci quasi-crystals will be reported. The conclusions and future perspectives will be summarized in *chapter 7*.

Chapter 2

Coherent Backscattering of light

In this chapter, coherent backscattering of light is presented. The physical origin is discussed as well as some of the most common and modern theoretical tools to analyze it. A model of the phenomenon, based upon the diffusion approximation is presented without going into details. A diagrammatic approach based on an expansion of multiple scattering on scattering orders is recalled, and the main results are shown. The standard integral model for coherent backscattering, which assumes isotropic scattering, is presented, and a generalization to anisotropic scattering is performed. This approach opens the way for a successive Monte-Carlo simulation that can provide the configuration averaging required to calculate the profile of the coherent backscattering cone in presence of global anisotropy.

In the first part of this thesis, we will investigate disordered media and light transport. There are few approximations which are very well justified by the experimental conditions, and which enable to formulate a simpler model.

2.1 Single scattering

The fundamental element in a multiple scattering process is the scattering from a single scatterer, which is the basic element composing the optical system. The transport of light is determined by how light is scattered by this microscopic unit and by the way the partial scattered waves interfere with each other. The latter depends on how the scatterers are distributed in the system, in an ordered or random fashion. Before approaching the collective effect of multiple scattering, we recall the single scattering results that have been known long ago [32, 31].

We consider a scattering event that takes place at the origin, $\mathbf{r} = 0$, of a wave with k-vector $\mathbf{k}_\mathrm{i}$ (and for simplicity with normalized amplitude); the scattered wave, in the far field can be described by

$$\mathcal{E}(\mathbf{r}) = \mathbf{f}(\mathbf{k}_\mathrm{i}, \mathbf{k}_\mathrm{f}) \frac{e^{i\mathbf{k}_\mathrm{f}\cdot\mathbf{r}}}{r}, \tag{2.1}$$

where $\mathbf{f}(\mathbf{k}_\mathrm{i}, \mathbf{k}_\mathrm{f})$ stands for the scattering amplitude and $\mathbf{k}_\mathrm{f}$ (with $|\mathbf{k}_\mathrm{f}| = |\mathbf{k}_\mathrm{i}| = k$) the scattered k-vector, $\mathbf{k}_\mathrm{f} = k\,\mathbf{r}/r$.

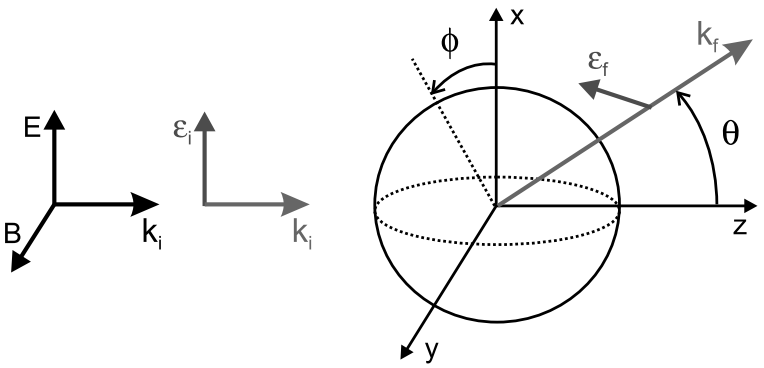

Figure 2.1: Scattering geometry.

The scattering amplitude contains all the information of the scattering process, but it is usually inaccessible to the experiments which typically measure only light intensities. For this reason, one usually prefers to deal with the squares of $\mathbf{f}(\mathbf{k}_\mathrm{i}, \mathbf{k}_\mathrm{f})$, which describes the light pattern scattered from each scatterer. It is called the *differential scattering cross-section*

$$\frac{d\sigma(\theta,\phi)}{d\Omega} = |\mathbf{f}(\mathbf{k}_\mathrm{i}, \mathbf{k}_\mathrm{f})|^2 \tag{2.2}$$

and quantifies the normalized intensity scattered in the solid angle $d\Omega$. It provides the time averaged power radiated by the scatterer in a direction $\mathbf{k}_\mathrm{f}$, which is labelled by (θ, ϕ), in a given polarization state, per unit solid angle and unit incident flux. The differential scattering cross-section in general depends on the incident polarization and direction of the light, the notation as in Eq. (2.2) contains implicitly these information.

The scattering mean free path depends on the total probability for a scattering event, being long if the probability is weak. The total probability for a scattering event is given by the total integrate differential scattering cross-section

$$\sigma_t = \int \frac{d\sigma(\theta,\phi)}{d\Omega}\, d\Omega \tag{2.3}$$

times the scatterer density n_p. In a diluted medium it can be demonstrated that ℓ_s is precisely the reciprocal of the above product,

$$\ell_s = \frac{1}{n_p\, \sigma_t}. \tag{2.4}$$

The interaction of radiation and matter can be described in most of the cases via the induction of electric or magnetic (we will restrict to electric dipoles; the magnetic case is analogous) dipoles in the excited matter [31]. This very general approach is suitable for scatterer with no geometrical resonances (Mie resonances [32]) and with no internal structure, and not for example for scatterers with coupled atomic levels, non-zero Verdet constant, optical non-linearity, etc... This requirements are easily fulfilled in a point-like scatterer, which by definition cannot sustain resonant optical modes [33].

Rayleigh scattering is inherently an elastic process, a linear dipole is induced, and then it radiates light at the same frequency as the incident one. The amplitude of the dipole is usually described by $\alpha(\omega)$, which is called the polarizability. Therefore

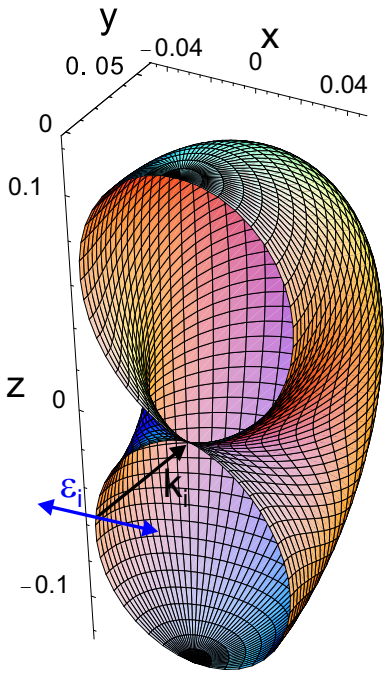

Figure 2.2: Rayleigh scattering differential cross-section, for a point-like dipole, for excitation light polarization $\boldsymbol{\epsilon}_\mathrm{i}$ and k-vector $\mathbf{k}_\mathrm{i}$.

the polarization of the radiated light is just the projection of the dipole polarization $\mathbf{p}(\omega) = \alpha(\omega)\,\epsilon_\mathrm{i}$ on the normal to the scattering direction $\mathbf{k}$. The differential scattering cross-section for such a Rayleigh scattering process is

$$\frac{d\sigma}{d\Omega}(\mathbf{k}_\mathrm{f}\epsilon_\mathrm{f};\mathbf{k}_\mathrm{i}\epsilon_\mathrm{i}) \propto \alpha^2(\omega)|\epsilon_\mathrm{f}^* \cdot \epsilon_\mathrm{i}|^2 \tag{2.5}$$

where $\mathbf{k}_\mathrm{i}\epsilon_\mathrm{i}$ and $\mathbf{k}_\mathrm{f}\epsilon_\mathrm{f}$ are respectively the incident and scattered k-vector and polarization, and the star denotes the complex conjugate.

Far from the resonance, the polarizability depends on the k-vector as $\sim k^2$. The variation of the scattering cross section with the fourth power of k is the known Rayleigh's law, which also explains why the sky is blue or the sunset red, as the blue light is scattered much more than the red one.

The dipole which has no internal structure can only emit a spherical wave, or in other words a photon is scattered with the same probability in any direction. The only constrain in the scattered light pattern is that the transversality of the light has to be preserved: the field is orthogonal to the k-vector, $\epsilon_\mathrm{f} \perp \mathbf{k}_\mathrm{f}$. Eq. (2.5) is exactly the transversality condition.

An extended scatterer of transverse dimension d can access a phase space which is the reciprocal of its size, and therefore the scattered pattern can show an angular structure proportional to $1/d$. While Rayleigh scattering is not peaked (Fig. 2.2), as the scatterer is point-like, large particles are responsible for what is called Mie scattering. Mie scattering objects are large, of size comparable to the wavelength of the light and thus they can sustain optical resonances. In Mie scattering the polarizability is a very complex function, which a priori depends also on the k-vectors. In this case,

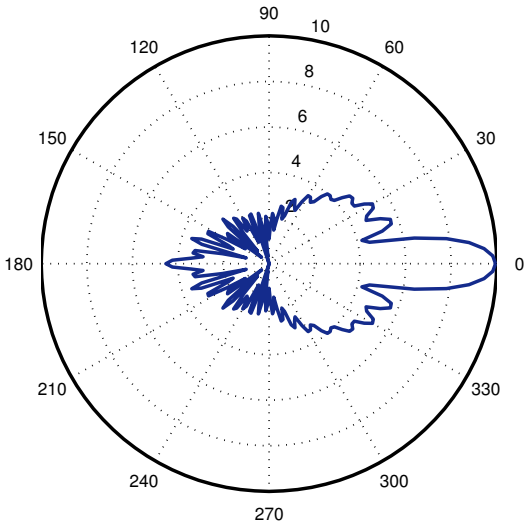

Figure 2.3: Differential scattering cross-section for a Mie sphere of size $a = kd = 20$, where d is the sphere diameter and relative refractive index of 1.25.

the scattering is very forward and has a rich structure, as shown in Fig. 2.3 for a Mie scatterer of size parameter $a = k\,d = 20$ and refractive index contrast of 1.25.

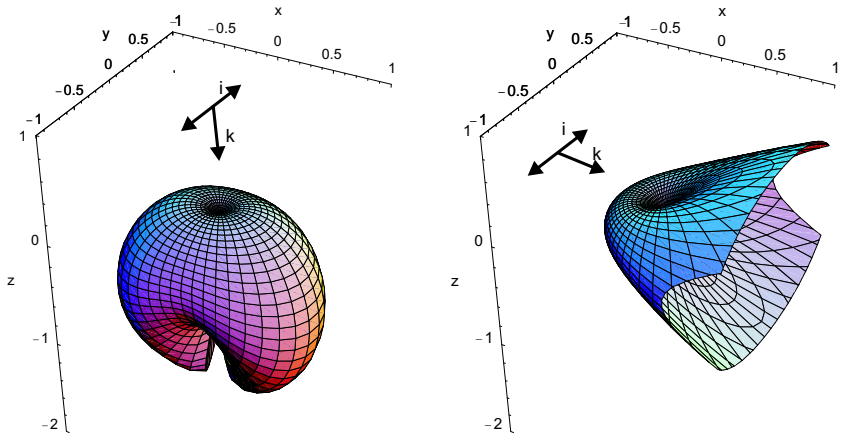

Figure 2.4: Ordered nematic scattering differential cross-section. The two very different shapes are associated with the two different k-vectors shown in the figure, and the same ordinary polarization $\epsilon_{\rm i} \equiv \mathbf{i}$. In both cases, the emerging polarization is extraordinary. In the left panel the differential scattering cross-section is almost symmetric while in the right panel it is very forward, and extends up to 4000 in the x-direction.

Later in the thesis we will investigate also light scattering in ordered nematic liquid crystals, which are neither Rayleigh nor Mie scatterers. Nematics are anisotropic scat-

tering materials whose scattering process has a different origin, as it relies on collective scattering due to global fluctuations in the dielectric function. We anticipate here that the scattering cross-section is very rich, it ranges from almost isotropic to very forward just changing the polarization and direction of the incident light. The very forward nature of this scattering process can be explained as it takes place over large volumes of nematics. In Fig. 2.4 we show few scattering cases, a more detailed description will be presented in chapter 4.

2.1.1 S-matrix

A microscopic single-scattering process can be modelled with scattering (**S**) and transition (**T**) matrices, which describe how the amplitude of the incident wave is altered by the scattering process.

The scattering matrix (**S** matrix) was introduced by Heisenberg to describe a scattering process without any assumption about the details of the interaction [34]. In this formalism, the process is thought of as a transformation of an incoming state ψ_{in} into an outgoing state ψ_{out}, which describe the system far away from the interaction potential. Hence, the **S** matrix describes the scattering process asymptotically. The mathematical transcription of this transformation is an operator relationship

$$\psi_{out} = \mathbf{S}\psi_{in}, \tag{2.6}$$

where **S** is called the **S** matrix [35]. In scattering by a time-independent potential (we shall restrict our discussion to this case), this means that the **S** matrix relates the far-field amplitudes of the incoming and outgoing fields.

The **S** matrix exhibits some properties that are independent of the specific problem under study. In particular, it is unitary and symmetric, these two properties reflecting probability (or energy) conservation in elastic scattering and reciprocity (notion that we will discuss in the next section), respectively [36]. The general aim is to get maximum information about the **S** matrix with minimum knowledge about the interaction itself.

As we have introduced in sec. 2.1, the scattered wave, in the far field regime can be described by

$$\mathcal{E}(\mathbf{r}) = \mathbf{f}(\mathbf{k}_\mathrm{i}, \mathbf{k}_\mathrm{f})\frac{e^{i\mathbf{k}_\mathrm{f}\cdot\mathbf{r}}}{r}, \tag{2.7}$$

where $\mathbf{f}(\mathbf{k}_\mathrm{i}, \mathbf{k}_\mathrm{f})$ stands for the scattering amplitude and $\mathbf{k}_\mathrm{f}$ (with $|\mathbf{k}_\mathrm{f}| = |\mathbf{k}_\mathrm{i}| = k$) the scattered k-vector, $\mathbf{k}_\mathrm{f} = k\,\mathbf{r}/r$. Introducing the van de Hulst [3] scattering matrix **S**, one can write

$$\mathcal{E}(\mathbf{r}) = \mathbf{S}\,\frac{e^{i\mathbf{k}_\mathrm{f}\cdot\mathbf{r}}}{ikr}. \tag{2.8}$$

The linearity of the boundary conditions imposed by the Maxwell equations allows the relationship between incident and scattered electric field of a plane wave scattered from an arbitrary scattering center, to be expressed in matrix form. Eq. (2.8) will be valid for all distances, as long as $\mathbf{r}$ is sufficiently far from the origin to be able to consider far-field objects.

2.1.2 T-matrix

The T-matrix formalism is very useful as it conveys all the information about the scattering process before energy conservation is build up. While the S-matrix is the

complete scattering response of the system, obtained from the superposition and interference of all the scattered wave components, the T-matrix can be regarded as the instantaneous scattering response before the time needed by the interference within the scattered wave to build up energy conservation. We will use it to calculate the propagating eigenmodes of the systems, or in other words the Green function of the system.

The T-matrix of a scattering event describes only the scattered component of the field, and it is linked to the S-matrix via:

$$\langle\psi_{in}|\mathbf{S}|\psi_{out}\rangle = \langle\psi_{in}|\psi_{out}\rangle - i2\pi\delta(\omega_i - \omega_0)\langle\psi_{in}|\mathbf{T}(\omega)|\psi_{out}\rangle, \tag{2.9}$$

for $\psi_{in} \equiv |\mathbf{k}_\mathrm{i}, \epsilon_\mathrm{i}\rangle$ and $\psi_{out} \equiv |\mathbf{k}_\mathrm{f}, \epsilon_\mathrm{f}\rangle$. The term $\delta(\omega - \omega_0)$ describes the on-shell condition, as we consider elastic scattering processes.

One can express the scattering amplitude $\mathbf{f}(\mathbf{k}_\mathrm{i}, \mathbf{k}_\mathrm{f})$ of Eq. (2.7) in terms of the T-matrix,

$$\mathbf{f}(\mathbf{k}_\mathrm{i}, \mathbf{k}_\mathrm{f}) = \langle\mathbf{k}_\mathrm{i}|\ \mathbf{T}\ |\mathbf{k}_\mathrm{f}\rangle \tag{2.10}$$

We are proceeding for increasing complexity, with the goal of describing multiple-scattering of light waves. Its basic ingredient is the single-scattering process. Once it is known and modelled for example with a T matrix, one faces the problem of taking into account all the contributions and interferences from the waves scattered by each of the single-scattering centers.

2.2 The multiple scattering model and its approximations

We will focus in this thesis on mesoscopic samples, in which phase-coherence is preserved. Their size (L) is intermediate between the microscopic molecular one, and the averaged bulk, they do not exceed the coherence length (L_ϕ) of the wave,

$$\lambda \ll \ell_s \ll L_\phi \approx L. \tag{2.11}$$

In Eq. (2.11) a crucial length appears, ℓ_s, which is the scattering mean free path. ℓ_s is the average distance between two scattering events, and for its statistical nature, as we will see, it is the first and most important element of the mesoscopic theory.

The model we are describing requires a few approximations. The multiple scattering process takes place in a *frozen* sample, i.e. with scatterers at fixed positions in space, even in liquid samples. This is justified as the photons spend a time ($t_p \sim 500$ ps) in the medium which is much smaller than the relaxation time ($t_r \sim$ ms) of the Brownian motion of the liquid. On the other hand the backscattered intensity is recorded for much longer times, ($t_m \sim$ s), long enough for averaging out the noise or the static scattered pattern (speckle). More precisely, the requirement for a fixed scattering sample, is that, during the light transit time t_p, the optical path changes much less than a light wavelength,

$$v_{scat} t_p \ll \lambda \tag{2.12}$$

where v_{scat} is the velocity of the Brownian motion.

Even more, diffusing-wave spectroscopy[1] [37, 38, 39] has thought us that that the condition on each scatterer motion has to be stricter. The sample is frozen if the total

[1]The theory of diffuse wave spectroscopy makes the connection between temporal intensity fluctuations of the speckle field emerging from the sample and the dynamics of the particles in the sample and has made it possible to use diffuse light to study the motion of particles in opaque suspensions.

path length variation, which is the cumulative result of the motion of N scatterers, is smaller than λ . The condition holds if the scatterer velocity satisfies

$$v_{scat} t_p \ll \frac{\lambda}{\sqrt{N_{max}}} \sim \frac{\lambda}{b} \tag{2.13}$$

(in isotropic samples, on average, the longest scattering path (N_{max}) is as long as the sample optical thickness squared, $N_{max} \sim b^2$).

Another important approximation is the *independent scattering approximation*, which is essential to avoid dependent scattering and to consider each scattering event as independent from all the others.

In order to model the system as a random one, it is important also that the scattering centers have *no positional correlation*, i.e. that there is no systematic relation between the scattered phases. This implies the *statistical translational invariance*, essential to perform the ensemble averaging. We need to neglect spatial or scattering correlations which would make the problem much more complicated. This requirement is easily fulfilled for a collection of uncorrelated point-like dipoles, as could be a cloud of atoms. Nematic liquid crystals show scattering correlations within a certain correlation distance ξ, which is usually much smaller than the scattering mean free path. For distances bigger then ξ also nematics can be considered as translational invariant.

However, the most important requirement is that the sample is *diluted*, i.e. that its scattering strength and its density are weak enough that the dimensionless parameter $k\ell_s \ll 1$. Such a condition is essential to perform a perturbative approach on $k\ell_s$ (later in the chapter) which allows for neglecting the recurrent scattering contributions, where one scatterer is visited more than once. If this requirement is not satisfied, the theory becomes at once extremely more complicated, the perturbative approach has to be abandoned, and one has to rely on more involved self-consistent methods [40].

In addition, we consider only *elastic* phenomena, in which the scattered photon has the same energy (wavelength) than the incident one.

The model we are presenting is in the regime of validity of a diffusive model, but has a more general nature, and can be easily generalized to those cases where the diffusive approach may not be justified, as for anisotropic scattering and nematic liquid crystals (in chapter 3).

2.3 The radiative transfer equation

The microscopic model of light scattering is provided by the Maxwell's equations for electro-magnetic waves, which contain multiple scattering but which are of difficult solution when many scattering centers have to be taken into account.

An alternative approach makes use of the radiative transfer equation, which is a local balance equation, similar to the Boltzman equation in kinetic theory, for the diffused intensity [3]. Radiative transfer is an old subject that goes back to the end of the 19^{th} century, when astrophysicists [41] formulated the equation of radiative transfer. In the equation of radiative transfer, light phase and interference is neglected, and a diluted medium is assumed. It can, however, be derived directly from Maxwell's theory.

In literature there exists many equations equivalent to the radiative transfer equation, and which have been written for specific geometries or in different formats, like the Bethe-Salpeter, the Boltzman and the Milne equation.

The radiative transfer equation can be solved also for anisotropic scattering [42] and nematic liquid crystals [43] but it is quite involved. Few approximations can decrease considerably the problem.

2.3.1 Diffusion approximation

The simplest model of light transport induced by multiple scattering can be obtained disregarding interference effects, and introducing a continuity equation for the light intensity which expresses the conservation of the transported energy. The validity of this model is only after distances longer than the light wavelength but also longer than the mean free path.

If we restrict to the light in the bulk, this condition holds, $L \ll \ell_s$, and we can neglect the effect of the specific incident light polarization and direction, and that of the sample border.

Then we can assume that the scattering probability is always the same in each point of the sample and for each light state. This is usually confirmed by the experimental evidence of the Beer-Lambert's law for the light (coherent) transmission in a opaque medium,

$$I(\mathbf{r}) = I(0) \exp -r/\ell_s. \tag{2.14}$$

We are now naturally lead to think that the step length probability $P(r)$ for a photon is exponential with the distance r,

$$P(r) \sim \exp -r/\ell_s. \tag{2.15}$$

This will be the first step towards a mesoscopic theory (see later), as it will allow to move from the microscopic picture of the not-averaged scattering amplitudes, to a model which is based on a bigger building block with stochastic nature. All the complex effects that take place for distances smaller than ℓ_s can be simplified in order to get a vaster view.

The diffusive model can be interpreted as a stochastic model for an energy wavepacket (a classical particle) with velocity v. The step length between two successive interactions (collisions) is given by a certain distribution $P(r)$. After each scattering event the photon is scattered elastically in a direction described by another distribution: the differential scattering cross-section. This is a random walk, whose mean displacement r as a function of time (t) satisfies

$$\left\langle \frac{r^2}{t} \right\rangle \xrightarrow[t\to\infty]{} 6\,\mathcal{D}, \tag{2.16}$$

for a costant $\mathcal{D}$. Eq. (2.16) can be considered as a one of the definitions of the *diffusion constant* $\mathcal{D}$.

The diffusive model describes very well the long-distance transport but requires an assumption on the boundary conditions. The typical assumptions will be discussed later in the section.

Following this random walk picture one finds the diffusion equation for the light intensity $I(\mathbf{r}, t)$, being the latter the energy flux per unit solid angle at position $\mathbf{r}$ and time t

$$S(\mathbf{r}, t) + \frac{\partial I(\mathbf{r}, t)}{\partial t} = \mathcal{D}\nabla^2 I(\mathbf{r}, t) - \frac{v}{\ell_a} I(\mathbf{r}, t) \tag{2.17}$$

where $S(\mathbf{r}, t)$ is the light source, and ℓ_a the absorption length, over which the light is attenuated by a factor e^{-1}.

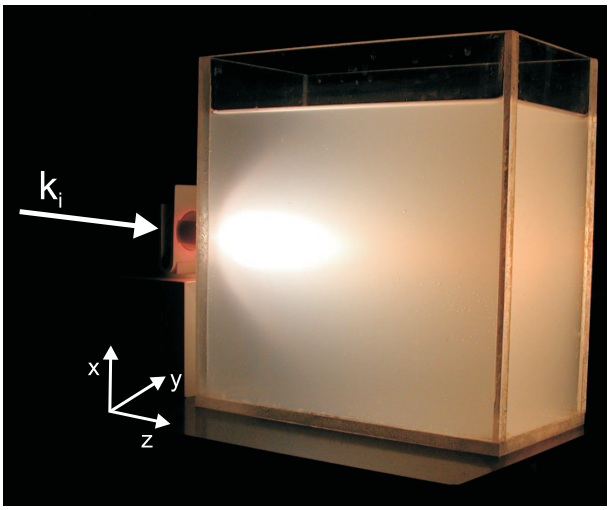

Figure 2.5: Light diffusion in a turbid liquid (courtesy of Francesco Io Bue, http://olympus.umh.ac.be/).

For comparison with the experiments, we will assume a slab geometry, and we will investigate the macroscopic light transport from the source through the scattering medium, as in Fig. 2.5. If the step length probability $P(r)$ is chosen to be exponential with the distance r, as in Eq. (2.15) consistently with the Beer-Lambert's law of attenuation of a spherical wave (radiated from the scatterer), then, from Eq. (2.16), the diffusion constant $\mathcal{D}$ can be expressed as a function of v and ℓ_t [44]

$$\mathcal{D} = \frac{1}{3} v \, \ell_t. \tag{2.18}$$

The central quantities in a diffusive process are the characteristic length ℓ_t and velocity v of the energy random walk in the disordered medium. The energy velocity can be very different from the light velocity in an equivalent dielectric medium, especially if scattering resonances are involved [45]. The transport mean free path (ℓ_t) can be defined as the average length after which the scattered photon has lost completely memory of its previous propagation direction. If no further complications are brought by anisotropy,

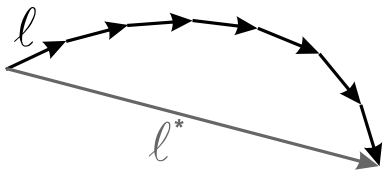

Figure 2.6: Transport mean free path and scattering mean free path.

birefringency or optical activity, i.e. if the microscopic anisotropy averages out and the overall diffusive process is isotropic, the transport mean free path can be calculated from

the scattering mean free path, taking into account the directionality of the scattering emission, weighting ℓ_s with the cosine of the scattering angle with respect to the forward direction:

$$\ell_t = \frac{\ell_s}{1 - \langle \cos\theta \rangle}. \tag{2.19}$$

On length scales smaller than ℓ_t, the scattering events are correlated, but for distances larger than ℓ_t the microscopic correlations are completely averaged out. The diffused light is transmitted as if the medium was thinner by a factor $(1 - \langle \cos\theta \rangle)$.

For isotropic scattering media $\ell_t = \ell_s$ as the average of the cosine of the scattering angle is zero. An example is Rayleigh scattering, where $\langle \cos\theta \rangle = 0$. For Mie scatterers we may easily have $\langle \cos\theta \rangle$ as big as 0.5 (see Fig. 2.3), therefore $\ell_t = 2\ell_s$ and two or more scattering events are required to lose completely the knowledge of the initial direction. Anisotropic media, as for example nematic liquid crystals, may have a strongly asymmetric scattering cross-section and therefore ℓ_t can be as big as hundreds of ℓ_s (see Fig. 2.4).

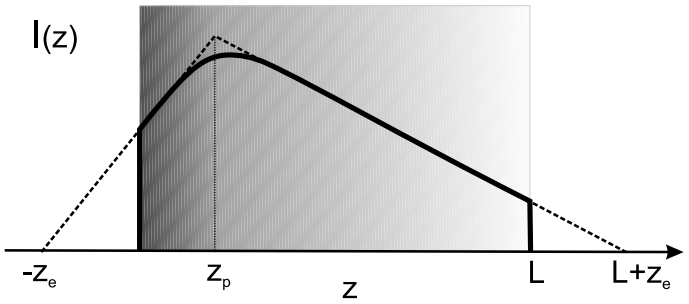

Figure 2.7: Photon concentration vs distance into the sample. Extrapolation length z_e and penetration depth z_p are shown.

The main limitation of a diffusion model is that it requires the external information about the boundary condition, or in other words that diffusion approximation cannot be used to predict light transport at the first scattering orders. The main boundary condition is the intensity distribution at the sample front surface, which results from the multiple scattering. This is accounted for with the extrapolation length z_e, the length over which the modes of diffusion can be considered zero (see Fig. 2.7). Usually the extrapolation length is chosen to be $z_e = 0.71\ell_t$ or $z_e = 2/3\ell_t$. In Fig. 2.7 also the penetration length z_p is shown, which is instead related to the source of light, and is typically set to its average value (for isotropic scattering), $z_p = \ell_t$.

2.4 Reciprocity

Maybe the most robust interference effect which is not included in the diffusive picture can be attributed to reversed paths, as illustrated in Fig. 2.8, where the photon follow the same path in the two opposite directions. Under general conditions, the phase coherence of these contributions is kept, and their interference has to be considered. A simple relation between the amplitudes of the reverse paths can be obtained with the reciprocity principle.

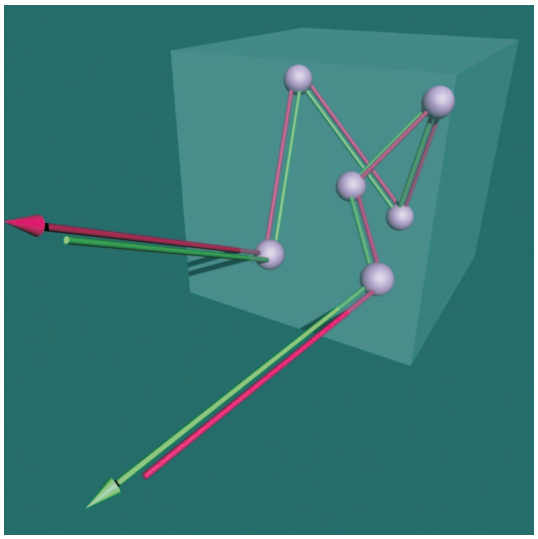

Figure 2.8: Reversed paths in a 3d random walk.

Optical measurements on linear physical systems obey the general principle of reciprocity, i.e., their results are invariant with respect to an interchange of source and detector[2] (see, e.g., [3]). A popular version of this law could be: "if I see you, you see me". The concept of reciprocity is strongly linked with that of time-reversal symmetry.

Maxwell's equations for the electromagnetic field are time-reversal invariant if the current is. A sufficient condition is the vanishing of free currents, as for example happens in dielectrics. The concept of time-reversal symmetry is often associated with optical *phase-conjugation*. One electromagnetic field is the phase conjugate of another if its phase is the complex conjugate of the other's. After phase-conjugation the wavefront retraces the evolution that it formerly underwent, even to the extent that distortions induced by a scattering medium are reversed. A time-reversal experiment requires the phase-conjugation of all the waves, unique condition to revert the full microscopic process. If one expresses a field in Fourier components, then the microscopical time reversal of

$$\mathcal{E}(\mathbf{r},t) = A\,\boldsymbol{\epsilon}\,e^{i\mathbf{k}\cdot\mathbf{r}}\,e^{-i\omega t} \tag{2.20}$$

whose real amplitude is A, polarization $\boldsymbol{\epsilon}$ and phase $e^{i\mathbf{k}\cdot\mathbf{r}-i\omega t}$, k-vector $\mathbf{k}$ and frequency ω, is

$$\mathcal{E}_{\rm rev}(\mathbf{r},t) = A\,\boldsymbol{\epsilon}^*\,e^{-i\mathbf{k}\cdot\mathbf{r}}\,e^{i\omega t} \tag{2.21}$$

whose phases are complex conjugated pairs (the star denotes the complex conjugation). Therefore, optical phase conjugation is equivalent to reversal of time.

As an example of this principle if one could invert the time for all the waves diffused from a laser beam incident on a scattering medium, then one would see all the scattered components reenter the medium, retrace back the path they formerly underwent, and interfere coherently into a coherent laser beam propagating backwards.

[2]The full electromagnetic system is reciprocal, meaning that for example in presence of a magnetic field one has to revert its sign to get the reciprocal configuration.

However reciprocity is not the same as time-reversal symmetry, since reciprocity relates input and output waves in pairs, irrespective of the presence or absence of other waves. Reciprocity states that the scattering matrix $\mathbf{S}$ and the T-matrix $\mathbf{T}$ are

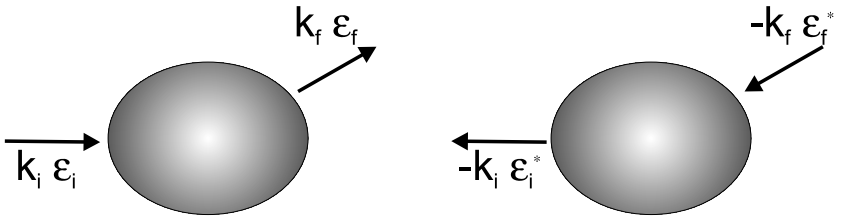

Figure 2.9: Reciprocal configurations, reciprocity ensures that the two processes have the same probability amplitude.

symmetric, and thus that

$$\langle \mathbf{k}_\mathrm{i}\epsilon_\mathrm{i}| \ \mathbf{T} \ |\mathbf{k}_\mathrm{f}\epsilon_\mathrm{f}\rangle = \langle -\mathbf{k}_\mathrm{f}\epsilon_\mathrm{f}^* \mid \mathbf{T} \mid -\mathbf{k}_\mathrm{i}\epsilon_\mathrm{i}^*\rangle \tag{2.22}$$

The condition of time-reversal invariance is equivalent to both energy conservation and reciprocity [35], therefore a scattering system may be reciprocal, without being conservative. In this case, e.g. in presence of (linear) absorption, the system is not time-reversal invariant, but the equivalence of the direct and reverse amplitude can be guaranteed by reciprocity.

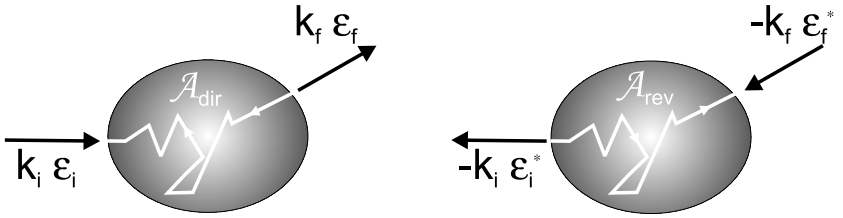

Figure 2.10: Reciprocal light path configurations, reciprocity ensures that the two light paths have the same scattering amplitude.

A practical and equivalent formulation of reciprocity, which is suitable for our proposes is the following: given two photon states $|\mathbf{k}_\mathrm{i}\epsilon_\mathrm{i}\rangle$ incident and $|\mathbf{k}_\mathrm{f}\epsilon_\mathrm{f}\rangle$ scattered from the system, reciprocity ensures that the two diffusion amplitudes (defined in analogy with $\mathbf{f}(\mathbf{k}_\mathrm{i}, \mathbf{k}_\mathrm{f})$, Eq. (2.7)), $\mathcal{A}_\mathrm{dir}$ and $\mathcal{A}_\mathrm{rev}$, for the direct and reverse paths are related by:

$$\mathcal{A}_\mathrm{dir} = \mathcal{A}(\mathbf{k}_\mathrm{i}\epsilon_\mathrm{i} \to \mathbf{k}_\mathrm{f}\epsilon_\mathrm{f}) \ = \ \mathcal{A}(-\mathbf{k}_\mathrm{f}\epsilon_\mathrm{f}^* \to -\mathbf{k}_\mathrm{i}\epsilon_\mathrm{i}^*) = \mathcal{A}_\mathrm{rev}. \tag{2.23}$$

The equality of the amplitudes of the direct and reverse paths is a consequence of the symmetry induced by reciprocity. When reciprocity is broken, for example in a magneto-active medium, then the direct and reverse paths may (and do) have different complex amplitudes and interference effects can be strongly reduced.

2.5 Coherent backscattering

One of the most robust interference phenomena that survives multiple scattering is coherent backscattering or weak localization of light [8, 9, 10, 11]. In weak localization, interference of the direct and reverse paths leads to a net reduction of light transport in the forward direction, similar to the weak localization phenomenon for electrons in disordered (semi)conductors and often seen as the precursor to Anderson (or strong) localization of light [12, 13, 14]. Weak localization of light can be detected since it is manifest as an enhancement of light intensity in the backscattering direction. This substantial enhancement is called the cone of coherent backscattering[3].

Weak localization has been initially studied for electronic systems, in the 1970s, where it has been reported as quantum interference (coherent echo) between electronic waves multiple scattered by impurities in conductors [46]. Weak localization manifests itself as an anomaly of the resistance of a conducting thin film [47, 48]. In electronic systems it has arisen much interest, as it is one of those unique cases where the superposition principle of quantum mechanics leads to observable consequences in the properties of macroscopic systems [49].

At the beginning of the 1980s, this concept based on interference has been successfully exported also to light waves [8, 9, 10, 11], which instead of electrons show very weak photon to photon interaction, have a much longer coherence time and are extremely sensitive to interference effects. On the other hand in optical experiment, it is hard to measure quantities like the total conductance, but it is possible, due to the long coherence length, to observe its counterpart, i.e. directly the interference-induced increase diffusion in backscattering: the coherent backscattering cone.

Since the first experimental observation of coherent backscattering from colloidal suspensions [8, 9, 10], the phenomenon has been successfully studied for electromagnetic waves in strongly scattering powders [50, 51], cold atom gases [52, 53], two-dimensional random systems of rods [54], randomized laser materials [55], disordered liquid crystals [56, 57], chaotic cavities [58] photonic crystals [59, 60] and even sea bottom [61]. The phenomenon is typical of any wave which is multiply scattered, and it has indeed been observed also for mechanical waves: acoustic waves in macroscopic disordered systems [62] and even seismic waves propagating in the earth crust [63].

Weak localization has its origin in the interference between direct and reverse paths in the backscattering direction. When a multiply scattering medium is illuminated by a laser beam, the scattered intensity results from the interference between the amplitudes associated with the various scattering paths; for a disordered medium, the interference terms are washed out when averaged over many sample configurations, except in a narrow angular range around exact backscattering where the average intensity is enhanced. This phenomenon, is the result of many two-waves interference patterns

$$I(\theta, \phi) = I_0 \left(1 + \zeta \cos(\mathbf{d} \cdot \Delta\mathbf{k})\right) \tag{2.24}$$

where I_0 is the total intensity forgetting interferences, ζ the contrast of the interference, θ and ϕ the angles with respect to the backscattering direction, and we assume no

[3]The two terms coherent backscattering and weak localization are often used through each other, but, if we want to be more precise, the former refers to the light which is backscattered more than expected by diffusion theory, while the latter to a decrease of the diffusion constant.

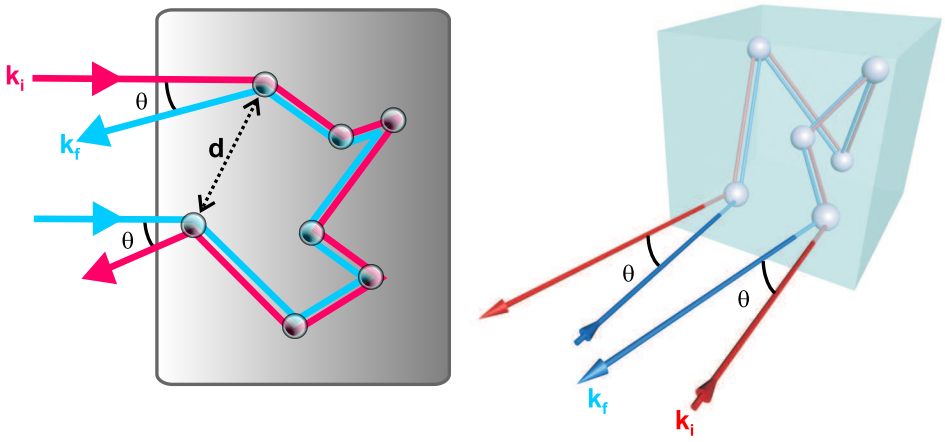

Figure 2.11: Counter-propagating light paths that give rise to coherent backscattering.

additional phase difference along the reverse paths exists. The incident and scattered k-vector $\mathbf{k}_\mathrm{i}$ and $\mathbf{k}_\mathrm{f}$ are written as

$$\begin{aligned} \mathbf{k}_\mathrm{i} &= (0,0,k) \\ \mathbf{k}_\mathrm{f} &= (-k\sin\theta\cos\phi, -k\sin\theta\sin\phi, -k\cos\theta). \end{aligned} \tag{2.25}$$

This interference is generated by counter-propagating light paths with entering-exiting distance $\mathbf{d} = \mathbf{r}_1 - \mathbf{r}_N$ and initial and final k-vectors $\mathbf{k}_\mathrm{i}, \mathbf{k}_\mathrm{f}$ such that $\Delta\mathbf{k} = \mathbf{k}_\mathrm{f} + \mathbf{k}_\mathrm{i}$ (see Fig. 2.11). Maximum interference is obtained when the counter-propagating paths have the same amplitude (and thus $\zeta = 1$), and only at $\theta = 0$, (see Fig. 2.12). Reciprocity is an important ingredient as it ensures the equality of the direct and reverse path amplitudes. For example, as predicted [64], it was experimentally observed [65, 66, 67] that the presence of an external magnetic field breaks the reciprocity and results in a decrease of the coherent backscattering enhancement as well as some rather complicated behavior of the cone shape [68]. Here onwards we will assume $\zeta = 1$.

The cone is the Fourier transform of the spatial distribution of the intensity of the scattered light on the sample surface, when the latter is illuminated by a point-like source [65]. The enhanced backscattering relies on the constructive interference between reverse paths. One can make an analogy with a Young's interference experiment, where two diffracting slits would be positioned in place of the "input" and "output" scatterers (see figure 2.11). If the slits are backlit with a plane wave (of wavevector $\mathbf{k}_\mathrm{i}$), the interference produces a sinusoidal fringe pattern in the far field, with a maximum intensity at $\theta = 0$ and a fringe spacing inversely proportional to the transverse spacing between the scatterers. The coherent backscattering cone comes from a superpositions of many of these fringes, which are all in phase only at $\theta = 0$ (see for example the top of figure 2.12).

The triangular top of the coherent backscattered profile is sensitive to the long and diffusive paths which have very far entrance-exit points, and thus short spatial frequency contribution. This can be evident if we look at the phase difference between

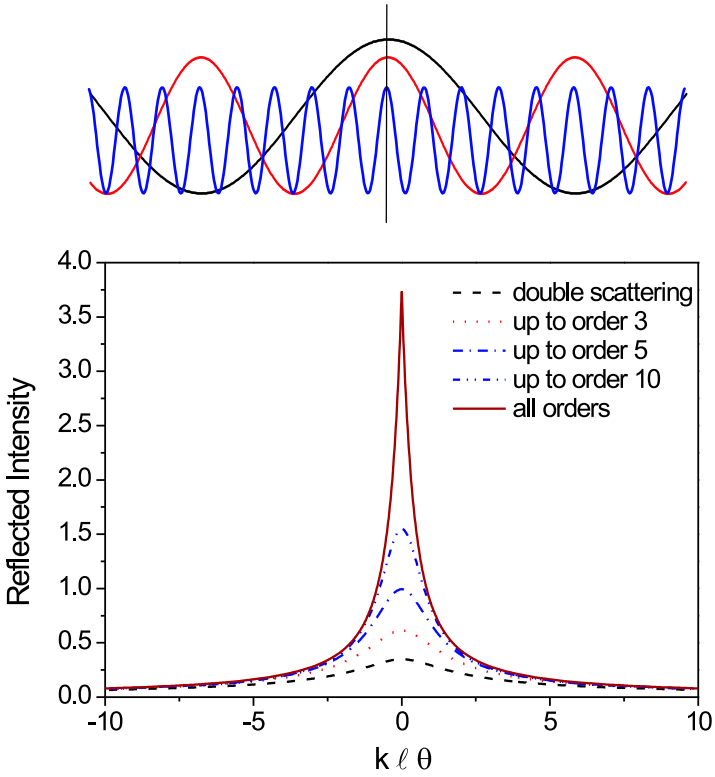

Figure 2.12: Coherent backscattering arises from many two-wave interference patterns which are all in phase at $\theta = 0$. In the figure, the full profile (full line) and the interference that results from only double scattering (dashed line), and a few lower scattering orders (dotted and mixed lines) are shown. The line profile is obtained with a Monte Carlo simulation for scalar waves. In the top panel, a few two-paths interference patterns are shown before averaging.

two paths, which is

$$\Delta\phi = \frac{2\pi}{\lambda}(\mathbf{d}\cdot\Delta\mathbf{k}) \tag{2.26}$$

and which can be simplified in the small θ limit (milliradians) into

$$\Delta\phi \approx \frac{2\pi}{\lambda}\ \theta\ |\mathbf{r}_N - \mathbf{r}_1| \tag{2.27}$$

If we replace in Eq. (2.27) $|\mathbf{r}_N - \mathbf{r}_1|$ by the mean separation between the first and last scattered, which is of the order of the transport mean free path (ℓ_t), the phase difference between the reciprocal paths becomes:

$$\Delta\phi \approx \frac{2\pi}{\lambda}\ \theta\,\ell_t. \tag{2.28}$$

Under diffusion approximation, one can find for the cone an opening angle (at full width half maximum) which is

$$W \simeq \frac{0.7}{k\ell_t}. \tag{2.29}$$

The first scattering orders (small N), are very important as they get less dephased (see Eq. (2.27)). The factor 0.7 of Eq. (2.29) comes from the averaging of many scattering order contributions, and it has a value close to unity: double scattering dominates.

The wings are influenced by the lower spatial frequencies, and therefore by the short paths due to low order scattering. The top and full width at half maximum are determined by the transport mean free path (ℓ_t), which is an averaged quantity, whereas the wings are strongly influenced by the details of the not-averaged single scattering differential cross section. In Fig. 2.12, the profiles of the interference that results from the different contribution are shown. The line profile is obtained with a Monte Carlo simulation for scalar waves. In the top panel, few two-paths interference patterns before averaging show the different spatial frequency contributions.

2.6 Theoretical approaches to multiple scattering of light

The interaction of light and matter can be described by the Maxwell's equations [69] which relate the microscopic fields with their induction fields. Under the approximation of a linear, frequency independent dielectric constant (and magnetic permeability equal to unity), and no free charges, we can write the wave equation for the electric field

$$\left[\nabla \times \nabla \times + \frac{1}{c^2}\frac{\partial^2}{\partial t^2}\,\varepsilon\right]\mathcal{E}(\mathbf{r},t) = 0 \tag{2.30}$$

where c stands for the light velocity in free space:

$$c = \frac{1}{\sqrt{\varepsilon_0\mu_0}}.$$

In random media, we can replace the dielectric tensor with

$$\varepsilon = \overline{\varepsilon} + \delta\varepsilon(\mathbf{r},t) \tag{2.31}$$

whose homogeneous part is $\overline{\varepsilon}$, and the randomly fluctuating part $\delta\varepsilon(\mathbf{r},t)$ is usually a Gaussian random variable described by a certain correlation function.

We then assume $\langle\epsilon\rangle = 1$ and non-absorbing medium $\mathrm{Im}(\epsilon) = 0$. Due to the linearity of the equation, harmonic modes can be separated into a space dependent field pattern, and the time dependence of Eq. (6.3) can be removed. After some algebra the wave equation can be put in the form of

$$\left[\nabla^2 + k^2\right]\mathcal{E}(\mathbf{r}) = V(\mathbf{r})\mathcal{E}(\mathbf{r}) \tag{2.32}$$

with a potential of the form

$$V(\mathbf{r}) = -k^2[\varepsilon(\mathbf{r}) - 1], \tag{2.33}$$

and $k = \omega/c$.

The special case of identical isotropic point-like scatterer (Rayleigh scattering) is very important as it is one of the few that can be solved completely: we can assume a white noise distribution of the fluctuating part of the dielectric constant, which has correlation function

$$k^4\ \langle\varepsilon(\mathbf{r})\varepsilon(\mathbf{r}')\rangle_{ensemble} = \gamma\ \delta(\mathbf{r}-\mathbf{r}') \tag{2.34}$$

This description of the dielectric constant is valid if the scale of the fluctuations of $\varepsilon(\mathbf{r})$ is large in comparison with λ, the so-called slow-varying envelope approximation. In such a case the interaction is localized at position R_i, the dielectric constant can be written as

$$\epsilon(\mathbf{r}) = 1 + \sum_i \alpha\ \delta(\mathbf{r} - R_i) \tag{2.35}$$

where α is the scatterer polarizability. The scalar wave equation then reads:

$$\left[\nabla^2 + k^2\right] \mathcal{E}(\mathbf{r}) = u \sum_i \delta(\mathbf{r} - R_i)\mathcal{E}(\mathbf{r}) \tag{2.36}$$

where the potential is parameterized by u, the potential strength, $u = -k^2\,\alpha$.

2.7 The Green function

A Green's function is an integral kernel that can be used to solve an inhomogeneous differential equation with boundary conditions.

We start here with a formalism typical of Quantum Mechanics, for matter waves, which can easily extended for light waves. To a system characterized by the Hamiltonian H

$$H_0|\varphi_E\rangle = E|\varphi_E\rangle \tag{2.37}$$

symbolically one can associate a Green function

$$G_0(E) = \frac{1}{E - H_0} \tag{2.38}$$

which satisfies the equation:

$$[H_0(\mathbf{r}) - E]\ G_0(\mathbf{r}, \mathbf{r}'; E) = -\delta(\mathbf{r}, \mathbf{r}'). \tag{2.39}$$

The Green function contains all the information on the system, it has a pole at the energy of each bound state, and each eigenfunction of the Hamiltonian can be obtained from G_0. The eigenvectors of the full problems, for $H = H_0 + V(r)$, can then be obtained from a superposition of Green functions of the unperturbed case [70].

For light waves we replace the Hamiltonian and the energy by

$$\begin{aligned} H &= -\nabla^2 + V(\mathbf{r}) \\ E &= k^2. \end{aligned} \tag{2.40}$$

2.7.1 Green function in the wave equation

The vacuum Green function is the solution of the vacuum wave equation ($V \equiv 0$) for a δ-function source, a point-like light emitter:

$$-[\nabla^2 + k^2]G_0(\mathbf{r}, \mathbf{r}', \mathbf{k}') = \delta(\mathbf{r}, \mathbf{r}'). \tag{2.41}$$

Formally this equation can be solved and the Green function calculated as

$$G_0 = \frac{1}{k^2 - H_0} = \frac{1}{k^2 + \nabla^2}. \tag{2.42}$$

Such a Green function is a spherical wave radiating from the scatterer:

$$G_0(\mathbf{r},\mathbf{r}',\mathbf{k}') = -\frac{e^{i\mathbf{k}'\cdot(\mathbf{r}-\mathbf{r}')}}{4\pi|\mathbf{r}-\mathbf{r}'|}. \tag{2.43}$$

The importance of the Green functions is that any solution of the inhomogeneous wave equation for a potential $V(\mathbf{r})$

$$[\nabla^2 + k^2]\varphi_k(\mathbf{r}) = -V(\mathbf{r})\varphi_k(\mathbf{r}) \tag{2.44}$$

which has associated the Green function

$$G = \frac{1}{k^2 - H} = \frac{1}{k^2 + \nabla^2 - V(\mathbf{r})}, \tag{2.45}$$

can be expressed in terms of the Green functions of the homogeneous equation (the vacuum Green functions), in terms of the integral equation (for simplicity we now drop the index k)

$$\varphi(\mathbf{r}) = \varphi_0(\mathbf{r}) - \int G_0(\mathbf{r},\mathbf{r}',\mathbf{k}')V(\mathbf{r}')\varphi(\mathbf{r}')\ d\mathbf{r}' \tag{2.46}$$

and of $\varphi_0(\mathbf{r})$, a solution of the vacuum wave equation:

$$[\nabla^2 + k^2]\ \varphi_0(\mathbf{r}) = 0. \tag{2.47}$$

The proof is direct if we apply $(\nabla^2 + k^2)$ to both sides of Eq. (2.46) and move it under the integral:

$$\begin{aligned}
(\nabla^2 + k^2)\varphi(\mathbf{r}) &= (\nabla^2 + k^2)\varphi_0(\mathbf{r}) - \int d\mathbf{r}\ (\nabla^2 + k^2)G_0(\mathbf{r},\mathbf{r}',\mathbf{k}')V(\mathbf{r}')\varphi(\mathbf{r}') \\
(\nabla^2 + k^2)\varphi(\mathbf{r}) &= 0 - \int d\mathbf{r}\ \delta(\mathbf{r},\mathbf{r}')V(\mathbf{r}')\varphi(\mathbf{r}') \\
(\nabla^2 + k^2)\varphi(\mathbf{r}) &= -V(\mathbf{r})\varphi(\mathbf{r})
\end{aligned} \tag{2.48}$$

2.7.2 The dressed Green function and the T-matrix

Iterating Eq. (2.46) yields

$$\varphi(\mathbf{r}) = \varphi_0(\mathbf{r}) - \int G_0(\mathbf{r},\mathbf{r}'',\mathbf{k}'')\mathbf{T}(\mathbf{r}'',\mathbf{r}',\mathbf{k}')\varphi(\mathbf{r}')\ d\mathbf{r}'d\mathbf{r}'' \tag{2.49}$$

which defines the T-matrix $\mathbf{T}(\mathbf{r},\mathbf{r}')$ given by

$$\begin{aligned}
\mathbf{T}(\mathbf{r},\mathbf{r}',\mathbf{k}') &= V(\mathbf{r})\delta(\mathbf{r},\mathbf{r}') + V(\mathbf{r})G_0(\mathbf{r},\mathbf{r}',\mathbf{k}')V(\mathbf{r}') + \\
&\quad + \int d\mathbf{r}''V(\mathbf{r})G_0(\mathbf{r},\mathbf{r}'',\mathbf{k}'')V(\mathbf{r}'')G_0(\mathbf{r}'',\mathbf{r}',\mathbf{k}')V(\mathbf{r}') + \ldots
\end{aligned} \tag{2.50}$$

One uses the term transition matrix since a T-matrix projects ingoing states of the incident light onto outgoing states.

A generic solution can always be expressed in terms of the vacuum Green function and of the single scattering T-matrix [71]

$$\varphi(\mathbf{r}') = e^{i\mathbf{k}\cdot\mathbf{r}'}\ +\ G_0(\mathbf{r},\mathbf{r}',\mathbf{k}')\ \mathbf{T}(\mathbf{r},\mathbf{r}',\mathbf{k}')\ e^{i\mathbf{k}\cdot\mathbf{r}} \tag{2.51}$$

where the first term represents the incoming wave transported to position $\mathbf{r}'$, with $\varphi_0 = e^{i\mathbf{k}\cdot\mathbf{r}}$. The second term in Eq. (2.51) is the wave transported to position $\mathbf{r}'$ by the vacuum Green function $G_0(\mathbf{r}', \mathbf{r})$ shown in Eq. (2.43), after it picked up a scattering factor $T(\mathbf{r}', \mathbf{r})$, the scattering amplitude, at the scatterer.

The single scattering T-matrix of the scattering process (of the full system), can be expressed as

$$T = V + VG_0V + VG_0VG_0V + VG_0VG_0VG_0V + \dots \tag{2.52}$$

In diagrammatic notation T is the sum of all the recurrent scattering events undertaken by a single scatterer:

$T_\alpha = \times_\alpha =$ 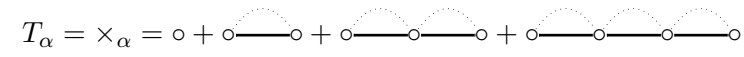 (2.53)

where $\circ$ is the single scattering from a given scatterer α, the second term is the double recurrent scattering from the same scatterer, and so on. At first order the scattered field induces an electric polarization. This polarization changes the scattering properties of the medium, which modifies the polarization (second order), and so on.

A potential $V(\mathbf{r})$ changes the bare amplitude Green function G_0 in such a way that G (the dressed one) can be described by the Lippmann-Schwinger equation [72]

$$G(\omega) = G_0(\omega) + G_0(\omega)\ V\ G(\omega), \tag{2.54}$$

which is analogous to Eq. (2.46).

The knowledge of T is equivalent of the knowledge of the complete Green function of the system as the latter can be expressed, without approximations in terms of T:

$$G(\omega) = G_0(\omega) + G_0(\omega)T(\omega)G_0(\omega) + G_0(\omega)T(\omega)G_0(\omega)T(\omega)G_0(\omega) + \dots \tag{2.55}$$

For consistency with the usual formalism we now onwards refer with ω to the energy dependence of the functions, as in Eq. (2.55).

The Green function in Eq. (2.54) and (2.55) is the propagator for a given scatterer configuration, and therefore it is not translational or rotational invariant, $G(\mathbf{r}_1, \mathbf{r}_2) \neq G(|\mathbf{r}_1 - \mathbf{r}_2|)$. Instead the dressed Green function, which is obtained from ensemble averaging of the Green function of Eq. (2.54), has these two symmetries.

2.8 The mesoscopic approach

In order to model the scattering from an ensemble of discrete scattering centers, we have to use the complete Green function of the system, which is the solution of the full wave equation that includes all the scattering centers, as in Eq. (2.32):

$$-[\nabla^2 + k^2]G + \sum_i V(\mathbf{r} - \mathbf{R}_i)G = \delta(\mathbf{r} - \mathbf{r}_0). \tag{2.56}$$

This is the *microscopic* approach. It provides exact equations which are usually impossible to solve without further approximations, as in an ordinary medium the number of scatterers can be easily as large as $10^9 - 10^{12}$. We are interested into properties averaged over the microscopic details, therefore a more effective approach is the *mesoscopic* one.

All the transport quantities we are interested in, like transmission, reflection, diffusion, etc..., can be expressed in terms of the amplitude G. Then one can average it, and obtain g, the average amplitude Green function. It is the vacuum Green function 'dressed' by the average interaction with the random scattering potential, which is the average inter-scattering propagator, which describes how the light is transported from one scatterer to the other, and in the presence of all the other scatterers.

Exact averaging over the disorder of the Green function is only possible in particular cases, and cannot be done in general. Facing such a problem, different theories have followed perturbative treatments, in order to discriminate between relevant and negligible contributions, and simplify substantially the equations. This means that one has to rely on a perturbative expansion of G in *scattering order* or in the diagrammatic approximation of the self-energy, developed in the *scatterer density*.

2.9 Diagrammatic approach for multiple scattering

The mesoscopic approach consists in expressing all the sought quantities in terms of the dressed Green function of the systems, and then to average them. This method has an equivalent representation in diagrams, which are very useful to visualize the equations. We choose to follow this approach as it can lead to integral equations which have a direct interpretation in terms of photon random walk, and thus can be very efficiently implemented in a Monte Carlo simulation.

We will go through the major results which have already been obtained [73], in order to introduce the concepts that we will extend and generalize for anisotropic scattering later in the chapter.

We consider an infinite system of randomly placed point scatterers. We want to calculate the dressed Green function, the average amplitude propagator in the disordered system. Such an operator takes into account that the propagation between different scattering centers is dressed with all the scattered fields, and therefore is the sum of all possible scattering paths that connect the two points in the system. It is therefore composed of the averaged T-matrix which is the sum of all the recurrent scattering events undertaken by a single scatterer.

We will in the following introduce the *self-energy* operator, and we will use it to obtain the average *intensity* propagator which describes what is measured in the experiments.

The conventions used throughout this thesis are that lower cases refer to averaged quantities, such that:

$$\begin{aligned} g_0 &\equiv \langle G_0 \rangle \\ g &\equiv \langle G \rangle \\ \mathbf{t} &\equiv \langle \mathbf{T} \rangle, \end{aligned} \tag{2.57}$$

and the symbols used in the diagrams are:

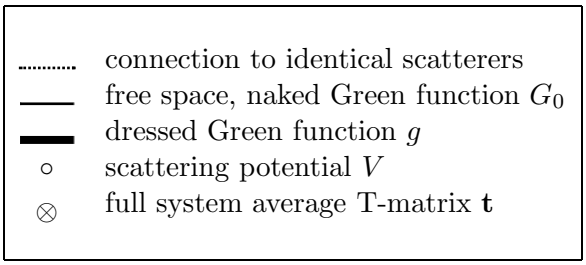

2.9.1 Averages of multiple scattering

When dealing with an ensemble of scatterers, in order to obtain meaningful properties that are not configuration-dependent, we have to calculate quantities averaged over many disorder configuration. Experimentally this is done by rotating the scattering sample, or letting the Brownian motion of a suspension average the position of the scatterers. Mathematically it involves the averaging, denoted by $\langle \cdots \rangle$, of the Green function and of the T-matrix. The brackets denote an ensemble averaging over all positions of the scatterers, in the so-called *thermodynamic limit*, where the number of individual scatterers as well as the size of the system tend to infinity, at constant density of the scatterers. Doing so, we are losing configuration-dependent properties, like light speckle, or some transient effects; on the other hand, the statistical approach that we are following allows to get rid of the microscopical details that complicate the microscopic Maxwell's equations.

2.9.2 Average amplitude Green function

The average Green function of the system, labelled with $g(\omega)$, is given by the sum over all scattering paths, therefore it is expressed in terms of the T-matrix, from Eq. (2.52):

$$g(\omega) = G_0(\omega) \; + \; \sum_{\alpha} \langle G_0(\omega) \mathbf{T}_\alpha G_0(\omega) \rangle \; + \; \sum_{\alpha \neq \beta} \langle G_0(\omega) \mathbf{T}_\alpha G_0(\omega) \mathbf{T}_\beta G_0(\omega) \rangle \; + \; \ldots \tag{2.58}$$

where the sum is performed over the scatterers.

If we assume that all the scatterers are *statistically independent*, then we can replace the average of the product of two T-matrix $\langle \mathbf{T}_\alpha \mathbf{T}_\beta \rangle$ by the product of the average $\langle \mathbf{T}_\alpha \rangle \langle \mathbf{T}_\beta \rangle$ and therefore Eq. (2.58) can be reduced to:

$g = \langle G \rangle$ =

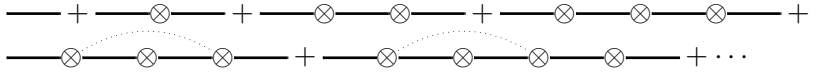

=

(2.59)

where $\otimes$ is the average T-matrix:

$\mathbf{t} = \langle \mathbf{T}_\alpha \rangle \equiv \otimes =$

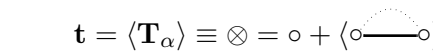

$+ \ldots$ (2.60)

Formally we have calculated the dressed propagator $g = \langle G \rangle$ averaging Eq. (2.55), with the help of $\mathbf{t}$, obtained from the averaging of Eq. (2.53). In the isotropic scattering medium, the T-matrix depends on the scatterer only for its position, and therefore, upon averaging $\mathbf{t}$ does not depend on the position of the scatterers (this is the statistic

translational invariance). But the series in Eq. (2.55) cannot be averaged over disorder analytically.

At this point, one is obliged to reduce the complexity of the problem and to rely on approximate solutions. One way is to omit the third and higher order contribution, this is the second order Born approximation, which is often used in electronic systems and is easier for small systems. A disadvantage of this approach is that it provides a diverging result in the thermodynamic limit of the system size which is increased to infinity.

2.9.3 The self-energy

In order to perform the ensemble averaging it is convenient to define the self-energy. It is the series of the recurrent scattering events that contributes to the Green function, and it is defined via the Dyson equation, which links the dressed or ensemble-averaged Green function to the naked one [74]:

$$\langle G \rangle = \langle G_0 \rangle + \langle G_0 \rangle \ \mathbf{\Sigma} \ \langle G \rangle. \tag{2.61}$$

Note that $g_0 = G_0$ as, in absence of the scattering potential, averaging over the disorder has no meaning. We rewrite then the Dyson equation, following the conventions defined in Eq. (2.57), as

$$g = g_0 + g_0 \ \mathbf{\Sigma} \ g \tag{2.62}$$

Eq. (2.62) expresses in a compact form an infinite perturbative series:

$$\begin{aligned} g &= g_0 + g_0\mathbf{\Sigma}g_0 + g_0\mathbf{\Sigma}g_0\mathbf{\Sigma}g_0 + ... \\ &= g_0 + g_0\mathbf{\Sigma}g \end{aligned} \tag{2.63}$$

which is a geometrical series, and thus can be formally solved as

$$g = \frac{1}{g_0^{-1} - \mathbf{\Sigma}}. \tag{2.64}$$

The role of the self-energy is to obtain a result for the full propagator g, valid at all scattering orders. The self-energy is an averaged quantity that cannot be defined for a single realization of the disorder. Its constitutive elements are the naked Green function and the averaged T-matrix. All the difficulties in calculating the dressed Green function are now moved to the self-energy, which is a macroscopic operator, function of $\mathbf{t}$, which instead has a microscopic nature.

The self energy can be developed in the density, and expressed in irreducible terms:

$\mathbf{\Sigma} =$ 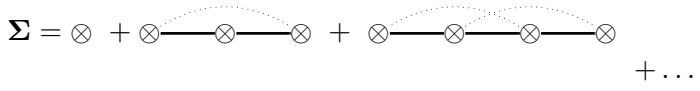 (2.65)

where $\otimes$ is the T-matrix as defined in Eq. (2.53), averaged over all positions of the scatterers, at *any* scattering order. *Irreducibility* means that any diagram that can be associated with the self energy cannot be separated into individual diagrams. Eq. (2.65) is made of many different contributions, which, apart from the first term, are all recursive (as indicated by the dotted lines). If we neglect recurrent scattering we can

stop the summation of Eq. (2.65) at the first element, and thus express the self-energy with the single scattering T-matrix.

$$\mathbf{\Sigma}(\omega) \approx n_p \; \mathbf{t}(\omega) = n_p \otimes \tag{2.66}$$

This approximation is valid only if the density (n_p) of the scatterers is not too high; this last requirement is very well accomplished if $k\ell \gg 1$. The extra scatterer density factors appear as a result of the averaging, and $\mathbf{t} = \langle \mathbf{T} \rangle$.

Finally we can calculate the dressed Green function from the knowledge of the self-energy, via Eq. (2.64). In the case of a uniform density medium, the propagator for the electric induction inside the effective medium is described by the dressed Green function [75]:

$$G(\mathbf{r}, \omega) = -\frac{k}{r}\, e^{ikr\mathcal{N}(\omega)} e^{i\frac{r}{2\ell_s}}. \tag{2.67}$$

The self-energy displaces the singularities of the Green function in the complex plane adding a real and imaginary part to G_0. A natural interpretation of Eq. (2.67) arises: the real part of $\mathbf{\Sigma}(\omega)$ contributes to the refractive index of the effective medium,

$$\mathcal{N}(\omega) \equiv 1 - \frac{\mathrm{Re}\mathbf{\Sigma}(\omega)}{k}, \tag{2.68}$$

while its imaginary part to the extinction of the wave,

$$\mathrm{Im}\mathbf{\Sigma}(\omega) = -\frac{1}{2\ell_s} \tag{2.69}$$

as it is connected with the scattering mean free path.

2.9.4 Average light intensity

We want to calculate the light intensity, and therefore we have to deal carefully with the average of the interference of the light amplitudes. The richness of the interference phenomena comes from the fact that average of the square is obviously not equal to the square of the average[4]. The diagrammatic approach enables to use a two-particle formalism which provides an equation equivalent to the Dyson equation for the self-energy, but for the light intensity. The knowledge of the average T-matrix ($\mathbf{t}$) is enough to know the self-energy ($\mathbf{\Sigma}$) and therefore the dressed Green function (g). We will arrive later in the chapter to the Bethe-Salpeter equation, which will connect the average intensity with the average tensorial product of two T-matrices, $\langle \mathbf{T}^\dagger \otimes \mathbf{T} \rangle$ [5].

The intensity, which is defined as the norm of the complex field amplitude $\mathcal{E}(r,t) = A\,\boldsymbol{\epsilon}\, e^{i\mathbf{k}\cdot\mathbf{r}+i\omega t}$,

$$\|\mathcal{E}\| = \mathcal{E}\,\mathcal{E}^* = A\,\boldsymbol{\epsilon}\, e^{i\mathbf{k}\cdot\mathbf{r}-i\omega t} \times A\,\boldsymbol{\epsilon}^*\, e^{-i\mathbf{k}\cdot\mathbf{r}+i\omega t}, \tag{2.70}$$

is the product of the amplitude of the field times its phase-conjugate, which is its time reversal counterpart (see section 2.4). We can extend this point of view, and separate the amplitude for a direct path from the amplitude for its reversed one,

$$\mathcal{A}_{\mathrm{dir}} = \mathcal{A}(\mathbf{k}_{\mathrm{i}}\epsilon_{\mathrm{i}} \to \mathbf{k}_{\mathrm{f}}\epsilon_{\mathrm{f}}) \quad \text{and} \quad \mathcal{A}_{\mathrm{rev}} = \mathcal{A}(-\mathbf{k}_{\mathrm{f}}\epsilon_{\mathrm{f}}^* \to -\mathbf{k}_{\mathrm{i}}\epsilon_{\mathrm{i}}^*), \tag{2.71}$$

[4] In multiple scattering theory, the latter term has the meaning of the so-called *coherent beam*, which is the part of the incident one which has not suffered any scattering event.

[5] Do not confuse the symbol $\otimes$ of the tensor product with that of the averaged T-matrix.

and consider them as independent contribution to the light intensity. What we are doing is just treat the advanced and retarded Green function independently. We can build up the intensity propagator pairing one retarded and one advanced amplitude Green function. The intensity Green function, not averaged over the scattering configurations, can be written as a sum of all possible diagrams like

$G^\dagger\, G =$ 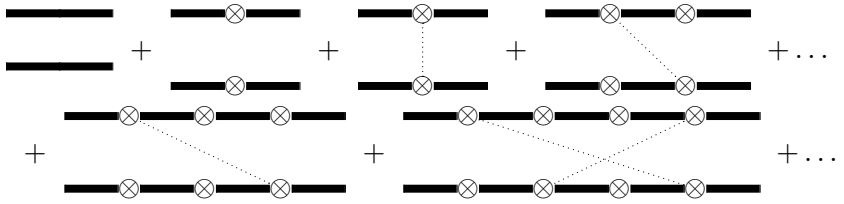

(2.72)

where the † is the transpose conjugate, the dotted lines connect identical scatterers and the full lines are the dressed Green functions that allow propagation from one scatterer to the other. Following our statistical approach, we are interested in the intensity propagator averaged over position of the scatterers which is obtained by the average of $G^\dagger G$:

$\langle\, G^\dagger\, G\rangle =$ 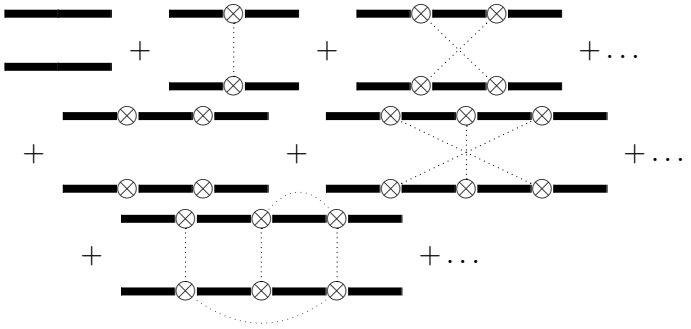

(2.73)

The diagrams in which G and $G^\dagger$ perform uncorrelated paths are averaged to zero, given the random nature of their phase difference. Note that even if scatterer to scatterer correlations are absent, (independent scattering approximation), there are many *correlated paths*, which can be in phase and survive averaging, as for example the class of reciprocal paths.

We can formulate a relation analogous to the Dyson equation (Eq. 2.62) for the intensity propagator, relation which is called the Bethe-Salpeter equation:

$$\langle G^\dagger G\rangle = g^\dagger g + g^\dagger g\; U\; \langle G^\dagger G\rangle. \tag{2.74}$$

Now the place of the self-energy is taken by the full irreducible vertex U:

$U \quad =$ 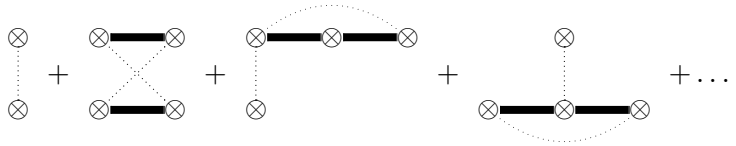 (2.75)

which is connected to the single scattering T-matrix via [76]

$$\langle \mathbf{T}^\dagger \otimes \mathbf{T}\rangle = U + U\; \langle G^\dagger G\rangle\; U + \ldots \tag{2.76}$$

Calculation of all possible diagrams is a very complex combinatory task and it provides an equation that is not easily solvable. For this reason one includes the interference effects one by one, loosening the approximation any time a new class of diagrams is included. As for the self-energy, here we keep only the first term of the perturbative expansion of U. In the lowest order in the scatterer density one can approximate

$U \quad \approx$  (2.77)

or equivalently:

$$U(\mathbf{k}_1\boldsymbol{\epsilon}_1, \mathbf{k}_2\boldsymbol{\epsilon}_2) = n_p\langle \mathbf{T}^\dagger(\mathbf{k}_1\boldsymbol{\epsilon}_1) \otimes \mathbf{T}(\mathbf{k}_2\boldsymbol{\epsilon}_2)\rangle \tag{2.78}$$

This approximation is equivalent to the radiative transfer equation, result which is surprising and encouraging, and confirms the validity of the mesoscopic approach.

Before continuing one needs to check the consistency of the approximation, namely the conservation of the energy. As we have shown, the averaged amplitude Green function suffers from extinction, it decays exponentially with the scattering mean free path (the imaginary part of the self energy, as in Eq. (2.67)). The electromagnetic energy is related to the average intensity, therefore to the irreducible vertex $U(\mathbf{k}_1\boldsymbol{\epsilon}_1, \mathbf{k}_2\boldsymbol{\epsilon}_2)$. Conservation of the energy is ensured by the Ward identity [76]:

$$\mathrm{Im}\boldsymbol{\Sigma}(\omega) = \sum_{\mathbf{k}_2,\boldsymbol{\epsilon}_2} U(\mathbf{k}_1\boldsymbol{\epsilon}_1, \mathbf{k}_2\boldsymbol{\epsilon}_2)\, \mathrm{Im}\, g(k_2, \omega). \tag{2.79}$$

In order to be consistent with the Ward identity of Eq. (2.79), the approximations on $\boldsymbol{\Sigma}(\omega)$ and $U(\mathbf{k}_1\boldsymbol{\epsilon}_1, \mathbf{k}_2\boldsymbol{\epsilon}_2)$ have to correspond to the same perturbative order. In Eq. (2.66) we kept only the first term, at zero-th order in $k\ell$, the so called *Born approximation*. One can prove [76] that the expression for the vertex $U(\mathbf{k}_1\boldsymbol{\epsilon}_1, \mathbf{k}_2\boldsymbol{\epsilon}_2)$ as in Eq. (2.77) is consistent with energy conservation.

In the radiative transfer equation for diluted media, the only terms that are considered are the field amplitude squared, without interference. One can construct this contribution with the above expression of U (Eq. (2.77)) which can be diagrammatically presented by the so called ladder term:

$L \quad =$ 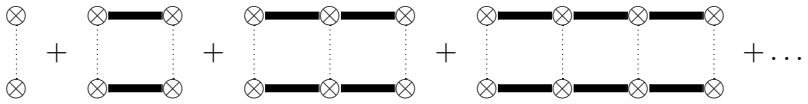 (2.80)

The first term is single scattering, only one scatterer is involved; the second one is the double scattering contribution, but without any interference: the scatterers are visited in the same order, and the result is just the single amplitude squared, and so on[6].

Refinements of this crude picture, that excludes all possible interference effects, involve the addition of some of the crossed diagrams that have been neglected. Coherent backscattering is originated from the *most crossed* diagrams which are:

$C \quad =$ 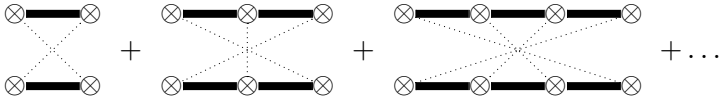 (2.81)

[6]This definition of the ladder term includes also single scattering. To be consistent with the literature we will change this definition in the next section.

The first term is the interference coming from the double scattering contribution, for paths such that the direct and reversed visit the same scatterers but in the opposite order; the second term is made of all the third order scattering paths, and so on. In Eq. (2.81) no recurrent diagrams are included, as we are assuming to be at low scatterer density, such that $k\,\ell_s \gg 1$, and thus paths which visit the same scatterer more than once have negligible contribution.

The ladder term conserves the energy, but the introduction of the crossed one causes further complications. The crossed term describes additional light intensity in the backward direction: the energy balance is not satisfied any more. The crossed term is intrinsically *not* self-consistent, it does not preserve the Ward identity (Eq. (2.79)), even if it is perfectly justified by intuition. The surplus intensity in backscattering which unbalances the energy conservation is proportional to $1/(k\ell)^2$ which is the solid angle involved in the coherent backscattering cone. We are performing a zero order perturbation on $(k\ell)$, and thus the energy missing in the balance, which is a second order contribution, is acceptable [7].

What we have calculated so far is valid in the bulk of the system, the ladder and the crossed diagrams start with the first scattering event. In order to calculate the light transport, the effect of the input and output coupling is very important. The mesoscopic approach, as a crucial difference with the diffusive, is valid also at the boundaries and no assumptions are needed to complete the calculations. The input and output coupling is just described by the Beer-Lambert's law (Eq. (2.14)) and therefore the intensity that arrives at the position of the first scattering event is just given by $\exp(-r/\ell_s)$ of the incident one, and analogously for the output coupling. This type of calculations will be clear in section 2.11 when we will traduce the diagrammatic approach into an integral one.

2.9.5 The weight of the ladder and crossed terms

One of the most important quantity that one want to measure in a coherent backscattering experiment is the enhancement factor, which is the ratio between crossed terms and all the other contributions. We should then compare Eq. (2.80) and Eq. (2.81). Usually single scattering, which has no counter-part in the crossed term, is not included in the ladder term, but it is considered independently as:

S = (2.82)

The new definitions of the ladder and the crossed term are

L = + + + ... (2.83)

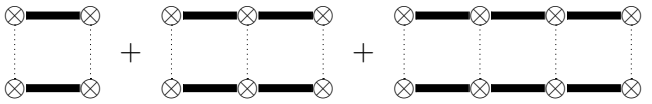

C = + + + ... (2.84)

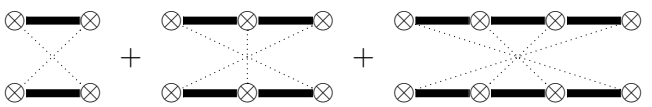

The reciprocity (section 2.4) ensures that each direct path has the same amplitude probability as its reversed one, and therefore also that each element of the crossed term

can be obtained from its ladder counter-part, just reverting the scattering sequence for the conjugate wave. The enhancement factor, at exact backscattering ($\theta = 0$), in absence of single scattering has therefore the value of 2, as

$$L = C \tag{2.85}$$

In presence of single-scattering the crossed term is not twice all the other contributions, and the enhancement is reduced from the value of 2 (see section 2.10.2).

2.10 The coherent backscattering cone line shape

2.10.1 The bistatic coefficient

What one wants to calculate is the component of the backscattered light which is enhanced compared to the diffusive background. We are interested in studying the so called "slab-geometry" where light is incident on a slab of infinite transverse extent, or the "semi-infinite geometry" when such a slab has infinite thickness. The quantity usually calculated in a scattering process is the bistatic coefficient as a function of angle, around exact backscattering. The bistatic coefficient is related to the scattering cross-section of the whole medium by [77]

$$\gamma(\mu_{\rm i}, \mu_{\rm f}) \equiv \frac{4\pi}{A} \left\langle \frac{d\widetilde{\sigma}}{d\Omega}(\mathbf{k}_{\rm i} \longrightarrow \mathbf{k}_{\rm f}) \right\rangle \tag{2.86}$$

which is a function of $\mu_{\rm i/f} = \cos_{\rm i/f}\theta$ the cosine of the incident and scattering angles; A is the illuminated area on the sample and $d\widetilde{\sigma}/d\Omega$ the differential scattering cross-section of the illuminated area of the sample. In this expression the brackets $\langle \ldots \rangle$ denote the an ensemble averaging over all positions of the scatterers, in the so-called *thermodynamic limit* defined in section 2.9.1. Note that Eq. (2.86) is valid only if $A \ll \ell_s$, for the average to be meaningful. The bistatic coefficient has the physical meaning of a normalized scattered intensity per solid angle,

$$\gamma = \frac{4\pi r^2}{A} \frac{\langle I(\mathbf{r}) \rangle}{I_0} \tag{2.87}$$

where I_0 is the incident intensity and $\mathbf{r}$ the distance of the observer from the sample. In general, if the scattering process depends also on other parameters, like polarization, we can define a more general bistatic coefficient, which has tensorial nature:

$$\gamma(\mathbf{k}_{\rm i}\epsilon_{\rm i}, \mathbf{k}_{\rm f}\epsilon_{\rm f}) = \frac{4\pi}{A} \left\langle \frac{d\widetilde{\sigma}}{d\Omega}(\mathbf{k}_{\rm i}\epsilon_{\rm i} \longrightarrow \mathbf{k}_{\rm f}\epsilon_{\rm f}) \right\rangle . \tag{2.88}$$

2.10.2 The enhancement factor

The total normalized backscattered intensity due to multiple scattering is the sum of a weakly angular dependent diffuse background $\gamma_{\rm L}$ and a contribution from the interference between reciprocal light paths $\gamma_{\rm C}$ [8, 9, 10]. These two components, called the *ladder* ($\gamma_{\rm L}$) and *crossed*($\gamma_{\rm C}$) terms, can be obtained from the summation of the ladder and crossed vertex described in the previous section. The $\gamma_{\rm L}$ term corresponds to the

backscattered intensity if interference were neglected, and it has a weak angular dependence $\gamma_{\rm L} \sim \cos(\theta)$ [42] that depends only on the system geometry[7]. This contribution is completely flat in the angular range of our experiment. All interference effects are contained in $\gamma_{\rm C}$. The enhancement factor E_F is defined as the enhancement of the intensity in the exact backscattering direction due to this interference. As we have seen in Eq. (2.85) the ladder and the crossed term are equal if single scattering is subtracted. This imply that at exact backscattering $\gamma_{\rm L} = \gamma_{\rm C}$, the interference is perfectly constructive and $E_F = 2$. In practice one has to account for single scattering ($\gamma_{\rm S}$) and stray light ($\gamma_{\rm stray}$) which reduce the observed enhancement factor. The normalized backscattered intensity $I(\theta)$, as a function of the scattering angle θ, is written [51]:

$$I(\theta) = \frac{\gamma_{\rm C}(\theta) + \gamma_{\rm L} + \gamma_{\rm S} + \gamma_{\rm stray}}{\gamma_{\rm L} + \gamma_{\rm S} + \gamma_{\rm stray}}, \tag{2.89}$$

where only $\gamma_{\rm C}$ depends rapidly on θ, because of its interferential nature, while the other contributions can be considered flat in the angular range of interest. The backscattering enhancement E_F is the value of Eq. (2.89) at $\theta = 0$, and it is the experimentally obtained enhancement factor. If only reciprocal contributions are considered, single scattering is eliminated, and stray light is completely shielded, then

$$E_F \equiv \frac{\gamma_{\rm C}(\theta = 0) + \gamma_{\rm L}}{\gamma_{\rm L}} = 2. \tag{2.90}$$

This result has been experimentally confirmed [81].

2.10.3 The crossed term in the diffusion approximation

We follow here a standard approach for calculating $\gamma_{\rm C}(\theta)$ in which one solves the radiative transfer equation for a random collection of point scatterers in a self-consistent way and upon diffusion approximation [11]. The solution is based on the summation of the crossed diagrams, neglecting recurrent scattering events where one scatterer is visited more than once.

In principle the radiative transfer equation could be solved without further approximations [42], but it is quite involved. The ladder diagrams could be summed up without relying on the diffusion approximation and the maximally crossed terms could be added to this classical transport picture, to account for interference effects and to predict coherent backscattering. The diffusion approach is much simpler and it can be very accurate. We will address its limitations further in the thesis, and we show here the solution obtained with the intensity propagator calculated from the diffusion equation (a detailed solution can be found, for example, in ref.s [78, 74]). Assuming that the random walk in the three orthogonal propagation directions is uncoupled, we obtain the crossed term in the isotropic case, for a semi-infinite slab:

$$\gamma_{\rm C}(\theta) = \frac{3}{2(\ell_t)^3 \alpha u} \frac{\alpha + u(1 - \exp(-2\alpha z_e))}{(u+\alpha)^2 + \eta^2}, \tag{2.91}$$

where $\eta \equiv k(1-\mu_{\rm s})$, $u \equiv 0.5\,\ell^{-1}(1+\mu_{\rm s}^{-1})$, $z_e = 2/3\,\ell_t$, $\mu_{\rm s} = \cos\theta$, and $\alpha = k\sin\theta$, and k the wave-vector of the light in vacuum. Here θ is the scattering angle, and ℓ_t the

[7] This is the reason why we see the sun or a spherical light bulb as uniformly illuminated, as this angular dependence compensate with the projection factor.

transport mean free path. For many practical case (almost all cases) one deals with cones of opening angle much smaller than 100 mrad (as all the experiments described in this thesis).

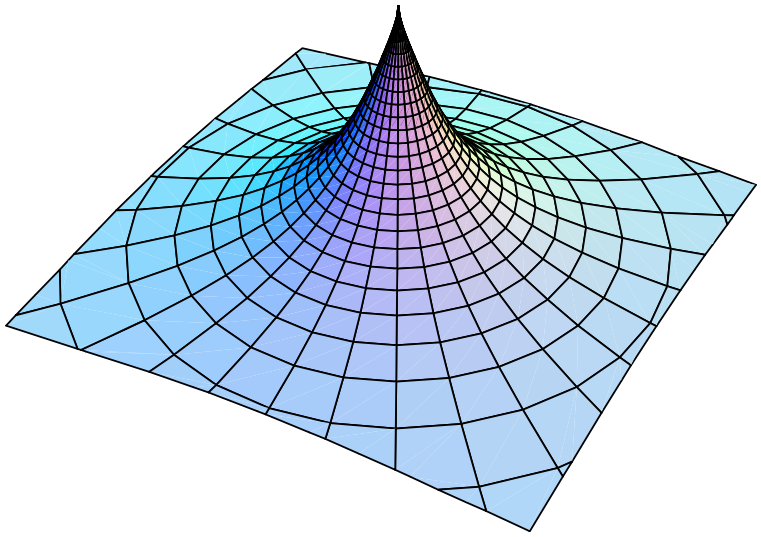

Figure 2.13: Theoretical shape of the coherent backscattering cone.

Fig. 2.13 shows the isotropic coherent backscattering cone as described in Eq. (2.91). Its full width half-maximum W is:

$$W(\theta) \simeq \frac{0.7}{2\pi}\frac{\lambda}{\ell_t}, \tag{2.92}$$

and its enhancement is 2.

In the presence of internal reflection at the sample interface, the full width at half-maximum W becomes [79]

$$W(\theta) \simeq \frac{0.7}{2\pi}\frac{\lambda}{\ell_t}(1-R), \tag{2.93}$$

where R is the average reflectivity coefficient of the interface, which can be calculated from diffusion theory and Fresnel coefficients [80]. In the following we will neglect internal reflections as in the experiments the samples are contained in a (quasi) index-matched quartz cell.

2.10.4 The crossed term from radiative transfer equation

The solution to the complete radiative transfer equation for scalar waves has been calculated [42]. The exact solution is plotted versus the diffusive solution in Fig. 2.14. As one can see, the two profiles are different, mainly in the tails. Diffusion theory underestimate the low orders of scattering, and in particular double scattering, which is the main large angle contribution [44].

As we will show in the next chapter, a Monte Carlo simulation of scalar waves in isotropic media (for which $\ell_t \equiv \ell_s$) gives a result which is indistinguishable from the radiative transfer solution provided by Amic *et al.*[42].

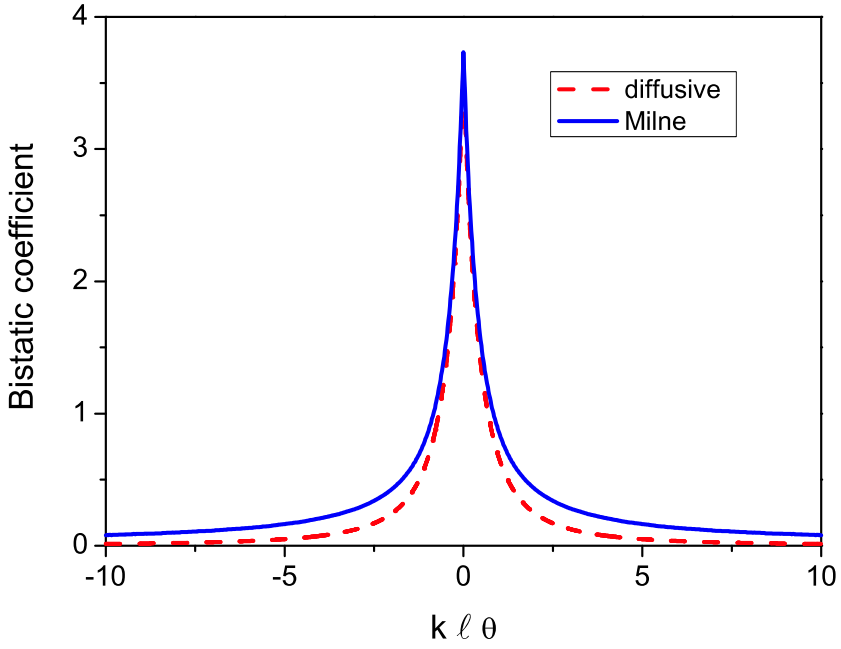

Figure 2.14: Theoretical shape of the coherent backscattering cone in the semi-infinite geometry, obtained from radiative transfer equation (full line) and from the diffusion equation (dotted line).

2.10.5 Effect of absorption, gain and recurrent scattering on the cone shape

In Eq. (2.91), absorption is neglected, which is a good approximation as typically the laser wavelength is outside the region where the medium is absorbing. The cone profile reflects the path-distribution inside the sample, which defines the weight of the various contributions. The presence of absorption, in general, changes the line-shape as it decreases the amplitude of the long paths exponentially more than the short paths. The result is a cone with a rounded top, as the highest spatial frequencies are absent. The effect is analogous to having a thin sample, which therefore does not support paths longer than its thickness squared.

Optical gain acts in the opposite direction as it increases the probability of a very long path, i.e. very small spatial frequency contribution to the cone. Such a condition reflects into a cone with a sharper top, but with the same enhancement factor of two, as both the reciprocal paths and the diffuse background are equally amplified.

In this context it is worth to mention also the more subtle effect of recurrent scattering events, the forerunners of Anderson localization. Recurrent events are present if the scattering density (or strength) is so high that a wave can be scattered more than once by the same scatterer, and thus that close paths are possible (see Fig. 2.15). For *same* scatterer, here, we do not mean the same point in space, as a random walker has zero mathematical probability of returning to the same point, even in the localized regime. Instead we speak about the return to the volume associated to the scattering center (determined by the total scattering cross-section and the light wavelength). The

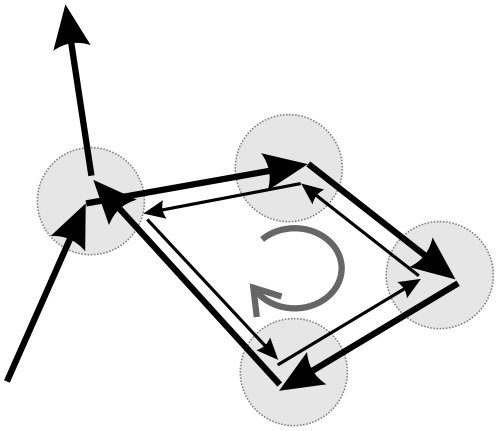

Figure 2.15: Recurrent scattering events. The single scattering cross-section is represented with the dotted circles.

recurrent path shown in Fig. 2.15 can be expressed in diagram form as:

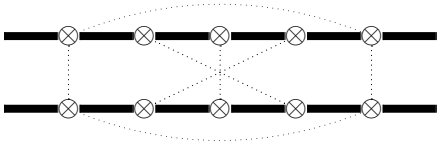

(2.94)

This is a diagram which is neither in the ladder series nor in the most crossed one. It has a non-negligible probability to happen only if the density is very high, such that $k\,\ell_s$ approaches the value of one (the so-called Ioffe-Regel criterion). Closed loop scattering paths have a reciprocal counterpart with which they can interfere coherently for any scattering direction since for such paths $\mathbf{r}_N = \mathbf{r}_1$ and $\Delta\phi = 0$ independent of $\mathbf{k}_\mathrm{f}$. These patterns are almost angle-independent and therefore they do not contribute to the cone, but to the flat background. If we look at the recurrent path of Fig. 2.15 we can also understand that the path has a contribution to the diffuse light which is very similar to single-scattering, and therefore acts to decrease the enhancement factor. This turns into a backscattering enhancement smaller than 2, but not into a rounded cone, as the path-length distribution is not changed. The experimental evidence of this phenomenon has been exhibited and it has been confirmed from a first order density correction of the diffusive theory [81].

2.10.6 Coherent backscattering from vector waves

Electromagnetic waves, in the far field, are vector waves, with a defined polarization transverse to the propagation direction. Vector waves are a theoretical complication to the equations, but can also be of help in the experiments. For circular incident polarization, the cone can be measured in the so-called helicity preserving channel (++) or in the helicity non-preserving (or reversing) channel (+−). When using linear polarization, the two polarization channels are the polarization preserving channel (lin$\|$lin) or the polarization non-preserving channel (lin$\perp$lin).

In the case of circular polarization, the vectorial nature can be exploited to suppress single scattering, an essential requirement to achieve the maximum enhancement of

2. What one can do is to use a quarter-wave plate and an analyzer to detect only photons in the helicity preserving channel. The quarter-wave plate converts the incident vertical polarized light to right circularly polarized before impinging into the sample. Backscattered light that is right-circularly polarized will be reconverted into vertical polarization upon traversing the quarter-wave plate for the second time, whereas left-circularly polarized light will be converted to horizontal polarization which will be blocked by the vertical transmission axis of the analyzer. This optical arrangement has the added benefit of suppressing the single scattering contribution to the backscattered intensity. For point-like scatterers, single scattering in the backscattering direction flips helicity, so for right-circularly polarized incident light the single scattering contribution is all left-circularly polarized, and therefore it is blocked by the polarization analyzer, and does not reach the detector. This is not always true if the scatterers are larger in size or without spherical symmetry.

Single scattering is all in the helicity-reversed channel, which has a weak enhancement. On the other hand the helicity preserving channel exhibits an enhancement value of 2 [81].

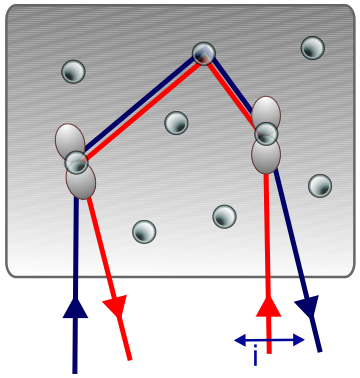

Figure 2.16: Polarization dependence of the first scattering orders for Rayleigh scatterers. The differential scattering cross-section is shown for two scattering events.

This single-scattering suppression technique cannot apply to the lin∥lin channel, and single scattering ($\sim 16\%$ of the scattered light for isotropic scalar Rayleigh scatterers) is always present in the measurements. The maximum enhancement is close to $1.8 - 1.9$ (1.86 for isotropic scalar Rayleigh scatterers). Due to the nature of the scattering processes that we will investigate in chapter 3, we will discuss only the case of linear polarization.

A linear polarization in or normal to the scanning plane introduces an anisotropy in the backscattered cone, due to trivial polarization effect, not related to anisotropic diffusion [82]. The direction of the polarization breaks the rotational symmetry of the system and thus marks the difference between the two different directions, parallel and orthogonal to it.

The difference lies in the first scattering events, where the differential scattering cross-section presents a minimum (with value zero) in the direction of the incident polarization: no light can be scattered if its polarization is orthogonal to the induced dipole, as the dipole can only radiate evanescent waves in the longitudinal direction.

The effect can be seen in the lin‖lin channel. At low scattering orders the input-

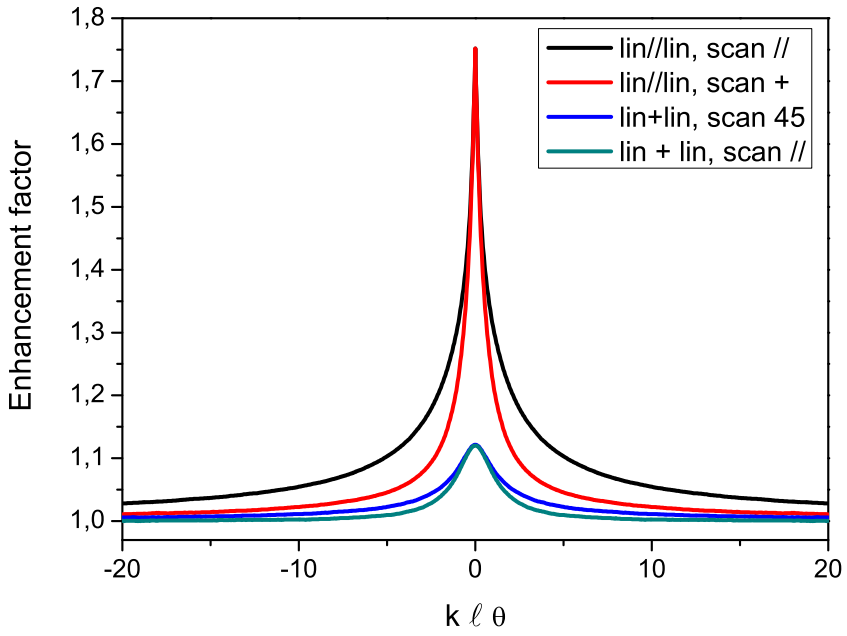

Figure 2.17: Monte Carlo simulation for coherent backscattering cone from a medium of vectorial Rayleigh scatterers (for details see chapter 4).

output distance of reciprocal paths is smaller in the direction parallel to the incident polarization, and the backscattering cone wider, while it is thinner in the direction orthogonal to the input polarization (see Fig. 2.17). For higher scattering orders, the polarization is completely scrambled and the two contributions, parallel and orthogonal to the incident polarization, are equivalent. For this reason, in the lin‖lin channel, the tops of the two scans have the same opening angle and circular symmetry: long paths have completely lost polarization memory and are thus symmetric, while the lower orders retains memory of the anisotropic single-scattering cross-section.

In the case of crossed polarized channel, lin⊥lin, the cone has a 4-fold symmetry, as the only symmetry axes that can exist are the bisectors of the incident and measured polarization [68]. If one performs a scan of the cone with the polarization at 45 deg with respect to the incident one, one finds an anisotropy and at the same time, a strongly reduced enhancement. This is again related to the scattering cross-section of a single dipole. As a result, a time-reversal path for the helicity reversing channel has less probability to occur than in the helicity preserving channel. The reciprocity argument does not hold now, as the couple of interfering path are not reverse pairs (see Eq. (2.23)), and therefore their amplitude are not equivalent. The amplitudes which interfere are

$$\mathcal{A}_{\mathrm{dir}} = \mathcal{A}(\mathbf{k}_{\mathrm{i}}\epsilon_{\mathrm{i}} \rightarrow \mathbf{k}_{\mathrm{f}}\epsilon_{\mathrm{f}}) \quad \text{and} \quad \mathcal{A}_{\mathrm{rev}} = \mathcal{A}(-\mathbf{k}_{\mathrm{f}}\epsilon_{\mathrm{i}}^{*} \rightarrow -\mathbf{k}_{\mathrm{i}}\epsilon_{\mathrm{f}}^{*}). \tag{2.95}$$

Reciprocity ensures that

$$\mathcal{A}(\mathbf{k}_\mathrm{i}\epsilon_\mathrm{i} \to \mathbf{k}_\mathrm{f}\epsilon_\mathrm{f}) = \mathcal{A}(-\mathbf{k}_\mathrm{f}\epsilon_\mathrm{f}^* \to -\mathbf{k}_\mathrm{i}\epsilon_\mathrm{i}^*), \tag{2.96}$$

but nothing is said about the lin⊥lin reversed path

$$\mathcal{A}_\mathrm{rev} = \mathcal{A}(-\mathbf{k}_\mathrm{f}\epsilon_\mathrm{i}^* \to -\mathbf{k}_\mathrm{i}\epsilon_\mathrm{f}^*). \tag{2.97}$$

In the lin⊥lin channel, depending on the shape of the path, the interference ranges from completely constructive to destructive. The small enhancement is due only to low scattering orders, as it is evident from the rounded top of the lin⊥lin cone.

2.11 The integral formulation of coherent backscattering enhancement

As shown in sec 2.3.1, one of the most intuitive picture to describe light propagation in random media is that of a *random walk* of light wavepackets, which we will call for simplicity photons, but which are of classical nature. In the simplest case of isotropic scatterers embedded in a dilute homogenous medium, one thinks of the photons as travelling in straight lines, ballistically, and changing direction upon scattering. The distance travelled between two scattering events, which on average is the scattering mean free path ℓ_s, is ruled by the probability of a scattering event: the weaker the scattering probability, the longer the distance travelled.

The random walk approach implies that all the scattering details of the scattering event are mapped into an effective average medium, in which the photons travel ballistically and perform elastic collisions. This mapping consists in including all the features of the transport process in few parameters, like the diffusion constant, the transport mean free path or the transport velocity. When the degrees of freedom of the scattering process start to increase, for example when polarization is included, or scattering anisotropy is present, or the scatterers have internal structure, then this approximation have to be carefully extended (or dropped).

We will here rewrite the expressions given in the previous sections with an integral formulation, which is analogous to the diagrammatic formulation, but more suitable for a Monte Carlo simulation (see chapter 5). The bistatic coefficient has to be averaged over the scatterer configuration to provide smooth and meaningful quantities. This averaging, in this thesis, is *not* accomplished with the diffusion approximation, but with the Monte Carlo simulation. This also means that averaged quantities like the transport mean free path ℓ_t do not appear in the equations.

2.11.1 Scalar wave in uniform and isotropic scattering media

A single scattering event is isotropic if the scattered light pattern is uniform in the full solid angle. This implies that the scattering differential cross-section is a scalar quantity, constant in any direction:

$$\frac{d\sigma}{d\Omega} = \frac{\sigma_t}{4\pi}, \tag{2.98}$$

equal to its angular averaging.

Light undergoes multiple scattering when it propagates through inhomogeneous media over distances much larger than one scattering mean free path ℓ_s. The passage from single to multiple scattering requires therefore the definition of $G(\mathbf{k}, \mathbf{r}_{12})$, the amplitude Green function of the system which describes how the light amplitude propagates between two scattering events. For isotropic scattering, one usually uses a direction independent propagator, which is the solution of the wave equation described in Eq. (2.56)

$$G(\mathbf{k}, \mathbf{r}_{12}) = -\frac{1}{4\pi r_{12}} \exp\left(ikr_{12}\right) \exp\left(-\frac{r_{12}}{2\ell_s}\right), \tag{2.99}$$

which is the scalar equivalent of the result of Eq. (2.67). The Green function in Eq. (2.99) is simply a spherical wave $\exp(ikr_{12})/4\pi r_{12}$ attenuated by the Beer-Lambert factor $\exp(-r_{12}/2\ell_s)$ which takes into account the presence of the scattering medium; k is modulus of the wave vector inside the medium (see Fig. 2.18).

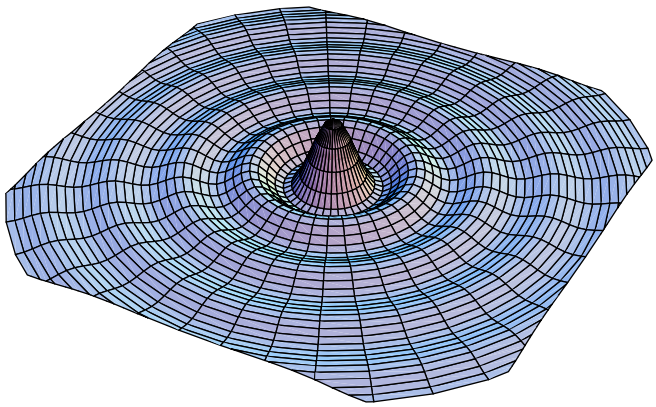

Figure 2.18: Real part of the vacuum Green function, which is a spherical wave. Note that in dressed Green function, Eq. (2.99), an extra exponential damping factor is present.

2.11.2 The ladder term

As already said, the ladder term corresponds to the backscattered intensity if interferences were neglected, and has a weak angular component that depends only on the medium geometry. The ladder term can be developed in scattering orders, as shown in Eq. (2.80). The contributions of the N-*th* scattering order is:

$$\begin{aligned}\gamma_L^{(N)} = \frac{4\pi n_p^N}{A} \int & e^{-z_1/\ell_s} \left(\frac{d\sigma}{d\Omega}\right)_1 (16\pi^2 G(k, \mathbf{r}_{12}) G^*(k, \mathbf{r}_{12})) \left(\frac{d\sigma}{d\Omega}\right)_2 \dots \\ & \dots \left(\frac{d\sigma}{d\Omega}\right)_{N-1} (16\pi^2 G(k, \mathbf{r}_{N-1,N}) G^*(k, \mathbf{r}_{N-1,N})) \left(\frac{d\sigma}{d\Omega}\right)_N \\ & e^{-z_N/\ell}\, d\mathbf{r}_1 d\mathbf{r}_1 \dots d\mathbf{r}_N\end{aligned} \tag{2.100}$$

where the integral is performed over all the possible $\{\mathbf{r}_1, \mathbf{r}_2, \ldots, \mathbf{r}_N\}$ positions of the scatterers. n_p is the scatterers density, A the illuminated area and the z-axis is orthogonal to the sample front face.

This integral is equivalent to a random walk model, and it can be interpreted as a collection of successive scattering events, represented by $(d\sigma/d\Omega)$, followed by ballistic propagation in the average medium, via the amplitude Green function $G(k, \mathbf{r}_{12})$, and then scattering again, and so on. The first and last exponentials are the boundary conditions, they account for the intensity lost in the medium before the first scattering $(\exp(-z_1/\ell_s))$ event and after the last one $(\exp(-z_N/\ell_s))$.

If one wanted to add an angular dependence, it would have considered not $\mathbf{k}_\mathrm{f} = -\mathbf{k}_\mathrm{i} = (0, 0, -k)$, but $\mathbf{k}_\mathrm{f} = (-k\sin\theta\cos\phi, -k\sin\theta\sin\phi, -k\cos\theta)$. A change of variable could get rid of this $\cos\theta$, and the ladder term would be the same, but with an extra weak angular dependence.

2.11.3 Crossed term

The crossed term is the non-diffusive contribution that is at the origin of the coherent backscattering cone (see section 2.10.2). It can be written formally as the ladder contribution, with in addition the interference term

$$\cos[(\mathbf{k}_\mathrm{in} + \mathbf{k}_\mathrm{out}) \cdot (\mathbf{r}_N - \mathbf{r}_1)], \tag{2.101}$$

for each scattering order, following Eq. (2.81), as

$$\begin{aligned}\gamma_C^{(N)} = \frac{4\pi n_p^N}{A} \int d\mathbf{r}_1 d\mathbf{r}_1 \ldots d\mathbf{r}_N \; e^{-z_1/\ell_s} \left(\frac{d\sigma}{d\Omega}\right)_1 (16\pi^2 G(k, \mathbf{r}_{12}) G^*(k, \mathbf{r}_{12})) \left(\frac{d\sigma}{d\Omega}\right)_2 \ldots \\ \ldots \left(\frac{d\sigma}{d\Omega}\right)_{N-1} (16\pi^2 G(k, \mathbf{r}_{N-1,N}) G^*(k, \mathbf{r}_{N-1,N})) \left(\frac{d\sigma}{d\Omega}\right)_N \\ e^{-z_N/\ell} \cos[(\mathbf{k}_\mathrm{in} + \mathbf{k}_\mathrm{out}) \cdot (\mathbf{r}_N - \mathbf{r}_1)].\end{aligned} \tag{2.102}$$

This integral equation is known in each of its components, but it is not so easily solved analytically. In the case of scalar and vectorial waves in isotropic point-like scatterers full solutions do exist but are quite involved [42].

The specific example of single and double scattering can help understanding the model.

2.11.4 Single scattering contribution for scalar waves

Single scattering has no counter-part in the crossed term, as no interference can take place with only one light path. The integral is very simple as no intra-scattering propagation is required.

$$\gamma_L^{(1)} = \frac{4\pi n_p}{A} \int e^{-r_{01}/\ell_s} \left(\frac{d\sigma}{d\Omega}\right) e^{-r_{10}/\ell_s} \, d\mathbf{r}_1 \tag{2.103}$$

The meaning is: the photon enters the medium at position $r = r_0$, then it propagates in the average medium where it suffers from Beer-Lambert's attenuation for the distance $r_{10} = r_1 - r_0$, expressed by the term $\exp(-r_{01}/\ell_s)$; at position $r = r_1$ it is scattered,

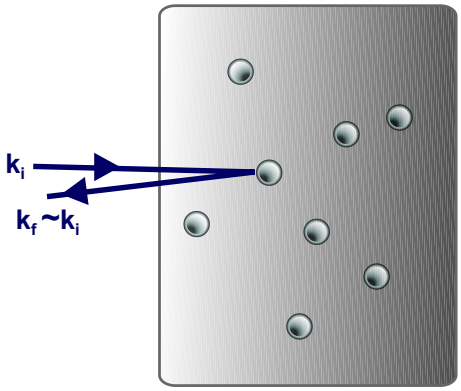

Figure 2.19: Single scattering event.

(expressed by $d\sigma/d\Omega$), and then it exits the medium following the same path and being attenuated again by $\exp(-r_{10}/\ell_s)$. Here we calculate the single scattering contribution at exact backscattering as it is so weakly angular dependent that with great accuracy it can considered constant in the angular range of interest. This means that $r_{01} = r_{10} = z_1$.

The translational symmetry in the x-y direction allows for a trivial integration over dx and dy

$$\gamma_L^{(1)} = \frac{4\pi n_p}{A} \int_A dx_1 dy_1 \int_0^\infty \left(\frac{d\sigma}{d\Omega}\right) \; e^{-2z_1/\ell_s} dz_1. \tag{2.104}$$

Using the isotropic scattering cross-section form Eq. (2.98) and by rescaling all the dimensions of a mean free path, $r \longrightarrow r/\ell_s$, the ladder term can be expressed as:

$$\gamma_L^{(1)} = \frac{4\pi n_p \ell_s}{A} \int_A dr_\perp \int \frac{\sigma_t}{4\pi} \; e^{-2z_1} dz_1 = \frac{4\pi n_p \ell_s}{A} \; A \; \left(\frac{\sigma_t}{4\pi}\right) \int e^{-2z_1} dz_1. \tag{2.105}$$

The integral can be calculated easily, using the relation $\sigma_t n_p = 1/\ell_s$ and first performing the integral over $dr_\perp$, the direction orthogonal to z, which is $\int_A dr_\perp = A$. Finally one obtains:

$$\gamma_L^{(1)} = \int_0^\infty \; e^{-2z_1} dz_1 = \frac{1}{2}. \tag{2.106}$$

2.11.5 Double scattering contribution to the ladder term for scalar waves

For double scattering an intermediate propagation step is required, between the first and last scattering event. Here we use the free space Green function $G(k, \mathbf{r}_{12})$ defined in Eq. (2.99), as we assume that the scattering centers are contained in an optically uniform medium. The double scattering ladder term is given by:

$$\gamma_L^{(2)} = \frac{4\pi n_p^2}{A} \int e^{-z_1/\ell_s} \left(\frac{d\sigma}{d\Omega}\right)_1 [16\pi^2 G(k, \mathbf{r}_{12}) G^*(k, \mathbf{r}_{12})] \left(\frac{d\sigma}{d\Omega}\right)_2 \; e^{-z_2/\ell_s} \; d\mathbf{r}_1 d\mathbf{r}_2 \tag{2.107}$$

which is rewritten using Eq. (2.99), via the variable change

$$\{d\mathbf{r}_1, d\mathbf{r}_2\} \longrightarrow \{d\mathbf{r}_1, d\mathbf{r}_{12}\} \longrightarrow \{d\mathbf{r}_1, r_{12}^2 dr_{12} d\Omega_{12}\} \tag{2.108}$$

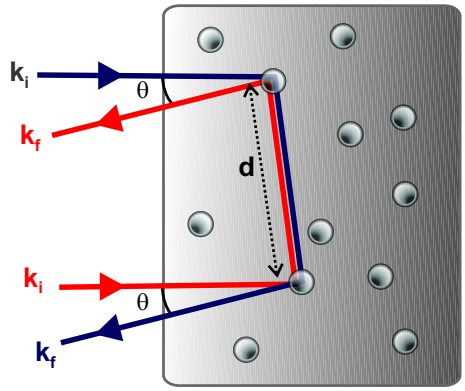

Figure 2.20: Double scattering event.

where r_{12} is the relative distance between two scattering events. Then we can perform the trivial integration over dx_1 and dy_1 which gives the illuminated area A and obtain:

$$\gamma_L^{(2)} = 4\pi n_p^2 \int e^{-z_1/\ell_s} \left(\frac{d\sigma}{d\Omega}\right)_1 e^{-r_{12}/\ell_s} \left(\frac{d\sigma}{d\Omega}\right)_2 e^{-z_2/\ell_s}\, dz_1 dr_{12} d\Omega_{12}. \tag{2.109}$$

In analogy with the calculation for single scattering, the double scattering contribution to the ladder term around $\theta = 0$ becomes:

$$\gamma_L^{(2)} = \int dz_1 dr_{12}\; e^{-z_1}\; e^{-z_2}\; e^{-r_{12}} = \frac{\ln(2)}{2}. \tag{2.110}$$

2.11.6 Double scattering contribution to the crossed term for scalar waves

The bistatic coefficient for the crossed term, in double scattering only, becomes:

$$\begin{aligned}\gamma_C^{(2)} \;=\; & \frac{4\pi n_p^2}{A} \int d\mathbf{r}_1 d\mathbf{r}_2\; e^{-z_1/\ell_s} \left(\frac{d\sigma}{d\Omega}\right)_1 [16\pi^2 G(k,\mathbf{r}_{12}) G^*(k,\mathbf{r}_{12})] \\ & \left(\frac{d\sigma}{d\Omega}\right)_2 e^{-z_2/\ell_s} \cos[(\mathbf{k}_{\text{in}} + \mathbf{k}_{\text{out}}) \cdot (\mathbf{r}_2 - \mathbf{r}_1)]\end{aligned} \tag{2.111}$$

The integral can be solved [76], and its value is given by $\mathcal{F}(\theta)$, which we will use again in chapter 5,

$$\mathcal{F}(\theta) = \left[2 \operatorname{arg\,cosh}\left(\frac{1}{|\cos\theta|}\right) - \operatorname{arg\,cosh}\left(\frac{1}{\cos^2\theta}\right)\right] / \sqrt{1-\cos^2\theta}. \tag{2.112}$$

The integral formulation of the crossed term is perfectly suitable for a numerical solution: when light scattering and propagation are known, a Monte Carlo technique can be used to perform the configuration averaging needed. In the next chapter (Fig. 5.7), we will show that a Monte Carlo simulation can be as accurate as to provide solutions indistinguishable from the analytical one with little computational time. A numerical solution can further help in calculating solutions also for anisotropic multiple scattering, problem which does not have analytical solutions.

2.12 Isotropic scattering of vector waves

If one wants to describe scattering of vector waves, one has to replace the scalar differential scattering cross-section of Eq. (2.98) with the vectorial

$$\frac{d\sigma}{d\Omega}(|\mathbf{k}_\mathrm{i},\epsilon_\mathrm{i}\rangle \longrightarrow |\mathbf{k}_\mathrm{f},\epsilon_\mathrm{f}\rangle) = \frac{3}{8\pi}\ \sigma_0\ |\epsilon_\mathrm{i}\cdot\epsilon_\mathrm{f}^*|^2. \tag{2.113}$$

And the propagator Green function of Eq. (2.99) with the vectorial one:

$$G(\mathbf{k},\mathbf{r}_{12}) = -\frac{1}{4\pi r_{12}}\exp\left(ikr_{12}\right)\exp\left(-\frac{r_{12}}{2\ell_\mathrm{s}}\right)\Delta_\mathbf{r}, \tag{2.114}$$

where $\Delta_\mathbf{r}$ is the projector perpendicular to $\mathbf{r}$ acting in the space of polarizations: $(\Delta_\mathbf{r})_{ij} = \delta_{ij} - r_i r_j/r^2$.

With these ingredients, all the integral described so far can be extended to the case of vector waves. The main new concept is the transversality of the electromagnetic waves, which reflects into the projector $\Delta_\mathbf{r}$. With all the mesoscopic ingredients presented so far, we can, in the next chapter, extend the multiple scattering model to anisotropic scattering and anisotropic weak localization.

Chapter 3

Multiple scattering anisotropy

A scattering event is anisotropic if the radiated pattern is not the same in all directions, in other words if the differential scattering cross section is not uniform at all angles; this happens for example with Mie scatterers (particles large compared with the light wavelength).

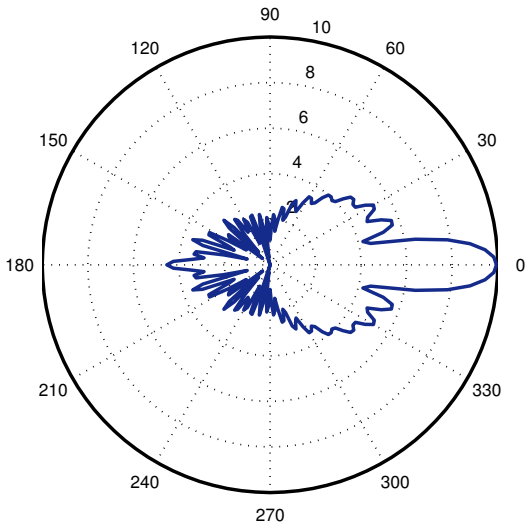

Figure 3.1: Polar plot of the differential scattering cross-section for a Mie sphere of size $a = kd = 20$, where d is the sphere diameter.

A Mie scatterer has a very forward peak in the differential scattering cross-section (see plot of Fig. 3.1), but its anisotropy has no preferential direction as the differential scattering cross-section depends only on the relative angle between incident and scattered directions. We are interested in the multiple scattering process of light by many scattering centers, and we want to apply a statistical approach. A random walker in an ensemble of Mie scatterers will encounter a series of anisotropic scattering events,

but whose scattering patterns are randomly oriented in the directions of the random scattered k-vectors. The average of these paths will *not* produce, in general, anisotropic diffusion of light, as the average of the microscopic anisotropy is usually *statistically isotropic*.

In order to break rotational symmetry of the scattering process we have to introduce one or more favorable directions of scattering. If this special axis (often called the optical axis) is not unique in the system, but is defined only on the microscopic scale (in local domains), like in the case of not-oriented nematic liquid crystal that we will investigate in the next chapter, then the configuration averaging will reduce the process to a macroscopic *isotropic* multiple scattering process.

If we can extend the locally oriented domains to the macroscopic size of the sample, then a global favorable scattering direction will survive averaging. When the single scattered pattern depends only on the direction of the incident k-vector, with respect to a global optical axis, then the anisotropy is only a *geometrical* effect, i.e. light diffuses differently in the two directions, parallel and orthogonal to the optical axis. The effect of the anisotropy is the same for all scattering events, thus it can be factorized out of the equations. The diffusion approximation applies and can be extended to include two different diffusion constants, $\mathcal{D}_\perp \neq \mathcal{D}_\parallel$ in the two directions $\parallel$ and $\perp$ to the optical axis [83]. The only effect of this form of anisotropy is to resize the transport quantities like the diffusion constant or the transport mean free path, differently in the two directions. The coherent backscattering results, as expected, anisotropic as one of the two directions is rescaled [84].

There are forms of anisotropy that do not average out upon multiple scattering and that arise much interest, as they can induce anisotropic light transport at all orders without causing only a geometrical effect, but changing also the light interference. They can induce an anisotropic differential scattering cross-section, which depends on the photon light state: the diffusive picture can break down. In such conditions, anisotropic weak localization is expected and many intriguing interference phenomena like Anderson localization or coherent random lasing could be affected.

Anisotropic multiple scattering and diffusion has been observed, for example, in the phenomenon of the photonic Hall effect, in which the Faraday effect induces an anisotropy of the dielectric constant of the scatterers [85]. In such case a macroscopic anisotropy survives the multiple scattering and the diffusion of light drifts towards a direction perpendicular to the propagation direction (and the applied magnetic field).

Here we will study anisotropic transport of light in a collection of anisotropic Rayleigh scatterers, namely (1) anisotropic propagation in an ensemble of isotropic scatterers and (2) scatterers with a preferential axis of polarizability. The first case induces only a geometrical effect, while the latter is characterized by a random walk with variable step-length according to the polarization of the photon relative to the optical axis, and is an intrinsic anisotropic process.

3.1 Anisotropic light transport

A random distribution of isotropic scatterers induces a scattering potential whose correlation function is a delta function $\delta(\mathbf{r}, \mathbf{r}')$, and hence has no long range correlation. This is the case, for example, for a Gaussian disorder, as shown in Fig. 3.2, where the potential is presented aside with its correlation function.

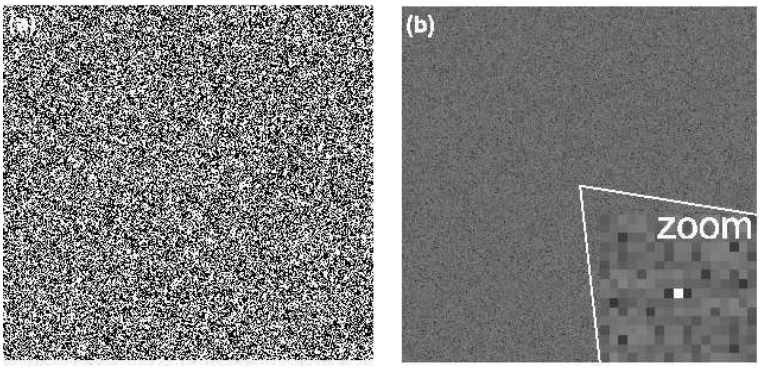

Figure 3.2: (a) Random scattering potential made of a random arrange of isotropic scatterers. (b) The potential correlation function, which is a delta function centered at $\mathbf{r} = 0$, as shown from the inset.

If one imagines stretching the position of the scatterers in this random arrangement, one does not induce correlations, but only changes the average density of scatterers. What one obtains is again a random potential, in which light propagate isotropically, as in Fig. 3.3. The action of stretching the space, which conserves the single-scattering isotropy, is a linear operation, which cannot induce new correlations. This can be

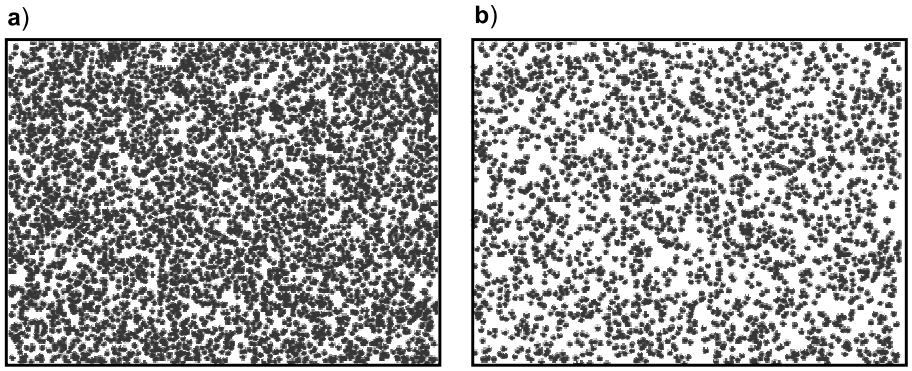

Figure 3.3: (a) Random scattering potential made of isotropic scatterers. (b) Random scattering potential stretched of a factor of 2 in the vertical direction. No correlations are visible, as confirmed by the two correlation functions which are a delta-function (not-shown here).

understood also thinking of the density of particles encountered by a ballistic walker in its propagation; in a given volume, the number of particles is the same (i.e. the density is a scalar), regardless the direction of propagation, the multiple scattering process has the same (isotropic) influence on propagation.

A different effect is originated by correlations in the positions of the scatterers, which can induce long range scattering correlations and thus make the isotropic picture anisotropic. In Fig. 3.4(a), the scattering potential is made of a periodic arrangement (hexagonal lattice) of isotropic scatterers. Its correlation function shows peaks at the positions of the inverse of the spacing between the particles (Fig. 3.4(b)).

For completeness and for further use, in chapter 6, we are presenting here also the

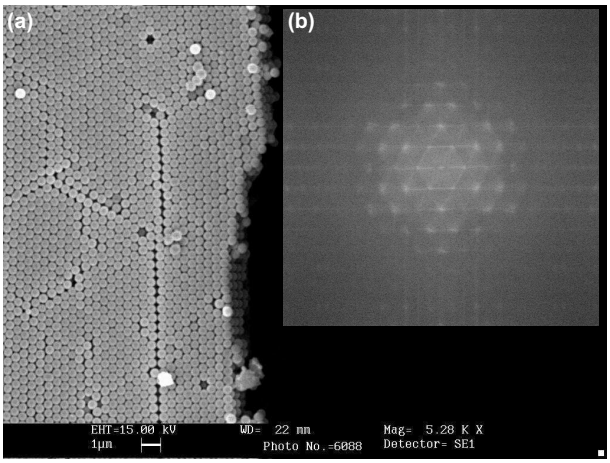

Figure 3.4: (a) Correlated scattering potential made of a periodic arrangement of isotropic scatterers, SEM image of a 3D photonic crystal of SiO_2 (done in collaboration with Stefano Gottardo). (b) The potential correlation function, shown peaks at the positions of the inverse of the spacing between the particles, with the same periodicity as the optical lattice.

case of a periodic potential, which show Bragg peaks in the correlation function (Fig. 3.4), and a 3D electronic icosahedral quasi-crystal of Zn-Mg-Ho, which has no periodicity but long range correlations (Fig. 3.5), which shows up in a complex diffraction pattern.

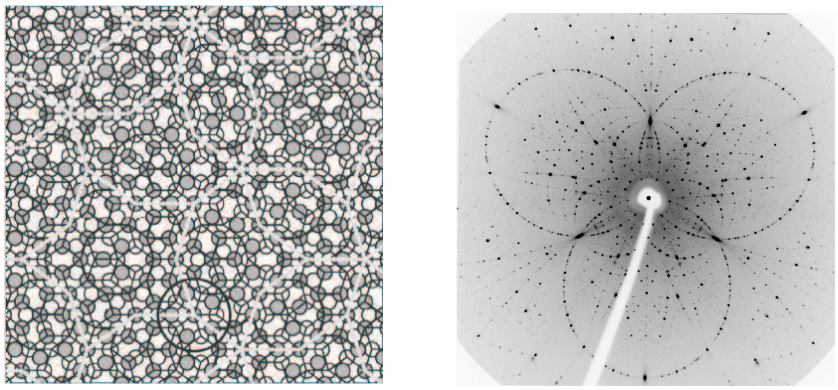

Figure 3.5: In the left panel a projection of the atom positions (41×41Å) of the decagonal $Al_{72}Ni_{20}Co_8$ quasicrystal is shown. The thin black lines show the Penrose tiling. The right panel is an X-ray transmission Laue photograph of the icosahedral electronic Zn-Mg-Ho quasicrystal (courtesy of Hiroyuki Takakura, [86].)

3.1.1 Anisotropic propagation in isotropic Rayleigh scatterers

The simplest way to obtain anisotropic light transport, without changing the single scattering cross-section is to change the inter-scatterer propagator. This can occur if there are scattering potential correlations.

In reality the propagator and the differential scattering cross-section are closely linked as they are both a function of the system T-matrix, and therefore both of them should be changed. In fact, this is only a simple model to understand the role of the anisotropy, testing one of the essential ingredients of the multiple scattering process. As we will show later, such a case can be very precisely described with an anisotropic diffusive model, if the isotropic diffusion constant $\mathcal{D}$ is replaced by an anisotropic diffusion tensor.

What we want to do is to change the isotropic propagator, making the length of the random walk step in between two scattering event longer (or shorter) in a special direction. As a result

$$G(\mathbf{r}_{12}) \neq G(|\mathbf{r}_{12}|). \tag{3.1}$$

The amplitude random step can now be calculated from the distribution

$$\exp\left(-\frac{\mathbf{r}_{12}\,\mathbf{R}\,\mathbf{r}_{12}}{2\ell_0 r_{12}}\right) \tag{3.2}$$

where ℓ_0 is the isotropic mean free path, and $\mathbf{R}$ is the spatial anisotropy matrix that defines the direction and the amount of anisotropy, via the parameter s. The matrix $\mathbf{R}$ is the dilation matrix and can be represented in the laboratory frame, in the basis $\{\widehat{\mathbf{s}}, e_1, e_2\}$ as:

$$\mathbf{R} = \begin{pmatrix} s & 0 & 0 \\ 0 & 1 & 0 \\ 0 & 0 & 1 \end{pmatrix} \tag{3.3}$$

$\widehat{\mathbf{s}}$ is the direction of anisotropy, s the amount of stretching ($s = 1$ gives is the identity transformation). The step length $\mathbf{r} = \mathbf{r}_{12}$ can be expressed from the isotropic step $\mathbf{r}_0$ as

$$\mathbf{r}_{12} = (s-1)(\mathbf{r}_0 \cdot \widehat{\mathbf{s}})\,\widehat{\mathbf{s}} + \mathbf{r}_0 \tag{3.4}$$

The result is shown in Fig. 3.6, the step vector $\mathbf{r}_{12}$ is increased in magnitude and it is

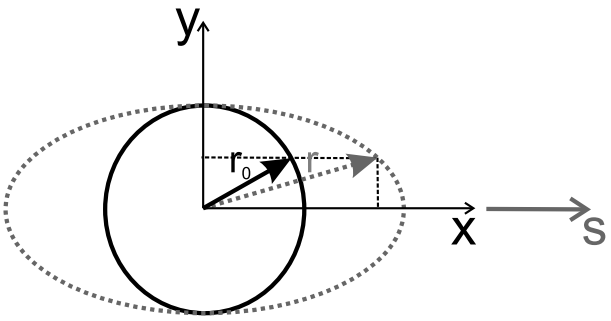

Figure 3.6: Effect of the anisotropy on the random walk vector: $\mathbf{r}_0$ is turned into $\mathbf{r}$. The direction of $\widehat{\mathbf{s}}$ is show, parallel to $\mathbf{x}$.

rotated towards the direction $\widehat{\mathbf{s}}$.

3.1.2 The anisotropic diffusion model

As we have already anticipated, this type of anisotropy can be very precisely described with an anisotropic diffusive model, such that the isotropic diffusion constant $\mathcal{D} = v\ell_t/3$

is replaced by an anisotropic diffusion tensor. The diffusion equation for the light intensity $I = I(\mathbf{r}, t)$ then reads:

$$S + \frac{\partial I}{\partial t} = \left(\mathcal{D}_{xx} \frac{\partial^2}{\partial x^2} + \mathcal{D}_{yy} \frac{\partial^2}{\partial y^2} + \mathcal{D}_{zz} \frac{\partial^2}{\partial z^2} \right) I - \frac{v}{\ell_a} I \tag{3.5}$$

where $S = S(\mathbf{r}, t)$ is the source, $\mathcal{D}_{xx}$, $\mathcal{D}_{yy}$, and $\mathcal{D}_{zz}$ the diagonal components of the diffusive tensor, v the energy velocity and ℓ_a the absorption time. The z axis is parallel to the slab normal.

The action of the anisotropy in the direction $\mathbf{x}$ of the space modifies the variables as:

$$\begin{array}{rl} \mathbf{x} \longrightarrow \mathbf{x}' = & s \times \mathbf{x} \\ \mathbf{y} \longrightarrow \mathbf{y}' = & \mathbf{y} \\ \mathbf{y} \longrightarrow \mathbf{y}' = & \mathbf{z} \end{array} \tag{3.6}$$

without changing the scattering cross-section. This is not a real change of variable, as it acts only on the intra-scattering propagation. From Eq. (3.6) it follows that

$$\frac{\partial^2}{\partial x'^2} \longrightarrow \frac{1}{s^2} \times \frac{\partial^2}{\partial x^2}. \tag{3.7}$$

Using this expression the diffusion equation can be rewritten in a form analogue to Eq. (3.5), including the parameter s in the diffusion tensor:

$$\mathcal{D}_{x'x'} \frac{\partial^2}{\partial x'^2} = \left(s^2 \times \mathcal{D}_{xx} \right) \frac{\partial^2}{\partial x^2} \tag{3.8}$$

An analogue way of obtaining the same result starts from the definition of the diffusion constant, and introducing the anisotropic transport mean free path

$$\mathcal{D}_{x'x'} = \left(\frac{v' \ell'_t}{3} \right)_{xx} = \left(\frac{sv \; s\ell_t}{3} \right)_{xx} = s^2 \, \mathcal{D}_{xx}. \tag{3.9}$$

We can generalize this relation, and express the diffusion tensor with $\mathbf{R}$, the spatial anisotropy matrix:

$$\mathcal{D}' = \mathbf{R} \mathcal{D} \mathbf{R}^\dagger = \frac{v\ell_t}{3} \begin{pmatrix} s & 0 & 0 \\ 0 & 1 & 0 \\ 0 & 0 & 1 \end{pmatrix} \begin{pmatrix} 1 & 0 & 0 \\ 0 & 1 & 0 \\ 0 & 0 & 1 \end{pmatrix} \begin{pmatrix} s & 0 & 0 \\ 0 & 1 & 0 \\ 0 & 0 & 1 \end{pmatrix} \tag{3.10}$$

In the special case of uniaxial medium, $\mathcal{D}'$ is directly proportional to $\mathbf{R}^2$,

$$\mathcal{D}' = \frac{v\ell_t}{3} \begin{pmatrix} s^2 & 0 & 0 \\ 0 & 1 & 0 \\ 0 & 0 & 1 \end{pmatrix} \tag{3.11}$$

If we add this results to a calculation of the coherent backscattering cone, we can conclude that the cone will be anisotropic, with anisotropy given by s. One expects that the cone will be s times wider in the y-direction. In chapter 5 this result will be confronted with a Monte Carlo simulation.

3.2 Anisotropic polarizability of Rayleigh scatterers

An anisotropic single scattering cross-section is a more subtle effect responsible for diffusion anisotropy than the Green function anisotropy. In the isotropic medium, the induced polarization of the Rayleigh dipoles is always parallel to the incident electric field and it is related to it by a scalar factor, the polarizability, that is independent of the direction along which the field is applied. This is no longer true for anisotropic media. The anisotropy that arises can affect both the single scattering radiated pattern and the inter-scattering propagator, even if the scattering density is uniform.

3.2.1 Anisotropic Rayleigh scattering

The polarizability of a medium can be non-isotropic, for example asymmetric molecules that can be more easily excited by a field in a given direction. This common axis ($\mathbf{n}$) will be the same for all dipoles, and will not average out upon multiple scattering: the overall pattern will be anisotropic. We can model the scatterer polarizability with an uniaxial anisotropic dielectric tensor,

$$\mathbf{D} = 1 + (a-1)|\mathbf{n}\rangle\langle\mathbf{n}|, \tag{3.12}$$

which has two degenerate eigenvalues. In the diagonal basis $\{\widehat{\mathbf{n}}, \widehat{\mathbf{e}}_\mathbf{1}, \widehat{\mathbf{e}}_\mathbf{2}\}$ it can be expressed as:

$$\mathbf{D} = \begin{pmatrix} a & 0 & 0 \\ 0 & 1 & 0 \\ 0 & 0 & 1 \end{pmatrix} \tag{3.13}$$

where a is the microscopic parameter determining the degree of anisotropy, being $a = \langle\mathbf{n}|\mathbf{D}|\mathbf{n}\rangle$, the value assumed by the dielectric tensor in the direction of the optical axis $\mathbf{n}$. In the following we will assume for simplicity prolate anisotropy, defined as $a > 1$, but an analogue treatment is valid for $a < 1$ (oblate anisotropy).

From now onwards, for the polarization, we will use the convention typical of the liquid crystal community,

$$\begin{aligned} \epsilon_\mathrm{i} &= \mathbf{i} \\ \epsilon_\mathrm{f} &= \mathbf{f} \end{aligned} \tag{3.14}$$

and at the same time we will consider only linear incident (and detected) polarization. The dipole $\mathbf{p}$ induced by the incident polarization $\mathbf{i}$ is then

$$\mathbf{p}(\mathbf{i}) = \mathbf{D}|\mathbf{i}\rangle = (a-1)(\mathbf{i}\cdot\mathbf{n})\mathbf{n} + \mathbf{i}. \tag{3.15}$$

If $a \neq 1$, the dipole is not unitary, being $|\mathbf{p}|^2 = (a^2-1)(\mathbf{i}\cdot\mathbf{n})^2 + 1$, and it is rotated towards $\mathbf{n}$: light emission is more probable for those scattered k-vectors in the plane orthogonal to $\mathbf{n}$, see Fig. 3.7. The physical picture for the dipole excitation is that the polarizability of the medium is stronger if the driving field $\mathbf{i}$ is parallel to $\mathbf{n}$, a preferential direction in space. The dipole changes direction but the scattering process is the same as for the isotropic case, the pattern is just rotated in the direction of $\mathbf{n}$. Explicitly the differential scattering has the form of:

$$\frac{d\sigma}{d\Omega}(|\mathbf{k}_\mathrm{i}, \mathbf{i}\rangle \longrightarrow |\mathbf{k}_\mathrm{f}, \mathbf{f}\rangle) = \frac{3}{8\pi}\ \sigma_0\ |\mathbf{p}\cdot\mathbf{f}|^2 = \frac{3}{8\pi}\ \sigma_0\ |\langle\mathbf{i}|\,\mathbf{D}\,|\mathbf{f}\rangle|^2, \tag{3.16}$$

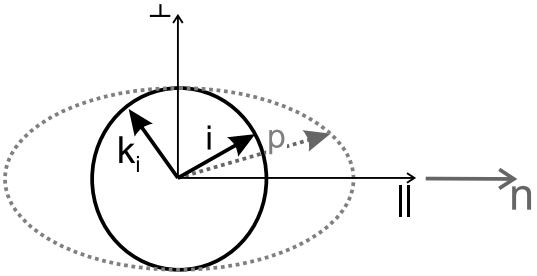

Figure 3.7: Effect of the anisotropy on the excited dipole $\mathbf{p} = \mathbf{D}\,\mathbf{i}$. The dipole is stronger and rotated towards $\mathbf{n}$; therefore the scattering is more probable in the direction orthogonal to $\mathbf{n}$.

We are interested in the probability of a scattering event in the direction $\mathbf{k}_\mathrm{f}$, and therefore we want to integrate over the scattered polarization states $d\sigma/d\Omega(|\mathbf{k}_\mathrm{i}, \mathbf{i}\rangle \rightarrow |\mathbf{k}_\mathrm{f}, \mathbf{f}\rangle)$, for each $\mathbf{k}_\mathrm{f}$. This sum which is sought is explicitly

$$\frac{d\sigma}{d\Omega}(|\mathbf{k}_\mathrm{i}, \mathbf{i}\rangle \longrightarrow |\mathbf{k}_\mathrm{f}\rangle) = |\langle \mathbf{i}\,\mathbf{D}^\dagger|\,\Delta_{\mathbf{k}_\mathrm{f}}\,|\mathbf{D}\,\mathbf{i}\rangle|^2, \tag{3.17}$$

where $\Delta_{\mathbf{k}_\mathrm{f}}$ is a projector, in the polarization space, onto the space orthogonal to $\mathbf{k}_\mathrm{f}$. It is defined as

$$(\Delta_\mathbf{k})_{ij} = 1 - \mathbf{k}_i\mathbf{k}_j, \tag{3.18}$$

it accounts for the transversality of the light and it is thus the only actor in an isotropic Rayleigh scattering.

The total scattering cross-section $\sigma_t(\mathbf{i})$, is the integral over all scattered states, all possible scattering directions and polarizations, and it is

$$\sigma_t(\mathbf{i}) = \int \frac{d\sigma}{d\Omega}\, d\Omega_\mathrm{f}, \tag{3.19}$$

where the integration is over $d\mathbf{k}_\mathrm{f}$ and over those $d\mathbf{f}$, such that $\mathbf{f} \perp \mathbf{k}_\mathrm{f}$: a photon state is allowed if the field is transverse to the direction of the k-vector.

For the anisotropic Rayleigh scattering this turns into

$$\sigma_t(\mathbf{i}) = \frac{3}{8\pi}\,\sigma_0 \int_{4\pi} \langle \mathbf{i}\mathbf{D}^\dagger|\Delta_{\mathbf{k}_\mathrm{f}}|\mathbf{i}\mathbf{D}\rangle\; d\mathbf{k}_\mathrm{f} = \sigma_0|\mathbf{D}\,\mathbf{i}|^2 = \sigma_0\;|\mathbf{p}|^2 \tag{3.20}$$

and using Eq. (3.15) this relation can be simplified into:

$$\sigma_t(\mathbf{i}) = \sigma_0[(\mathbf{i}\cdot\mathbf{n})^2(a^2-1)+1]. \tag{3.21}$$

Each polarization state induces a different σ_t and therefore has a different probability of being scattered. The mean free path ℓ_s is therefore not isotropic, and depends on the polarization of the light. ℓ_s depends on the scattered direction $\mathbf{k}_\mathrm{f}$, Fig. 3.8, as for each direction of emission there is a well defined (transverse) polarization that can be radiated by the dipole, orthogonal to $\mathbf{k}$ in the plane of the dipole $\mathbf{p}$.

3.3 The dressed Green function for anisotropic Rayleigh scattering

In the previous section, we have shown that, in presence of anisotropic Rayleigh scattering, the total scattering cross-section is not isotropic. This implies that the scattering mean free path is not constant any more, (Eq. (3.22)) and therefore also that the dressed Green function is not isotropic. The scattering mean free path experienced by a photon with polarization $\mathbf{i}$ is

$$\ell_s(\mathbf{i}) = \frac{1}{\sigma_0} \frac{1}{(\mathbf{i}\cdot\mathbf{n})^2(a^2-1)+1}. \tag{3.22}$$

Fig. 3.8 shows a specific case to illustrate the anisotropy in the scattering mean free path. A photon with polarization $\mathbf{i}$ excites a dipole $\mathbf{p} = \mathbf{D}\mathbf{i}$ that we assume to be in the y-direction. A radiated photon emerging in the direction $\mathbf{k}_\mathrm{f}$ from the dipole has a polarization which is orthogonal to $\mathbf{k}_\mathrm{f}$ and experiences a total scattering cross-section shown by the polar plot in Fig. 3.8, which ranges from σ_0 to $(a^2\sigma_0)$, depending to the scattering direction.

3.3.1 Optical theorem and scattering cross-section

The T-matrix describes the transfer of energy from the incident beam, which we will call the coherent beam, into all the other modes. This information is also conveyed by the differential scattering cross-section

$$\frac{d\sigma}{d\Omega}(|\mathbf{k}_\mathrm{i},\mathbf{i}\rangle \longrightarrow |\mathbf{k}_\mathrm{f},\mathbf{f}\rangle) \propto |\langle \mathbf{k}_\mathrm{i},\mathbf{i}|\mathbf{T}(\omega)|\mathbf{k}_\mathrm{f},\mathbf{f}\rangle|^2 \tag{3.23}$$

An important relation between the scattering cross-section and the T-matrix comes from the *optical theorem*, which states that:

$$\sigma_t(\mathbf{k}_\mathrm{i},\mathbf{i}) = -2L^3\ \mathrm{Im}(\langle \mathbf{k}_\mathrm{i},\mathbf{i}|\,\mathbf{T}(\omega)\,|\mathbf{k}_\mathrm{i},\mathbf{i}\rangle). \tag{3.24}$$

The value of $\mathbf{T}(\omega)$ over the input and output states quantifies the amount of light amplitude transferred from the coherent beam $|\mathbf{k}_\mathrm{i},\mathbf{i}\rangle$ to the scattered mode $|\mathbf{k}_\mathrm{f},\mathbf{f}\rangle$, and therefore $\mathrm{Im}\langle \mathbf{k}_\mathrm{i},\mathbf{i}|\mathbf{T}(\omega)|\mathbf{k}_\mathrm{i},\mathbf{i}\rangle$ is what is scattered back into the coherent mode.

The scattering cross section is connected with the probability of scattering forward, which is the process in which both $\mathbf{k}_\mathrm{i}$ and $\mathbf{i}$ do not change, which is the same as the case when no scattering occurs. The physical meaning of Eq. (3.24) is that the total scattered wave is given by the incident wave minus the part which is not scattered, and thus propagates forward after the scattering event. Energy conservation requires that all that is taken out of the coherent beam $|\mathbf{k}_\mathrm{i},\mathbf{i}\rangle$ is transferred to other modes and not dissipated.

It is worth to notice that the optical theorem puts a constrain on the phase of the scattered wave, which is related to the total scattering cross-section.

3.3.2 Anisotropic self-energy

We can write the scattering cross-section as a linear operation on the input and output electric field polarization. We can use the dielectric tensor $\mathbf{D}$ which accounts for the excited dipole, as defined in Eq. (3.13) and the transverse operator $\Delta_{\mathbf{k}_\mathrm{f}}$ which ensure

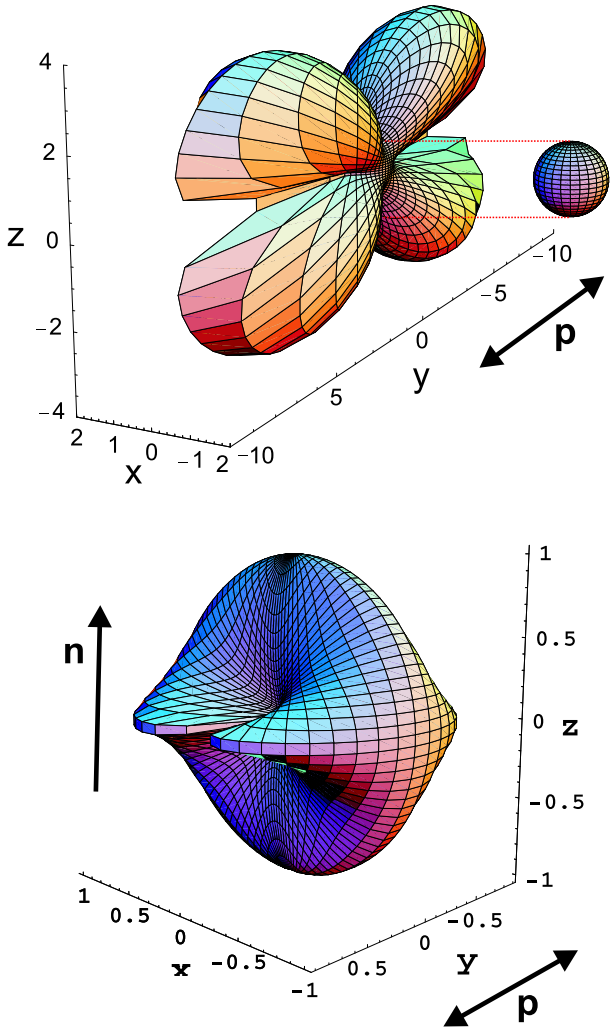

Figure 3.8: Total scattering cross-section distribution (top panel) and scattering mean free path (lower panel) for an anisotropy of $a = 3$ in the direction $\mathbf{n} = \hat{\mathbf{z}}$. The excited dipole is in the $\hat{\mathbf{y}}$ direction. On the top right the symmetric σ_t for $a = 1$ is shown.

the transverse nature of light. The dipole $\mathbf{p}$ induced by the incident polarization $\mathbf{i}$ is $\mathbf{p} = \mathbf{Di}$. The transverse operator $\Delta_{\mathbf{k}_\mathrm{f}}$ which projects on the subspace transverse to $\mathbf{k}_\mathrm{f}$ is, as defined in Eq. (3.18), is here redefined as (we only drop the index f)

$$\Delta_{\mathbf{k}} = 1 - |\mathbf{k}_\mathrm{f}\rangle\langle\mathbf{k}_\mathrm{f}|. \tag{3.25}$$

The differential scattering cross-section is related to the excited dipole and to the transversality condition, as shown in Eq. (3.17). In Eq. (3.17) no dependence on the incident direction is evident, as the dependence on $\mathbf{f}$ is eliminated with the transversality relation ($\mathbf{k}_\mathrm{f} \perp \mathbf{f}$), and by the constraint on the scattered polarization $\mathbf{f}$, which has to be in plane of the dipole and orthogonal to $\mathbf{k}_\mathrm{f}$. Rayleigh scattering is not sensitive on the incident direction $\mathbf{k}_\mathrm{i}$ as the dipole is generated only by the incident polarization.

Explicitly $\mathbf{D}^\dagger\Delta_\mathbf{k}\mathbf{D}$ is:

$$\begin{aligned}\mathbf{D}^\dagger\Delta_\mathbf{k}\mathbf{D} &= [(a^2-1)-(a-1)^2(\mathbf{n}\cdot\mathbf{k}_\mathrm{f})^2]|\mathbf{n}\rangle\langle\mathbf{n}| - |\mathbf{k}_\mathrm{f}\rangle\langle\mathbf{k}_\mathrm{f}| + \\ &\quad +1-(a-1)(\mathbf{k}_\mathrm{f}\cdot\mathbf{n})(|\mathbf{n}\rangle\langle\mathbf{k}_\mathrm{f}| + |\mathbf{k}_\mathrm{f}\rangle\langle\mathbf{n}|). \end{aligned} \tag{3.26}$$

Combining equations (3.23) and (3.17), as the two operators act on the same subspace of the space of $\{\mathbf{k},\boldsymbol{\epsilon}\}$, we can write the identity:

$$|\langle\mathbf{k}_\mathrm{i},\mathbf{i}|\ \mathbf{T}\ |\mathbf{k}_\mathrm{f},\mathbf{f}\rangle|^2 = |\langle\mathbf{i}|\ \mathbf{D}^\dagger\Delta_\mathbf{k}\mathbf{D}\ |\mathbf{i}\rangle|^2. \tag{3.27}$$

In the measurements one usually observes only intensities, quantities like σ_t and no information of the phase of the scattered wave are obtained. The optical theorem (Eq. 3.24) relates this phase with the σ_t, showing that the modulus and phase of the scattered wave are not two independent quantities. We leave here the phase unknown, but we can assume that far from the resonances it has a slow variation; we consider it constant for the light states we are investigating, within the spectral width of the incident laser light. We can conclude that

$$\mathbf{T}_\mathbf{k} = \mathbf{D}^\dagger\Delta_\mathbf{k}\mathbf{D}, \tag{3.28}$$

where $\mathbf{T}_\mathbf{k}$ now acts only on the polarization states, $\langle\mathbf{k}_\mathrm{i},\mathbf{i}|\mathbf{T}|\mathbf{k}_\mathrm{f},\mathbf{f}\rangle = \langle\mathbf{k}_\mathrm{i}|\mathbf{T}_\mathbf{k}|\mathbf{f}\rangle$, as scattered direction ($\mathbf{k}_\mathrm{f}$) and polarization ($\mathbf{f}$), are related, as we have just shown. With the help of Eq. (2.66), for dilute media, we can now express the self-energy as:

$$\boldsymbol{\Sigma}(\mathbf{k}_\mathrm{f}) \simeq n_p\ \mathbf{T}_\mathbf{k} = n_p\ \mathbf{D}^\dagger\Delta_\mathbf{k}\mathbf{D}. \tag{3.29}$$

Our system is made of point-like scatterers in vacuum (or in an homogenous medium) and therefore the only object that can play a role for light propagation is the T-matrix responsible for the scattering event, as confirmed in Eq. (3.29).

3.3.3 The dressed Green function for anisotropic Rayleigh scatterers

As shown so far, for *anisotropic point-like scatterers*, the average Green function of the system can be calculated from the knowledge of the self-energy,

$$G(\mathbf{r}_1,\mathbf{r}_2,\mathbf{k}_\mathrm{f}) = -\frac{e^{i\mathbf{k}_\mathrm{f}|\mathbf{r}_{12}|}}{4\pi|\mathbf{r}_{12}|}\ \exp(-i\boldsymbol{\Sigma}(\mathbf{k}_\mathrm{f})|\mathbf{r}_{12}|)\Delta_\mathbf{r}, \tag{3.30}$$

where $\mathbf{r}_{12} = \mathbf{r}_1 - \mathbf{r}_2$.

The self-energy contains all information about the intra-scattering propagation, Eq. (3.30) can be interpreted as related to the dispersion law in the medium. As shown in Eq. (2.68), we can introduce the refractive index matrix

$$\mathcal{N}(\mathbf{k}_\mathrm{f}) = 1 - \frac{\mathrm{Re}\boldsymbol{\Sigma}(\mathbf{k}_\mathrm{f})}{k}, \tag{3.31}$$

the average value of $\boldsymbol{\Sigma}(\mathbf{k}_\mathrm{f})$ over the scattered polarization states provides the scattering mean free path,

$$\langle\mathbf{f}|\,\mathrm{Im}(\boldsymbol{\Sigma}(\mathbf{k}_\mathrm{f}))\,|\mathbf{f}\rangle = -\frac{1}{2\ell_s} \tag{3.32}$$

and its eigenvectors are the principal polarization of the scattered light.

The propagator can be expressed in the same form as the vacuum propagator,

$$G(\mathbf{r}_1, \mathbf{r}_2, \mathbf{k}_\mathrm{f}) = -\frac{e^{ik\mathcal{N}(\mathbf{k}_\mathrm{f})|\mathbf{r}_{12}|}}{4\pi|\mathbf{r}_{12}|}\, e^{-i\frac{|\mathbf{r}_{12}|}{2\ell_s}}\, \Delta_{\mathbf{r}}. \tag{3.33}$$

The difference now is that the self-energy is no more diagonal in the light polarization, and not all the directions of propagation are the same. The same effect is present in an ensemble of atoms in an external magnetic field [87].

3.3.4 Diagonalization of the self-energy: the principal directions of propagation

The self-energy can be diagonalized and brought into the form:

$$\mathbf{\Sigma}(\mathbf{k}) = -i\frac{n_p\ \sigma_0}{2}\begin{pmatrix} 1 & 0 & 0 \\ 0 & 1+(a^2-1)(1-(\mathbf{k}\cdot\mathbf{n})^2) & 0 \\ 0 & 0 & 0 \end{pmatrix} \tag{3.34}$$

if calculated on the eigenbase $\{\mathbf{e_1}, \mathbf{e_2}, \mathbf{e_3}\}$ made of the vectors:

$$\begin{array}{lccc} \mathbf{e}_1 = & \mathbf{k}\times\mathbf{n} & & \text{ordinary} \\ \mathbf{e}_2 = & (\mathbf{k}\cdot\mathbf{n})\mathbf{k} - [(a-1)(1-(\mathbf{k}\cdot\mathbf{n})^2)]\mathbf{n} & & \text{extraordinary} \\ \mathbf{e}_3 = & \mathbf{k} - (\mathbf{k}\cdot\mathbf{n})(a-1)/a & & \text{longitudinal} \end{array} \tag{3.35}$$

where in the limiting case of $(\mathbf{k}\cdot\mathbf{n}) = 0$ the extraordinary mode $\mathbf{e_2} = \mathbf{n}$. These are the eigenmodes of the polarization, which propagate in the medium without being altered. The average medium in the presence of anisotropic Rayleigh scattering is *dichroic*. A generic polarization rotates upon propagation as the Green functions of the modes are not "dressed" in the same way.

If one looks at the eigenvalues λ_i of the self-energy, one sees that the *ordinary* mode behaves as in the isotropic medium ($\lambda_1 = 1$), the *extraordinary* one has a different mean free path, (see Eq. (3.32)), ($\lambda_2 = 1 + (a^2-1)(1-(\mathbf{k}\cdot\mathbf{n})^2)$) and the third mode, which is *longitudinal*, has $\lambda_3 = 0$, and is the non-propagating one parallel to the group velocity in the medium.

The total scattering cross-section experienced by the two propagating modes $\mathbf{e}_{1,2}$ is not the same:

$$\begin{aligned} \sigma_{ord} \equiv \sigma_t(\mathbf{e}_1) &= \sigma_0 \\ \sigma_{ext} \equiv \sigma_t(\mathbf{e}_2) &= \sigma_0\ [1+(a^2-1)(1-(\mathbf{k}\cdot\mathbf{n})^2)] \end{aligned} \tag{3.36}$$

The value of the total scattering cross-section can be computed from the optical theorem of Eq. (3.24), as for low density we have approximated $\mathbf{\Sigma}$ with $\mathbf{T}$. σ_t is the diagonal value of $\mathbf{\Sigma}$ calculated on $\mathbf{i}$, and it is perfectly consistent (and equal) with the value calculated from the standard Rayleigh formula:

$$\sigma_t(\mathbf{f}) = \sigma_0\ |\ \mathbf{i}\,\mathbf{D}|^2 = \frac{2i}{n_p}\ \langle\mathbf{i}|\ \mathbf{\Sigma}(\mathbf{k})\ |\mathbf{i}\rangle, \tag{3.37}$$

obtained from Eq. (3.36).

3.3.5 Evolution of polarization

The two polarization eigenmodes experience a different Lambert-Beer attenuation. This implies that a generic superposition

$$|\boldsymbol{\epsilon}(z=0)\rangle = \varepsilon_1|\mathbf{e}_1\rangle + \varepsilon_2|\mathbf{e}_2\rangle \tag{3.38}$$

of these two modes will rotate upon propagation as its components on $\mathbf{e_1}$ and $\mathbf{e_2}$ will evolve differently:

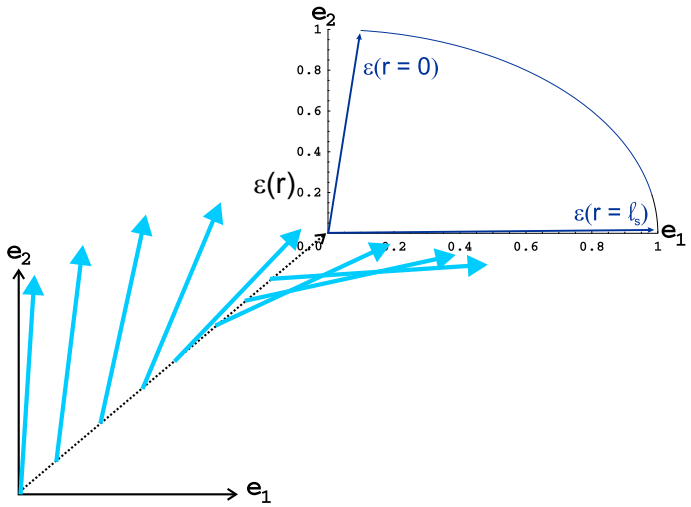

Figure 3.9: Evolution of the polarization vector as a function of the propagated distance r/ℓ_s. Initially at $r = 0$ the light is almost completely polarized extraordinary $\varepsilon_1 = 0.1$ and $\varepsilon_2 = 0.995$, while at large r it becomes more and more ordinary. Anisotropy $a = 3$.

$$\begin{aligned} |\boldsymbol{\epsilon}(z)\rangle &= (\boldsymbol{\epsilon}(0)\cdot\mathbf{e}_1)\,|\mathbf{e}_1\rangle + (\boldsymbol{\epsilon}(0)\cdot\mathbf{e}_2)\,\exp\left(-r\frac{\sigma_{ext}-\sigma_{ord}}{2}\right)|\mathbf{e}_2\rangle \\ &= \varepsilon_1\,|\mathbf{e}_1\rangle + \varepsilon_2\,\exp\left(-r\frac{\sigma_{ext}-\sigma_{ord}}{2}\right)|\mathbf{e}_2\rangle \end{aligned} \tag{3.39}$$

where $(\sigma_{ext} - \sigma_{ord})$ is a positive quantity for $a > 1$, thus the polarization experiences a total scattering cross-section which varies with the propagation following the law:

$$\sigma_t(\boldsymbol{\epsilon}(z)) = 1 + (a^2-1)(\boldsymbol{\epsilon}(z)\cdot\mathbf{n})^2. \tag{3.40}$$

The polarization rotates towards $\mathbf{e_1}$ because $\boldsymbol{\epsilon}(z)\cdot\mathbf{e}_2$ tends to zero upon propagation, as shown in Fig. 3.9.

The total scattering cross-section experienced by the photon upon propagation reduces gradually to the value of $\sigma_t(\mathbf{e}_1) = 1$. We have calculated σ_t combining Eq. (3.39) with the expression of σ_t of Eq. (3.40), and taking into account the normalization of the vectors $\mathbf{e}_{1,2}$.

$$\sigma_t(z) = 1 + \varepsilon_2^2\,(a^2-1)\exp(-r\ \beta)\left[\frac{a(\mathbf{k}\cdot\mathbf{n})^2-(a-1)}{\mathbf{k}(\mathbf{k}\cdot\mathbf{n})-(a-1)(1-(\mathbf{k}\cdot\mathbf{n})^2)\mathbf{n}}\right]^2 \tag{3.41}$$

where β is

$$\beta = \sigma_{ext} - \sigma_{ord} = (a^2 - 1)(1 - (\mathbf{k} \cdot \mathbf{n})^2). \tag{3.42}$$

Fig. 3.10 shows the evolution of $\ell_s(z)$ as a function of the propagated distance $r/\ell_s(ord)$. After a scattering mean free path the polarization is almost completely ordinary and ℓ_s very close to the ordinary value of $\ell_s(ord) = 1/n_p\sigma_0$.

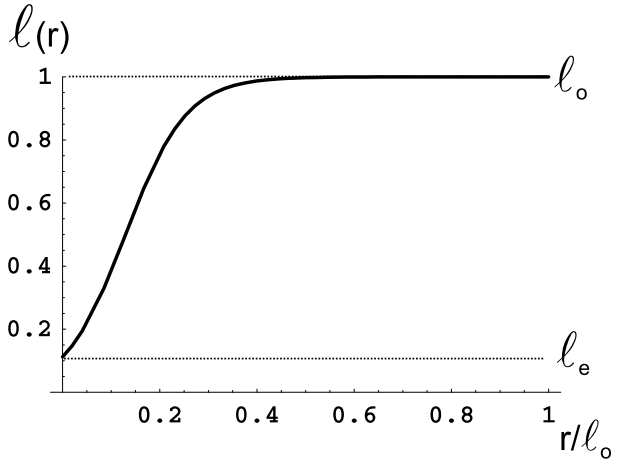

Figure 3.10: Evolution of the scattering mean-free path as a function of the propagated distance $r/\ell_s(ord)$. Initially at $r = 0$ the light is almost completely polarized extraordinary ($\ell_s \simeq \ell_s(ext)$), $\varepsilon_1 = 0.0999$ and $\varepsilon_2 = 0.995$, while at large r it becomes more and more ordinary ($\ell_s \simeq \ell_s(ord)$). Anisotropy $a = 3$ ($\mathbf{k}_\mathrm{i} = x$ and $\mathbf{n} = z$).

3.3.6 Propagation step-length distribution

If we now look closer at what happens to the scattered photon, we can see that while it propagates in the average medium, and its polarization rotates, the probability of a new scattering event decreases accordingly. The probability of travelling a distance r before a new scattering event is usually described by a step-length probability $P(r)$. In the isotropic case, when the total scattering cross-section is a constant $\sigma_t(z) = \sigma_0$, this function is an exponential with decay constant equal to $\ell_s = 1/n\sigma_0$:

$$P(r) = \exp(-r\, n_p\, \sigma_0)(n_p\, \sigma_0) = \exp\left(-\frac{r}{\ell_s}\right)/\ell_s. \tag{3.43}$$

In the anisotropic case the total scattering cross-section is not constant but decreases with the travelled space, as in Eq. (3.41). As a direct consequence ℓ_s increases upon propagation up to its ordinary value. The anisotropic random walk has a step-length probability which depends on the space travelled:

$$P(r) = \exp\left(-r\ n_p\ \int_0^r \sigma_t\ dr\right) \times \left(n_p\ \int_0^r \sigma_t\ dr\right). \tag{3.44}$$

Explicitly this function is:

$$P(r) = \exp\left(-\frac{r}{\ell_s(r)}\right)/\ell_s(r) = \left(e^{-r/\ell_s(\mathbf{e}_1)}\varepsilon_1^2 + e^{-r/\ell_s(\mathbf{e}_2)}\varepsilon_2^2\right)/\ell_s(r) \tag{3.45}$$

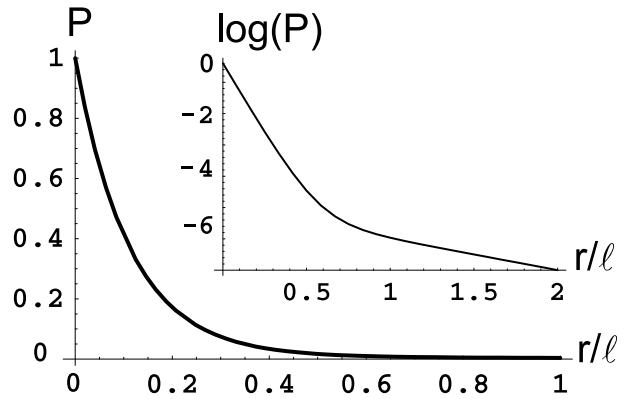

Figure 3.11: Step-length distribution in an anisotropic rayleigh scattering medium. At the beginning the distribution is dominated by the extraordinary $P(r)$ which is more steep as $\ell_s(ext) < \ell_s(ord)$, while for larger distances the ordinary $P(r)$ takes over. Note that $\ell_s(ext) = (1/a)\ell_s(ord)$. Initially at $r = 0$ the light is almost completely polarized extraordinary $\varepsilon_1 = 0.0999$ and $\varepsilon_2 = 0.995$, while at large r it becomes more and more ordinary. Anisotropy $a = 3$.

where the decay constants of the two exponentials are the scattering mean free path of the two ordinary and extraordinary eigenmodes (Fig. 3.11). This is consistent with Eq. (3.39) (which is the superposition principle).

3.4 Conclusions

We have shown that a mesoscopic model can be very well applied to an anisotropic scattering medium as an ensemble of anisotropic Rayleigh scatterers. The self-energy is no more diagonal, but the principal propagation directions can be calculated, and an anisotropic random walk model can be constructed. Given all these ingredients a Monte Carlo simulation can be employed to model the light transport and to predict the shape of the coherent backscattering cone.

Chapter 4

Anisotropic coherent backscattering from ordered nematic liquid crystals

Liquid crystals in the nematic phase are strongly scattering materials that differ fundamentally from common isotropic random media. The nematic phase of a liquid crystal is characterized by a global alignment of the molecules in a direction called the nematic director $\mathbf{n}(\mathbf{r})$, and an otherwise translational disorder. The strong opacity of the nematic phase comes about from local fluctuations in the nematic director $\mathbf{n}(\mathbf{r},t) = \mathbf{n}_0 + \delta\mathbf{n}(\mathbf{r},t)$, that elastically scatter light [22, 23, 24]. Transmission experiments have shown that light transport in ordered nematic liquid crystals indeed shows anisotropic features, both in static [88] and dynamic [89] experiments, and that diffusive models and radiative transfer theory can describe light transport in such a complex medium [90].

Pioneering experiments on coherent backscattering from nematics have been performed, but only the existence of the interference phenomenon could be confirmed and no other information could be extracted from the experimental data [56, 57, 91]. Anisotropy in coherent backscattering due to an anisotropic transport mean free path has been predicted numerically in Monte-Carlo simulations [92, 93]. Only recently, in our experiment, anisotropy in weak localization from ordered nematic liquid crystals has been observed and the cone fully resolved [94], opening the way for further investigation on light transport in such a complex medium.

The main property of liquid crystals is the dielectric anisotropy that can be oriented with an external magnetic or electric field. This is the crucial property that allows the switching of the pixels in liquid crystal displays [95]. Multiple light scattering in these media is a recent subject of fundamental investigation as they are suitable candidates to observe anisotropic light transport and to study anisotropic interference phenomena.

Since their discovery [96] more than a hundred years ago by Reinitzer and Lehmann, liquid crystals are now being used in a wide range of applications, as for example in display technology. They are also used to construct light valves and spatial light modulators utilized in real-time image processing and optical computing applications. Even dynamic scattering in liquid crystals is considered for possible applications due to the fact that only a relatively small voltage is needed to achieve a large magnitude of light scattering.

In this chapter we present briefly the main properties of nematic liquid crystals such as elastic properties, interactions with external electric and magnetic fields, birefringency and diamagnetism. We then focus on light scattering and on the experimental measure of the anisotropic coherent backscattering cone from oriented nematic liquid crystals.

4.1 Physical properties of liquid crystals

The states of matter whose symmetric and mechanical properties are intermediate between those of a crystalline solid and an isotropic liquid are called "liquid crystals"[1] [97]. Liquid crystals are materials that exhibit one or more intermediate phase(s) between crystalline solid and isotropic liquid phases. In this intermediate phase they retain the ability to flow like ordinary liquid, but also possess long-range orientational order. Some liquid crystals may also have positional order as well.

The basic difference between crystals and liquids is that the molecules in a crystal are ordered whereas in a liquid they are not. The existing order in a crystal is usually both positional and orientational, i.e. the molecules are constrained both to occupy specific sites in a lattice and to point their molecular axes in specific directions. In liquid crystals, translational symmetry typical of liquids exists but rotational invariance holds only for certain axis of symmetry, as it occurs in solids. The liquid crystals can flow as liquids, but they are liquid in which some orientational order is gained, and in these mesophases the degree of freedom of the liquid are decreased, its symmetries reduced.

Liquid crystals show self-assembly and a form of self-organization at molecular level which originates from the complex interplay of molecular interactions and thermal fluctuations. In ordinary samples the alignment and the optical properties depend strongly on surface effects which compete strongly with all other external potentials. We are here investigating *bulk* optical properties, as our sample has a volume of ~ 200 ml, with a cell thickness of 8 cm, a much different configuration than in ordinary experiments, where the cell thickness is of the order of 100 μm ($\sim 50\mu$m in LCD screens).

4.1.1 The phases of liquid crystals

In nature, many types, or better many phases, of liquid crystals exist which depend on the molecular order of the system, on its symmetry. In Fig. 4.1, two very common phases are shown. The *nematic* phase occurs if the rotational order is only along one axis. In the *smectic* phase the system can be viewed as a set of two-dimensional liquid layers stacked on each other with a well defined spacing. In each plane the smectics are aligned along a director.

Usually nematics and smectics are made of *elongated* objects (as shown in fig. 4.1) but there exists liquid crystals, like the columnars, which are made of *disk-like* molecules (not shown here). Recently also biaxial nematic liquid crystal have been synthesized with boomerang-shaped molecules [98, 99]. Liquid crystalline materials in general may

[1] Discovered at the end of the 19^{th} century (1888-Reinitzer), liquid crystals were considered an oddity with only pure academic value until 1960, when they were first considered for use in display technology.

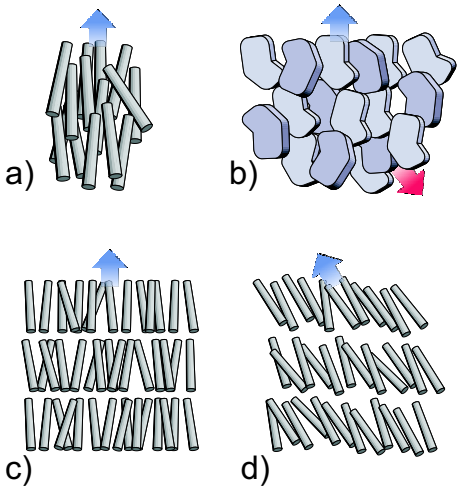

Figure 4.1: Various phases of liquid crystals: in (a) the uniaxial nematic phase, in (b) biaxial nematic phase, in (c) the smectic A phase and in (d) the smectic C phase.

have various types of molecular structure. What they all have in common is that they are anisotropic.

Liquid crystals are mesogenic species, as they can exhibit a multitude of transitions involving new phases. Transitions to the mesophases may be brought about in two different ways; one by purely thermal processes, like change of the temperature, and the other by the influence of solvents. Liquid crystals obtained by the first method are called *thermotropics*. This is the only case that we will investigate in this thesis. The phase of a thermotropic liquid crystal changes from crystalline solid to liquid crystal when the temperature is raised above its melting point (T_M). When the temperature is further increased, the phase of the substance changes from liquid crystalline phase to isotropic liquid phase. This temperature is called the clearing point (T_C). In this thesis the interest in liquid crystals is restricted to nematics, which occur in the temperature range $T_M < T < T_C$ (see Fig. 4.2), so in next sections only the properties of such a phase will be described.

For example 5CB liquid crystals present a melting temperature $T_M \simeq 297$ K, and a clearing temperature $T_C \simeq 309$ K [100]. These values have to taken with care, as they depend strongly on the environment conditions, especially on the characteristics of the cell in which the liquid crystals are contained. We obtained a good nematic sample keeping the temperature in the safe range of $299 < T < 303$ K.

4.1.2 Elastic properties of nematics

The nematic phase is the simplest liquid crystal phase. In this phase the molecules maintain a preferred orientational direction as they diffuse throughout the sample. There exists no positional order but there is a long-range orientational order.

Nematic liquid crystals, depicted in Fig. 4.2(b), show some order in the direction of the molecules. They tend to be parallel to a common axis labelled *nematic director* $\mathbf{n}$. Because of the axial symmetry of the molecules, optically a nematic is an uniaxial medium with the optical axis along $\mathbf{n}$. Another remarkable property is that nematics

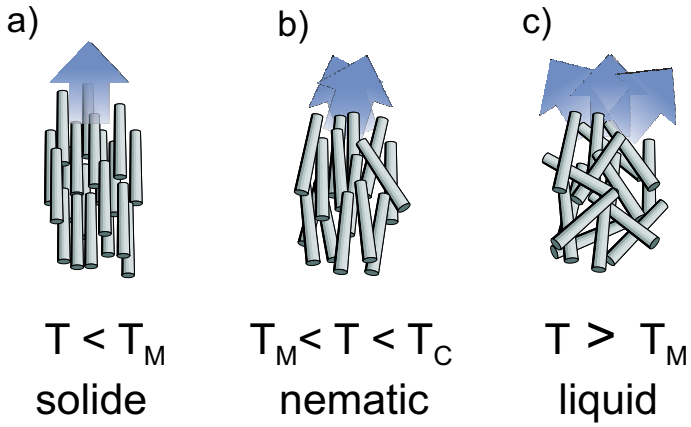

Figure 4.2: Phase transition of the liquid crystals. If the temperature is lower than the melting point (T_M) the liquid crystals are behave as a solid (a). If $T_M < T < T_C$ there is the nematic regime (b). For temperatures higher then the clearing point (T_C) they behave as an isotropic liquid.

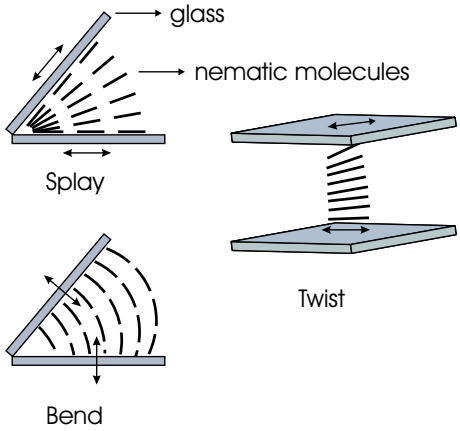

Figure 4.3: The three types of deformations occurring in nematics.

flow like liquids. The nuclear magnetic resonance (NMR) spectrum shows line splitting caused by the uniaxial symmetry, and, at the same time, such lines are narrow enough to identify rapid molecular motion (like for conventional liquids).

All the elastic properties of nematic liquid crystals can be summarized in an energy balance equation, which is the well-known Frank expression for the free energy [101]

$$F_e = \frac{1}{2}[K_{11}(\nabla \cdot \mathbf{n})^2 + K_{22}(\mathbf{n} \cdot (\nabla \times \mathbf{n}))^2 + K_{33}(\mathbf{n} \times (\nabla \times \mathbf{n}))^2] \,, \qquad (4.1)$$

where K_{ij} are the Frank elastic constants, which represent the principal components of the elastic deformation tensor. The Frank expression is derived from the continuum theory, which considers only liquid crystals elastic energy, and in which the main hypothesis is that the order parameter Q (a measure of the strength of the local correlation among adjacent molecules, and at the same time the degree of global orientation) varies over distances ≥ 1 μm, much larger than typical molecular dimensions ~ 20 Å.

The constants K_{ii} (i=1,2,3), introduced in Eq. (4.1), are associated with the three basic types of deformations present in liquid crystals, displayed in Fig. 4.3. For simplicity in the following we will refer to K_{ii} as K_i.

K_1 describes splay ($\nabla\cdot\ \mathbf{n}\neq 0$)

K_2 describes twist ($\mathbf{n}\cdot(\nabla\times\ \mathbf{n}) \neq 0$)

K_3 describes bend ($\mathbf{n}\times(\nabla\times\ \mathbf{n}) \neq 0$).

The typical values for K_i are in the order of $10^{-11} - 10^{-12}$ N. For 5CB liquid crystals the Frank constants are $K_3 = 5.3 \times 10^{-12}$ N, $K_1 = 0.79K_3$ and $K_2 = 0.43K_3$.

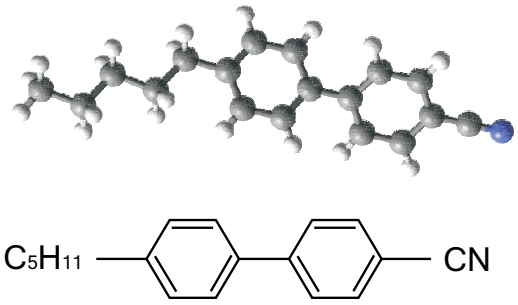

Figure 4.4: In the upper part the molecular structure of 5CB is depicted, while in the lower part the chemical formula with two benzene rings.

We will not go into the details of the chemical properties of the types of liquid crystals. For our interest, we present briefly 5CB (*p*-penthyl-*p'*-chanobiphenyl) that has two benzene rings, as shown in Fig. 4.4, such as many others liquid crystals, which are diamagnetic. A benzene ring, when exposed to a magnetic field **H**, tends to rotate and to align its plane along the field to minimize the electro-magnetic energy.

4.1.3 Magnetic field effect

An external magnetic (or electric) field can induce a global alignment of the crystals, which find energetically convenient to be parallel to the field (Fig. 4.5). The free energy becomes

$$F = F_e + F_m + F_{el} \tag{4.2}$$

where F_m and F_{el} are respectively the magnetic and electric contributions.

The coupling energy between **H** and a diamagnetic molecule is $(\mu_b H)^2/U$, where μ_b is the Bohr magneton and U is the electronic excitation energy. For one molecule $(\mu_b H)^2/U \sim 10^{-18}$ eV (an elastic energy $F_e \sim 10$ eV and $H \sim 1$ Gauss) which is $\ll kT$, which means that the thermal agitation is stronger with respect to field alignment. The properties of nematics are collective, so within one coherence length cube (called ξ, see later in the section), one can consider a global degree of freedom and not all the individuals for each molecule. In a ξ^3 volume (there are typically $N \sim 10^{22}$ molecules), all molecules rotate together, and the coupling energy is of the order of $N(\mu_b H)^2/E \gg kT$. The collective orientational energy is stronger than the thermal agitation and the sample aligns its optical axis **n** parallel to **H**.

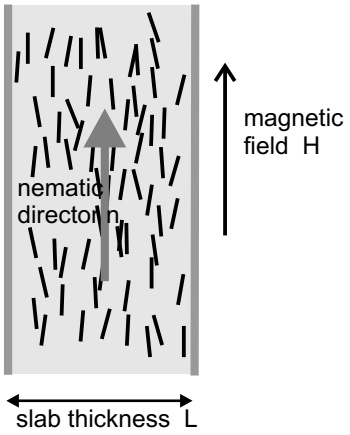

Figure 4.5: An external magnetic field can induce a global alinement of the nematic liquid crystals around a common direction $\mathbf{n}$ called the nematic director, parallel to the magnetic field $\mathbf{H}$.

To investigate the effects of an external magnetic or electric field on nematics, we have calculate the free energy density. Let's start with the magnetization $\mathbf{M}$ induced by the magnetic field $\mathbf{H}$. If we suppose an arbitrary angle between $\mathbf{n}$ and $\mathbf{H}$, the magnetization will be:

$$\mathbf{M} = \chi_\perp \mathbf{H} + (\chi_\parallel - \chi_\perp)(\mathbf{H}\cdot\mathbf{n})\mathbf{n}\,, \tag{4.3}$$

where the magnetic susceptibilities $\chi_\parallel$ and $\chi_\perp$ are negative (diamagnetism) ($\sim 10^{-6}$), but the difference $\chi_\parallel - \chi_\perp = \chi_a$ is positive in nematics. The free energy density becomes

$$F = F_e - \int_0^H \mathbf{M}\cdot \mathrm{d}\mathbf{H} = F_e - \frac{1}{2}\chi_\perp H^2 - \frac{1}{2}\chi_a(\mathbf{n}\cdot\mathbf{H})^2 \tag{4.4}$$

that is minimized when $\mathbf{n}$ is parallel to $\mathbf{H}$ ($\chi_a > 0$)[2].

The nematic liquid orientation parallel (or orthogonal) to the field is energetically favored, in absence of other sources of perturbation, which can be induced by defects, impurities, surface anchoring, etc... The resulting orientation is preserved over a length ξ, called *the coherence length*, which is defined as the distance over which the disturbance of the alignment propagates through the sample. At no field such a perturbation propagates undisturbed, such that all the nematic molecules are aligned following a fixed one: the coherence length becomes infinite. The presence of the magnetic field opposes to such a rotation and the coherence length becomes finite. If we suppose to be in the one constant approximation ($K_i = K$), we have

$$\xi(H) = \frac{1}{H}\sqrt{\mu_0 \frac{K}{\chi_a}}\,. \tag{4.5}$$

For 5CB and $H = 0.5$ Tesla, the coherence length is 4.2μm. This expression is derived starting from Eq. (4.4) (for details see ref. [102]).

The coherence length is very important as it defines the extent of positional order (Fig. 4.6), and subsequentially the scattering correlations.

[2]Note that no anchoring energy is present as we assume infinite distance between the cell walls.

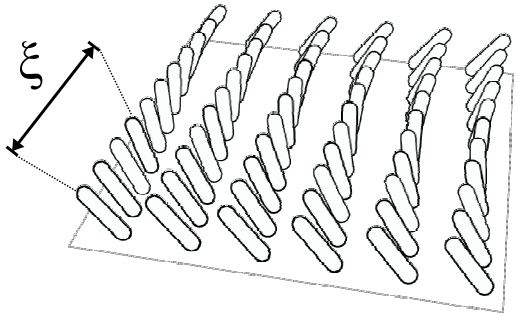

Figure 4.6: Coherence length for nematics under a torsion (courtesy of L. Nobre, http://matagalatlante.org/).

4.1.4 Electric field effect: dielectric anisotropy

A nematic liquid crystal can be considered in first approximation as an insulator. In this hypothesis, the coupling between a nematic and an external electric field **E** involves only the anisotropy of the dielectric constant. What happens is somehow similar to the case of coupling between **H** and nematics caused by diamagnetism.

The dielectric tensor of the medium is given by

$$\varepsilon = \varepsilon_\perp \mathbf{1} + (\varepsilon_\parallel - \varepsilon_\perp)\, \mathbf{n}\mathbf{n}^{\mathrm{T}}. \tag{4.6}$$

The dielectric tensor components, for 5CB nematics, have been determined to be, at 300 K and for 488 nm, $\varepsilon_\perp = 2.894$, and $\varepsilon_\parallel = 2.338$ (for Merck 5CB) [103]. Typical values of the refractive indexes for 5CB liquid crystals are, at 300 K and 488 nm, $n_o = 1.53$ and $n_e = 1.70$, and for temperatures above 308 K, $n_{iso} \simeq 1.57$. Suppose we apply an electric field to a cell filled with nematics, in which the angle between **E** and **n** is generic. We obtain for the electric displacement **D**

$$\mathbf{D} = \varepsilon_\perp \mathbf{E} + (\varepsilon_\parallel - \varepsilon_\perp)(\mathbf{n}\cdot\mathbf{E})\mathbf{n} \tag{4.7}$$

where, as a difference with the magnetic case, $\Delta\varepsilon = \varepsilon_\parallel - \varepsilon_\perp$ (dielectric anisotropy) can be positive or negative. In particular, from a chemical point of view, $\Delta\varepsilon > 0$ if the liquid crystal has a dominant dipole associated with the $C \equiv N$ group. This means that a permanent electric dipole exists parallel to the long axis of the molecule (this is the case of 5CB shown in Fig. 4.4). In other nematics one can have also a reversed situation, where the permanent electric dipole is orthogonal to the long axis, for example if the dipole associated to the $N - O$ groups is dominant, which means $\Delta\varepsilon < 0$.

The electric dipole contribution to the free energy density is

$$F_{el} = -\frac{1}{4\pi}\int_0^E \mathbf{D}\cdot \mathrm{d}\mathbf{E} = \frac{\varepsilon_\perp}{8\pi}E^2 - \frac{\Delta\varepsilon}{8\pi}(\mathbf{n}\cdot\mathbf{E})^2\ . \tag{4.8}$$

In this case if $\Delta\varepsilon > 0$ the free energy density will be minimized for a parallel alignment, otherwise for $\Delta\varepsilon < 0$ we expect a perpendicular alignment. Usually the dielectric anisotropy is $\Delta\varepsilon \sim 0.5$ ($\Delta\varepsilon = 0.556$ for 5CB, at 300 K and 488 nm), and becomes zero when the temperature is above the clearing point.

4.2 Scattering properties of nematic liquid crystal

No universal recipe exists to generalize a diffusive model for the case of anisotropic scattering. That is, it is not evident how to perform the passage from an anisotropic single-scattering process to anisotropic multiple-scattering and subsequently to anisotropic diffusion. A diffusive model is limited by the fact that all characteristics of the transport process have to be contained in one single parameter: the diffusion constant. Single scattering is described by a scattering cross section that depends on incoming and outgoing wavevectors and polarization vectors and can therefore contain various types of anisotropy. The chance of being scattered can depend on propagation direction and polarization, but also the distribution of the light after scattering can be highly anisotropic. In addition, the propagation velocity of the light during the multiple scattering process can be anisotropic as well. A diffusive model in which all these anisotropies have to be contained in one single parameter is potentially an over-simplification of the problem. In addition, the effect of anisotropy on the boundary conditions, required to solve the diffusion equation, is unknown but of crucial importance.

Ordered nematic liquid crystals are anisotropic scattering media in which light polarization plays a central role: the average medium is birefringent and scattering selection rules favor polarization to flip at each scattering event. Moreover the scattering cross-section and scattering mean free path depend strongly on the polarization state and scattering direction [104]. These intricate scattering properties would suggest that a complete solution of the transport equation is more appropriate than a diffusive model. Unfortunately the coupled hydrodynamics equations of nematic liquid crystals and of the electromagnetic field are very difficult to solve [105].

4.2.1 The polarization eigenmodes

Optical birefringence in ordered nematics is present as rotational symmetry is broken by the nematic director $\mathbf{n}$. Light propagates through nematic liquid crystals in two characteristic modes. These are the *ordinary* mode $|\mathbf{k}, \mathbf{o}\rangle$, which has polarization $\mathbf{o}$ orthogonal to $\mathbf{n}$ and $\mathbf{k}$ and the *extraordinary* one $|\mathbf{k}, \mathbf{e}\rangle$ whose polarization $\mathbf{e}$ is in the plane of $\mathbf{k}$ and $\mathbf{n}$. A third mode exists, the longitudinal one, but it does not propagate. The ordinary mode behaves as in an isotropic system, while the extraordinary mode is not transverse and possesses a direction-dependent index of refraction: its phase and group velocities are not equal and not parallel. Birefringence lifts the polarization degeneracy of the propagating modes which become distinct (see Fig. 4.7). The dispersion laws and the directions of the two polarization modes are given by [92]:

$$\begin{aligned}
&\textit{ordinary mode} && \textit{extraordinary mode} \\
&\mathbf{k}_\mathrm{i}^o = \sqrt{\varepsilon_\perp}\frac{\omega}{c} \equiv n_o\frac{\omega}{c}; && \mathbf{k}_\mathrm{i}^e = \sqrt{\frac{\varepsilon_\perp\varepsilon_\parallel}{\varepsilon_\parallel\cos^2\vartheta + \varepsilon_\perp\sin^2\vartheta}}\frac{\omega}{c} \equiv n_e\frac{\omega}{c}; \\
&|\mathbf{o}\rangle = \frac{\mathbf{k}_\mathrm{i}\times\mathbf{n}}{|\mathbf{k}_\mathrm{i}\times\mathbf{n}|}; && |\mathbf{e}\rangle = \frac{\varepsilon_\parallel\langle\mathbf{k}_\mathrm{i}|\mathbf{n}\rangle\,\mathbf{k}_\mathrm{i} - \langle\mathbf{k}_\mathrm{i}|\varepsilon|\mathbf{k}_\mathrm{i}\rangle\,\mathbf{n}}{|\mathbf{k}_\mathrm{i}\times\mathbf{n}|\sqrt{\langle\mathbf{k}_\mathrm{i}|\varepsilon^2|\mathbf{k}_\mathrm{i}\rangle}}.
\end{aligned} \tag{4.9}$$

where ϑ is the angle between the incident light k-vector and the nematic director, and ε the dielectric tensor defined in Eq. (4.6). The two eigenstates experience a different refractive index $n_o \neq n_e$, and therefore interference between them can be neglected

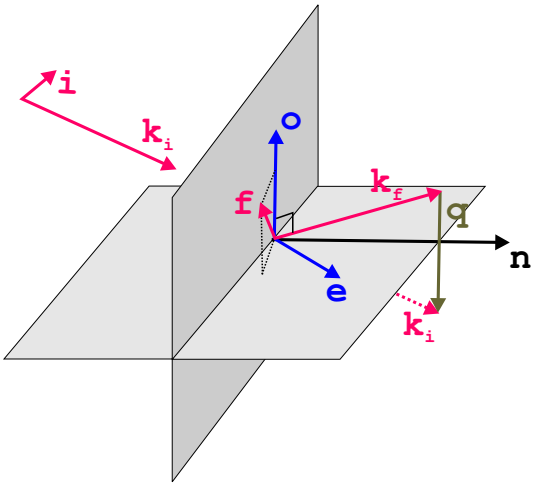

Figure 4.7: Scattering geometry: the photon state $|\mathbf{k}_\mathrm{i}, \mathbf{i}\rangle$ is scattered into $|\mathbf{k}_\mathrm{f}, \mathbf{f}\rangle$. The nematic director $\mathbf{n}$ and the transferred momentum $\mathbf{q} = \mathbf{k}_\mathrm{f} - \mathbf{k}_\mathrm{i}$ are shown. $\mathbf{k}_\mathrm{f}, \mathbf{n}$ and $\mathbf{e}$ are in the same plane, orthogonal to $\mathbf{o}$. The polarization can be decomposed into the two propagation eigenmodes $\mathbf{o}$ and $\mathbf{e}$.

after a distance $\Delta r \simeq \lambda/(n_o - n_e)$. For nematics, $\Delta r \simeq 2-3\mu$m, which is much smaller than the length scales of the scattering process, $\Delta r \ll \ell_\mathrm{s} \simeq 50 - 100\mu$m [104]. For this reason the two eigenstates can be treated independently. It is important to note that, for the same reason, no elliptical polarization can propagate in an anisotropic medium without changing its state, because its different linear components correspond to the two different eigenmodes. Therefore, a constant phase difference between the two linear polarizations cannot be maintained over a distance longer than few wavelengths [106].

4.2.2 The scattering mean free path

For isotropic systems, the scattering mean free path ℓ_s is usually defined as the average distance between two scattering events, and is inversely proportional to the scattering cross section:

$$\ell_\mathrm{s} = \frac{1}{\rho\sigma_t} = \left[\rho \int \frac{d\sigma}{d\Omega}\, d\Omega\right]^{-1}, \tag{4.10}$$

where ρ is the spatial density of the scatterers. In nematics, the scattering mean free path ℓ_s will depend also on the incident direction Ω_i (and on the polarization as we will see later) as a result of the anisotropy of the medium:

$$\ell_\mathrm{s}(\Omega_i) = \left[\rho \int \frac{d^2\sigma}{d\Omega_i d\Omega_f}\, d\Omega_f\right]^{-1}. \tag{4.11}$$

For k-vectors in the direction of the nematic director, the polarization modes $|\mathbf{o}\rangle$ and $|\mathbf{e}\rangle$ are degenerate and their scattering mean free paths are equal.

An estimation of the scattering mean free path can be obtained from a scalar approximation [92, 107], thus neglecting all polarization effects:

$$\ell_s^{\mathrm{scalar}} = \frac{9\pi\,\varepsilon_\perp^2\,K_3}{k_\perp^2\,\Delta\varepsilon^2\,k_B T}, \tag{4.12}$$

where $k_\perp = k\sqrt{\varepsilon_\perp}$. In the case of 5CB liquid crystals, ℓ_s^{scalar} is

$$\ell_s^{\text{scalar}} \sim 0.7\,\text{mm}. \tag{4.13}$$

We will see later in the chapter that this value is surprisingly very close to the measured vectorial one, $\ell_s^{\text{exp}} \sim 0.7 - 0.8\,\text{mm}$.

The propagator $G(|\mathbf{k}, \mathbf{e}/\mathbf{o}\rangle, \mathbf{r}_{12})$ of each of the eigenmodes of the medium is related to the scattering mean free path $\ell_s(|\mathbf{k}, \mathbf{e}/\mathbf{o}\rangle)$. The Beer-Lambert's law that determines the exponential attenuation of the wave intensity reads:

$$I(\mathbf{r}_2, |\mathbf{k}, \mathbf{e}/\mathbf{o}\rangle) = I(\mathbf{r}_1, |\mathbf{k}, \mathbf{e}/\mathbf{o}\rangle) \times \exp\left(-\frac{|\mathbf{r}_2 - \mathbf{r}_1|}{\ell_s(|\mathbf{k}, \mathbf{e}/\mathbf{o}\rangle)}\right). \tag{4.14}$$

If one tries to identify a dominant transport direction, one is tempted to look at the scattered k-vectors which correspond to maxima of the radiated pattern $d^2\sigma/d\Omega_i d\Omega_f$. In a birefringent anisotropic system, this can be inaccurate however: a local maximum in the differential cross-section for a given direction is not directly a local peak in the photon density. In a direction of the scattered wavevector in which $d^2\sigma/d\Omega_i d\Omega_f$ is large, $\sigma_t(\Omega_f) = \int (d^2\sigma/d\Omega_f d\Omega'_f)\, d\Omega'_f$ can be large as well, so that the scattering mean free path is short. Many photons are radiated in such a direction, but they suffer from intense scattering into all angles which depletes the light flow along that direction.

We stress here that light transport quantities can be properly defined only after ensemble averaging of the above picture. This averaging can be done in a numerical but exact way with Monte Carlo simulations or with a diffusion model [104].

4.2.3 The differential scattering cross-section

Light scattering in ordered nematics occurs because of fluctuations in the orientation of the nematic directors, $\mathbf{n}(\mathbf{r}, t) = \mathbf{n}_0 + \delta\mathbf{n}(\mathbf{r}, t)$, which in turn reflects into a variation of the dielectric tensor $\boldsymbol{\varepsilon} = \varepsilon_\perp \mathbf{1} + (\varepsilon_\parallel - \varepsilon_\perp)\,\mathbf{n}\mathbf{n}^{\mathrm{T}}$. The dielectric correlation function is given by [108],

$$\Gamma_{ijkl}(\mathbf{r}) = \langle \varepsilon_{ij}(\mathbf{0})\varepsilon_{kl}(\mathbf{r})\rangle = \frac{\Delta\varepsilon^2 kT/4\pi K_1}{r}\ \exp(-r/\xi)\,\Pi_{ijkl}. \tag{4.15}$$

This relation is valid only for $r \gg \xi$, as for distances smaller than the coherence length there are no fluctuations but coherence. The amplitude of the thermal fluctuations depends on the anisotropy in the dielectric constants $\Delta\varepsilon = \varepsilon_\parallel - \varepsilon_\perp$ and on the elastic constant K_1. At a wavelength of 488 nm and a temperature of 300 K, $\Delta\varepsilon = 0.556$ for 5CB. The fluctuations are weak but with long range. The tensor Π_{ijkl} is responsible for the polarization selection rules, which are the peculiarity of light scattering in nematic liquid crystals.

Before considering the scattering cross-section it is convenient to introduce the eigenmodes of the fluctuations $\delta\mathbf{n}$, which are the unit vectors m_α ($\alpha = 1, 2$):

$$m_1 = m_2 \times \mathbf{n} \quad \text{and} \quad m_2 = \frac{\mathbf{q} \times \mathbf{n}}{|\mathbf{q} \times \mathbf{n}|} \tag{4.16}$$

where $\mathbf{q} = \mathbf{k}_\text{f} - \mathbf{k}_\text{i}$ is the scattering wave vector.

The scattering event is ruled by the single scattering cross-section (see Eq. (4.17)), which depends on the input and output state and in particular on the orientation of the

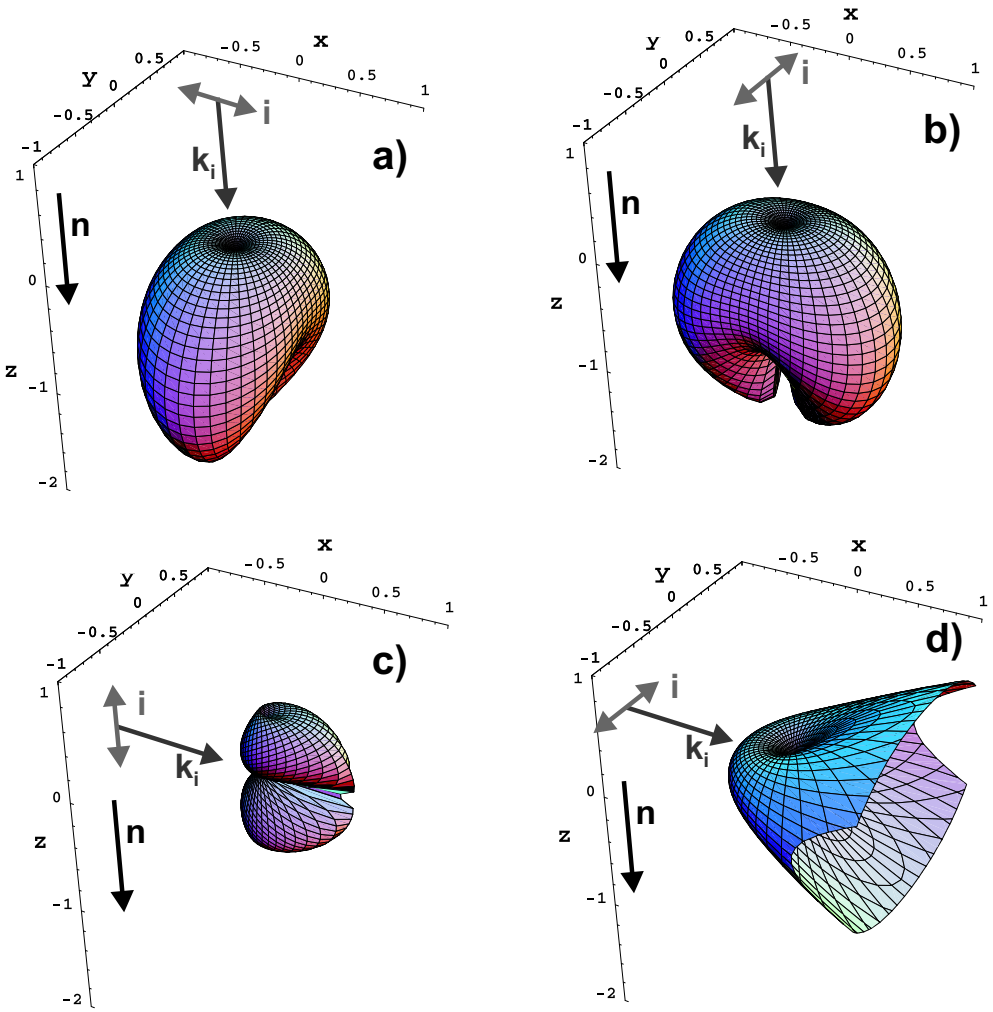

Figure 4.8: Spherical plot of the differential scattering cross-section (Eq. (4.17)) for nematic liquid crystals for few case. The nematic director is along z. The incident k-vector and polarization are shown for each panel, as well as the nematic director. In panel a), b) and d) the polarization flips from ordinary to extraordinary (or viceversa), while in the case c) it is extraordinary before and after the scattering event. Panel d) shows the very forward peak (which extends up to 4000) typical of nematics. 5CB liquid crystals a magnetic field of 0.5 T, $K_3 = 5.3 \times 10^{-12} N$, $K_1 = 0.79 K_3$ and $K_2 = 0.43 K_3$, $\xi = 4.2 \mu$m.

polarization and propagation vectors with respect to the nematic director [22, 23, 24], and which is

$$\frac{d^2\sigma}{d\Omega_i d\Omega_f} = V \left(\frac{\Delta\varepsilon k^2}{4\pi} \right)^2 \sum_{\alpha=x,y} \frac{k_B T (i_\alpha f_z + i_z f_\alpha)^2}{K_\alpha q_\perp^2 + K_3 q_\parallel^2 + K_1 \xi^{-2}}, \tag{4.17}$$

(here we follow the formalism defined in De Gennes's book [22, 23, 24] depicted in Fig. 4.7). K_i are the Frank elastic constants. The polarization product $i_\alpha f_z + i_z f_\alpha$ determines the polarization selection rules, while the denominator is dominated by $K_1 \xi^{-2}$ which depends on the external magnetic field. The dependence on q^{-2} accounts

for the strong directionality of the cross-section, whose divergence for $|\mathbf{q}| \longrightarrow 0$ is prevented by a finite value of ξ. The pre-factors in Eq. (4.17) are the temperature T, the Boltzman constant k_b, the modulus of the light k-vector k, and the scattering volume V.

Fig. 4.9 shows the anisotropy of the total scattering cross-section σ_t for different polarization eigenmodes of the input and output polarization, as a function of the emerging direction (k-vector) after the scattering event. In the case of scattering of an extraordinary mode into an ordinary, the total scattering cross-section is extremely small for k-vectors in the direction of the nematic director (panel a), while for the extraordinary-extraordinary case also the plane orthogonal to $\mathbf{n}$ exhibits a minimum value of σ_t (panel b). A striking effect, for example, is that ordinary polarization has to change its state of polarization upon scattering, or that an extraordinary mode propagating parallel to the optical axis will never be scattered in the forward direction (see Fig. 4.9).

4.2.4 Double scattering process

The process of double scattering is depicted in Fig. 4.10 for the case of ordinary light incident with k-vector parallel to $\mathbf{n}$, scattered into extraordinary light and then double-scattered into ordinary light after an average distance ℓ_s, shown by the length of the arrows. The emerging light distribution is calculated with a second scattering cross-section. The smaller is the second scattering cross-section, the lower the scattering probability, and therefore the longer the scattering mean free path. One can see that already for the simplest process of two events of scattering, both of the two light eigenmodes are involved, ordinary and extraordinary, and that their scattering cross-sections are very different.

In view of these features, in the Monte Carlo simulation any scattered photon has to be projected onto the birefringent eigenmodes along which then it can propagate ballistically. Their direction of propagation follows the photon group velocity in the nematic average medium and the travelled distance, before the following scattering event, is governed by an anisotropic Lambert-Beer's probability (see Eq. (4.14)) which itself depends on the photon state: it is an *anisotropic random walk*.

4.3 Multiple light scattering experiments in ordered nematics

As we have seen so far, single-scattering in nematics is already a very rich and complex subject of study. Very thin films of liquid crystals are indeed the subject of a vast literature, especially as far as the technological applications are concerned. Multiple scattering occurs in samples optically thick, i.e. many scattering mean free paths thick. Our extraordinary requirements are therefore a bulk liquid crystal sample, and a high accuracy setup to record light transport and coherent backscattering.

4.3.1 The experimental setup

The observation and study of weak localization from liquid crystals requires an extremely high angular resolution of at least 20 μrad. To achieve such resolution, we use the following measurement scheme. A diffraction limited 8 cm diameter collimated

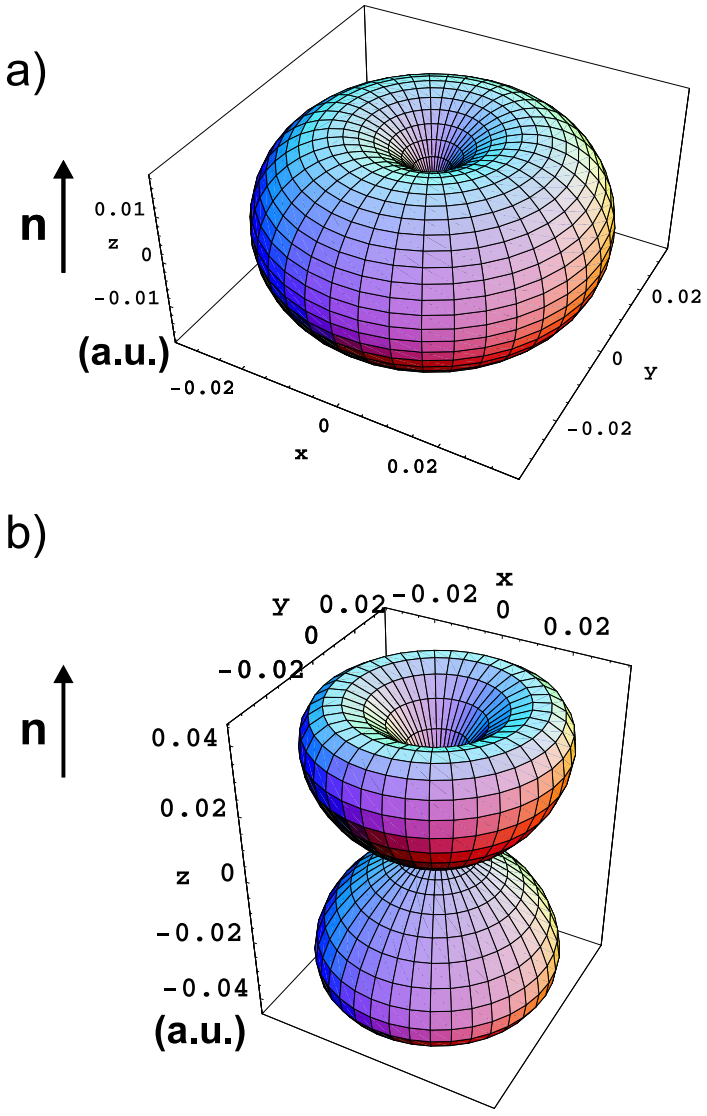

Figure 4.9: Total integrated cross-section σ_t for light scattering in nematic liquid crystals: panel a) an extraordinary mode into an ordinary (or ordinary into extraordinary); panel b) an extraordinary mode into an extraordinary. One can see that σ_t, the total probability for a photon of being scattered, depends on the direction of propagation and on the polarization state. Nematic director in the z-direction for all cases. 5CB liquid crystals in a magnetic field of 0.5 T, $K_3 = 5.3 \times 10^{-12} N$, $K_1 = 0.79 K_3$ and $K_2 = 0.43 K_3$, $\xi = 4.2 \mu$m.

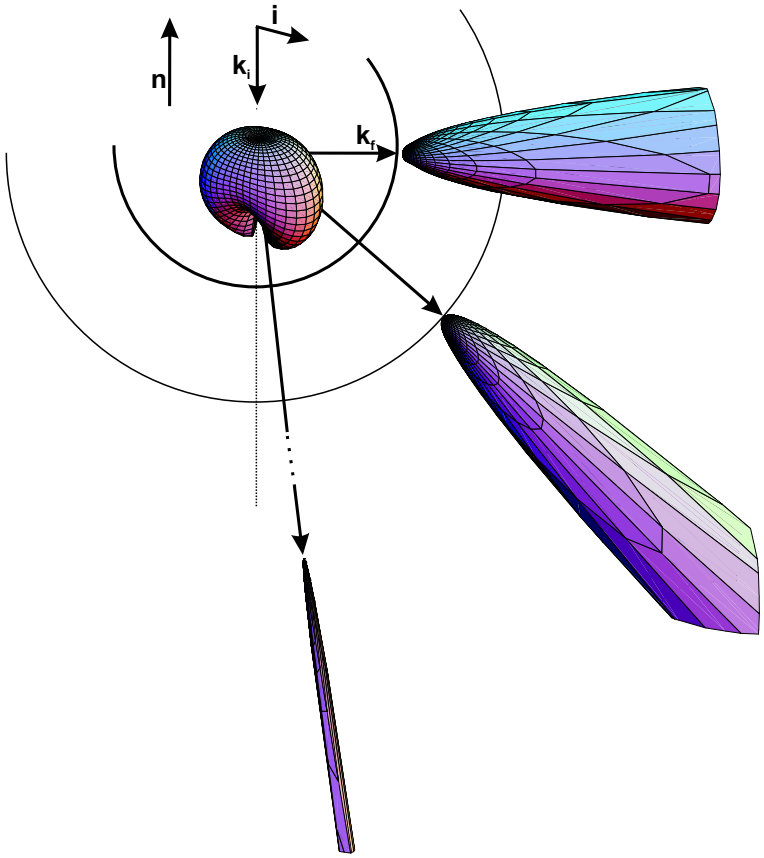

Figure 4.10: Double scattering process in ordered nematic liquid crystals. Ordinary light incident with k-vector parallel to $\mathbf{n}$ is scattered into extraordinary light with a differential cross-section shown in the center of the picture. Three possible directions are shown. Light propagates for an average distance given by ℓ_{s}, shown by the length of the arrows, before the second scattering event. The second scattering cross-section is plotted for the case in which the emerging light is ordinary. The top most scattering event occurs at a distance extremely long and is very rare.

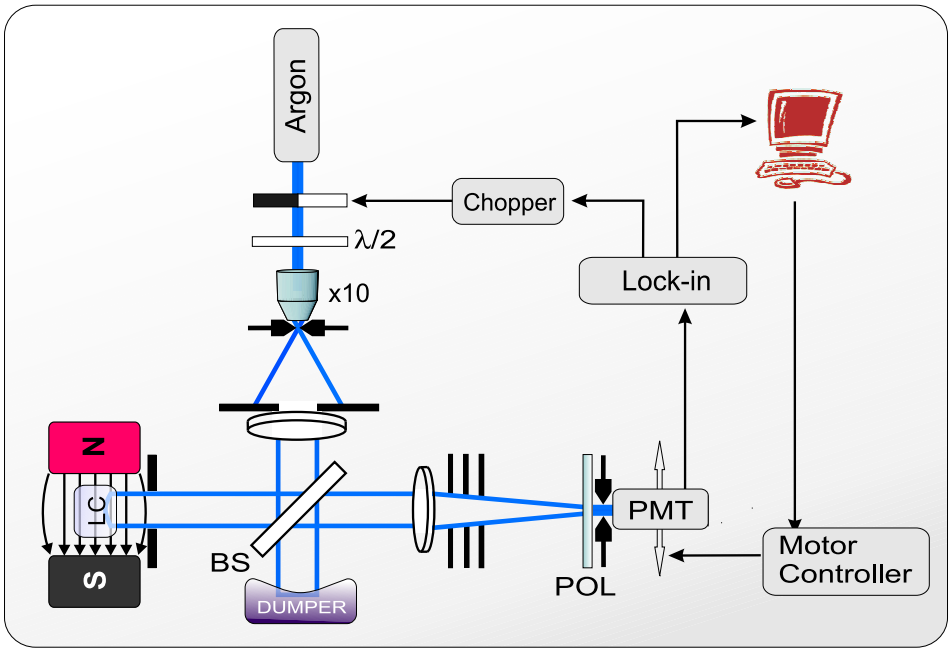

Figure 4.11: Sketch of the setup for the coherent backscattering measurement. A diffraction limited 8 cm diameter collimated laser beam is obtained by expanding and spatially filtering the output of a single mode Argon laser (2W, 488nm). This beam is reflected from a 15 cm wide beam splitter (BS) onto the sample (LC) which is placed between the poles of an electromagnet. The backscattered light from the sample is collected through the beam splitter by a wide achromatic triplet lens (f=1250 mm) and monitored by a photomultiplier tube (PMT) through a polarizer (POL) and a 10 μm diameter pinhole placed exactly in the focal plane of the achromatic lens.

laser beam is obtained by expanding and spatially filtering the output of a single mode Argon laser (2W, 488nm). This beam is reflected from a 15 cm wide beam splitter onto the sample. The backscattered light from the sample is collected through the beamsplitter by a wide achromatic triplet lens (f=1250 mm) and monitored by a photomultiplier tube through a polarizer and a 10 μm diameter pinhole placed exactly in the focal plane of the achromatic lens. The detection system is mounted on a stepper-motor driven x-y translation stage ($< 1\mu$m resolution); it acted as a high-resolution, low noise, window-less CCD camera with unlimited scanning area. The cost of the detection apparatus is 100 times less than an ordinary CCD camera with the same characteristics, but the price we pay is the acquisition time, which in our case is of the order of 3 s per pixel (up to 1 hour per measurement). All lenses are aligned perpendicular to the optical beams to avoid astigmatism, and the response of the setup is carefully checked to be isotropic. The cell (quasi-index matched) is tilted off-axis so as to keep its window reflection well away from the detector. The measured noise level is always lower than 1% of the signal. An angular resolution of 10 μrad is obtained, two orders of magnitude better than previous liquid crystal work, and 10 times better than the highest resolution reported in the literature. This angular resolution enabled us to measure transport mean free paths larger than one millimeter, opening up the possibility to perform weak localization studies on complex fluids and biological tissue,

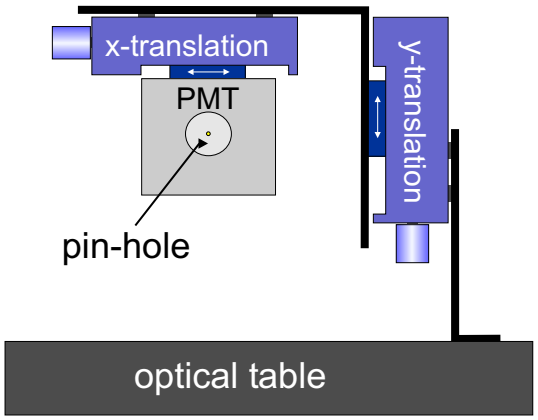

Figure 4.12: Acquisition device, analogous to an ordinary CCD camera. The compact photomultiplier tube (PMT) is mounted on a x-y translation stage. A 10μm pin-hole is placed in the focal plane of the acquisition lens (not shown here).

inaccessible to previous coherent backscattering instruments.

The intensity variation across the beam should be small, otherwise the reciprocal paths will have different amplitudes and the enhancement will be lowered. For this reason the gaussian beam is expanded and only the central part, which has a flat intensity profile, is selected and filtered.

Experiments dealing with weak scattering media, like nematic liquid crystals, are always bounded to face the problem of measuring weak signals, restricted to a narrow angular range. Great care has been taken to remove the noise from the measured cone. This noise comes from incoherent backscattered light, scattered from the surrounding equipment (which results into a speckle pattern) and stray light in the room. The ambiental noise which is not coming from unwanted scattering of the laser light usually can be easily filtered out with the lock-in amplifier or with a narrow band frequency filter. The remaining noise can be reduced only with use of spatial filters.

A high level of incoherent background means a smaller enhancement of the cone. The incoherent background is not only coming from artifacts, but it can be originated also from the scattering in the sample. In order to reduce the diffuse background, one has to prevent light paths which exit the sample from outside the illuminated area, to reach the detector. These paths cannot have a counterpart, therefore they cannot contribute to the crossed term, but they decrease the enhancement. This extra source of diffuse background can be reduced with carefully placed diaphragms.

A more tricky unwanted light is the one that reenters the beam path after being scattered off the main beam. This source of noise is hard to filter, as it is of the right wavelength, and in phase with the signal beam. The path difference between the coherent beam and a scattered one is of the orders of meters, which turns into a delay of $\simeq$ tens of nanoseconds. Our lock-in operates at 100 kHz, therefore we can discriminate light contributions which are separated by milliseconds. This means that all the scattered light is in phase. It can however be blocked by placing many screens cleverly in the beam path and checking the isotropy of the cone obtained from an isotropic scattering solution of TiO_2 (in $2-$methylpentane$-2,4-$diol).

The liquid crystals samples consist of p-penthyl-p'-cyanobiphenyl (5CB), and are

contained in a cylindrical cell of 8 cm diameter, and 4 cm thickness which satisfies the requirement of having an optically thick sample. The width of the beam limits the angular resolution as it bounds the exiting distance **d** (Eq. 2.24) of the reciprocal paths.

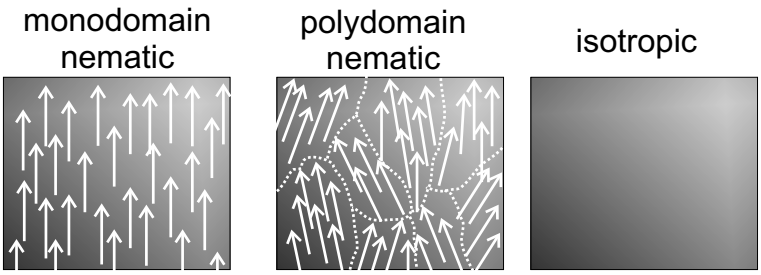

Figure 4.13: Monodomain, polydomain and isotropic nematic liquid crystals. The dotted line is only for illustration, as the transition from one domain to the other is very smooth: a continuous picture is more appropriate.

A monodomain nematic phase is obtained by heating the system above the nematic-isotropic phase transition at 309 K, which brings the liquid crystal into the optically transparent isotropic phase, and then cooling slowly overnight to 301 K in an external magnetic field of 0.5 Tesla (see section 4.1.1 for the thermotropic properties of nematic liquid crystals). The sample is left in the magnetic field for several days to assure good director alignment. Magnetic fields have been observed to modify multiple light scattering leading to fascinating phenomena such as the photonic Hall effect [85], the breaking of time-reversal symmetry [65], and the elegant Hanle effect in coherent backscattering [68]. None of these effects play a role in our samples since the anisotropy is an intrinsic optical property of the nematic phase. Scattering in nematics is dominated by fluctuations of the otherwise aligned director and the magnetic field is used to obtain a monodomain phase. In addition it suppresses long range orientational fluctuations in the sample that are larger than the magnetic coherence length ξ. In our case the field strength is modest (0.5 Tesla) and $\xi = 4.2\,\mu$m, much larger than the wavelength, but orders of magnitude smaller than all sample dimensions, which assures that surface anchoring effects can be neglected.

4.4 The measured anisotropic coherent backscattering cone

In Fig. 4.14 we report the observed coherent backscattering cone for two monodomain cases and one polydomain case. The director in the two monodomain cases is in the sample plane either in the x or y direction. The polarization is linear in the x-direction and the polarization conserving channel is monitored. A clear angular anisotropy is visible. The top panel (Fig. 4.14a) corresponds to the nematic director in the x direction, and the bottom panel (Fig. 4.14c) to the nematic director in the y direction. The anisotropy clearly depends on the nematic director orientation.

The middle panel (Fig. 4.14b) shows the results for a polydomain nematic phase which was obtained by heating the sample into the isotropic phase and cooling down in

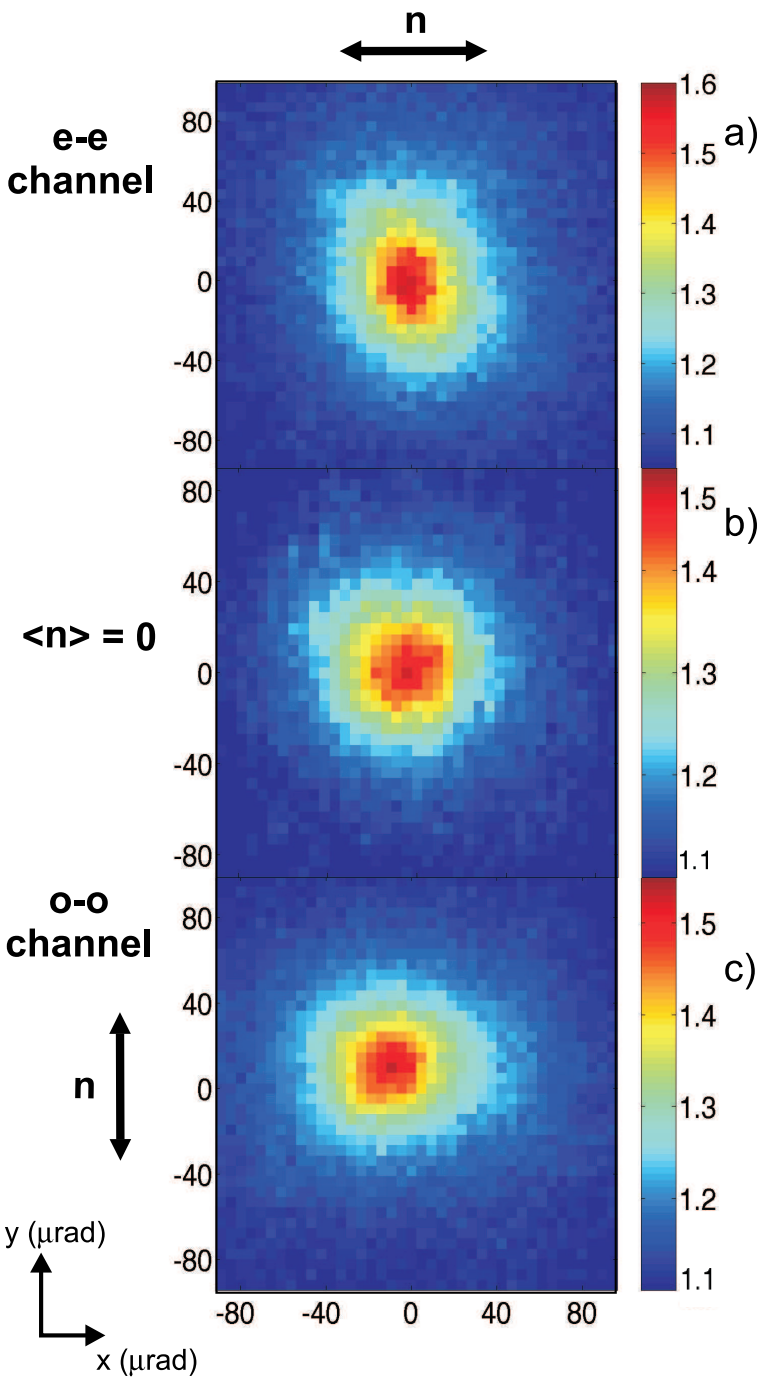

Figure 4.14: Coherent backscattering cones in polar colour plots from nematic liquid crystal for three cases of the nematic director. Top: nematic director in x, bottom: director in y, middle: polydomain phase. The anisotropy in the backscattering cone is clearly visible. The polarization is in the x-direction in all cases.

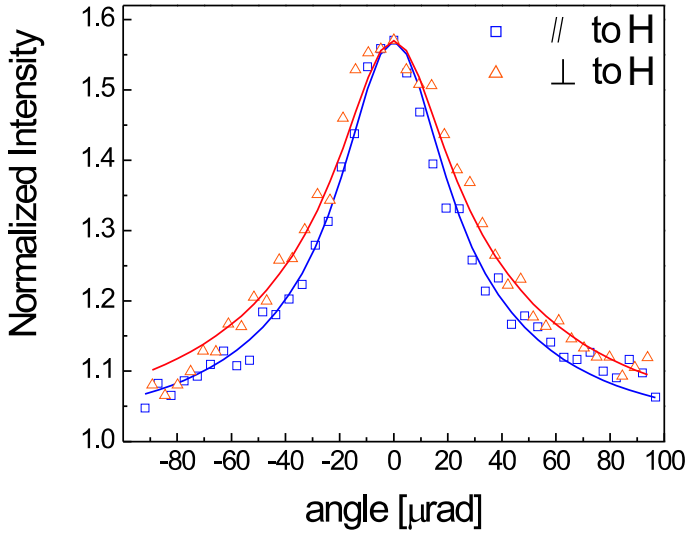

Figure 4.15: Coherent backscattering from a monodomain nematic for both orthogonal scanning directions, in a linear plot. Nematic director and polarization in the x-direction. The squares and the triangle indicate, respectively, the scanning direction parallel or orthogonal to the magnetic field.

zero field while vibrating the system. In a polydomain phase the scattering anisotropy still exists but only on length scales much smaller than the sample size. Hence the anisotropy in the mean free path averages out over the whole sample volume and one expects to observe an isotropic coherent backscattering cone. We observe from Fig. 4.14b that the anisotropy indeed disappears in the polydomain nematic case.

A more conventional but also instructive way of reporting coherent backscattering data is the linear plot shown in Fig. 4.15. Here we report the coherent backscattering cone as recorded in long linear scans in the two orthogonal scanning directions, after precise determination of the exact backscattering angle. The light is incident normal to the front sample interface, and the magnetic field is in the plane orthogonal to $\mathbf{k}_i$. Again we can observe that the coherent backscattering cone in the scattering plane parallel to the nematic director is narrower than the cone in the perpendicular plane. Note the observed anisotropy cannot be due to polarization effects at the sample surface (like e.g. birefringent internal reflection [109]) since we are comparing angular scans with the same polarization direction. The solid line in Fig. 4.15 was obtained from a fit with a simple coherent backscattering model generalized for an anisotropic system (described in the next section), and based on the diffusion approximation even if no actual justification of the validity of this model can be given at this point. In order to perform the fit, the theoretical curve is convoluted with the instrumental resolution, which is obtained from a direct measurement of the focal spot-size ($\sim 10 - 12\mu$m) at the detector, if the sample is replaced with a mirror. (The advantage of convolving the theoretical curve instead of deconvolving the experimental one is that no assumptions regarding the shape of the latter are needed.)

Fig. 4.15 confirms that the experimental data agree with the classical theoretical cone shape. The rounded top is due to the finite experimental resolution.

Anisotropy in coherent backscattering due to an anisotropic transport mean free path has been predicted numerically in Monte-Carlo simulations [92, 93]. However, no exact theory on coherent backscattering from nematic liquid crystals is currently available. As a preliminary step in the direction of a full theory, it is instructive to generalize the standard coherent backscattering model for an anisotropic mean free path.

We observe in Fig. 4.15 that the enhancement factor is 1.55 ± 0.05 which is an excellent result considering the difficulties associated with resolving such a narrow backscattering cone [110].

4.5 A first model of anisotropic weak localization

We follow here a standard approach for calculating $\gamma_{\mathrm{C}}(\theta)$, as explained in sec. 2.10.3, in which one solves the radiative transfer equation for a random collection of point scatterers in a self-consistent way and upon diffusion approximation [11]. In an anisotropic system like a nematic liquid crystal, the distribution of distance becomes anisotropic, leading to an anisotropic backscattering cone. Assuming the random walks in the three orthogonal propagation directions are uncorrelated, we obtain (see section 2.10.3) for the interference contribution in the anisotropic case:

$$\gamma_{\mathrm{c}}(\theta,\varphi) = \frac{3}{2\ell^3\alpha u}\,\frac{\alpha + u(1-\exp\left(-2\alpha z_0\right))}{(u+\alpha)^2+\eta^2}, \tag{4.18}$$

where $\eta \equiv k(1-\mu_{\mathrm{s}})$, $u \equiv 0.5\,\ell^{-1}(1+\mu_{\mathrm{s}}^{-1})$, $z_0 = 2/3\,\ell$, $\mu_{\mathrm{s}} = \cos\theta$, and $\alpha = k\sin\theta$ with $\ell = \ell_\perp \sin\varphi + \ell_\parallel \cos\varphi$ and k the wave-vector of the light in vacuum. Here θ is the scattering angle, φ the angle of the scattering plane with respect to the nematic director $\mathbf{n}$, and $\ell_\parallel$ and $\ell_\perp$ are the transport mean free paths parallel respectively perpendicular to the nematic director. Doing this we have assumed that upon multiple scattering a diffusive transport mean free path can be defined which is not any more a scalar quantity, but a vectorial one. We denote its components parallel and perpendicular to $\mathbf{n}$ by $\ell_\parallel$ and $\ell_\perp$ respectively [94, 111]. The director $\mathbf{n}$ lies in the sample plane. Absorption is negligible since the laser wavelength is outside the region where 5CB is absorbing. Eq. (4.18) describes an anisotropic backscattering cone of which the full width half-maximum W in the two orthogonal scattering planes is a measure of $\ell_\parallel$ and $\ell_\perp$:

$$W(\varphi=0) \simeq \frac{0.7}{2\pi}\frac{\lambda}{\ell_\parallel} \qquad W(\varphi=\frac{\pi}{2}) \simeq \frac{0.7}{2\pi}\frac{\lambda}{\ell_\perp}. \tag{4.19}$$

In Fig. 4.16 we report a comparison between the data and the theoretical curves, plotted in a polar graph.

A *two-dimensional* fit of the measured coherent backscattering data can be used to extract values for the transport mean free paths. The only fitting parameters are the enhancement factor and the values of $\ell_\parallel$ and $\ell_\perp$. For the extraordinary polarization case we find mean free paths $\ell_\parallel = 0.71$ mm and $\ell_\perp = 0.83$ mm, with a fitting error of about 2.5% and a statistical error of 4%. The fitting error refers to the uncertainty in the values of the fitting parameters for each measurement, while the statistical one is related to the spreading of these values when repeated measurements are performed. To our knowledge these are the first experimental data on the absolute values of the transport

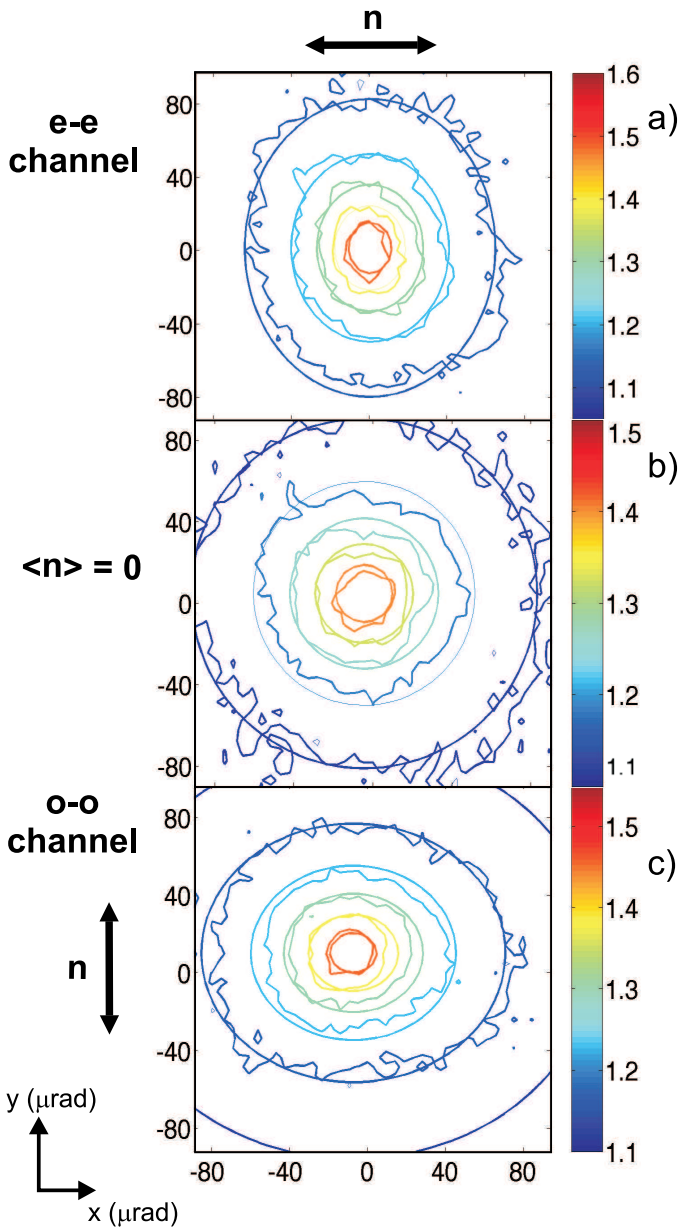

Figure 4.16: Comparison between data and theoretical curves to determine the anisotropy in the mean free path. The constant intensity contours are circular in the isotropic middle panel (polydomain) while they are ellipses in the other two case (monodomain) with the minor axis in the direction of the director.

mean free paths in nematic liquid crystals. The resulting anisotropy is: 1.17 ± 0.04. For the bottom panel (director in y, ordinary polarization) we find: $\ell_{\parallel} = 0.67$ mm and $\ell_{\perp} = 0.77$ mm, and $\ell_{\parallel}/\ell_{\perp} = 1.15 \pm 0.04$. The isotropic case in the middle panel the fit gives: $\ell_{\parallel}/\ell_{\perp} = 1.01 \pm 0.04$. These anisotropy values are in good agreement with available theories regarding anisotropic diffusion in nematics [90] that predict a mean free path anisotropy of about 1.18. For future studies it would be interesting to examine the magnetic field dependence of the mean free paths and anisotropy. The mean free paths are expected to get longer with increasing magnetic field due to a reduction of the magnetic coherence length, and the anisotropy is expected to become smaller. These effects should become observable for magnetic field strengths above 10 Tesla [90].

4.6 The polarization reversing channel, a controversy solved.

Our accurate apparatus also enabled us to resolve a discrepancy in the literature about multiple scattering from liquid crystalline nematics. The liquid crystal birefringence leads to a substantial phase difference between the ordinary and extraordinary modes of propagation (much more than 2π over the length scale of the mean free path) and hence there should be no backscattering enhancement in the polarization reversing channel [91, 57]. While the experiment by Vithana et al. [91] observed no cone in this channel, the experiment by Kuzmin et al. [57] revealed the presence of a 3-5% backscattering enhancement for reversing polarization (see Fig. 4.17).

In Fig. 4.18 we show the backscattered signal in the polarization reversing channel (lin$\perp$lin) from our liquid crystal in the monodomain nematic phase. The setup was aligned in the polarization conserving channel and great care was taken to maintain optical alignment while changing polarization channels. We confirmed there was no residual backscattering cone in the polarization reversing channels (ordinary-extraordinary and extraordinary-ordinary) within the noise level of our experiment of 1%. If we assume that the cone in the polarization reversing channels has the same width as in the other channels, but it is just weaker, then we could observe it in a fit of the data. Such a fit would have an accuracy $\sqrt{N_d}$ better than the 1% mentioned above, as it would be obtained from N_d significant points. We conclude that no enhancement cone is present within $1.0/\sqrt{10}\,\% \sim 0.3\%$.

In the polarization non-preserving channels, two processes act to destroy the interference between the direct and the reverse path. Birefringency of nematics implies that the two paths, which have different polarization, experience different dispersion laws ($n_o \neq n_e$) and therefore get off-phase after a distance smaller than the scattering mean free path: interference is destroyed. Another process that decreases (without killing completely) the enhancement is related to the differential scattering cross-section, which depends strongly on the input polarization state. In the lin$\perp$lin channel, the amplitudes of the direct and reverse paths are thus different and the interference visibility reduced.

The presence of a 3-5% backscattering enhancement [57] (see Fig. 4.17) is not compatible with our measurements and with the theoretical explanation. A possible reason for this discrepancy could be the presence of a coherent backscattering contribution also from unwanted scattering sources, like a dirty interface or the sample cell or from the damped beam at the beamsplitter.

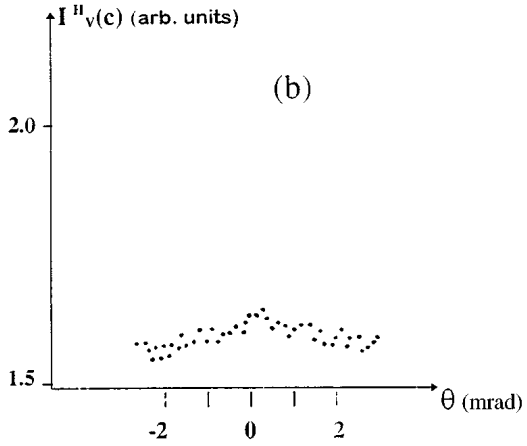

Figure 4.17: The coherent backscattering (I_v^H is the light intensity) as a function of angle in the liquid crystals, for the polarization reversing channels (courtesy of Vladimir Kuzmin, [57]). An 3-5% backscattering enhancement is visible.

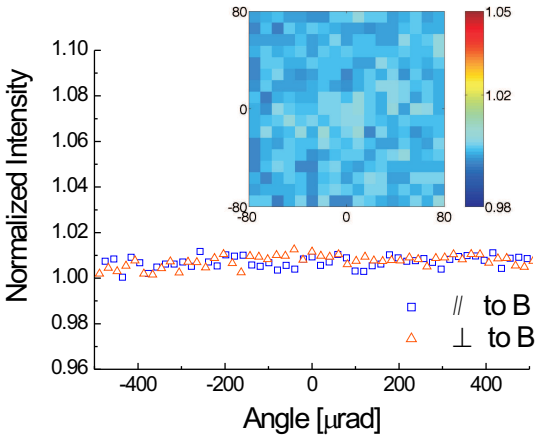

Figure 4.18: Backscattered intensity in the polarization non-preserving polarization channel. No enhancement is observed within the noise level of our data (1%). Wider scans up to 2 μrad are flat as well.

4.7 Conclusions

In summary we have investigated weak localization in anisotropic systems, in particular nematic liquid crystals. We observed an angular anisotropy associated with an anisotropic transport mean free path in a high-order multiple-scattering interference phenomenon. The observation of an anisotropic backscattering cone implies that the weak localization effect is stronger for particular propagation directions inside the system. Interesting future studies could involve strongly scattering anisotropic systems, for example anisotropic meso-porous semiconductors, with mean free paths of order one wavelength. While our results imply that the weak localization correction can be direction dependent, it is as yet completely unknown how anisotropy influences the Anderson localization transition.

Chapter 5

Monte Carlo simulations of anisotropic multiple light scattering

The Monte Carlo method has long been recognized as a powerful technique for performing certain calculations, generally solutions to integral equations. Multiple scattering equations can be easily put in an integral form, and a Monte Carlo simulation employed to perform the required configuration averaging [112]. Our strategy is based on an approach with increasing complexity. We start with a model of isotropic Rayleigh scattering. Then we extend it to include scattering and spatial anisotropy, at first keeping the intra-scattering medium homogeneous and isotropic and then with the anisotropic propagation eigenmodes. As a last stage, not presented here, light scattering in ordered nematics can be modelled without ambiguity. In this chapter we present the numerical calculation of the coherent backscattering cone from a set of anisotropic Rayleigh scatterers, for different form of anisotropies. In the last section the extension to the case of scattering from ordered nematics is outlined for a future development.

5.1 The Monte Carlo technique

A Monte Carlo technique is any technique making use of random numbers to solve a problem. Historically, the first large-scale calculations to make use of the Monte Carlo method were studies of neutron scattering and absorption, random processes for which it is quite natural to employ a statistical approach [113]. Whether or not the Monte Carlo method can be applied to a given problem does not depend on the stochastic nature of the system being studied, but only on our ability to formulate the problem in such a way that random numbers may be used to obtain the solution.

At least in a formal sense, all Monte Carlo calculations are equivalent to integrations. This follows from the definition of a Monte Carlo calculation as producing a result F which is a function of random numbers r_i. Let us assume for simplicity the usual case that the r_i are uniformly distributed between zero and one. Then the Monte Carlo result $F = F(r_1, r_2, \ldots, r_n)$ is an unbiased estimator of the multidimensional integral

$$I = \int_0^1 F(x_1, x_2, \ldots, x_n)\, dx_1 dx_2 \ldots dx_n \tag{5.1}$$

or, stated another way, the expectation of F is the integral I. Each iteration of the numerical procedure we calculate a partial result F, which is then summed up to all the others and averaged to get the integral I, average which is performed over all the possible random numbers in $[0, 1]$.

When the problem to be solved is explicitly the problem of integrating a positive function f, the F above is not to be identified with $\int f$ but rather with the Monte Carlo estimate of its integral

$$\int_{Volume} f(\mathbf{x})\, d\mathbf{x}. \tag{5.2}$$

The formal equivalence of Eq. (5.1) can be used to lay a firm theoretical justification for Monte Carlo techniques [113]. If F has finite variance, then it can be demonstrated that the Monte Carlo estimate converges to the true value of the integral for very large number of iterations N, as a direct consequence of the central limit theorem.

$$\lim_{N\to\infty} \sum_{N} F(r_1, r_2, \ldots, r_n) = \int_0^1 F(r_1, r_2, \ldots, r_n)\, dr_1 \ldots dr_n = \int_{Volume} f(\mathbf{x})\, d\mathbf{x}. \tag{5.3}$$

The Monte Carlo estimate is asymptotically *normally distributed*, it approaches a gaussian density. The standard deviation, the square root of the variance, of the Monte Carlo estimate is given by

$$\text{std} = \frac{\sqrt{V(F)}}{\sqrt{N}} \tag{5.4}$$

where $V(F)$ is the effective variance of the single iteration F [113], i.e. $V(F) = \left[\int f^2 - \left(\int f\right)^2\right]$.

5.1.1 The crude Monte Carlo integration

Imagine we want to calculate the integral $\int f dx$. We can bound the function f with a box, and then divide the box area into squares with a grid on it, as in Fig. 5.1. A numerical way to calculate the integral consists in choosing randomly in the grid

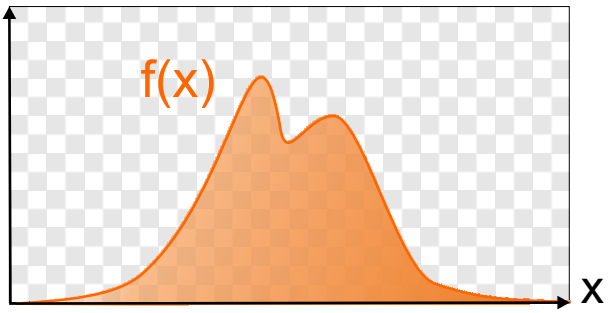

Figure 5.1: Hit-or-miss Monte Carlo simulation to calculate the area of the function f.

a unit square, and decide whether it hits or misses the area under the function. Via iteration of this procedure we can calculate the probability of hitting the area that we want to calculate. If we multiply this probability by the area of the box we get the

estimate of the integral of f. That's why the crudest Monte Carlo simulation is also called hit-or-miss.

$$(\text{box area}) \times \frac{\#\text{hits}}{\#\text{total trials}} \; (N \to \infty) \; = \; \int f dx \tag{5.5}$$

The variance is related to the number of attempts N (Eq. (5.4)), to the finest division of the grid, and to the ratio of the area of $f(x)$ to that of the box (if the box is too large the probability of hitting the area under the function is very small).

5.1.2 Efficiency: variance-reduction techniques

In order to decrease the variance of the integration, we could increase N, but this improves (converges) very slowly $\sim \sqrt{N}$, while the CPU time required is usually linear in N. Another way is to try to decrease the effective variance $V(f)$. There are many ways to do so, in our case we employed only the *importance sampling* technique that we are going to describe.

We may feel intuitively that the reason why Monte Carlo integration has such a large uncertainty is that the points are chosen randomly in the bounding box, therefore they cover it uniformly. What we are doing is just over-sampling regions of the box where the function is very small. Monte Carlo calculations will be most efficient when each point (event) has nearly the same weight, when f is almost constant. This can be arranged by choosing a large number of points in regions of the sampling space where the function value is largest and compensating for this overpopulation by reducing the function values in these regions. This technique is called *importance sampling*, and consists mathematically in a change of variable in the integral.

$$f(x)dx \longrightarrow f(x')\frac{dG(x')}{g(x')} \tag{5.6}$$

Points are chosen according to $G(x)$ instead of uniformly, and f is weighted inversely by $g(x) = dG(x)/dx$. This is equivalent to choose the random points below $g(x)$, which is clearly more efficient that choosing them in the box, and the probability of hitting the area below $f(x)$ (the convergence) is much higher. The relevant variance is now $V(f/g)$, which will be small if g has been chosen close to f in shape. In the best case, if we can integrate analytically f (note that in this case the numerical integration is not necessary) then we may change the variable in order to have

$$\int_0^1 f(x)dx \longrightarrow \int_{F(0)}^{F(1)} f(x')\frac{dF(x')}{f(x')} = \int_{F(0)}^{F(1)} dF(x') = F(1) - F(0), \tag{5.7}$$

therefore the Monte Carlo would be a trivial sum of identical values and the variance would be zero. A clever choice of g, with the requirements that $G(x) = \int g(x)\,dx$ exists and is invertible ($\exists G^{-1}(y) = x$) in order to apply the above described change of variable, can reduce considerably the computational time required for the simulation.

As a side note, importance sampling is the only general method for removing infinite singularities in the integrand f, by using a sampling function g with a similar singularity in the same place.

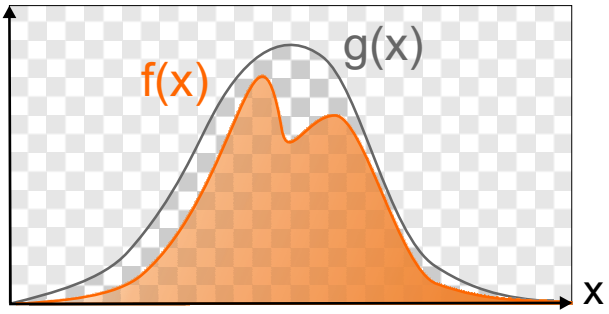

Figure 5.2: Hit-or-miss Monte Carlo simulation whose efficiency has been improved via importance sampling. The boxing is replaced with the function $g(x)$ which is much closer to $f(x)$.

5.1.3 Random Numbers

The Monte Carlo integration is based on the random choice of the parameters, or the system configurations. In the algorithm, this can be accomplished with random numbers. In principle, a random number is simply a particular value taken on by a random variable, and thus has a truly unpredictable and unreproducible nature.

In a Monte Carlo calculation, random numbers are replaced by *pseudo-random* numbers, which are sequences of numbers which, once they have been determined, are not at all random in the statistical sense, but may have some properties which are similar to the properties of a truly random sequence. They are generated according to a strict mathematical formula, and therefore reproducible, but are supposed to be indistinguishable from a sequence generated truly randomly.

In order to prevent possible correlations between the random values we have chosen to use the routine `rand`$[a, b]$, together with `gsl_rng_taus2`[1] which ensures a period of the random series of 2^{88}, out of reach in our simulations.

5.1.4 Random value from a Distribution

One of the crucial steps in a Monte Carlo simulation is when a random number is picked up in a given probability distribution $f(x)$. The starting point is the random number generator, which provide a random deviate in a given range $[a, b]$, as for example `rand`$[a, b]$.

The distribution $f(x)$ is positive, integrable and $\in \mathcal{C}^0$, with an analytical expression for its integral $h(x) = \int_{-\infty}^{x} f(p)dp$, and with invertible integral, $x(y) = h^{-1}(y)$. Then a random value $\widetilde{x}_f$ distributed as $f(x)$ can be found by:

$$\begin{cases} y = \texttt{rand}[0, \int_{-\infty}^{\infty} f(x)dx] \\ \widetilde{x}_f \equiv h^{-1}(y) = \{\int_{-\infty}^{y} f(p)dp\}^{-1} \end{cases} \tag{5.8}$$

where `rand` is a random deviate in the range $[0, \int_{-\infty}^{\infty} f(x)dx]$. The obtained set of random value $h^{-1}(y)$ are distributed as $f(x)$. Operatively one first choose a random

[1] It is a maximally equidistributed combined Tausworthe generator by L'Ecuyer [114]. From the GNU Scientific Library (GSL), http://www.gnu.org/software/gsl/.

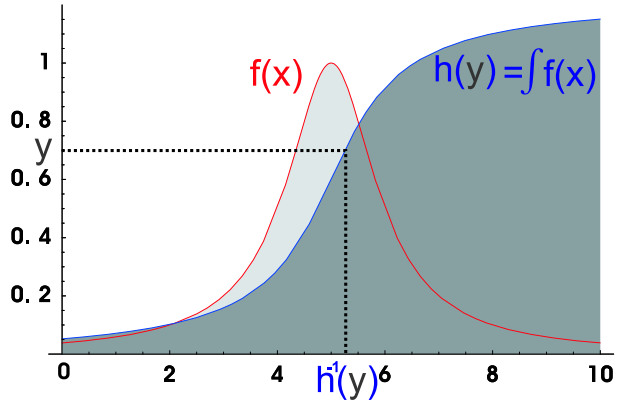

Figure 5.3: Illustration of the technique that allows to sample a random value from the distribution $f(x)$.

deviate in $[0, \int_{-\infty}^{\infty} f(x)dx]$ and then calculate the corresponding x inverting the integral $h(y) = \int_{-\infty}^{y} f(p)dp$.

As an example a random deviate from an exponential distribution $f(x) = \exp(-x/\ell)/\ell$ can be obtained calculating

$$\begin{cases} y = \texttt{rand}[0,1] \\ \widetilde{x}_f \equiv h^{-1}(y) = -\ell \, \log(1 - \texttt{rand}[0, \int_0^{\infty} f]). \end{cases} \tag{5.9}$$

When the function $h(y)$ does not exist analytically, which is the most common case, then $\widetilde{x}_f$ can be obtained using the so called *Rejection Method*.

5.1.5 Rejection Method

This method consists in bounding the given distribution $f(x)$ with another $g(x)$ such that $g(x) > f(x), \forall x$, and with $\int_{-\infty}^{x} g(p)dp$ invertible [115]. The method proceeds in steps:

1. Calculate a x' distributed as $g(x)$ ($x' \in \widetilde{x}_g$, i.e. it is distributed as $g(x)$), with the inversion method described in the previous section
2. Generate a random deviate $y(x') \equiv \texttt{rand}[0, g(x')]$ in the interval $[0, g(x')]$
3. Confront this value with the value $f(x')$. If $y(x') < f(x')$ then the couple $(x', y(x'))$ is a random point within $f(x)$ and x' is accepted, $x' \in \widetilde{x}_f$ and the loop stops. Otherwise $y(x')$ is rejected. Go back to step 2 and restart the procedure.

This procedure is repeated for all the random number required. The obtained set of accepted $\{x', y(x')\}$ is distributed as $\{x, f(x)\}$.

5.1.6 Multidimensional distributions

If we want to get a value from a multidimensional distribution, as for example the direction of scattering when the differential scattering cross-section depends on the

k-vector and also on the polarization, care has to be taken to extend the previous methods.

We want to generate a set of $\{x, y\}$ distributed as $f(x, y)$. The easy case occurs when the distribution is separable, such as that

$$f(x, y) = g(x)\, h(y). \tag{5.10}$$

This means that the variables x and y are uncorrelated and we can sample them independently. Otherwise, the distribution along each dimension

$$D_y(x) = \int_{y1}^{y2} f(x, y)dy \tag{5.11}$$

has to be calculated. Then first x is generated according to $D_y(x)$ and then y is obtained from the conditional probability of getting y after x has been chosen.

Mathematically, given the joint probability density function $f(x_1, x_2, \ldots, x_N)$, we want to calculate the conditional density functions

$$h_m(x_m|x_1, x_2, \ldots, x_{m-1}). \tag{5.12}$$

This probability is calculated via the marginal distributions g_m

$$\begin{aligned} g_m(x_1, x_2, \ldots, x_m) &= \int f(x_1, x_2, \ldots, x_n)\; dx_{m+1}dx_{m+2}\ldots dx_n \\ &= \int g_{m+1}(x_1, x_2, \ldots, x_{m+1})\; dx_{m+1} \end{aligned} \tag{5.13}$$

which are the probability of choosing the set $(x_1, x_2, \ldots, x_m)$. The conditional density function h is then given by:

$$h_m(x_m|x_1, x_2, \ldots, x_{m-1}) \equiv \frac{g_m(x_1, x_2, \ldots, x_m)}{g_{m-1}(x_1, x_2, \ldots, x_{m-1})} \tag{5.14}$$

and the sought distribution $f(x, y)$ can now be factorized into

$$f(x_1, x_2, \ldots, x_n) = h_1(x_1)\, h_2(x_2|x_1)\ldots h_n(x_n|x_1, x_2, \ldots, x_{n-1}). \tag{5.15}$$

All the random variables x_i can be obtained from the first one x_1 with an iterative procedure.

An alternative to this process consists in using a multidimensional rejection method. For example to obtain a random unit vector (a vector in a sphere) I can just sample randomly three numbers a, b, c make with them a vector (abc) and check if it is unitary (very inefficient![2]). The global multidimensional rejection method and the choice of a value from a multidimensional distribution are two techniques which are equivalent, the best strategy depends on the specific case in analysis.

[2]In the code a random vector has been obtained first choosing c randomly in $[-1, 1]$, and then applying the rejection method to a and b to have a vector in the circle at $z = c$.

5.2 Multiple scattering path integral

In chapter 2 an exact formulation of the crossed and ladder bistatic coefficient has been presented. For scattering of scalar and vectorial waves in isotropic scattering media, exact analytical solutions have been found [42], but none can be easily applied for anisotropic scattering or light in nematic liquid crystals.

The bistatic coefficient have an integral formulation which can be well implemented in a Monte Carlo simulation. We recall here the integral formulation of the coherent backscattering problem as defined in Eq. (2.102). The contribution for each scattering order to the crossed term is

$$\begin{aligned}\gamma_C^{(N)} = \frac{4\pi n_p^N}{A} \int d\mathbf{r}_1 d\mathbf{r}_2 \dots d\mathbf{r}_N \; e^{-z_1/\ell_s} \left(\frac{d\sigma}{d\Omega}\right)_1 (16\pi^2 G(k,\mathbf{r}_{12}) G^*(k,\mathbf{r}_{12})) \left(\frac{d\sigma}{d\Omega}\right)_2 \dots \\ \dots \left(\frac{d\sigma}{d\Omega}\right)_{N-1} (16\pi^2 G(k,\mathbf{r}_{N-1,N}) G^*(k,\mathbf{r}_{N-1,N})) \left(\frac{d\sigma}{d\Omega}\right)_N \\ e^{-z_N/\ell} \times \cos[(\mathbf{k}_{\text{in}} + \mathbf{k}_{\text{out}}) \cdot (\mathbf{r}_N - \mathbf{r}_1)]\end{aligned} \tag{5.16}$$

while the ladder one has the same structure without the interference factor at the end (Eq. (2.100))

$$\begin{aligned}\gamma_L^{(N)} = \frac{4\pi n_p^N}{A} \int e^{-z_1/\ell_s} \left(\frac{d\sigma}{d\Omega}\right)_1 (16\pi^2 G(k,\mathbf{r}_{12}) G^*(k,\mathbf{r}_{12})) \left(\frac{d\sigma}{d\Omega}\right)_2 \dots \\ \dots \left(\frac{d\sigma}{d\Omega}\right)_{N-1} (16\pi^2 G(k,\mathbf{r}_{N-1,N}) G^*(k,\mathbf{r}_{N-1,N})) \left(\frac{d\sigma}{d\Omega}\right)_N \\ e^{-z_N/\ell} \; d\mathbf{r}_1 d\mathbf{r}_2 \dots d\mathbf{r}_N \, .\end{aligned} \tag{5.17}$$

These are the two integrals that we want to calculate with the Monte Carlo simulation.

The principle of a Monte Carlo simulation is to probe the system in a large number of configurations, and to use the average result to describe the whole system. Many light wavepackets, which we will call for simplicity photons, but which are of classical nature, are launched into the system and properly propagated; the exiting intensity is then recorded. The coherent backscattering cone arises in the diffuse intensity, averaged over the disorder. In the following we perform the average over the position of the scatterers with a Monte Carlo method, extended for anisotropic scattering. The method is flexible as it allows to compute many transport quantities at the same time and can be easily extended to different scattering processes [112].

Before choosing the best numerical strategy, we can look qualitatively at the integrals. The propagators $G(k,\mathbf{r}_{12})$ give contributions that are exponentially weaker for long paths than for short ones: a crude Monte Carlo would be extremely inefficient, with very slow convergency, as it would consider with the same weight the short paths (the dominating contributions) and the many long paths (exponentially attenuated). A variance reduction techniques can be very effective here, so we have decided to sample the modulus of the random vector $\mathbf{r}_{12}$ from an exponential distribution $\exp(r_{12}/\ell_s)/\ell_s$. The same strategy can be employed to avoid scattering directions for which $(d\sigma/d\Omega)$ is extremely weak (or zero). This can be accounted for, choosing the direction of the random vector $\mathbf{r}_{12}$ from an appropriate distribution, with the same shape as the differential scattering cross-section.

Doing this, a natural physical interpretation arises, as the photon we are describing with the position vector $\mathbf{r}$ is scattered in a direction given by $(d\sigma/d\Omega)$ and propagates for a distance given by $G(k, \mathbf{r}_{12})$: it is a *random walk*. The Monte Carlo technique consists in computing the photon random walk (labelled by the variable $\mathbf{r}_w$) and then in summing up the contribution of each photon to the bistatic coefficient. Self-consistency is ensured stopping the summation when the photon exits the slab.

The contribution of a single photon to the ladder and crossed terms is now reduced to a very simple form

$$\gamma_L = \int_{\mathcal{S}_{rw}} e^{-z_N/\ell_s}\, d\mathbf{r}_w \tag{5.18}$$

$$\gamma_C = \int_{\mathcal{S}_{rw}} e^{-z_N/\ell_s}\, \cos[(\mathbf{k}_{\text{in}} + \mathbf{k}_{\text{out}}) \cdot (\mathbf{r}_N - \mathbf{r}_1)]\, d\mathbf{r}_w \tag{5.19}$$

Following the previous reasoning on the variance of the Monte Carlo, one could think that for the ladder term the Monte Carlo has almost zero variance, as we are calculating the integral of an exponential, which has known primitive. This unfortunately is not true, as the all problem is now transferred to the boundary conditions, and the simulations essentially calculates the volume of the subspace $\mathcal{S}_{rw}$ defined by the condition that the photon is inside the slab, by the points z_N.

We will investigate the case of isotropic and anisotropic Rayleigh scattering processes. The algorithm has been written for the C programming language, following the ANSI[3] standard [116].

5.2.1 The photon random walk

The first requirement of the code is to simulate a photon random walk in the medium. This is achieved from the knowledge of the single scattering cross-section which describes the scattered pattern at each event and the dressed Green function that tells how much light can reach the following scatterer (in chapter 2).

The (random) choice of the positions of the various scatterers is done successively starting from the first one, then determining the position of the second one, then the position of the third one, and so on. Each time the direction of propagation of the photon is chosen with probability given by the single scattering differential cross-section $d\sigma/d\Omega$ and the position of the next scatterer, in a random direction from the previous scatterer, is exponentially distributed accordingly to $G(\mathbf{k}, \mathbf{r}_{12})$ (Eq. (2.114)). These two steps are equivalent to a variable change in the multiple scattering integrals (as described in section 5.1.2) and they increase the efficiency of the simulation.
More precisely, the algorithm is the following one.

1. Choose randomly the depth of the first scatterer according to an exponential distribution.

2. Choose randomly the direction of emission according to $d\sigma/d\Omega$.

3. Choose randomly the position of the next scatterer from the previous scatterer at a distance given by an exponential distribution, as in Eq. (5.9). If the chosen position is outside the medium, stop the current scattering path and initiate a new one (go to step 1).

[3] the American National Standards Institute.

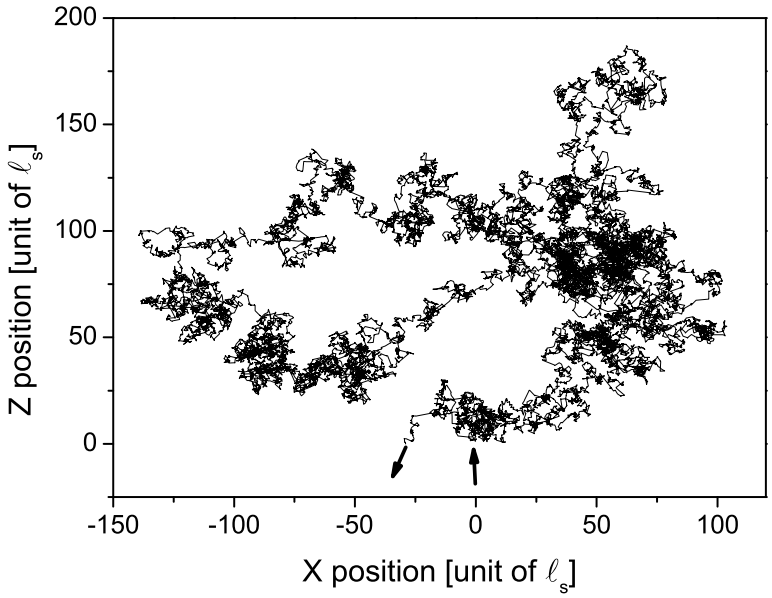

Figure 5.4: Isotropic random walk. 34871 scattering events.

4. Go to step 2 and continue the random walk repeating the procedure until the scattering order N is reached.

5. If the scattering order is N, compute the contribution of this photon.

6. Inject a new photon and restart the full procedure.

A photon random walk obtained from the algorithm is shown in Fig. 5.4. As predicted by diffusion theory, the average space travelled in the x-direction is $\sim \sqrt{N} \times \ell_t$. The specific photon shown in Fig. 5.4 has travelled a path which is ~ 200 times longer than the physical thickness of the slab. After 34871 scattering events it exits the medium from the same face it entered from. The sum of all the intensity contribution of the diffused photons is the incoherent transport of light, as described by diffusion approximation. For example the transmitted photon cloud can be calculated, as shown in Fig. 5.5

When we consider the semi-infinite geometry, we should consider arbitrary long paths, but this is evidently impossible in a real simulation, as a cut-off has to be introduced to keep control over the computing time. We thus fix a maximum scattering order and an optical thickness b and we discard photons which exceed these values. This means that we are always underestimating the backscattered contributions. In the case of the isotropic Rayleigh scatterers, the systematic absolute error induced in the bistatic coefficients is $\simeq 4.5/b$ [117]. This means that the cones are ~ 1 % (for $b = 100$) smaller than they would be in a real semi-infinite medium.

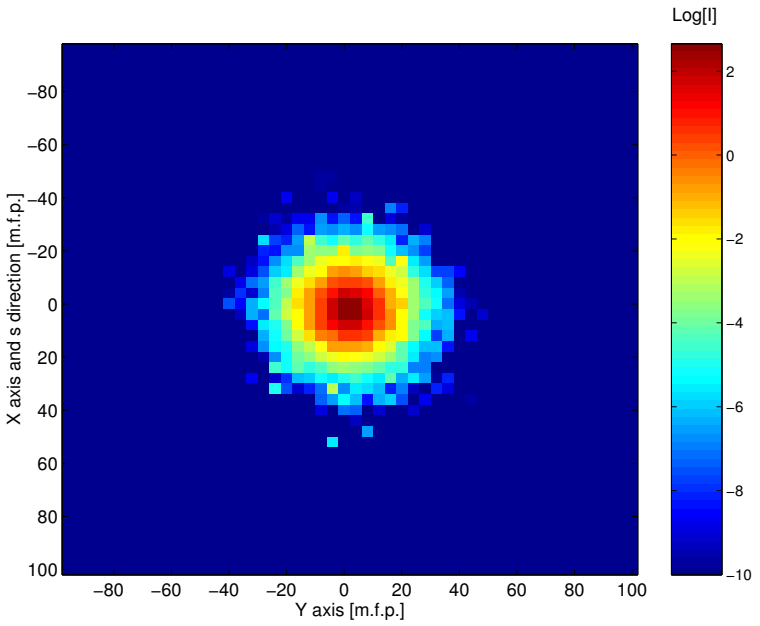

Figure 5.5: Simulation of the photons transmitted from a slab of spatially isotropic medium, of optical thickness $b = 10$. The cloud of photons is symmetric.

Before calculating the crossed and ladder contributions it is important to introduce the partial photon method that reduces considerably the computing time.

5.2.2 The partial photon method

A crucial point, which saves a lot of computing resources, is to remark that, when calculating the N-th scattering contribution, all the scattering order inferior to N (as the $(N-1)$-th, the $(N-2)$-th, etc ...) can be obtained at almost no extra cost. The contribution of each scattering event to the backscattered (or transmitted) intensity can be computed independently from the existence of a successive scattering event (or order). Thus, a scattering path with N scattering events can be used for all orders of scattering from 1 to N (this is the *partial photon* method discussed in Appendix C of Ref. [118]). This trick essentially saves a factor N in the calculation, where N is the typical scattering order of a path in the medium. In the diffusion approximation, N is of the order of the square of the optical thickness of the medium. With the optical thickness in the experiments one finds $N \sim 10^3$, so that the saving is substantial. The whole procedure actually relies on the "ladder" structure of the diagram (see chapter 2): the diagram at scattering order N is obtained from the diagram at order $(N-1)$ by simply adding an additional rung to the ladder.

In the procedure described in the previous section we can now compute the contribution to the ladder and crossed bistatic coefficient at each scattering order, during each random walk. During step 3 of the random walk algorithm, the integrals in Eq. (5.16) and Eq. (5.17) are computed for each scattering event just summing up the values of the exponentials $\exp(-z_N/\ell_s)$ which account for the transport of the intensity to the sample surfaces (whose distance is z_N). By restarting the full procedure as soon as

the position of a scatterer is outside the medium, we ensure automatically the correct weights of the various scattering orders.
More precisely, the algorithm is the following one.

1. Choose randomly the depth of the first scatterer according to an exponential distribution.
2. Choose randomly the direction of emission according to $d\sigma/d\Omega$.
3. Choose randomly the position of the next scatterer from the previous scatterer at a distance given by an exponential distribution, as in Eq. (5.9). If the chosen position is outside the medium, stop the current scattering path and initiate a new one (go to step 1).
4. Compute the contribution of this photon to the present scattering order.
5. Go to step 3 in order to compute the next step in the random walk.

In principle we should be careful in using the partial photon method, as it could induce small correlations between the scattering events, as they all belong to the same random walk. This is completely negligible for isotropic scattering, as the photon direction and polarization are completely randomized after few scattering events, but may play a role in anisotropic media. This problem is completely avoided if the parameter space is well sampled, if the average is made over many photons and many scattering events (we use $\sim 10 - 100$ thousands photons and thousands of scattering events for each photon). Evidence of such a correlation problem would appear in unusual oscillations in the tails of the cone; with the present simulations we did not experience this problem.

5.3 The simulated coherent backscattering cone

5.3.1 Isotropic scalar coherent backscattering cone

For the case of isotropic scattering of scalar waves, the simulation can be performed with little computing time ($\sim$ minutes on a Intel ^{TM} Pentium 4, 32-bit processor, 2.8 GHz CPU speed, standard architecture, Linux operating system). There exists also an analytical solution to the Milne equation, as discussed in chapter 2 and in ref. [42], which can be confronted with the simulated profile. The comparison is shown in Fig. 5.7, for the case when 100.000 photons are launched in a semi-infinite medium: the agreement between theory and simulation is excellent.

5.3.2 Isotropic vectorial coherent backscattering cone

The vectorial nature of light waves affects both the elementary scattering event and the propagation in the average medium. The scattering cross section depends on the polarization of the incident light but not on the relative orientation of the incoming and outgoing directions. In order to include scattering of vector waves, one has to use the scattering cross-section for isotropic vectorial Rayleigh scattering (Eq. (2.113)),

$$\frac{d\sigma}{d\Omega}(|\mathbf{k}_\mathrm{i}, \mathbf{i}\rangle \longrightarrow |\mathbf{k}_\mathrm{f}, \mathbf{f}\rangle) = \frac{3}{8\pi}\, \sigma_0\, |\mathbf{i} \cdot \mathbf{f}|^2. \tag{5.20}$$

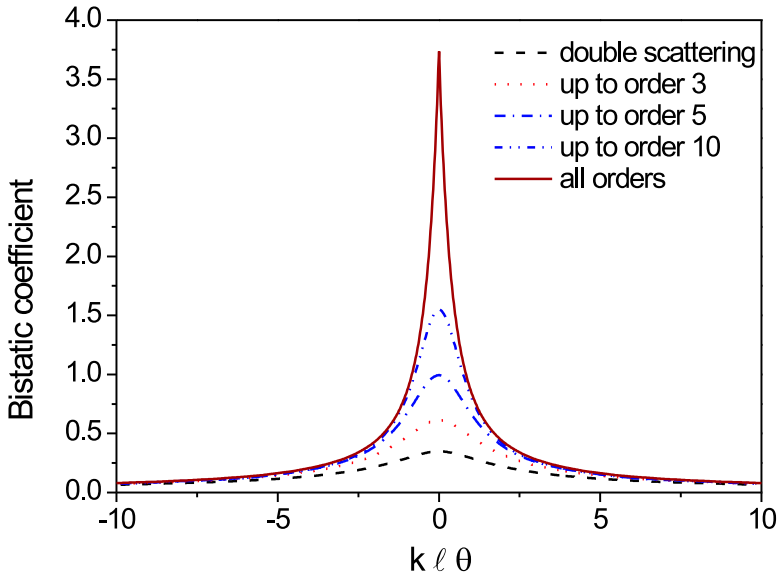

Figure 5.6: In the figure, the full profile (full line) and the interference that results from only double scattering (dashed line), and a few lower scattering orders (dotted and mixed lines) are shown. The line profile is obtained with a Monte Carlo simulation for scalar waves and isotropic scattering (single scattering has been subtracted and the ladder term has been fixed to 1 for all orders).

and the vectorial Green function propagator

$$G(\mathbf{k}, \mathbf{r}_{12}) = -\frac{1}{4\pi r_{12}} \exp(ikr_{12}) \exp\left(-\frac{r_{12}}{2\ell_s}\right) \Delta_{\mathbf{r}}. \tag{5.21}$$

The differential cross section is no longer isotropic, which means that the scattering directions are not all equiprobable. We have used two different methods: either choose randomly the scattering direction at each scattering event and weight the contribution by the probability of the event (proportional to the differential cross section) or choose directly the scattering direction with a probability distribution matching the differential cross section. We have checked that both methods give the same results [112], although the second one is more accurate, as the integrand in the Monte Carlo integration is constant, at the price of the integration volume harder to compute (see section 5.2.2). The Monte Carlo simulation uses the rejection method to obtain a scattering direction from the distribution shown in Eq. (5.20); after the scattered direction is chosen, a projection of the excited dipole on the subspace orthogonal to $\mathbf{k}_f$ allows for getting the scattered polarization $\mathbf{f}$.

The numerical calculation of the bistatic coefficient is similar to the calculation for scalar waves. The only difference is that the polarizations of the incoming, outgoing, and intermediate photons must be taken into account. Special care is needed when

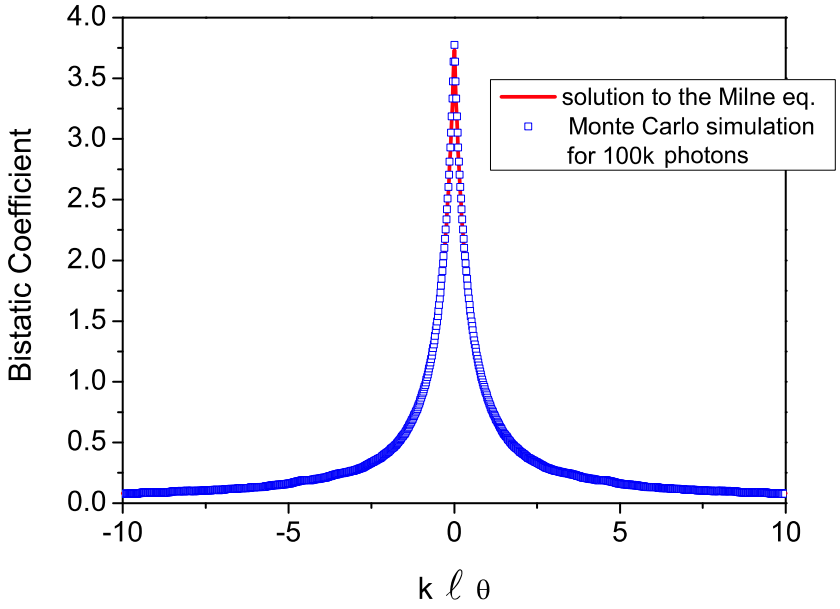

Figure 5.7: Comparison between the simulated coherent backscattering cone for scalar waves and the solution of the Milne equation. The agreement is excellent. Crossed term only, while the ladder is $\gamma_L \simeq 4.25$.

considering the polarization state of scattered photons. Indeed, given a multiple scattering path, the contributions of the possible polarizations of the photon between two consecutive scatterers must be taken into account. For long paths, the number of contributions increases very rapidly. In the isotropic scattering case (only), the average amplitude propagator is the same for all polarizations, which means that they all are attenuated with the same mean-free path. It is thus possible to use a given multiple scattering path to sum exactly the various contributions having different intermediate polarizations.

The result is shown in Fig. 5.8. As expected the cone shows, in the lin$\parallel$lin channel, a difference between the two scanning direction with respect to the incident linear polarization, as a result of a trivial anisotropy related to the first scattering orders [82]. The cone in the helicity-reversing channel shows a much smaller enhancement which is due only to the depolarized component of the multiple scattered light. In the case of the lin$\perp$lin channel, there is anisotropy between the scans at 45 deg of the cone, and at the same time the enhancement is strongly reduced, as expected from the theory (see section 2.10.6).

For vectorial waves an exact expression of the cone is available from the theory, but it is extremely involved [42]. Instead there exists a simple exact solution for the special case of only double scattering [76].

5.3.3 Double Scattering Coherent Backscattering cone: a test for the code

As a special case, we can test the Monte Carlo simulation against the theoretical calculations of the profile of the coherent backscattering cone for only the second scattering order.

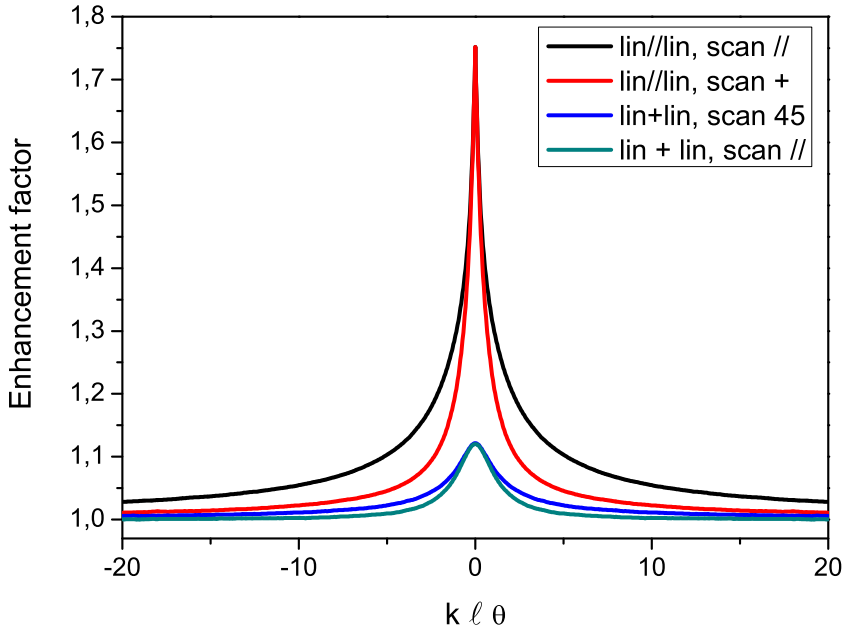

Figure 5.8: Coherent backscattering cone simulated for vectorial waves scattered from a collection of isotropic Rayleigh scatterers.

For only double scattering, the profile of the coherent backscattering cone can be calculated analytically, as it has been done by Cord Müller [76]. The coherent backscattering signal as a function of the reduced angle of detection $\mu = k\ell_t\theta$, is given by:

$$\gamma_C^{(2)}(\mu,\phi) = \frac{9}{16\pi}\int_0^{\pi/2} d\theta \int_0^{2\pi} d\varphi \frac{\sin\theta\, c_1(\theta,\varphi,\phi)}{1+\cos\theta-\mu^2\cos\theta\cos^2\varphi} \tag{5.22}$$

where $c_1(\theta,x,\phi)$ is

$$c_1(\theta,x,\phi) = \frac{1}{4}(1+x^2)^2 + \frac{1}{8}(1-x^2)^2 + \frac{(1-x^2)^2}{8}X^2\cos 4\phi + \frac{1-x^4}{2}X\cos 2\phi$$

$$X = -2\frac{\sqrt{(1+x^2)^2+\mu^2(1-x^2)}-1-x}{(1-x)\mu^2}$$

The solution of Eq. (5.22), for the case linear $\parallel$ linear is

$$\begin{aligned}\gamma_C^{(2)}(\mu,\phi) \;=\; & \frac{3}{512(1-\mu^2)^4}[-288+48\mu^2-252\mu^4-138\mu^6+ \\ & +(222-144\mu^2+237\mu^4)\sqrt{1+\mu^2} \\ & +(192-384\mu^2+720\mu^4-336\mu^6+123\mu^8)\mathcal{F}(\mu) \\ & +A_1(\mu)\cos 2\phi + A_2(\mu)\cos 4\phi]\end{aligned} \tag{5.23}$$

where

$$A_1 = 28\mu^{-2}[2(2-8\mu^2-4\mu^6-5\mu^8)+(-4+18\mu^2-14\mu^4+15\mu^6)\sqrt{1+\mu^2}]+ \\ +12\mu^2(16+8\mu^2+6\mu^4+5\mu^6)\mathcal{F}(\mu) \quad (5.24)$$

$$A_2 = \mu^{-4}[2(24-76\mu^2+64\mu^4+24\mu^6-106\mu^8-35\mu^{10})+ \\ +(-48+176\mu^2-222\mu^4+88\mu^6)+111\mu^8)\sqrt{1+\mu^2}] \quad (5.25)$$

and the auxiliary real function $\mathcal{F}(\mu)$ is given by

$$\mathcal{F}(\mu) = [2\,\mathrm{arg\,cosh}\left(\frac{1}{|\mu|}\right) - \mathrm{arg\,cosh}\left(\frac{1}{\mu^2}\right)]/\sqrt{1-\mu^2} \quad (5.26)$$

Half of the function $\mathcal{F}$ is the crossed bistatic term for double scattering of a scalar wave scattered in a semi-infinite medium of point-like scatterers.

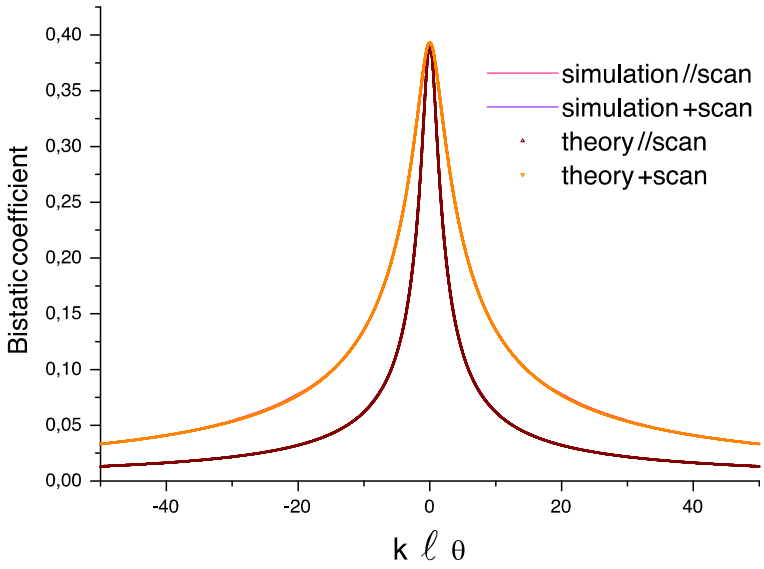

Figure 5.9: Bistatic coefficient for double scattering of a vectorial wave by point-like scattering medium. x-y scans of the two linear polarizations channels are shown in the lin||lin channel. The profiles from theory and simulation are indistinguishable.

The Monte Carlo simulations show an excellent agreement with the predicted cone profile, as it is clear from the plot of the theory and simulation together, Fig. 5.9.

5.4 Anisotropic Coherent Backscattering cone from anisotropic propagator

We can generalize this isotropic picture and allow for a non-isotropic Green function propagator. As a first model, we can change the intra-scattering propagator, and introduce an anisotropic mean free path in the Green function. We are not changing each individual scattering cross-section, which should be anisotropic as well. It is indeed a first model, only to understand the role of the anisotropy, that we will include in the

next sections. This fist case as been presented already in section 3.1.1, and it has been described with a diffusion equation generalized for anisotropic mean free path. Here we present the result of a Monte Carlo simulation for anisotropic scattering mean free path, which confirms such analysis.

5.4.1 Light transmission

The transmitted light from a slab of a medium with such an anisotropy, and large optical thickness $b > 7 - 8$ is dominated by anisotropic light diffusion [119]. Within the diffusion approximation, the angular spread of the diffuse cloud does not depend on the transport parameters ℓ_t or $\mathcal{D}$, as light explore a forward cone of angular opening $\Delta\theta \sim \pi/2$, which is only due to the equiprobability of a random step in the x, y or z direction. The width of the isotropic distribution, in the multiple scattering regime

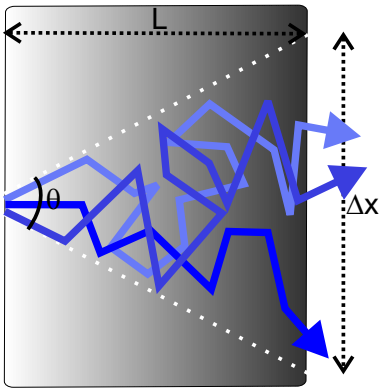

Figure 5.10: Illustration of the transmitted photons from a slab of scattering isotropic medium. The cloud of photons is symmetric.

($\ell < L$) depends only on the slab optical physical thickness L, and it is $\Delta x = \Delta y \sim 2L$.

On the contrary the relative shape of the cloud depends on the ratio between the transport mean free paths ℓ_x in the x and ℓ_y in the y direction [83]. The ratio ℓ_x/ℓ_y describes the probability of a diffusion step in the direction $\widehat{\mathbf{x}}$ as compared to the same probability in the y-direction. In section 3.1.2 we have shown that

$$\frac{\Delta x}{\Delta y} = \frac{\ell_x}{\ell_y} = s. \tag{5.27}$$

If the diffusion velocity in the two directions (x-y) is the same, then $\Delta x/\Delta y$ can be used to know the anisotropy of the diffusion constant as

$$\frac{\Delta x}{\Delta y} = \frac{\ell_x}{\ell_y} = \sqrt{\frac{\mathcal{D}_{xx}}{\mathcal{D}_{yy}}} = s. \tag{5.28}$$

As a reference, the isotropic case is plotted in Fig. 5.5: it presents a circular profile of width $\sim 2L$.

Fig. 5.11 is obtained from the Monte Carlo simulation and shows the distribution of the light exiting from the slab when the scatterer are anisotropically distributed,

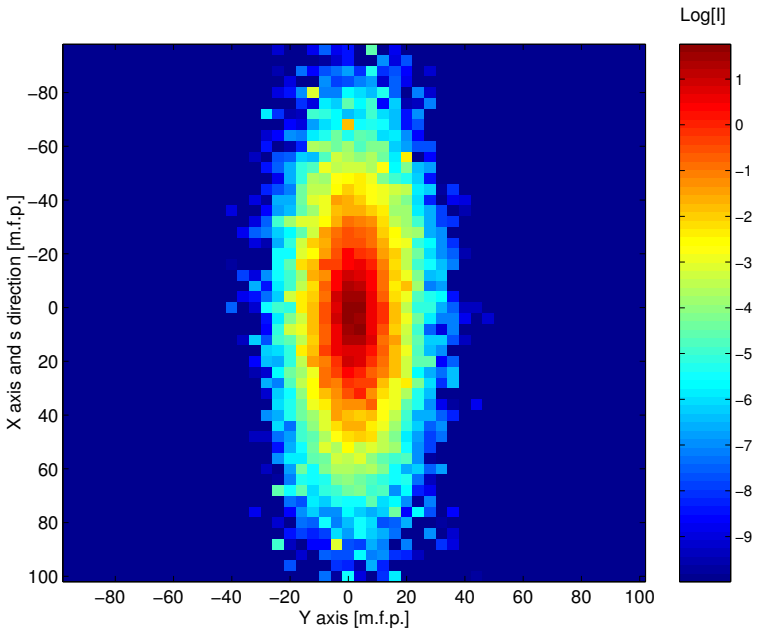

Figure 5.11: Simulated transmitted photons from a slab of spatially anisotropic medium, of optical thickness $b = 10$ and $s = 3$. The cloud is wider in the same direction of $\widehat{\mathrm{s}}$ and $\Delta x/\Delta y \simeq s = 3$.

further apart in the x direction, $s = 3$ times more distant (see section 3.1.1). The cloud is more extended in the x-direction and the ratio $\Delta x/\Delta y$ is as expected equal to the anisotropy parameter s.

5.4.2 The coherent backscattering cone

A Monte Carlo simulation of the coherent backscattering cone from such a medium has been performed [120] and it is shown in Fig. 5.12. The line profile in the $\widehat{y}$ direction is unchanged, while the x-cut is narrower proportionally to s. This means that $\ell_x = \ell_\parallel$ is longer than $\ell_y = \ell_\perp$. Here, the single scattering term γ_{S} does not depend on the parameter s, and therefore the height of the bistatic coefficient is the same as for the isotropic case.

While dynamical experiments can show that a diffusive process is anisotropic, and therefore that $\mathcal{D}_{xx} \neq \mathcal{D}_{yy}$, no information is obtained regarding the transport mean free paths $\ell_\parallel$ and $\ell_\perp$ if the diffusion velocity is not known. The knowledge of $\mathcal{D} = v\ell/3$ is not enough, as v could also be anisotropic. The coherent backscattering cone in a medium with a spatial anisotropy can be used to measure directly the transport mean free path, via the measure of the cone width.

The effect of the anisotropy is shown in figure 5.13, where the ratio between the FWHMs of the cones, which is $W_\perp/W_\parallel$, is plotted as a function of the anisotropy parameter s. $W_\perp$ is not affected by the anisotropy, while $W_\parallel$ decreases. Accordingly to $W_\parallel \sim 0.7/k\ell_\parallel$, also $\ell_\parallel$ decreases as expected,

$$1/\ell_\parallel = 1/(\ell_0\, s), \tag{5.29}$$

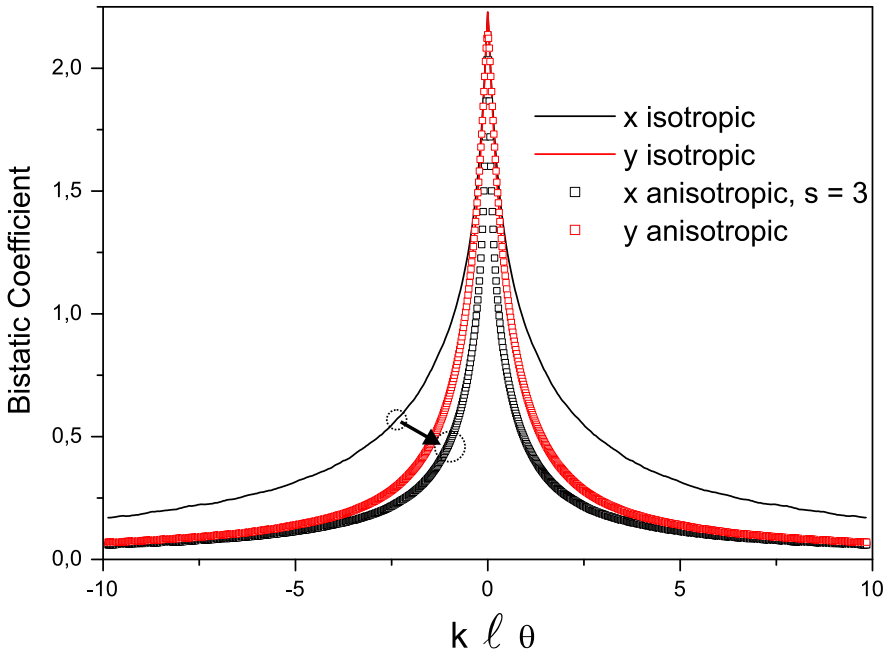

Figure 5.12: Coherent backscattering cone for isotropic Rayleigh scattering (line) and for spatial anisotropy (symbols), $s = 3$ and $\widehat{s}$ in the $\widehat{x}$ direction. The cut in the $\widehat{y}$ direction is unchanged by the stretching in the $\widehat{x}$ direction, while the x-cut is narrower. The optical thickness calculated for ℓ_0 is $b = 30$.

where ℓ_0 is the isotropic transport mean free path. The expected behavior of the width anisotropy is then

$$\frac{W_\perp}{W_\parallel} \sim \frac{1/\ell_0}{1/(\ell_0 s)} \sim s, \tag{5.30}$$

as predicted with an anisotropic diffusion equation in section 3.1.1. The linearity of the relation in Eq. (5.30) is confirmed by Fig. 5.13.

This effect is the same, but with different origin, as the anisotropy usually reported in literature (see for example in Ref. [83]), where it is originated from Mie scattering from elongated objects all oriented in the same direction. In the next section we will investigate a more subtle form of anisotropy that arises from anisotropic polarizability of Rayleigh scatterers and which cannot be directly included into a diffusive model.

5.5 Anisotropic Coherent Backscattering cone from anisotropic polarizability of the scatterers

We can generalize this isotropic picture and allow for non-isotropic polarizability of the medium, ex. asymmetric molecules that can be more easily excited by a field in a given direction. We can model the scatterer polarizability with an uniaxial anisotropic dielectric tensor $\mathbf{D} = 1 + (a-1)|\mathbf{n}\rangle\langle\mathbf{n}|$, where a is the anisotropy parameter that quantifies the degree of anisotropy (see section 3.2). In this case a diffusive approach is not strictly justified, and its validity is controversial.

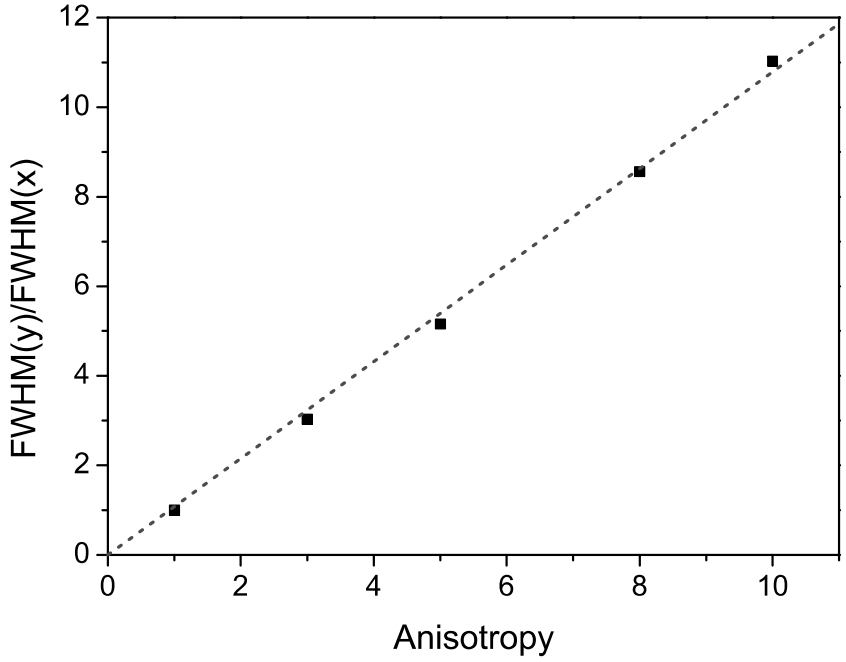

Figure 5.13: Anisotropy of the coherent backscattering cone, $W_\perp/W_\parallel$, lin$\parallel$lin channel, as a function of the spatial anisotropy parameter s. Increasing the spatial anisotropy in the $\widehat{x}$ direction the x-cut of the cone gets thinner while it does not change in the $\widehat{y}$ dir. The line is a linear fit. 1 million photons launched in a slab of optical thickness $b = 30$.

The simulation is performed as described in the previous section, light is incident normal to the slab, and the optical axis $\mathbf{n}$ lies in the plane of the slab surface. We have performed two different simulations, for the two input polarization state of the light, parallel and perpendicular to $\mathbf{n}$. In both cases we have used a propagator which has the same form as the isotropic one, but which is generalized for an anisotropic scattering mean free path, neglecting the anisotropy-induced dichroism.

An important difference with isotropic scattering systems is that in this case there is a strong sensitivity in the input light state. One of the major effects is in the penetration length of the incident photons, which is very different for the two input polarization states.

5.5.1 The penetration length

The backscattered light profile is crucially determined by the penetration length z_p (see section 2.3.1) of the photon in the medium, before the first scattering event, see Fig. 5.14. In the anisotropic medium, two different penetration lengths are important, for input polarization parallel or perpendicular to $\mathbf{n}$. A different z_p implies a different number of scattering events before exiting the medium, therefore a different mixing of the two mean free path $\ell_\perp$ and $\ell_\parallel$.

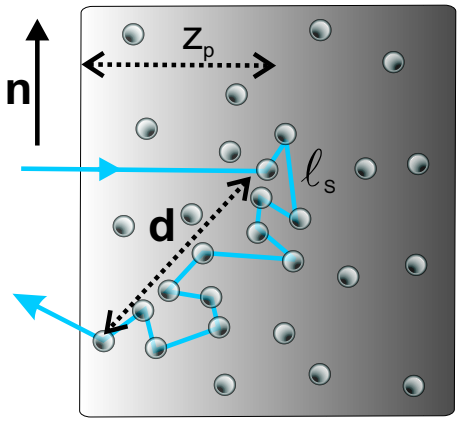

Figure 5.14: Diffusion in backscattering due to anisotropy. The penetration length is z_p while the exiting distance d is obtained from the interplay of z_p and the scattering mean free path ℓ_s (see section 2.3.1).

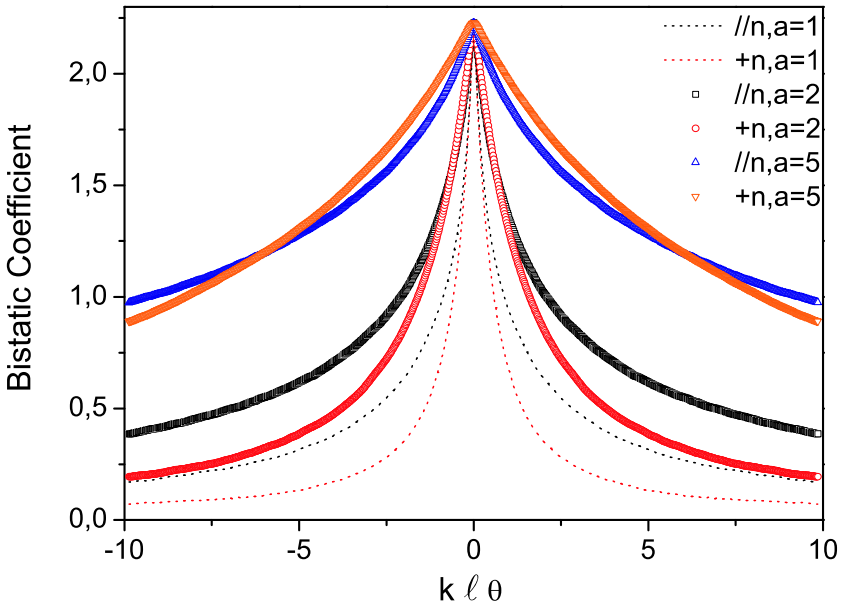

Figure 5.15: Comparison of the coherent backscattering cone for isotropic polarizability (dotted line) and the cone in presence of angular anisotropy. Extraordinary input polarization, $\mathbf{i} \parallel \mathbf{n}$, short penetration length. Plots as a function of anisotropy a, for optical thickness $b = 30$, and 100 000 photons launched. Anisotropic bistatic coefficients are rescaled to be compared with the isotropic one.

5.5.2 The simulated cones

Fig. 5.15 shows the simulated cones for extraordinary polarization, parallel to $\mathbf{n}$ [120]. The penetration length in this case is very short, $z_p = \ell_s/a^2$, a^2 times smaller than the isotropic scattering mean free path. Therefore few events are enough for the photon to escape the medium. The exiting distance of the photons is thus dominated by low

scattering orders, which have strong signature of the single scattering anisotropy. This reflects into the large anisotropy of the cone wings.

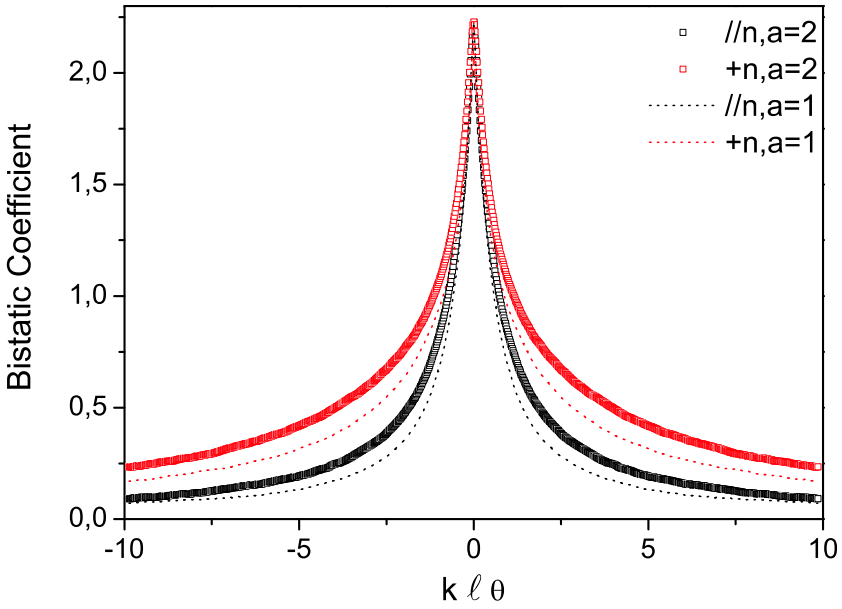

Figure 5.16: Comparison of the coherent backscattering cone for isotropic scattering (dotted line) and the cone in presence of angular anisotropy. Ordinary input polarization $\mathbf{i} \perp \mathbf{n}$, long penetration length. Optical thickness $b = 30$, and 100 000 photons launched. Anisotropic bistatic coefficients are rescaled to be compared with the isotropic one.

Fig. 5.16 shows the case of ordinary incident polarization. The penetration length is long, $z_p = \ell_s$, equal to the isotropic scattering mean free path and therefore a photon has to perform many more scattering events before exiting the medium (as shown in Fig. 5.14). Light transport will be dominated by the higher scattering orders and therefore by the averaged transport mean free path. Again the wings profile is a clear indication of an averaging process that reduces the effect of single scattering anisotropy: both the parallel and perpendicular cuts show a large angle behavior similar to the isotropic case, which is clearly different from the other polarization case reported in Fig. 5.15. On the contrary, if one looks at the diffusive top, and one extracts the information about the opening angle, one sees a clear anisotropy between the angular openings $\theta_{\perp}^{-1}$ and $\theta_{\parallel}^{-1}$, which increases with the parameter a.

5.5.3 Angular opening of the cone

When one is entitled to apply a diffusive model to multiple light scattering in ordered nematics or anisotropic media, then one can describe the coherent backscattering cone with an effective length, the transport mean free path, which has a simple relation with the opening of the cone, being $W(\theta) \sim 0.7/k\ell_t$. If one can generalize the isotropic diffusion equation and obtain an anisotropic diffusive picture, then one can replace the isotropic cone width W with two different widths in the two orthogonal directions, and describe the cone with $W_{\parallel} \sim 0.7/k\ell_{\parallel}$ et $W_{\perp} \sim 0.7/k\ell_{\perp}$ (as done in first approximation in section 4.4).

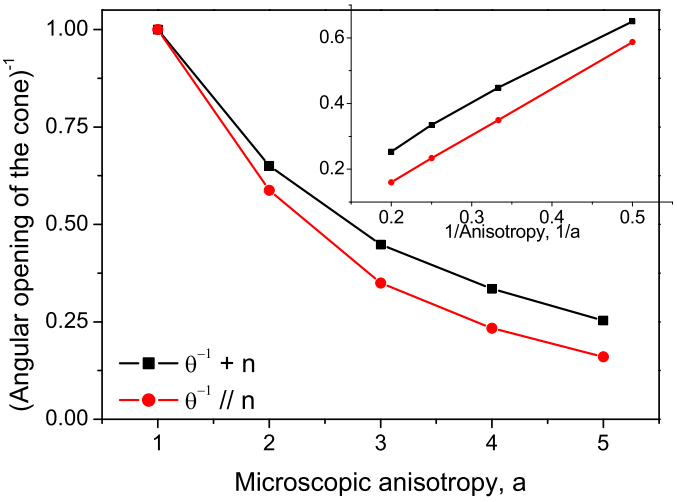

Figure 5.17: Reciprocal of the opening angle of the cone as a function of the anisotropy a, for incident extraordinary polarization, $\mathbf{i} \parallel \mathbf{n}$, 100 000 photons launched, optical thickness $b = 100$. In first approximation the behavior of $\theta^{-1}_{\perp,\parallel}(a)$ is hyperbolic. It is important to notice the anisotropy that opens up between the two angles. The values are normalized to the opening angle for $a = 1$.

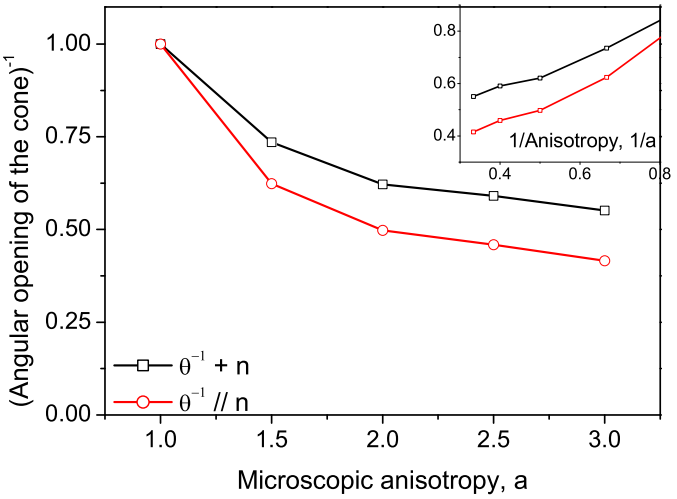

Figure 5.18: Reciprocal of the opening angle of the cones as a function of the anisotropy a, for incident ordinary polarization, $\mathbf{i} \perp \mathbf{n}$, 100 000 photons launched, optical thickness $b = 100$. Again anisotropy opens up between $\theta^{-1}_{\perp}$ and $\theta^{-1}_{\parallel}$. The values are normalized to the opening angle for $a = 1$.

In the case of anisotropic Rayleigh scattering, it is not evident how to apply a diffusive picture, given the tensorial and non-isotropic nature of the scattering function. One is tempted to relate the width of the cone to an "effective" transport mean free path, but no solid justification of such a theoretical step can be provided so far. We have chosen to describe the cones by their opening angles.

The opening angle of the cone is extracted from linear fits of the triangular top of the cone. Two angles are obtained, $\theta_{\parallel}$ and $\theta_{\perp}$, in the direction parallel and perpendicular, respectively, to the nematic director. In Fig. 5.17 we show how, in the case of extraordinary incident polarization, the reciprocal of the opening angle of the cone (normalized with the opening angle for $a = 1$) evolves as a function of the single scattering anisotropy a. Both opening angles decrease hyperbolically, as seen from the inset. We can perform the same analysis for the ordinary incident polarization (Fig. 5.18) and find a similar behavior.

5.5.4 Angular anisotropy

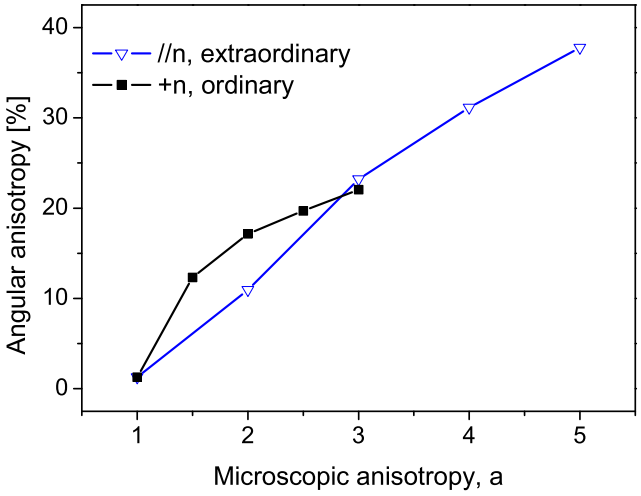

Figure 5.19: Anisotropy of the reciprocal of the opening angle of the cone, $(\theta_{\perp}^{-1} - \theta_{\parallel}^{-1})/\theta_{\perp}^{-1}$, as a function of the microscopic anisotropy a, for $\mathbf{i} \parallel \mathbf{n}$ extraordinary incident polarization (empty triangles) and $\mathbf{i} \perp \mathbf{n}$ ordinary incident polarization, (full squares). 100 000 photons launched, optical thickness $b = 100$. The lines are a guide to the eyes.

A very important quantity is the angular anisotropy $(\theta_{\perp}^{-1} - \theta_{\parallel}^{-1})/\theta_{\perp}^{-1}$, which is plotted in Fig. 5.19 and which increases with a, as qualitatively expected.

In Fig. 5.19, while, for both incident states, the anisotropy increases with a, there is also a difference between the two cases. This means that there is not complete depolarization upon multiple scattering, and a memory of the incident polarization, associated with its scattering mean free paths, survive the global averaging. This is a signature that a simple diffusive picture may not be enough to describe these scattering

systems.

Also in the isotropic case ($a = 1$) a polarization anisotropy is present in the wings of the cone, but not in the opening angle of its top. This effect is known and related to the first scattering orders which show polarization anisotropy (see section 4.3) which is not related to the microscopic anisotropy a.

5.5.5 Non-diffusive behavior

If one looks at the cones in Fig. 5.15, for example, one can see that for large enough anisotropies ($a > 2 - 3$), the cone wings overlap, and the cone profiles are not just the rescaling of the isotropic ones. This is related to the lowest scattering orders which have an anisotropy-dependent role (see section 5.5.1). This is a very important result which we would like to compare with the experiments shown in chapter 2 for the case of ordered nematic liquid crystals. Unfortunately the weakness of the anisotropy in the case of ordered nematics ($a \sim 1.15 - 1.17$) makes the effect too weak to be evident in our measurements.

In the Monte Carlo we do not make use of the diffusion approximation, so we can investigate features which are beyond the results of the usual diffusion theory.

5.6 The anisotropic propagator

So far we have simulated light propagation with the isotropic propagator, generalized for anisotropic scattering mean free path [120]. This means that we are neglecting the induced dichroism presented in section 3.3.4. In order to include also this effect (see section 9) we have diagonalized the self-energy of the problem, and found the polarization eigenvectors $\mathbf{e}_1$ extraordinary and $\mathbf{e}_2$ ordinary.

The two eigenmodes of propagation have to be treated independently as far as attenuation and scattering probability is concerned. In principle one should project the scattered field onto $\{\mathbf{e}_1, \mathbf{e}_2\}$, propagate them independently, each of them with its scattering mean free path $\ell_{1,2}$ and calculate the interference of the two modes at each scattering event. This complex picture can be simplified via the independent scattering approximation, if each scattering event can be considered independently. In order to neglect the probability for two different scattering paths to cross each other at a certain scatterer we need a medium sufficiently diluted, such that $k\ell_s \gg 1$. In order to neglect the interference of the two eigenmodes, and propagate them independently, the two modes have to be completely out of phase after a distance smaller than a scattering mean free path. This condition is easily fulfilled in birefringent media like nematic liquid crystals. In the case of anisotropic Rayleigh media, the relative amplitude of the two eigenmodes is exponentially different as they propagate with different scattering mean free paths. This condition is weaker than for ordered nematics, but allows us to consider independently the two polarizations.

The integral representing the sought quantity, e.g. transmitted intensity, backscattering probability, etc..., is then calculated from an independent summation of all the independent scattering paths. One strategy could be to propagate two modes each scattering event, and then to scattered them into four, and so on. This procedure requires an enormous amount of CPU power, as after N scattering events one has to take track

of 2^N photons (N can be thousands). Our choice is then to chose only one of the two possible photons, choosing it with the appropriate probability.

Operatively this integral is calculated in the following way: the photon is scattered and then a scattered state $|\mathbf{k}_\mathrm{f}, \mathbf{f}\rangle$ has to be chosen; we first determine if the output channel is *ordinary* ($\mathbf{e}_1$) or *extraordinary* ($\mathbf{e}_2$), according to the total probability of scattering in the two channels:

$$\sigma_t^{o/e} = \int \frac{d\sigma}{d\Omega}(|\mathbf{k}_0, \mathbf{e}_0\rangle)\ d|\mathbf{k}, \mathbf{e}^{o/e}\rangle \tag{5.31}$$

Once the scattering channel is chosen one can determine the scattering state $|\mathbf{k}, \mathbf{e}^{o/e}\rangle$ from the conditional probability distribution, $d\sigma/d\Omega(\mathbf{k}|e/o)$.

$$\frac{d\sigma}{d\Omega}(|\mathbf{k}_0, \mathbf{e}_0\rangle \longrightarrow |\mathbf{k}, \mathbf{e}\rangle|e/o) = \frac{d\sigma}{d\Omega}(\mathbf{e}_0, |\mathbf{k}, \mathbf{e}^{e/o}\rangle) \tag{5.32}$$

This scattered state $|\mathbf{k}_\mathrm{f}, \mathbf{f}\rangle = |\mathbf{k}, \mathbf{e}^{e/o}\rangle$ is now an eigenstate and propagates according to its scattering mean free path $\ell^{o/e}$, and without polarization rotation:

$$|\mathbf{k}, \mathbf{e}^{o/e}\rangle(\mathbf{r}) = |\mathbf{k}, \mathbf{e}^{o/e}\rangle \exp(-\frac{|\mathbf{r}|}{2\ell^{o/e}}) \tag{5.33}$$

We repeat this procedure until the photon exits the medium, and then we sum up all contributions from all scattering paths. In the limit of a large number of scattering paths, the sum converges to the scattering integral. Note that the choice of direction and polarization can be inter-changed, the above procedure can be inverted, first determining the direction and then the polarization of the photon.

If the eigenvalues of the self-energy (section 3.3.4) have also a real part, then the average medium is not only dichroic but also *birefringent*. This means that the two polarization eigenmodes will experience a different refractive index. The two eigenmodes of the self-energy will then propagate following different directions, their group velocities which will not be parallel to the k-vector. This is the case of light propagating in ordered nematic liquid crystals.

5.7 Multiple scattering in ordered nematics, a future development

Monte Carlo simulations with full anisotropic propagator are under development, as well as simulations of light transport in ordered nematics. In ordered nematics, care has to be taken in order to treat properly the two essential ingredients, the differential scattering cross-section and the Green function propagator.

The choice of the direction of emission at the scattering event is complicated by its dependence on the full photon state, k-vector and polarization, of both incident and scattered photons. This means that one has to calculate the scattered photon state from a multidimensional distribution, as shown in section 5.1.6, choosing with the right weight scattered direction and polarization state.

One fundamental problem of a Monte-Carlo simulation of multiple light scattering from long-range dielectric fluctuations is the concept of a "scatterer". A thermal fluctuation is not a scatterer in the sense a particle is. We deal with a collective excitation of an ensemble of molecules that induces a fluctuation in the refractive index. The

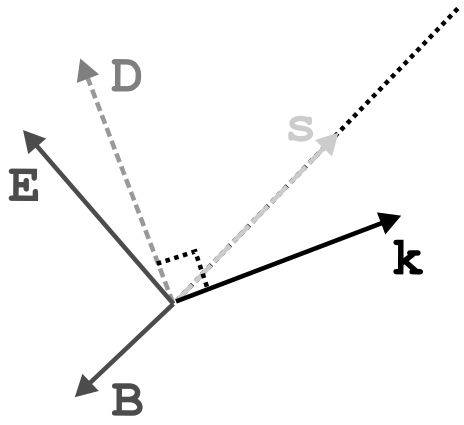

Figure 5.20: Energy and phase velocities in a birefringent medium, which are parallel, respectively, to **s** and **k**.

range of this movement is described by the correlation length. A numerical simulation can only be done if the scattering mean free path is much larger than the correlation length. Only in this case we may assume that the far-field region of the precedent scattering process is reached before a new collision takes place. Fortunately, the condition $\ell_s/\xi \gg 1$ is fulfilled for typical parameters of the experiments. A magnetic field of 0.5 Tesla applied to 5CB corresponds to $\xi = 4.2\,\mu$m, whereas the scattering mean free path is of the order of 100 μm.

In an anisotropic medium with a homogeneous dielectric tensor $\boldsymbol{\varepsilon}$ the electromagnetic field travelling along the unit vector $\mathbf{k}$ has two modes with different indices of refraction and electric polarizations. We assume non-magnetic medium, and therefore $\mathbf{B} = \mu_0\,\mathbf{H}$. The polarization and the displacement field are related by $\mathbf{D} = \boldsymbol{\varepsilon}\,\mathbf{E}$, where $\mathbf{E}$ is the electric field ($\mathbf{E} \equiv \boldsymbol{\epsilon}$), and the orthogonality relation $\mathbf{D} \cdot \mathbf{k} = 0$ holds at the place of the transversality in free space $\mathbf{E}_0 \cdot \mathbf{k}_0 = 0$. While $\mathbf{D}$ is transverse, $\mathbf{E}$ is no more [33].

The propagator eigenmodes are the ordinary and extraordinary eigenmodes of the birefringent medium. As described in the previous section, they can be propagated independently, along their group velocity, given by the Poynting vector

$$\mathbf{s}_{\mathrm{e/o}} = \mathbf{E}_{\mathrm{e/o}} \times \mathbf{H} = \boldsymbol{\epsilon}_{\mathrm{e/o}} \times \mathbf{H} \tag{5.34}$$

which is not parallel to the scattered k-vector

$$\mathbf{k} \propto \mathbf{D} \times \mathbf{B} = \boldsymbol{\varepsilon}\mathbf{E}_{\mathrm{e/o}} \times \mathbf{B} = \boldsymbol{\varepsilon}\boldsymbol{\epsilon}_{\mathrm{e/o}} \times \mathbf{B}, \tag{5.35}$$

(see Fig. 5.20). We have here defined two different Poynting vectors, $\mathbf{s}_{\mathrm{e/o}}$, one for the extraordinary and one for the ordinary polarization, which are along different directions.

On top of this, the computational effort required is heavier as the scattering function of ordered nematics is very forward, meaning that many more scattering events are required for the photon to escape the medium in the backscattering direction, and in order to perform a satisfactory averaging, many more photon have to be launched.

5.8 Conclusions

We have observed angular anisotropy in weak localization of light from highly scattering, orientationally ordered, nematic liquid crystals. No exact theory is available at this moment to describe the phenomenon. To approach it with a simpler and clearer model we have performed Monte Carlo simulations of vectorial waves propagating in anisotropic Rayleigh scattering media, with isotropic propagator and anisotropic scattering mean free path. We obtain anisotropic coherent backscattering cones as a function of the microscopic parameter a that rules the anisotropy of the single-scattering cross-section. The cone profile can be described well with a diffusive model only as far as the top is concerned. The wings show a more complex behavior, which is a consequence of the sensitivity of the penetration length on the incident light state. As further investigation, the Monte Carlo simulation will be extended to include also birefringent light propagation in ordered nematic liquid crystals, and the nematic single scattering cross-section.

Chapter 6

Photonic Bloch oscillations and Fibonacci quasi-crystals

6.1 Introduction

In this thesis, so far we have investigated the optical properties of disordered photonic systems. Light transport has been approached with a random walk model, which describes light propagation in terms of photons performing a random walk in the medium. A diffusive model can be applied with success to isotropic disordered scattering systems, where the isotropic diffuse picture is appropriate. Light interference is a correction to this model, and can be added to the random walk model. Coherent backscattering can be very well predicted and the comparison with the experiment is very satisfactory.

Anisotropic systems can be included in the diffusive model only for special forms of anisotropy, namely those anisotropies that are related only to the direction of the incident light. The most interesting case of anisotropic polarization-dependent scattering, anisotropic polarizability of Rayleigh dipoles, or anisotropic scattering from ordered nematics, cannot be easily included in such a simple model. A random walk model can be generalized to such cases and a Monte Carlo simulation can predict the characteristics of the diffuse light and of the line shape of the coherent backscattering.

The breaking of fundamental symmetries of nature manifests itself in various optical phenomena and is essential for our understanding of the interaction between light and complex matter. The novelties in anisotropic scattering systems lay in the breaking of one or more *symmetries*, i.e. rotation and translation, or polarization independence, typical of the isotropic random medium. These optical systems show that an approach based on the incoherent average of the scattered intensities, as employed so far, is incomplete.

On the other hand, one can think of *ordered systems* as a set of systems which can be modelled directly without an averaged approach, as the correlation in the position of the scatterers cannot be neglected (see Fig. 6.1). The periodicity leads to a cooperative form of scattering with important contributions from all points of the sample. Artificially engineered ordered (periodic) photonic materials are well known as *photonic crystals* where light behaves akin electronic waves in ordinary crystals [20]. Interference effects in this case cannot be regarded as a correction of a diffusive picture, but are

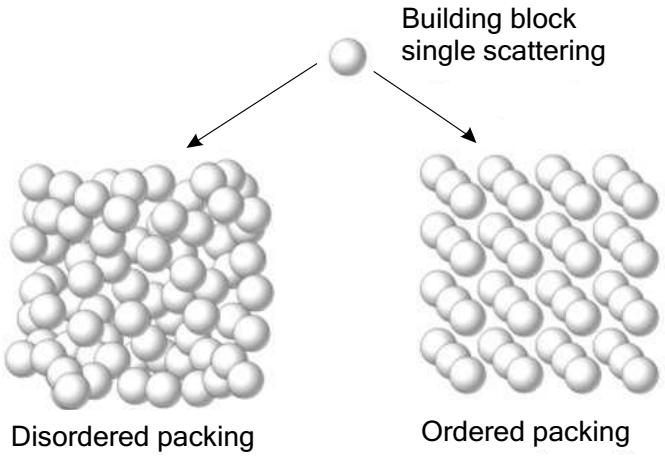

Figure 6.1: Ordered and disordered packing of a single-scattering unit.

instead the main process ruling light propagation.

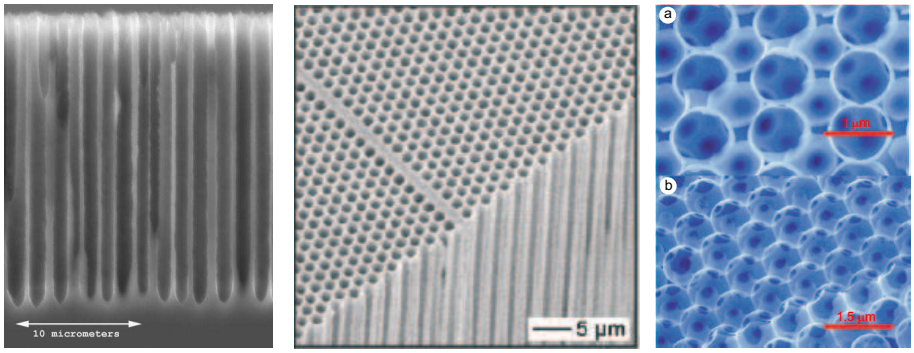

Figure 6.2: (From left to right) One-dimensional photonic crystal: SEM micrograph of the cross sectional view of a porous Si multilayer (courtesy of Luca Dal Negro) [121]; two-dimensional photonic crystal made of porous silicon (courtesy of Kurt Bush [122]). Three-dimensional photonic crystal: SEM images of internal facets of silicon inverse opal: a, (110) facet. b, (111) facet (courtesy of Alvaro Blanco [19]).

Photonic crystal structure can be made assembling in an ordered fashion a unitary element whose dielectric constant is different from the surrounding medium (Fig. 6.1). The advances of techniques like electron lithography, self-assembly, chemical vapor depositions, chemical etching, etc ... have made possible to design and construct one-dimensional, two dimensional and three-dimensional photonic crystals, as shown in Fig. 6.2.

Periodic structures, such as gratings and photonic crystals, offer the possibility to control light propagation. Since reflection from these objects is strongly wavelength sensitive, it can generate iridescent colors of structural origin. Quite recent investigations, however, have also sought to discover photonic band-gap structures in natural

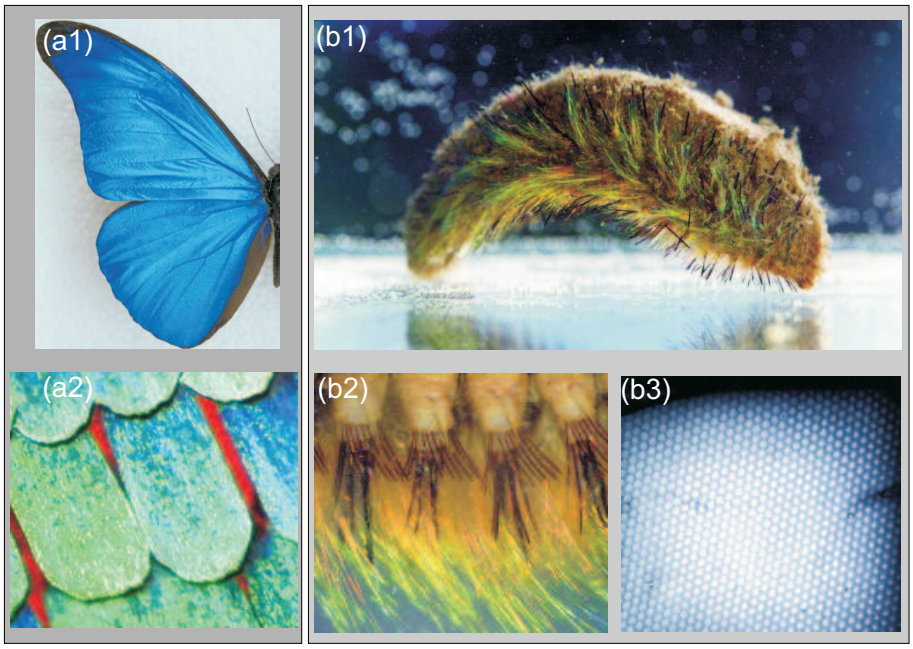

Figure 6.3: Natural photonic crystals. (a1) Iridescence in the butterfly Morpho rhetenor (South America), real color image of the blue iridescence from a Morpho rhetenor wing; (a2) detail of its scales (from [123]). (b1) Sea mouse, (b2) its iridescent threads, (b3) SEM cross-section of a spine (from [125]).

specimens as well, in opals and in some animals, a characteristic that allows them to display gleaming colors, even in the absence of pigments, as for example the colorful speckles of opals, some crystallites on the wings of butterflies and the spine of the sea-mouse [123] (see Fig. 6.3). Many have existed naturally for millennia, yet the sheer physical complexity of these natural systems often renders an accurate representation of their structure extremely difficult [124].

Despite the far-reaching analogies between electronic waves in semiconductors and electromagnetic waves in photonic crystals, there are pronounced differences between the two. Electrons are described by a scalar wavefield. In contrast, the electromagnetic field is vectorial by nature. Furthermore, the time-independent Schrödinger equation allows solutions with negative energy eigenvalues, whereas the corresponding wave equation in electrodynamics (see section 2.7) contains only the square of the eigenfrequencies, hence negative eigenvalues are excluded from the outset: no bound states can exists for photons.

In order to get a complete picture of light propagation in ordered and disordered systems, it is interesting to study also the case of all these families of systems that lie in between these two extremes.

In this second half of the thesis, we will start from the fully ordered case and we will break the periodicity of the ordinary photonic crystal. First, ordered photonic crystals are introduced, and the main results presented; then a linear gradient is introduced in the periodic dielectric constant, in order to break the translational invariance which characterizes the intimate nature of the Bloch states. Photonic Bloch oscillations can

be predicted and experimental evidence of their existence in specially tailored photonic crystals has been provided [26].

Quasi-periodic dielectric systems like Fibonacci quasi-crystals, which lie in between ordered and disordered systems, can also be realized [126] and their interesting time-resolved transport properties will be shown [127].

6.1.1 Tailoring the photonic density of states

Photonic-band-gap materials are a distinct class of dielectrics which favor two fundamentally new optical principles, namely the localization of light and the controllable inhibition of spontaneous emission of light from atoms and molecules [21]. On the other hand, in 3D samples, the possibility of suppressing light propagation for any k-vector could open the way for an omnidirectional reflector.

A complete bandgap entails a complete suppression of the density of states, a modification of the electromagnetic vacuum density of states. A small impurity inside such a photonic band gap material will give rise to a localized mode around this impurity.

It has been recognized for some time that the spontaneous emission by atoms is not necessarily a fixed and immutable property of the coupling between matter and the electromagnetic vacuum, but that it can be controlled by modification of the properties of the radiation field. If a local source is placed in a three-dimensionally periodic dielectric structure which has an electromagnetic band gap, and thus which has zero local density of states, then spontaneous emission can be rigorously forbidden [128]. Rather, a bound photon-atom state is formed [129].

Light localization is also expected in a disordered dielectric medium [130] when

$$\pi^2 c\, \rho(\omega)\, \ell_t^2 \simeq 1. \tag{6.1}$$

Here, c is the speed of light in vacuum, $\rho(\omega)$ is the photon local density of states at frequency ω, and ℓ_t is the transport mean free path for photons, determined by the degree of disorder in the medium. For photons in ordinary vacuum ($\omega = c\,k$),

$$\rho(\omega) = \frac{\omega^2}{\pi^2 c^3} \tag{6.2}$$

and this condition reduces to the Ioffe-Regel condition, $k\ell_t(\omega) \simeq 1$. However, in a photonic crystal, ℓ_t represents the transport mean free path for optical Bloch waves arising from the deviations of the medium from perfect periodicity. The very low density of states near the complete band gap provides a very favorable scenario for the photon localization according to criterion (6.1) even when $k\ell_t(\omega) \gg 1$. Localization in these structures arises from a delicate interplay between order and disorder.

6.2 Ordered systems

So far in this thesis, we have investigated the optical properties of disordered systems. As for disordered media, also for ordered structure the starting point of our approach is the wave equation

$$\left[\nabla \times \nabla \times + \frac{1}{c^2}\,\frac{\partial^2}{\partial t^2}\;\varepsilon\right] \mathcal{E}(\mathbf{r}, t) = 0 \tag{6.3}$$

for the field amplitude

$$\mathcal{E}(\mathbf{r},t) = A\,\boldsymbol{\epsilon}\,e^{i\mathbf{k}\cdot\mathbf{r}}e^{-i\omega t},$$

where $\boldsymbol{\epsilon}$ is the field polarization, ε is the dielectric tensor and c stands for the light velocity in free space:

$$c = \frac{1}{\sqrt{\varepsilon_0\mu_0}}.$$

In section 2.6, for the disordered case, we have replaced the dielectric tensor with

$$\varepsilon = \overline{\varepsilon} + \delta\varepsilon(\mathbf{r},t) \tag{6.4}$$

whose homogeneous part is $\overline{\varepsilon}$, and the randomly fluctuating part $\delta\varepsilon(\mathbf{r},t)$ is a Gaussian random variable described by the correlation function (2.6).

Periodic optical media are materials whose dielectric (and permeability) tensor is a periodic function of $\mathbf{x}$

$$\varepsilon(\mathbf{x}) = \varepsilon(\mathbf{x}+\mathbf{a}) \tag{6.5}$$

which reflects the translational symmetry of the crystal.

The theory of electromagnetic propagation in periodic media has a strong analogy with the theory of electrons in crystals, and thus adopts concepts like Bloch waves, forbidden gaps, evanescent waves, etc... The essential underlying physics is the same in both electronic and photonic case, namely constructive interference that gives rise to Bragg refraction in certain well defined directions or, in the simplest one-dimensional geometry, to Bragg reflection. For these reasons, regular arrays of materials with different refractive index are called photonic crystals.

In 3D periodic media, Eq. (6.5) holds for any $\mathbf{a}$ vector linear combination of the lattice vectors $\mathbf{a}_i$, $\mathbf{a} = \sum_i m_i\mathbf{a}_i$, $\forall m \in \mathbb{Z}$. An obvious difference between ordinary and photonic crystals is the scale of the lattice constant, which is of the order of Angstrom for the former and microns for the latter (and visible light).

The translational symmetry of the medium allows us to take (normal) modes for the field, as

$$\mathcal{E} = \mathcal{E}_{\mathbf{K}}(\mathbf{x})e^{-i\mathbf{K}\cdot\mathbf{x}} \tag{6.6}$$

where

$$\mathcal{E}_{\mathbf{K}}(\mathbf{x}) = \mathcal{E}_{\mathbf{K}}(\mathbf{x}+\mathbf{a}). \tag{6.7}$$

This is the Bloch condition, which enables us to apply a plane-wave-like model to a periodic medium, providing that a new dispersion relation is used:

$$\omega = \omega(\mathbf{K}) \tag{6.8}$$

Electric field in a crystal obeys the Helmotz equation, which is derived from the wave equation in Eq. (6.3) after Fourier transforming with respect to time

$$\left[\nabla\times\nabla\times - \frac{\omega^2}{c^2}\,\varepsilon(\mathbf{x})\right]\mathcal{E}(\mathbf{r}) = 0 \tag{6.9}$$

This equation is usually solved in the reciprocal lattice space, where both the field and the dielectric function can be expanded in Fourier series:

$$\varepsilon(\mathbf{x}) = \sum_{\mathbf{G}} \varepsilon_{\mathbf{G}}\,e^{-i\mathbf{G}\cdot\mathbf{x}} \tag{6.10}$$

with

$$\mathbf{G} = p_x \frac{2\pi}{a_x}\,\widehat{\mathbf{x}} + p_y \frac{2\pi}{a_y}\,\widehat{\mathbf{y}} + p_z \frac{2\pi}{a_z}\,\widehat{\mathbf{z}} \qquad p_i = 0, \pm 1, \pm 2, \ldots \tag{6.11}$$

which are the reciprocal lattice vectors. The electric field can then be expressed as Bloch waves

$$\mathcal{E}(\mathbf{r}) = e^{-i\mathbf{K}\cdot\mathbf{r}}\,\mathcal{E}_{\mathbf{K}}(\mathbf{r}) \tag{6.12}$$

i.e. plane waves modulated by $\mathcal{E}_{\mathbf{K}}(\mathbf{r})$ which is a periodic function of $\mathbf{r}$ with the same periodicity as the potential $\mathcal{E}_{\mathbf{K}}(\mathbf{r}) = \mathcal{E}_{\mathbf{K}}(\mathbf{r} + \mathbf{a})$. If the medium is homogeneous in the x and y direction, and has a periodic modulation in z, then the result is of the form

$$\mathcal{E}(\mathbf{r}) = e^{-i(\mathbf{K}_x x + \mathbf{K}_y y)} e^{-i\mathbf{K}_z z}\,\mathcal{E}_{\mathbf{K}}(z) \tag{6.13}$$

where $\mathcal{E}_{\mathbf{K}}(z)$ is a periodic function of z.

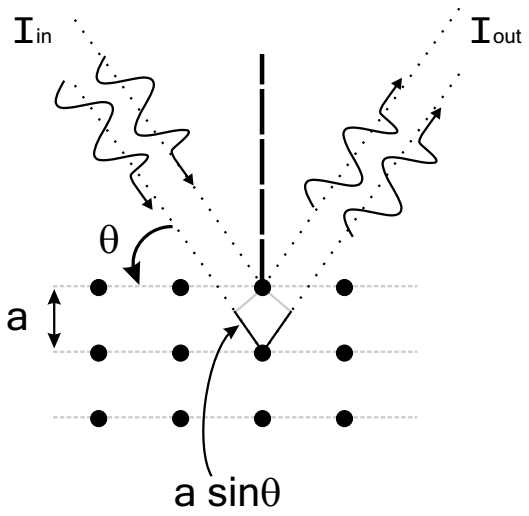

Figure 6.4: Bragg condition for constructive interference in reflection.

The Bloch waves solution of the periodic wave equations are *delocalized*, as they extend over all the crystal: the difference between the field at a lattice point or another is only a phase factor (Eq. (6.12)). The probability of finding a photon in a given position is the same in any point of the lattice. This is the main result of the Bloch theory, both for electrons and photons.

6.2.1 Photonic band structure

The absolute value of these Bloch waves remains finite for all z provided that the wavenumber $\mathbf{K}_z$ is real. This, in turn, is possible only if $\mathbf{K}_z$ falls into one of certain closed intervals on the real axis, which are separated by forbidden zones. There can exist frequency regions where $\mathbf{K}_z$ becomes a complex number with non-zero imaginary part, so that the Bloch wave is evanescent. These are the forbidden bands of the periodic medium: in general light incident within this band will be totally reflected. Intuitively, this refers to the case where a certain $\mathbf{K}_z$ does not satisfy the Bragg condition for

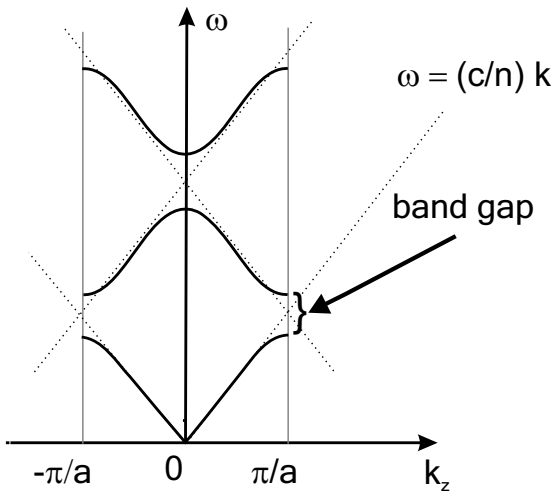

Figure 6.5: Dispersion relation for a 1D photonic crystal (solid line). The boundary of the first Brillouin zone is denoted by two vertical lines. The dispersion in the uniform material is denoted by straight dashed lines. We are plotting the reduced Brillouin zone, as we exploit the periodicity of $\omega(k)$. The various plots in the vertical axis differ from each other by a multiple of $2\pi/a$.

constructive interference, $m\lambda = 2a\sin\theta$, where m is an integer and θ the incidence angle.

The interference between the incident wave scattered at first order with all the following scattering orders is destructive: after a propagation distance of the order of the wavelength the transmitted beam is completely depleted: very efficient reflection occurs. This technique is widely employed to produce high quality reflectors. On the other hand, when the interference is constructive the incident light propagates in the medium with almost no attenuation, as if it was transparent. This are the allowed bands (or pass bands) of the photonic system. Interference plays a central role in light propagation in strongly correlated systems (like ordered structures), where no diffusive model can apply.

The full three-dimensional periodicity of $\lambda/2$ in the refractive index can result in a forbidden gap in the electromagnetic spectrum near the wavelength λ, *regardless of propagation direction*. This a full 3D photonic bandgap. The photonic band structure is evident in the dispersion relation shown in Fig. 6.5. As customary in solid-state physics, the spectrum has been reduced to the fundamental Brillouin zone, ranging from $K_z = -\pi/a$ to $K_z = \pi/a$. This zone coincides with the periodicity interval of the dispersion relations.

The lowest band dispersion can be well approximated with a simple cosine function

$$\omega(K_z) \propto -\cos(K_z a) \tag{6.14}$$

which is characteristic for tight-binding models with interaction among nearest-neighbor lattice site only [131]. Associated with a dispersion relation which deviates from its

value in free space, i.e. $\omega(k) = c/n\,k$, there is a modification of the group velocity and of the density of states. The group velocity, which is

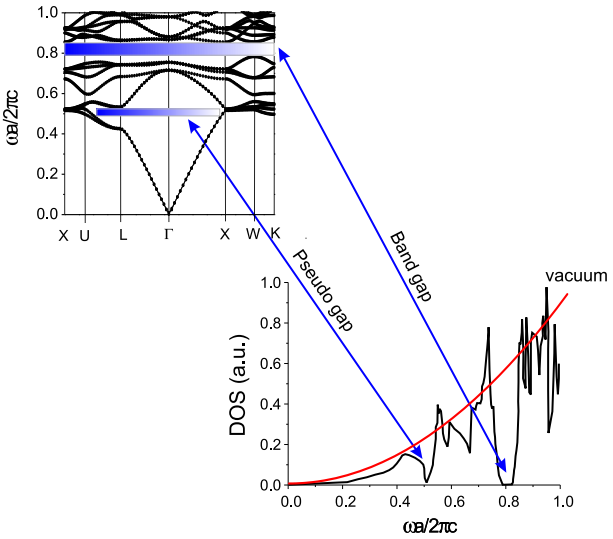

Figure 6.6: Calculated band diagram for a three-dimensional photonic crystal with an FCC structure (panel a). The band gap opens around $\omega a/2\pi c = 0.8$ and a main stop band is present around $\omega a/2\pi c = 0.5$. The density of states (DOS) is shown, note that the DOS is zero in the bandgap and that its behavior is very different from the parabolic one in vacuum. (Courtesy of Sajeev John)

$$v_g(K_z) = \frac{\partial\omega(K_z)}{\partial K_z}, \tag{6.15}$$

is strongly reduced in the vicinity of the bandedges, up to halt of energy transport for k-vectors equal to $\pm m\,\pi/a$, when $v_g(\pm m\,\pi/a) = 0$. In the tight-binding model, this is evident in the explicit expression for v_g, obtained combining Eq. (6.14) and (6.15)

$$v_g(K_z) \propto \sin(K_z a), \tag{6.16}$$

which is zero if $K_z = \pm m\,\pi/a$. In this case a standing wave is formed and no transport can occur.

The density of states $\rho(\omega)$ can be calculated from:

$$\rho(\omega) = \frac{1}{v_g(\omega)}. \tag{6.17}$$

$\rho(\omega)$ diverges at the proximity of the bandedges, where the group velocity tends to zero. Inside a photonic bandgap the group velocity is no longer defined, in general no energy transport occurs and the density of states falls to zero.

6.3 1D photonic crystals

The light transport in photonic crystals is often easier to investigate in one-dimensional (1D) multilayer structures. 1D multilayers can be realized in a very controlled manner

[132, 133] and allow for an exact theoretical description [134]. Ordered dielectric multilayer structures are widely employed as highly reflective Bragg mirrors with limited bandwidth. The introduction of a defect layer turns them into a narrow-band filter with a transmission state within the forbidden band gap.

A 1D photonic crystal is a periodic arrangement of layers of materials with different dielectric constants. Fig. 6.7 shows the intensity distribution inside such a structure as a function of the light k-vector. The plot shows the scattering state map, for ordered (photonic crystal) and disordered (random multilayer) stacking. The scattering

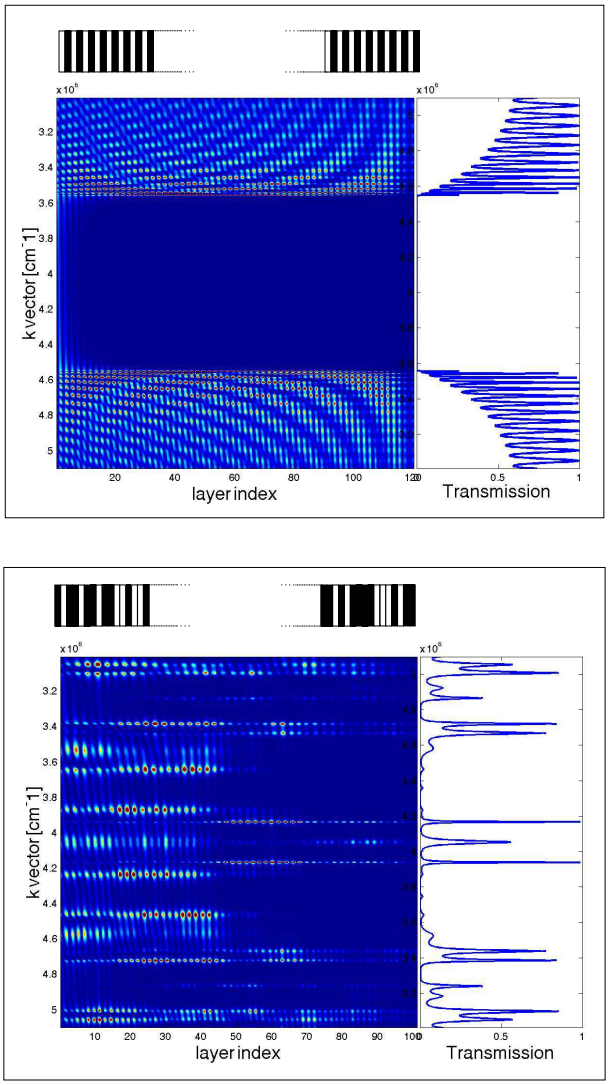

Figure 6.7: Calculated scattering state map for 1D ordered (top) and disordered (bottom) systems. The colorbar refers to the intensity of the field, being red the maximum value and dark blue the minimum. On the right the transmission spectrum is shown. On the top of each panel a sketch of the multilayer structure is shown (dark layers have higher refractive index.)

state map is obtained with a numerical procedure based on transfer matrices, which is explained in section 6.3.1.

On the right hand side of Fig. 6.7, the transmission spectrum is shown. In the top panel, a spectral range with no transmission is visible, which is the 1D photonic bandgap (also called stop-band), as well as spectral windows of high transmission, almost 100%, which are called pass-bands. At the transition frequency from the pass-band and the stop-band, sharp resonances, the bandedge resonances, are visible. These special states extend from the front to the end of the sample, they have a long lifetime and can store much energy.

On the other hand, the random stacking shown in the lower panel in Fig. 6.7 presents many sharp resonant states, which do not necessarily extend over all the structure, which can have very long life-time and which are separated by very weak transmission spectral areas. Counterintuitively, both ordered and disordered dielectrics can be used to decrease locally the density of states and to design high quality reflectors.

6.3.1 Transfer Matrix

Light propagation and interference in multilayer dielectrics, i.e. 1D systems, can be very efficiently described with transfers matrices, which are a well know technique to solve exactly the wave equation, Eq. (6.9) [135]. Because of the linearity of the wave equation, the field at a given point z_0 is related to the field at any other point z by a matrix transformation.

This equivalent to say that we can describe light propagation as a scattering process with an $\mathbf{S}$ matrix as introduced in section 2.1.1. Due to the one-dimensionality of the structure, the S-matrix will be a 2×2 matrix.

We consider light propagation through a film of dielectric material. An incident beam undergoes external reflection, transmission and internal reflections at the plane interfaces that separate the film of refractive index n from external medium at n_0 and the substrate at n_s, as in Fig. 6.8.

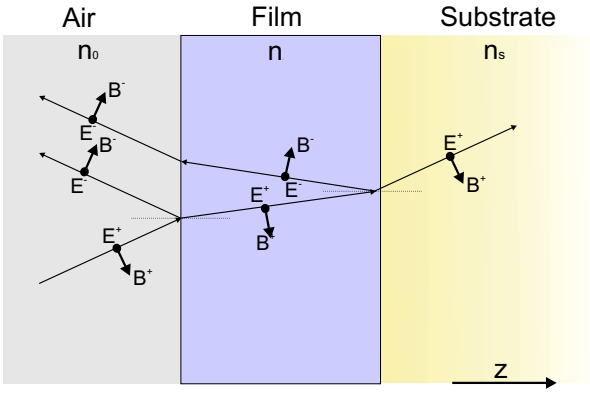

Figure 6.8: Reflection of a wave from a single-layer film.

In the S-matrix formalism, we would consider light states of the form $|\mathbf{k}_\mathrm{i}, \epsilon_\mathrm{i}\rangle$, k-vector and polarization, and the scattered states would be given by the relation

$$|\mathbf{k}_\mathrm{f}, \epsilon_\mathrm{f}\rangle = \mathbf{S}\,|\mathbf{k}_\mathrm{i}, \epsilon_\mathrm{i}\rangle. \tag{6.18}$$

Whereas this representation is convenient for multiple scattering of light from randomly distributed scattering centers, it is not for scattering from a multilayer. In the $|\mathbf{k}, \boldsymbol{\epsilon}\rangle$

representation the propagation between the scatterers is very simple, in the direction of $\mathbf{k}$, but the continuity of the field at the boundary condition is more complicated to be fulfilled, as it is described by the Snell's law. If we instead use a representation on the electric and magnetic field,

$$|E_{\rm f}, B_{\rm f}\rangle = \mathbf{M}\,|E_{\rm i}, B_{\rm i}\rangle, \tag{6.19}$$

the propagation direction of the wave is calculated from $\mathbf{k} \propto \mathbf{E} \times \mathbf{B}$ (each slab is homogenous) but the boundary conditions are very simple, just the continuity of the tangential component of the electric field at the interface (and of the normal component of $\mathbf{B}$). In the following we will follow this second more convenient strategy.

The transfer matrix $\mathbf{M}(z)$

$$\mathbf{M}(z) = \begin{pmatrix} m_{11} & m_{12} \\ m_{21} & m_{22} \end{pmatrix} \tag{6.20}$$

is obtained adding the amplitudes of all the individual reflected or transmitted beams to find the resultant reflectance and transmittance. It is important to take into account also the magnetic field $\mathbf{B}$ in order to determine the propagation direction of the wave.

In the literature, transfer matrices have been defined in various but equivalent ways [136]. We chose as basis of the transfer matrix the total electric (E) and magnetic field (B) (we define the sign of B in this way):

$$\begin{aligned} E(z) &= E^+(z) + E^-(z) \\ B(z) &= B^+(z) + B^-(z) = \gamma(E^+(z) - E^-(z)) \end{aligned} \tag{6.21}$$

where $\gamma = n/c$ at normal incidence, $E^+(z)$ is a plane wave propagating from left to right and $E^-(z)$ for right to left ($k = 2\pi n/\lambda_0$)

$$\begin{aligned} E^+(z) &= E_0 \exp(-ikz) \\ E^-(z) &= E_0 \exp(ikz). \end{aligned} \tag{6.22}$$

If we want to consider oblique incidence, then the two polarization states (TE and TM) are not equivalent, and we have to consider

$$\begin{aligned} \gamma_{\rm TE} &= \frac{n\,\cos\theta}{c} \\ \gamma_{\rm TM} &= \frac{n}{c\,\cos\theta} \end{aligned} \tag{6.23}$$

where θ is the angle of propagation inside the layer, calculated with the Snell's law.

The field at the input surface, defined by the index l (for left), and the field at the output, labelled with r (for right), can be calculated through:

$$\begin{pmatrix} E_l \\ B_l \end{pmatrix} = \mathbf{M} \begin{pmatrix} E_r \\ B_r \end{pmatrix}$$

The special case of the matrix of a single-layer film, is

$$\mathbf{M}_1 = \begin{pmatrix} \cos\delta & i\frac{\sin\delta}{\gamma} \\ i\gamma\sin\delta & \cos\delta \end{pmatrix}$$

where $\delta = k\,n\,d\cos(\theta)$ is the phase acquired upon propagation in a layer of thickness d.

The transfer matrix method can be applied also for absorbing or amplifying media, as it has been recently shown by Artoni *et al.* in ref. [136].

6.3.2 Scattering states

In order to calculate the reflected and transmitted field, we assume that no light is incident from the right, at $z = L$ and that the source light is incident from the left of the structure $z = 0$.

$$\begin{aligned} E^+(z=0) &= E_l^+ = 1 \\ E^-(z=L) &= E_r^- = 0 \end{aligned} \tag{6.24}$$

As a side note, the description here onwards holds only in the classical regime, when no electromagnetic vacuum is considered. Otherwise one should add the vacuum to the boundary conditions, which would make the analysis more complicated.

The transfer matrix of a multilayer made of a sequence of N layers of dielectric and permeability constant ϵ_i, μ_i is just the product of the matrices $\mathbf{M}_i$ of the single i-th layer:

$$\mathbf{M}(z) = \prod_{i=1}^{N} \mathbf{M}_{N-i}(z) = \mathbf{M}_N \cdot \mathbf{M}_{N-1} \cdot \ldots \cdot \mathbf{M}_1 \tag{6.25}$$

Transmission and reflection coefficients for a multilayer of N layers can then be calculate from the full matrix $\mathbf{M}(z)$.

Transfer matrices can provide the unique information of the field distribution inside the multiple-layer film, the *scattering states*. These states provide more information than the total transfer matrix can do, as the latter describes only the overall transmission and reflection of the sample. The knowledge of the scattering states is equivalent to that provided by all the transfer matrices with the correct boundary conditions.

A photon impinging an interface can either be reflected or transmitted. The reflection and transmission coefficient can be calculated from the relation

$$\begin{pmatrix} 1+r \\ \gamma_0(1-r) \end{pmatrix} = \begin{pmatrix} m_{11} & m_{12} \\ m_{21} & m_{22} \end{pmatrix} \begin{pmatrix} t \\ \gamma_s t \end{pmatrix} \tag{6.26}$$

$$r(\omega) = \frac{E_l^-}{E_l^+} = \frac{(m_{11} + m_{12}\gamma_s)\gamma_0 - (m_{21} + m_{22}\gamma_s)}{(m_{11} + m_{12}\gamma_s)\gamma_0 + (m_{21} + m_{22}\gamma_s)} \tag{6.27}$$

$$t(\omega) = \frac{E_r^+}{E_l^+} = \frac{2\gamma_0}{(m_{11} + m_{12}\gamma_s)\gamma_0 + m_{21} + m_{22}\gamma_s} \tag{6.28}$$

where γ_0 is the coefficient of the space on the left of the film and γ_s of the substrate on the right. The transmissivity $\mathcal{T}$ and reflectivity $\mathcal{R}$ (for the intensity) are

$$\mathcal{R} = |r|^2 \qquad\qquad \mathcal{T} = \frac{\gamma_s}{\gamma_0}|t|^2 \tag{6.29}$$

It is possible to obtain the field in each layer of the multilayer, i.e. calculate the scattering states, using the following expression for the fields at the j-th layer

$$\begin{aligned} E_j &= (1+r)m_{22}^j - (1-r)m_{12}^j\gamma_0 \\ B_j &= -(1+r)\, m_{21}^j + (1-r)m_{11}^j\gamma_0 \end{aligned} \tag{6.30}$$

Another possibility is to start from the last layer and go back to the first, in that case the equivalent expression is

$$\begin{aligned} E_j &= t\, m^j_{11} + t\, m^j_{12}\gamma_s \\ B_j &= t\, m^j_{21} + t\, m^j_{22}\gamma_s \end{aligned} \tag{6.31}$$

These formulas comes from the solution of the partial transfer matrix

$$\mathbf{M}^j = \prod_{i=1}^{j} \mathbf{M}_{j-i}(z) \tag{6.32}$$

with the appropriate boundary conditions. We have calculated the field at layer $j = 0$, as $E_0 = 1 + r$. This means that we can invert the relation:

$$\begin{pmatrix} E_0 \\ B_0 \end{pmatrix} = \begin{pmatrix} m^j_{11} & m^j_{12} \\ m^j_{21} & m^j_{22} \end{pmatrix} \begin{pmatrix} E_j \\ B_j \end{pmatrix} \tag{6.33}$$

into

$$\begin{pmatrix} E_j \\ B_j \end{pmatrix} = \begin{pmatrix} +m^j_{22} & -m^j_{12} \\ -m^j_{21} & +m^j_{11} \end{pmatrix} \begin{pmatrix} E_0 \\ B_0 \end{pmatrix} = \begin{pmatrix} +m^j_{22} & -m^j_{12} \\ -m^j_{21} & +m^j_{11} \end{pmatrix} \begin{pmatrix} 1+r \\ \gamma_0(1-r) \end{pmatrix} \tag{6.34}$$

and obtain $E(z,\omega)$, the total field inside the structure, which is also called the *scattering state map* (Eq. (6.30)).

When the multilayer is periodic, with period a, the overall transfer matrix can be calculated with the power of the single cell transfer matrix $\mathcal{M}$ (which can be made of many layers), which is

$$\mathbf{M} = \prod_{i=1}^{N} \mathbf{M}_i(z) = \mathcal{M}^N. \tag{6.35}$$

6.3.3 Time-resolved response

We have calculated so far the amplitudes $t(\omega)$, $r(\omega)$ and $E(z,\omega)$ for each monochromatic wave at ω. We are interested in the propagation of a coherent light beam incident from the left onto the photonic structure. We can describe the light beam by its frequency profile with $Q(\omega)$, which is usually a gaussian. In order to calculate the transmitted light amplitude with phase $T(\omega)$[1], we just multiply $Q(\omega)$ by the transfer function, in the frequency domain:

$$T(\omega) = t(\omega)\, Q(\omega). \tag{6.36}$$

The temporal evolution $T(t)$ of the transmitted light can be obtained by Fourier transform of $T(\omega)$

$$T(t) \propto \int t(\omega)\, Q(\omega)\, e^{i\omega t}\, d\omega. \tag{6.37}$$

The same can be done for the matrix $E(z,\omega)$, which is the field inside the multilayer, Fourier transforming in ω, and obtaining a function $E(z,t)$:

$$E(z,t) \propto \int E(z,\omega)\, Q(\omega)\, e^{i\omega t}\, d\omega. \tag{6.38}$$

[1]Do not confuse the transmitted signal T with the T-matrix which is not employed here.

Transfer matrices allow for a calculation of the light amplitude distribution inside the multilayer and for the temporal propagation of a light pulse incident on the multilayer.

We have calculated the transfer matrix via a simple and flexible numerical code. This method is equivalent to numerical solution of the 1D Maxwell's equations in the multilayer, with the correct boundary conditions.

6.4 Optical microcavities

The importance of one dimensional optical systems lays in the ease of calculating the light propagation in any given structure and the ease of tailoring these multilayers, just changing the sequence of refractive indexes and the optical path of each layer. The only parameters that determine the transmission spectrum are the refractive index contrast (n_j/n_{j+1}) which determines the interface transmission and reflection, in each layer (labelled by j), and the optical thickness $\delta_j = n_j d_j$ of each slab which accounts for the acquired phase $\exp(ik\delta_j)$ and then for the subsequent interference. In other words n_j/n_{j+1} fixes the amplitude and δ_j the phase of the interfering partial waves that participate in the scattering process.

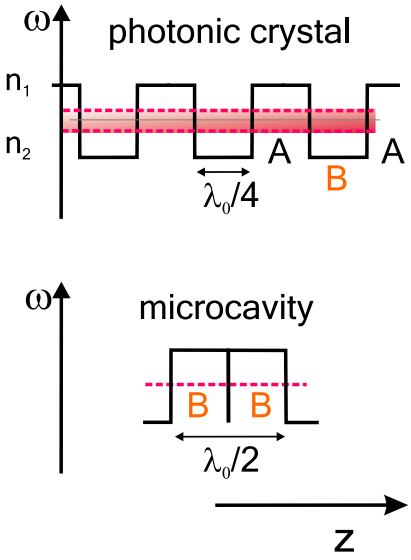

Figure 6.9: In the upper panel a Bragg mirror made of a periodic series of layers, at different refractive indices labelled $ABAB\ldots$, is shown. In the lower panel a microcavity made of two layers BB is presented. An illustration of the spectrum is shown in the vertical axis.

A photonic bandgap is easily obtained with the mirror making technique, with a sequence of layer with the same $\lambda_0/4$ optical thickness and different refractive index. No transmission occurs at the wavelength λ_0, light is efficiently reflected, this is a Bragg mirror (see Fig. 6.9). The physical thickness of each layer was chosen such that the optical thickness $\delta \equiv n \times d$, with n the refractive index and d the physical layer thickness, was equal to $\lambda_0/4$. The choice of quarter-wavelength layers is not crucial, but maximizes the interference, and thus in this way each cavity has the minimum required

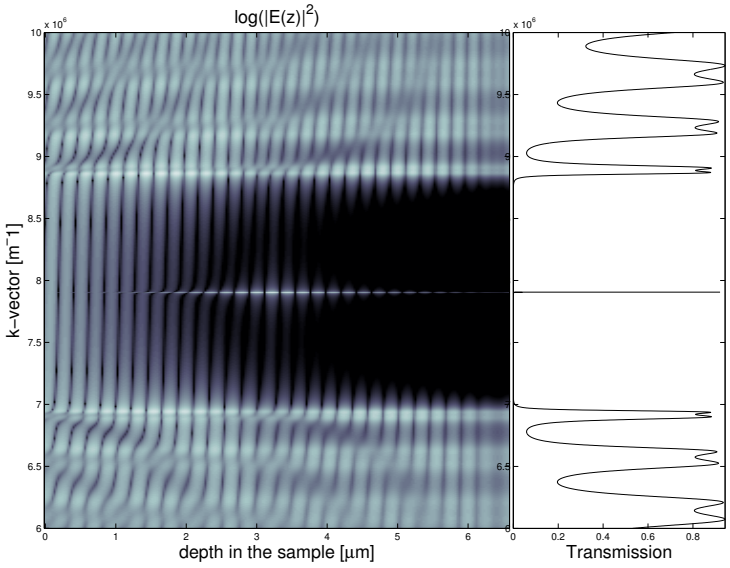

Figure 6.10: (left panel) Scattering state map of a single microcavity made of an extra A layer, surrounded by two Bragg mirrors made of 30 periods AB. Darker areas have a lower intensity. In the middle of the bandgap, the single microcavity is visible. (right panel) The transmissivity of the structure. The two refractive indices are $A = 1.58$ and $B = 2.21$ and the central wavelength is $\lambda = 800$ nm.

thickness to be resonant at λ_0.

If we place a defect state, an extra layer in between two Bragg mirrors, we are constructing a microcavity (see Fig. 6.9). A microcavity is a potential well of optical thickness $\lambda_0/2$ and thus with only one resonant state, at λ_0, in the spectral window of interest. The resonant spectrum of a microcavity is given by the condition that the mode wavelength is an integer sub-multiple of λ_0:

$$\lambda_r = \frac{1}{m}\,\lambda_0 = \frac{2\delta}{m}. \tag{6.39}$$

The scattering state map of a single microcavity presents a single isolated state in a middle of the photonic bandgap, as shown in Fig. 6.10. The state is distributed over the all structure, from the first to the last layer, and the wavefunction has a maximum in the microcavity (which, in photonic crystal context, would be called a defect state). The next resonant state is $\lambda_r = \lambda_0/2$ which is outside the spectral region of interest.

6.4.1 Coupled Microcavities

When two microcavities resonant at $E_1 = hc/\lambda_1$ and $E_2 = hc/\lambda_2$ (h is the Plank constant[2]) are allowed to interact, i.e. when the weak exponential coupling through the Bragg mirrors is not negligible, then the general phenomenon of *avoided crossing* occurs. The effect of a conservative coupling between two degenerate levels is a splitting

[2]For analogy with the electron case we here speak of resonant energy and not frequency, but the results presented are within classical optics.

of their resonance frequency, splitting which is proportional to the strength of the coupling between them.

The energy of the resulting modes (E_+,E_-), for fixed optical coupling energy W_{12}, as a function of the microcavities detuning, is maximum when the two microcavities are degenerate [72]:

$$\begin{aligned} E_+ &= \frac{(E_1+E_2)}{2} + \frac{1}{2}\sqrt{(E_1-E_2)^2+4|W_{12}|^2} \\ E_- &= \frac{(E_1+E_2)}{2} - \frac{1}{2}\sqrt{(E_1-E_2)^2+4|W_{12}|^2} \end{aligned} \tag{6.40}$$

as shown in Fig. 6.11.

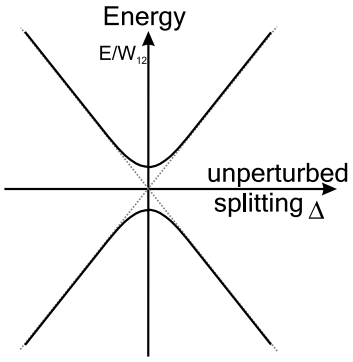

Figure 6.11: Anti-crossing behavior of the energy values of the coupled system as a function of the modal energy separation normalized for W_{12}, $\Delta = (E_1 - E_2)/2W_{12}$.

The splitting of the resonance frequency of two coupled microcavities is visible in the scattering state map, in Fig. 6.12. The structure is *dbr dbr dbr A dbr A dbr dbr dbr*, where the Bragg mirror labelled as *dbr* is made of 10 periods AB. Two sharp frequencies are visible in the middle of the bandgap. The dynamical counterpart of Fig. 6.12 is a resonant tunnelling of the photon which oscillates between the two microcavities. If a short wavepacket of light is incident on the left interface, then it will tunnel into the multilayer, the intensity in the first microcavity will grow, and then it will oscillate between the two cavity sites for resonant tunnelling (see Fig. 6.13).

6.4.2 The optical superlattice

An optical 1D superlattice can be obtained by coupling many identical cavities. This can be achieved stacking together two types A and B of dielectric multilayers with different refractive indices. In particular we used the following sequence: BABABABAB $(AA)_1$ BABABABAB $(AA)_2$ ... $(AA)_{10}$ BABABABAB. This structure is a series of m coupled microcavities $(AA)_m$ where the BABABABAB sub-structure functions as a Bragg reflector. The refractive indices of layers A and B were taken $n_A = 1.4$ and $n_B = 2.1$ to obtain good optical contrast between the layers. The physical thickness of each layer was chosen, as discussed, to be equal to $\lambda/4$. Taking thicknesses that are multiples of d would provide similar results but require growing thicker samples. The optical coupling between the microcavities is tuned by changing the reflectivity of

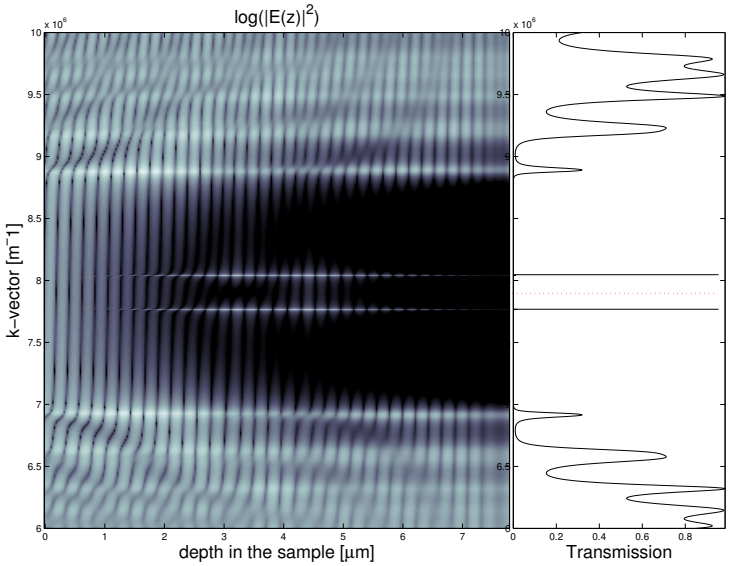

Figure 6.12: (left panel) Scattering state map of a two coupled microcavity whose structure is $dbr\ dbr\ dbr\ A\ dbr\ A\ dbr\ dbr\ dbr$. Darker areas have a lower intensity. In the middle of the bandgap the two splitted resonance frequencies are visible. (right panel) The transmissivity of the structure. The two refractive indexes are $A = 1.58$ and $B = 2.21$ and the central wavelength is $\lambda = 800$ nm.

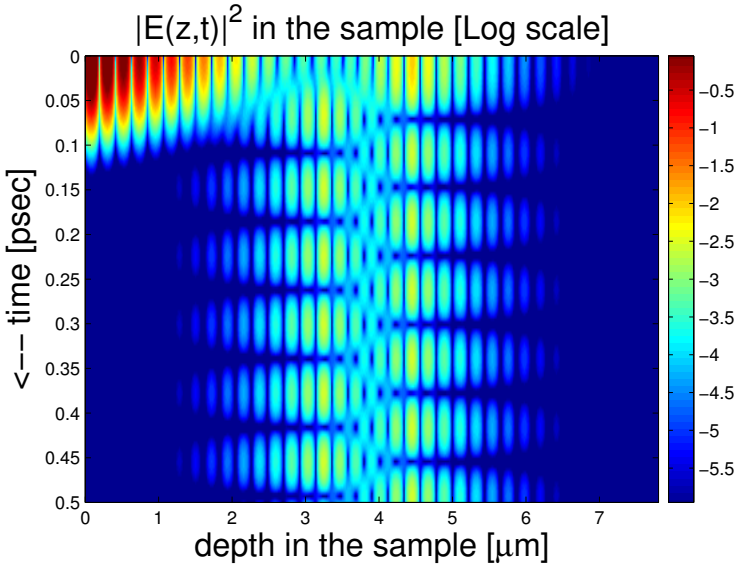

Figure 6.13: Simulated time-resolved response of a short pulse (of 50fs) incident on the two coupled microcavity structure ($dbr\ dbr\ dbr\ A\ dbr\ A\ dbr\ dbr\ dbr$). The wavepacket enters from the left at time equal to zero (top left) and then oscillates for resonant tunnelling between the two microcavities. Darker areas have a lower intensity. The two refractive indexes are $A = 1.58$ and $B = 2.21$ and the central wavelength is $\lambda = 800$ nm.

the Bragg reflectors, and it causes the formation of extended photonic states (optical resonances) in analogy with the electronic coupling of separate quantum wells in a superlattice. When identical microcavities are coupled, degenerate mode repulsion arises (Fig. 6.14). Each degenerate optical resonance splits up and a photonic miniband forms. Due to the periodicity of the structure the photonic minibands are separated by photonic bandgaps in which propagation is prohibited.

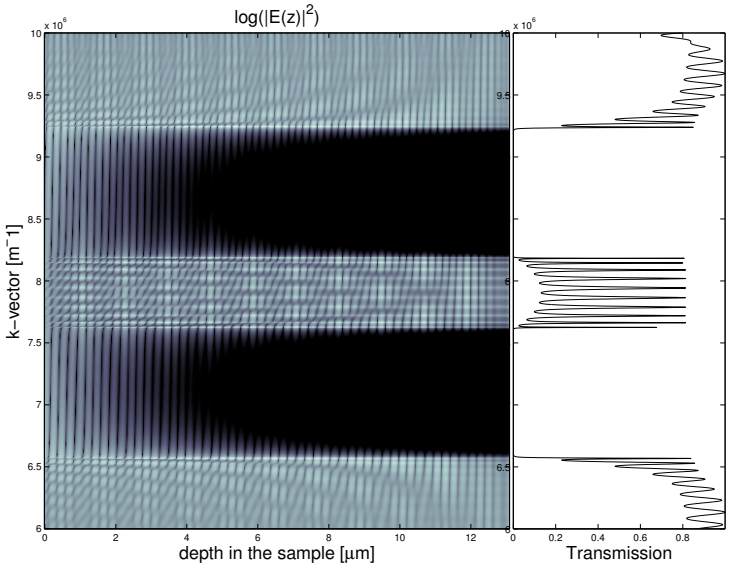

Figure 6.14: Optical superlattice made of 10 coupled microcavities (A) separated by a Bragg mirror with 5 periods AB. A miniband opens. Darker areas have a lower intensity. The two refractive indexes are $A = 1.58$ and $B = 2.21$ and the central wavelength is $\lambda = 800$ nm.

6.4.3 Porous silicon multilayers

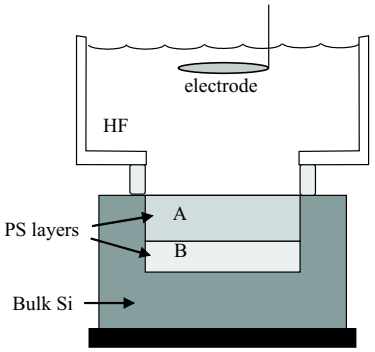

Figure 6.15: Example of formation of a two layer structure etching porous silicon wafers (PS) from bulk silicon (Si). The anodic current is modified and the porosity of the layer changes consequently [121].

The structure described so far can be realized using controlled etching of porous silicon [137, 132] [3]. The refractive index of porous silicon depends on the porosity which in turn depends on the current density used in the electrochemical etch. This allows to produce dielectric multilayers by modulating the current and hence the local porosity during the etching process. The electrochemical etch parameters determine the thickness and refractive index of each layer. We used (100)-oriented p^+-type silicon wafers (resistivity 0.01 Ωcm). The electrolyte was prepared mixing 30 vol.% aqueous HF (48 wt.%) with ethanol. A current density of 50 mA/cm^2 was used to obtain the low refractive index A layers ($n_A = 1.4$, etch duration 5.9 s) and 7 mA/cm^2 for the high refractive index B layers ($n_B = 2.1$, etch duration 21.5 s) (for λ= 1.55 μm). Alternating these two currents in the appropriate way we created samples formed by 10 coupled microcavities as described above, as well as single cavities or modulated aperiodic structures.

Free standing samples were obtained by detaching the sample from the silicon substrate by a high current pulse applied at the end of the etch (400 mA/cm^2, 1 s). The exchange of the electrolyte was improved via etch stops after each layer growth and the use of a magnetic stirrer. Moreover, the natural refractive index drift was compensated by changing the etching times for each layer.

6.5 Breaking the translational symmetry: Photonic Bloch Oscillations

So far we have described the optical properties of ordered photonic structures, which, in analogy with electronics, can be described with delocalized Bloch waves. When the periodicity is broken, this picture is changed and Bloch oscillations can occur. The phenomenon has been first introduced to explain the effect of an electric field on an ideal electronic conductor. We will start from this case, and we will generalize it to the photonic case.

6.5.1 Electronic Bloch Oscillations

A quantum particle in a periodic potential (a crystal) is described by Bloch waves, which are delocalized in space and exhibit an energy spectrum characterized by conduction bands and energy gaps. If such a particle is accelerated by a constant external field, its velocity will increase until it reaches the Brillouin band edge where the energy band dispersion leads to a net reduction of the particle velocity up to an inversion of its sign.

When an external electric field $\mathbf{E}_0$ is added to the crystal picture, from the acceleration theorem [138] the evolution of the crystal momentum can be described as

$$\hbar \frac{\partial \mathbf{K}_z}{\partial t} = e\mathbf{E}_0 \tag{6.41}$$

where e is the electron charge, which means that the crystal momentum distribution will move through k-space at a constant speed, while preserving its shape. In the absence of interband tunnelling (Zener tunnelling) and scattering processes, the time evolution of $\mathbf{K}_z$ is

$$\mathbf{K}_z(t) = \mathbf{K}_z(t_0) + \frac{e}{\hbar}\mathbf{E}_0(t - t_0) \tag{6.42}$$

[3] The etching has been done in the group of Lorenzo Pavesi, University of Trento and INFM, by Mher Ghulinyan and Claudio J. Oton.

The wavepacket describing the electron retains its validity over a time span, in the form of a 'Bloch particle'. The wavepacket group velocity is periodic and has the lattice periodicity (see sec. 6.2.1). This means that the electron will be accelerated up to the end of the first Brillouin zone edge, where its velocity vanishes, and then will turn direction of propagation, with negative velocity, back to its original position. This phenomenon is known as electronic Bloch oscillation [139, 140]. This process is a coherent wavepacket oscillation, with an amplitude equal to Δ_{band}/eE_0, where Δ_{band} is the width of the energy band in which the electrons are moving. The frequency of the electronic Bloch Oscillations is

$$\omega_B = \frac{eE_0 d}{\hbar} \tag{6.43}$$

The phenomenon can be approached also from the band picture. The linear potential tilting effectively bends the energy bands. Energy conservation restricts the allowed space for the electron motion. In unbiased crystals the electron can move freely, without being scattered (translational invariance), but when the bands are bent, it will encounter a band edge which will reflect it, as in Fig. 6.16.

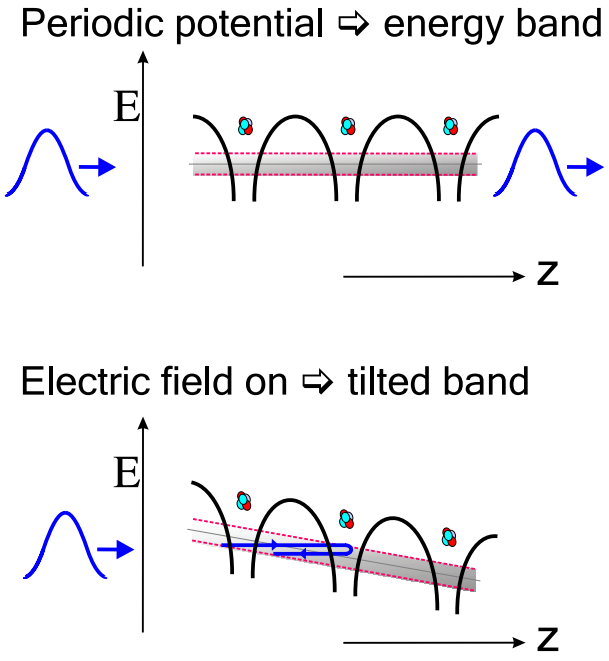

Figure 6.16: Sketch of the electron motion in absence and presence of an external DC electric field.

Bloch oscillations were predicted by Bloch and Zener already in 1928 [139], which lead to several controversies that continued for over 60 years [141]. One of the issues was the counterintuitive result that an external stationary field could lead to an oscillating current. Electronic Bloch oscillations in regular crystals are difficult to observe in practice because electrons loose their coherence on a time-scale much shorter than the expected period of the Bloch oscillations. The remaining incoherent electron transport

is a regular diffusion process described by Ohm's law of conductance. The first confirmation of the Bloch-Zener model came as the observation of a Wannier-Stark ladder in the electron energy bands when an external stationary field was applied [142]. The Wannier-Stark ladder is the frequency domain counterpart of time-resolved Bloch oscillations and consists in the formation of equidistant energy levels. These observations were made possible by the availability of semiconductor superlattices with very narrow bands [143]. The existence of electronic Bloch oscillations was only recently confirmed with time-resolved experiments [144, 145, 146] and it was shown that several oscillation periods can indeed be observed [147, 148].

6.5.2 Bloch Oscillations of matter-waves

Bloch oscillations has been observed also for matter waves, for ultracold cesium atoms in the ground energy band of the potential induced by an optical standing wave [149]. The atoms driven by a constant inertial force are found to perform Bloch oscillations. Bloch oscillations have been experimentally observed also for Bose-Einstein condensates loaded into one-dimensional, off-resonant optical lattices and accelerated by chirping the frequency difference between the two lattice beams. [150].

6.5.3 Optical Bloch Oscillations

The analogies between photons and electrons naturally raises the question whether it is possible to mimic the effect of an electric field in photonic systems and observe the optical counterpart of electronic Bloch oscillations and Zener tunnelling. The role of the electric potential in photonic systems is played by the refractive index as whereas electrons move to minimize the potential energy, photon density is higher in higher refractive index zones.

The optical equivalent of a Wannier-Stark ladder has been discussed theoretically [151, 152] and different photonic systems have been proposed to observe Bloch oscillations of light waves [153, 154]. In pioneering experiments on two-dimensional dielectric systems, spatial Bloch oscillations have been observed [155]. These experiments intrinsically rely on a two-dimensional structure, however, since the light wave follows an oscillatory path in space due to lateral confinement [154]. Optical superlattices have been proposed as a potentially ideal system to observe Bloch oscillations for light waves, using a refractive index gradient *parallel* to the light propagation direction as the optical equivalent of an external force (the static electric field in the electron case) [156].

Bloch oscillations are intimately an effect related to the wave-nature of the quantum particle. This is at the basis of the electron-photon analogy and can be understood easily if one thinks at Bloch oscillations as position-dependent Bragg reflection. This point of view is analogous to the previous description, it is the real space analogue of the crystal momentum picture.

The electron embedded in the crystal, and subjected to the electric field, starts moving towards region at lower potential energy $V_{el} = eE_0 z$, thus conserving the total energy $E_{tot} = E(k) + V_{el}(z)$. When the potential decreases, energy conservation implies that the crystal momentum has to increase. This process goes on up to the point when the de Broglie wavelength associated to the electron matches the lattice wavelength, $2d \sin\theta = n\lambda$, thus leading to Bragg reflection of the wavepacket [157]. The electron

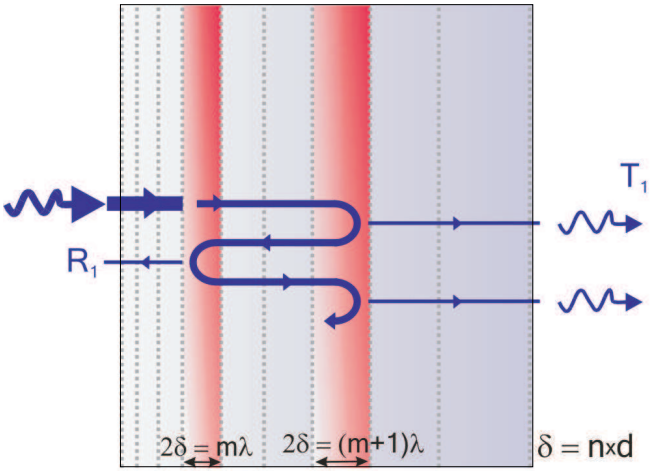

Figure 6.17: Bloch oscillations as position-dependent Bragg reflection. The wavepacket propagates in the multilayer, until a Bragg reflection occurs. Then it propagates backwards, until a new Bragg reflection occurs. It's a Bloch oscillation.

is then pushed towards region at higher potential energy, so its crystal momentum decreases, up to the next Bragg resonance, where it will invert its propagation direction, and so on. The electron orbits are closed, and the oscillation in real space are the Bloch oscillations. Partial translation symmetry implies that there exists a small family of these resonances, the Wannier-Stark ladder, displaced by n lattice-constants and with an energy difference equal to the potential drop per period eE_0d.

This description is perfectly suitable also for light waves, in which the quantum particle is a photon with associated its wavelength, and the role of the electric field is played by linear gradient in the dielectric constant. What is different is only the point of view (Fig. 6.17).

6.5.4 Translational symmetry breaking: the Wannier-Stark ladder

In a perfectly periodic structure, the eigenmodes of the system are the Bloch waves. With superpositions of Bloch waves we can construct Wannier states, which are localized at the atomic sites, but which are not stationary. If the translational invariance is lifted by a potential gradient (as could be an electric field for electronic crystals), then a new set of states exhibits the property of being stationary: the Wannier-Stark states, which are localized but which extend over many lattice sites.

In order to observe Bloch oscillations, the one-dimensional translational symmetry of the system has to be broken. This is done by introducing a gradient in the optical thickness of the layers, that we express with $\Delta\delta = (\delta_{z_m} - \delta_{z_1})/\delta_{z_1}$. This gradient is the optical counterpart of the external electric field used in electronic superlattices. The small gradient in the optical thickness changes slightly the resonance of each microcavity while preserving the mode coupling, which results in a spatial tilting of the minibands and the photonic bandgaps. In this way, the extended photonic states are turned into a discrete sequence of energy levels with level spacing ΔE_B, which is the optical equivalent of the Wannier-Stark ladder.

This strategy encounters the problem of the finite size of the samples we can grow. While in electron systems the crystal extends over many periods, can always be considered infinite, and the application of an external field is a very easy experimental task, in optical systems these two essential ingredients are much harder to handle. We have to cope with finite-size samples, and with a small range of available optical drift.

For these reasons we have to resort to a way to tilt the optical band within the sample size. The many efforts that have been done to observe electronic Bloch oscillations provide us with a winning strategy: if a miniband is designed in the structure, then a much smaller drift can be enough to tilt it. In electronic systems this idea has been exploited to decrease the period of the Bloch oscillations, to make it shorter than the decoherence time of electron waves. For different reasons, we are lead to grow samples conceptually analogous. The drawback of a superlattice is that it presents partially-discrete states even in absence of optical drift (see Fig. 6.18). Bloch oscillations can occur only if the level splitting induced by the optical drift is bigger than the finite-size effect. Only in this case we can consider the miniband as continuous and apply the Bloch theory. For drifts smaller than a certain value, as we will see later, the continuum approximation does not hold and the light transport is dominated by front-end reflections.

Transfer matrix calculations can be used conveniently to calculate the scattering state maps of the light distribution inside our system. In Fig. 6.18, the light intensity distribution is compared for the two cases $\Delta\delta = 0$ and 14%. The linear gradient in the optical thickness induces, to first order, a linear miniband tilting. The resonance of the first microcavity is given by: $E(z_1) = hc/2\delta_{z_1}$ with c the vacuum velocity of light. The variation of the resonance energy from layer 1 to layer m is $\Delta E(z_1, z_m) = E(z_1) - E(z_m)$ and can be written in terms of the gradient as:

$$\frac{\Delta E(z_1, z_m)}{E(z_1)} = \frac{1}{1 + \Delta\delta} - 1. \tag{6.44}$$

This describes a linear tilt and compression of the band. For a narrow miniband, $E(z_1)$ can be considered constant within the band and the Wannier-Stark states are equidistant. In Fig. 6.18b one can clearly see how the miniband (between the white dashed lines) and surrounding photonic bandgaps (dark regions) are tilted. The Wannier-Stark states are visible as bright horizontal lines that extend between the two tilted photonic bandgaps. Such a system is expected to exhibit optical Bloch oscillations of period $T_B = h/\Delta E_B$ (h is the Planck constant).

6.5.5 Transmission spectra: probing the Wannier-Stark ladder

Transmission spectra of the photonic structure are very precious information, but very high resolution is required to resolve the Wannier-Stark states. An ordinary spectrometer signal is a trade off between spectral resolution, which demands very closed slits at the monochromator, and enough light at the detector, which on the contrary is favored by wide open slits. For this reason we decided to opt also for a high resolution setup, in which no monochromator is present, as a narrow-band tunable laser source acts as the almost monochromatic probe (see Fig. 6.19). Tuning its frequency and measuring the transmitted intensity we can reconstruct the transmission spectrum of the sample.

A NetTest TUNICS-BT 1560 IR tunable laser in the wavelength range from 1500 to 1610 nm was coupled to a multimode fiber of 115 μm diameter (Fig. 6.19). We

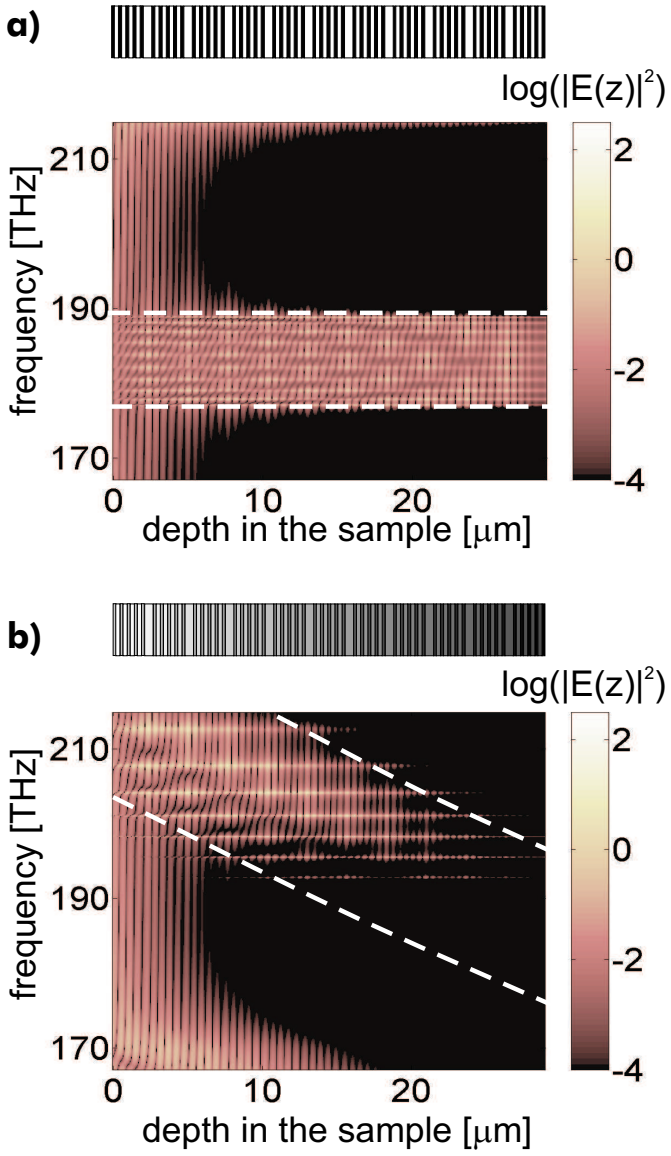

Figure 6.18: Scattering state calculation of the distribution of the energy spectrum inside an optical superlattice composed of 10 coupled microcavities. The parameters used in the calculations correspond to samples used in the actual experiment. Panel a) flat band situation, $\Delta\delta = 0$. Panel b) tilted band situation, $\Delta\delta = 14\%$. The dashed lines indicate the theoretical tilting of the miniband as obtained from Eq. 6.44. Above each panel the coupled microcavity structure is schematically shown; the gray scale refers to the refractive index variation along the depth in the sample (the darker the larger n).

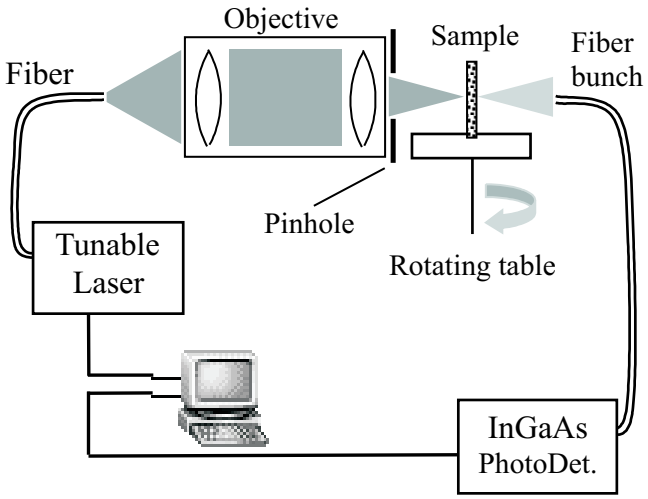

Figure 6.19: High resolution setup built in Trento by Claudio Oton, for the fine transmission spectra.

used a microscope 25x objective to focalize the laser beam in a spot of 35 μm diameter on the sample surface. This way, we were able to illuminate a very small area on the sample, thus highly reducing the broadening of peaks due to lateral inhomogeneities. A 1 mm diameter pinhole was placed just after the objective in order to reduce the numerical aperture of the input light. A fiber bunch was placed far from the sample ($\sim$15-20 cm) which allowed the collection of the signal with a very small numerical aperture ($\sim$0.0075). An InGaAs detector coupled to the fiber bunch was used to measure the transmitted intensity. The sample was mounted on a rotating table to carry out angle-dependent transmission measurements. The tunable laser, rotating table and an InGaAs photodetector were interface-controlled through a computer. The transmission spectra are normalized with respect to the signal recorded without the sample. The high resolution setup is able to resolve perfectly a peak of less than half a nanometer width.

In Fig. 6.20 we report the transmission spectrum of a multilayer sample with optical thickness gradient $\Delta\delta = 10$ %. One can clearly see the occurrence of the Wannier-Stark ladder as a series of narrow (2 nm of full width at half maximum and 15 nm spaced) transmission peaks.

6.5.6 The porous silicon optical superlattice

The samples were realized using controlled etching of porous silicon as described in section 6.4.3, for a central wavelength of λ= 1.55 μm. We created samples formed by 10 coupled microcavities, the total sample consisted of 110 layers. The duration of the etch stops controls the refractive index gradient and hence the variation $\Delta\delta$ in the optical thickness of each layer. We were able to control the optical thickness producing samples with different gradients in the range from $\Delta\delta = 2$ to 14 %. The limits are set by the two extremes: almost bulk silicon, with the minimum amount of pores to allow further etching, which has a maximum refractive index of 2.4, and the opposite one,

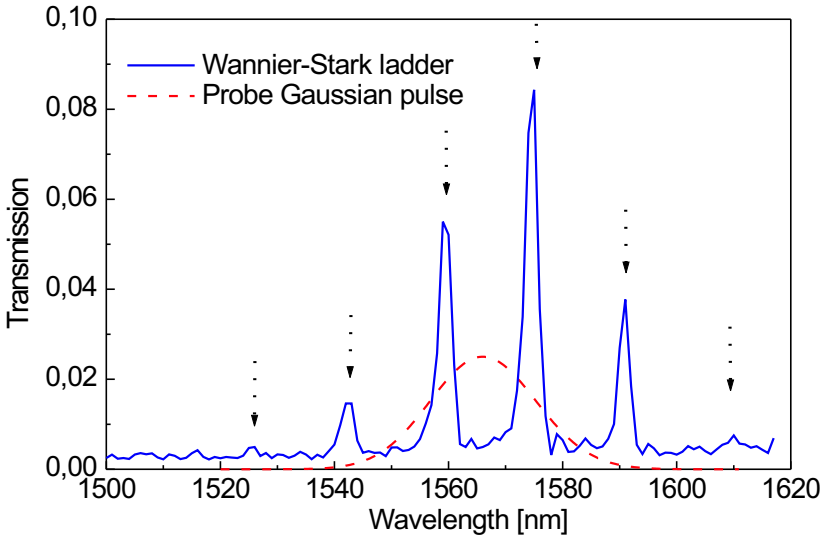

Figure 6.20: Transmission spectrum of a sample with gradient $\Delta\delta = 10\%$. The optical equivalent of the Wannier-Stark ladder is seen as a series of equidistant transmission peaks. The arrows refer to the expected spectral positions of the transmission peaks obtained by transfer matrix calculations. The dashed line is the wavelength profile of the incident Gaussian laser pulse used to perform the time-resolved measurements.

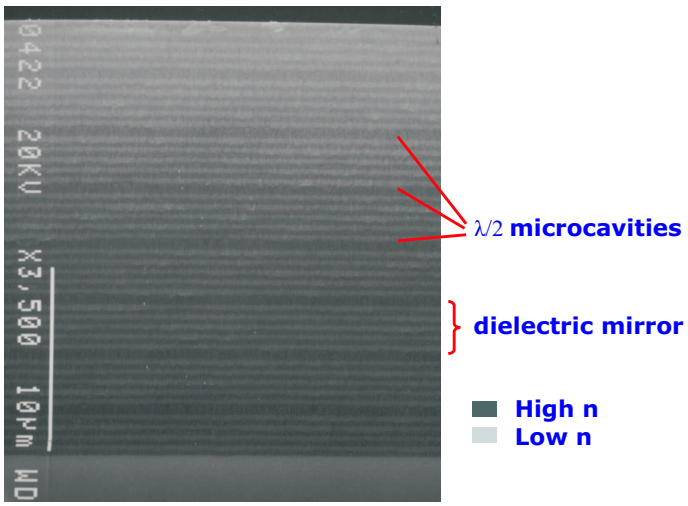

Figure 6.21: SEM picture of an optical superlattice made of 10 coupled microcavities (in collaboration with Mher Ghulinyan.)

almost only air, with the minimum amount of porous silicon to sustain the structure, which has refractive index 1.3-1.4. Fig. 6.21 is a SEM picture of the optical superlattice that was grown in Trento. The optical microcavities are shown.

In Fig. 6.22 transmission spectra from optical superlattices at different optical thick-

ness gradient $\Delta\delta$ are shown. The higher the gradient, the further apart the Wannier-Stark states are, as predicted by Eq. (6.44).

6.6 Time resolved spectroscopy with nonlinear optical gating

Spectral measurements, as shown in Fig. 6.22, are essential in characterizing the photonic structure grown, probing the amplitude of the transmitted light at different wavelengths, but they lack the information about the phase of the electric field. Time resolved measurements on the contrary add the precious knowledge of light propagation in the multilayer. A gaussian pulse incident on an homogeneous structure with wavelength independent transmission, like a constant refractive index layer, will be transmitted preserving its shape; if the same pulse encounters sharp resonances and bandgaps it experiences delays due to multiple reflection and deformations of its envelope due to resonances and beatings (group velocity dispersion).

6.6.1 Time-resolved setup

The time-resolution which is required to observe photonic Bloch oscillations, which have an estimate period of 500 fs, is out of reach for fast detectors (a fast-photodiode is limited by a ns-resolution, a streak camera cannot go beyond few picoseconds) or electronic shutters. We need to resort to a different strategy. Can we use a slow detector, and sample the time? In other words, can we take a slow measure with a very short time window? Observing this time-frames, one after the other, would be like watching a movie of the phenomenon, which reconstructs the time-evolution. This can be achieved with a technique which has been widely employed in the chemistry of ultra-fast reaction [158] and which translate the problem of resolving tens of fs into tens of μm, via the space-time relation $x = ct$ (for light in vacuum 10 fs correspond to 3 μm). Ordinary translation stages can easily move with an accuracy better then 1 μm, as the one mounted in the delay line of our the setup, Fig. 6.23.

In order to perform time-resolved transmission experiments, an optical gating technique has been applied. This involves mixing a reference beam together with the transmitted signal beam in a 0.3 mm thick non-linear BBO (beta barium borate) crystal to produce a sum frequency signal. This is a well-known non-linear phenomenon [159] which can act as an optical gating.

In the process of sum-frequency generation, the laser beams at ω_1 and ω_2 interact in a nonlinear crystal and generate a nonlinear polarization $\mathbf{P}^{(2)}(\omega_3 = \omega_1 + \omega_2)$, which is a collection of oscillating dipoles, and that acts as a source of radiation at $\omega_3 = \omega_1 + \omega_2$. In principle, the radiation can be emitted in every direction, but the phase-coherence between the waves determines a strongly peaked output in a certain direction. This can be determined by the phase-matching conditions as to effectively transfer energy from the pump waves at ω_1 and ω_2, both momentum and energy must be conserved. The energy conservation requires that $\omega_3 = \omega_1 + \omega_2$, while the momentum conservations $\mathbf{k}_3 = \mathbf{k}_1 + \mathbf{k}_2$. The latter condition implies that efficient non-linear conversion can be obtained only if the mixed waves are in phase during their propagation in the crystal. We have chosen the $o - o \rightarrow e$ phase-matching configuration, in which two ordinary waves are mixed to generate an extraordinary one. The mixed waves have the same polarization, and the sum-frequency radiation is polarized in the orthogonal direction.

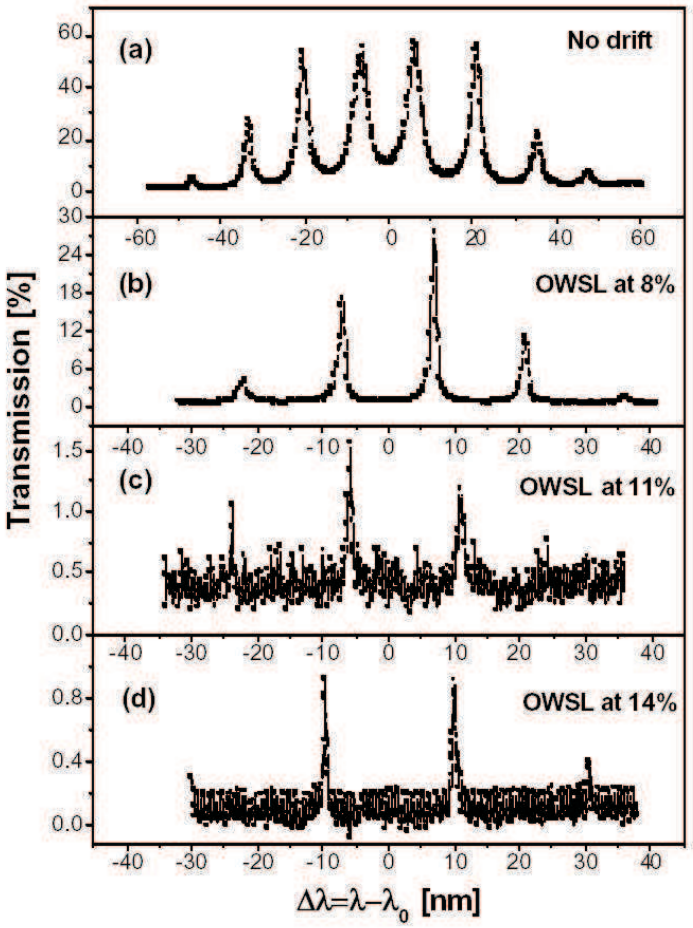

Figure 6.22: High resolution transmission spectra of different coupled microcavities structures with different gradients of the optical thickness of the layers (0 = 1.55 m is the central wavelength). The top spectrum corresponds to the non drifted sample, with thickness compensation. The others (b), (c) and (d) show 8%, 11% and 14% drifts. As drift increases, the optical Wannier-Stark ladder (OWSL) forms, and is observable as equidistant narrow transmission peaks

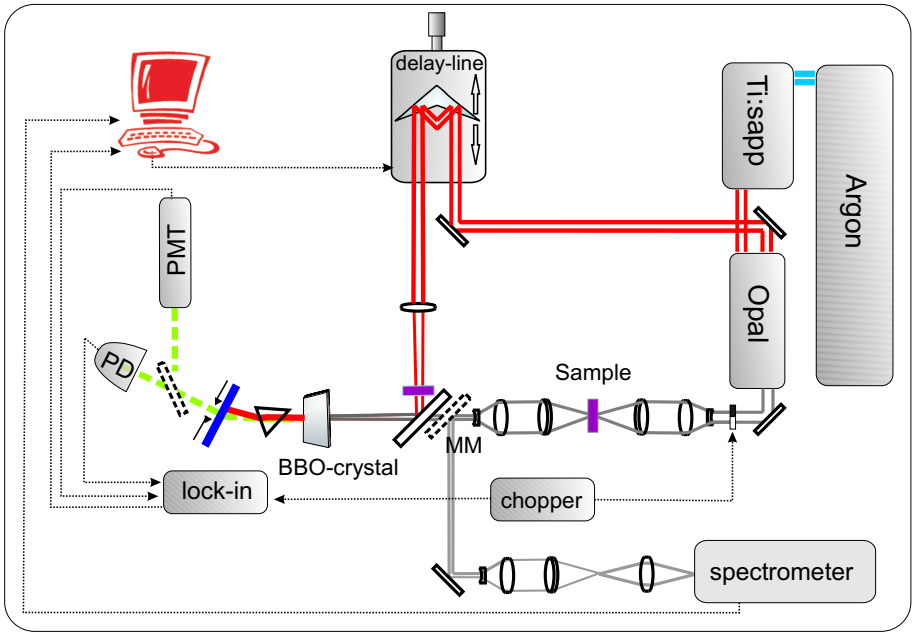

Figure 6.23: Setup build for the time-resolved measurements. Originated from the laser sources on the right, the Opal light is sharply focussed on the sample. After the sample, the signal is collected and sent to the spectrometer or to the BBO-crystal for mixing with the residual Ti-Sapphire light. The sum-frequency signal is collected by a photodiode and filtered by a lock-in amplifier.

The phase-matching condition, turns into a relation between the refractive indexes n_e and n_o, that the waves experience in the material:

$$\mathbf{k}_{e3}(\vartheta) = \mathbf{k}_{o1} + \mathbf{k}_{o2} \tag{6.45}$$

or

$$n_e(\omega_3)\omega_3 = n_o(\omega_1)\omega_1 + n_o(\omega_2)\omega_2 \tag{6.46}$$

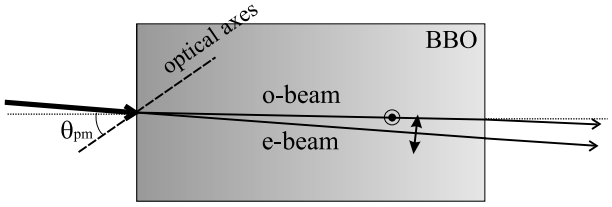

Figure 6.24: Propagation of the ordinary and extraordinary beam in a BBO crystal, cut at the phase-matching angle θ_{pm}.

Phase-matching cannot be fulfilled in a normally dispersive medium, as the refractive index is a monotone function of the wavelength. The most common ways to overcome the problem are *temperature tuning* and the use of *birefringency*. β-BBO (β-Barium Borate, $\beta-BaB_2O_4$) is a birefringent crystal, which combine unusually wide

transparency, high non-linear parameters ($\chi^{(2)}$), easy phase-matching (angular tuning), low agroscopicity and high threshold damage, wide temperature bandwidth and excellent optical homogeneity. Phase-matching is obtained changing the angle between light propagation and the optical axes (Fig. 6.24), as the extraordinary refractive index is angle-dependent, Eq. (6.47), and so it can be tuned to satisfy Eq. (6.46).

$$n_e(\vartheta) = \frac{n_o n_e}{\sqrt{n_e^2 \cos^2 \vartheta + n_o^2 \sin^2 \vartheta}} \tag{6.47}$$

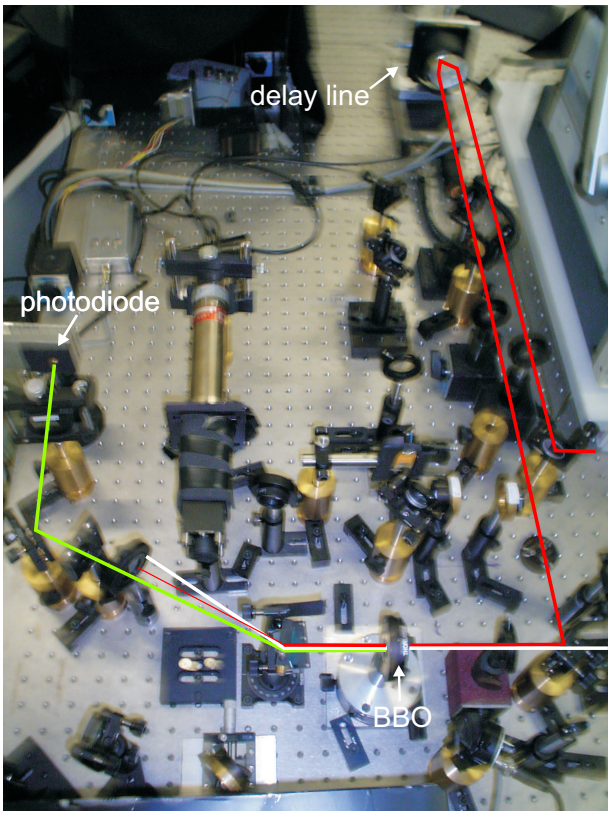

Figure 6.25: Photo of the non-linear part of the time-resolved setup as shown in Fig. 6.23.

The optical gating technique lays its bases in the fact that the efficiency of the non-linear process is strongly dependent on the overlapping between the pump and the signal waves, both in space and in time. The time-evolution is obtained changing the pump-signal delay and measuring the up-conversion efficiency. The intensity of the generated signal at ω_3 is proportional to the correlation function between the pump and the probe pulse intensities,

$$I_{\omega_3}(t) \propto \int I_{\omega_1}(t-\tau) I_{\omega_2}(t) d\tau. \tag{6.48}$$

A delay line on the reference beam path allows to tune the time delay between signal and reference, and thus the longitudinal spatial overlapping (see Fig. 6.25). This technique allows for measuring in a time window equal to the pulse duration, 130

fs. The constant time profile of the generated signal at 510-540 nm allows for a time resolution of less than 100 fs. The probe beam is obtained from an optical parametric oscillator (called OPAL) pumped by a Ti:Sapphire laser at center wavelength 810 nm (pulse duration 130 fs, average power 2.0 W, repetition rate 82 MHz) yielding short pulses tunable from 1300 to 1600 nm (average power 100 mW). The reference pulse at 810 nm is obtained from the residual Ti:sapphire beam (450 mW average power). The sum frequency signal is detected by a photodiode and a standard lock-in technique is used to suppress noise.

Due to possible sample inhomogeneities, what one would like to do is to check the spectral response of the multilayer in-situ, on the $30-50\mu$m diameter spot illuminated on the sample. The apparatus is designed such that also the transmission spectrum of the sample can be monitored during the time-resolved measurement, by sampling a fraction of the transmitted light via the kinematic mirror which couples the signal beam to a spectrometer (see Fig. 6.23).

6.6.2 The time-resolved Bloch oscillations

In the top panel of Fig. 6.26, we plot the system response without sample from which we determine the temporal response to be about 250 fs.

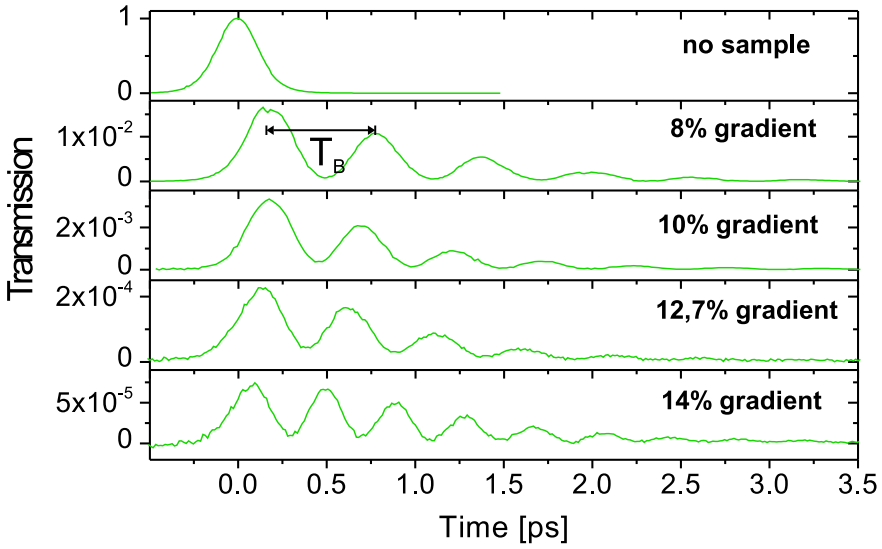

Figure 6.26: Temporal response of the system for various values of the gradient $\Delta\delta$. The observed oscillations are the optical counterpart of time-resolved Bloch oscillations. The period of the oscillations decreases while increasing $\Delta\delta$, and the transmission decreases. The top panel reports the undisturbed probe pulse without sample.

Fig. 6.26 shows a series of time-resolved transmission measurements for various values of the gradient $\Delta\delta$. Our transfer matrix calculations predict that above $\Delta\delta \approx 7\%$, a Wannier-Stark ladder is formed in our samples. From the time-resolved data we can observe that indeed oscillations occur in transmission. More than 8 periodic

oscillations are observed in the transmitted intensity, with a period T_B that decreases as $\Delta\delta$ increases. In addition, as the gradient increases the transmitted intensity decreases which can be understood from the increased tilt of the bandgap (see also Fig. 6.18). The oscillations are damped with a characteristic time τ_B.

6.6.3 Period and decay time of the Bloch oscillations

The main parameter ruling the dynamics of Bloch oscillations is the oscillation period T_B. In Fig. 6.27 we compare the measured T_B with the one extracted from our trans-

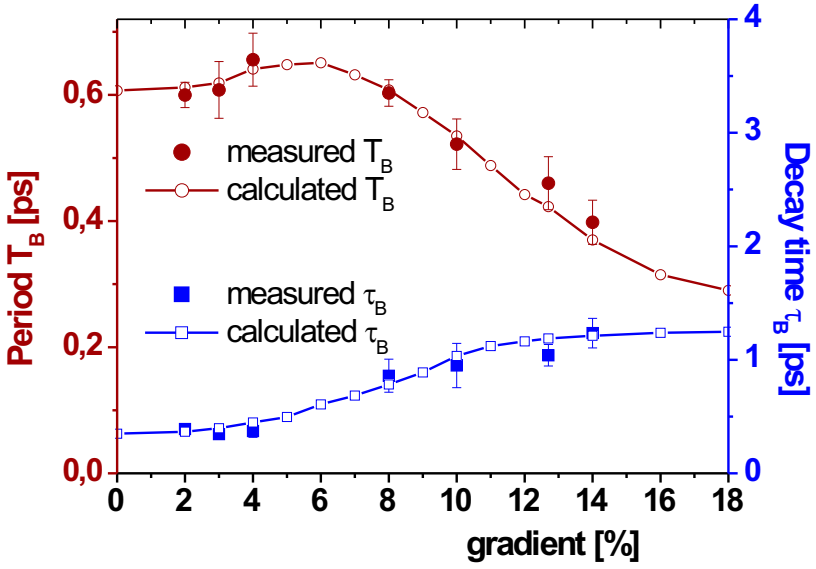

Figure 6.27: Experimentally observed oscillation period T_B and decay time τ_B as a function of the gradient $\Delta\delta$. The error bars are the standard deviations obtained from various measurements on several positions on the sample and represent therefore the effect of lateral sample inhomogeneities. The solid line is the predicted behavior from transfer matrix calculations.

fer matrix model for various values of the gradient. As expected, the experimentally observed values of T_B decrease while increasing $\Delta\delta$ because the miniband tilting gets steeper. The period depends only on the relative energy tilting from the front to the end of the sample and not on the sample thickness. Below $\Delta\delta \approx 7\%$ the increase of T_B saturates. Here the optical thickness gradient is not enough to fully tilt the miniband within the sample thickness and the remaining oscillations are simply due to internal reflection at the sample boundaries. In this regime the residual variation in T_B of a few percent is due to a decrease in the optical coupling between the microcavities. The experimental data are in very good agreement with the calculated theoretical dependence of T_B on optical thickness gradient (solid line).

Another interesting observation in Fig. 6.27 is that the decay time τ_B by which the oscillations are damped increases when $\Delta\delta$ increases. This is a direct consequence of the increased confinement of the optical modes in the Wannier-Stark ladder. As the

Wannier-Stark ladder gets steeper the reflection at the bandedge becomes more efficient and the transmission losses decrease accordingly. At large gradient values, τ_B saturates to about 1.2 ps. This saturation is caused by scattering and residual absorption losses in the porous silicon sample. Hence the total decay time τ_B can be written as

$$\tau_B = (\tau_{BO}^{-1} + \tau_{ext}^{-1})^{-1}, \tag{6.49}$$

where τ_{BO} is the intrinsic decay time of the Bloch oscillation as due to the release of energy from the system and τ_{ext} is the extinction time due to absorption and scattering losses. The solid line in Fig. 6.27 is obtained by taking $\tau_{ext} \sim 1.3$ ps which corresponds to an extinction coefficient (absorption + scattering) of $\alpha_{ext} \sim 100$ cm^{-1}, in agreement with previously determined loss values [132].

6.6.4 Zener tunnelling

For completeness it is worth to mention the optical analogue of electronic Zener tunnelling [160] that our group has recently resolved in time [161]. When the linear gradient is strong enough, two minibands can overlap and Zener tunnelling can occur between them, in analogy with the Zener breakdown in semiconductors. The expected behavior of the system, obtained via the transfer matrix model is in very good agreement with experimental observations [161].

6.7 Fibonacci quasi-crystals

Quasicrystals are a novel form of solids, which show very high structural order, nevertheless they do not possess periodicity as ordinary crystals do.

They were discovered [162] in 1984, being revealed by a rotational symmetry of X-ray or electron diffraction patterns (for instance, five-fold or ten-fold) which is impossible for true periodic crystals. As an example we have shown a diffraction pattern from a quasi-crystal in chapter 3, in Fig. 3.5. The class of *quasicrystals* belongs to the intermediate regime between periodic and random [27]. In these deterministic non-periodic structures, translational order is absent. Ten years before their discovery in nature, quasiperiodic patterns with the same geometric properties as those calculated from five-dimensional hyperspace were described by Roger Penrose [163]. Photonic quasicrystals are very interesting as they show features of the periodic systems, while reducing the orientational order so that the systems are more isotropic. The presence of high symmetries make easier the occurrence of a complete photonic bandgap for all directions, and allows for structures which are more robust against imperfections and disorder.

An important class of deterministic aperiodic structures is represented by the Fibonacci binary quasicrystals [164]. It has been the subject of an extensive theoretical and experimental effort in the last two decades [164, 165]. The Fibonacci structure is realized by stacking two different dielectric layers accordingly to the simple Fibonacci generation rule

$$\mathrm{F}_m = \mathrm{F}_{m-1}\,\mathrm{F}_{m-2}. \tag{6.50}$$

In 1985, Merlin *et al.* reported the first realization of Fibonacci quasicrystals [166]. It has been shown that the transmission spectrum of the Fibonacci system consists of

a rich fractal (self-similar) structure of narrow modes separated by numerous band-gap regions with almost zero density of modes, called "pseudo band-gaps", despite the global structure is not periodic, analogous to the forbidden regions in periodic media [167, 168] (see Fig. 6.28). This has been confirmed by various authors [168, 169]. The pseudo-band gaps are a consequence of the multifractal nature of the Fibonacci quasiperiodic order. Moreover, the states outside the bandgap are critically localized, with the electric field profile decaying slower than exponentially [170, 171].

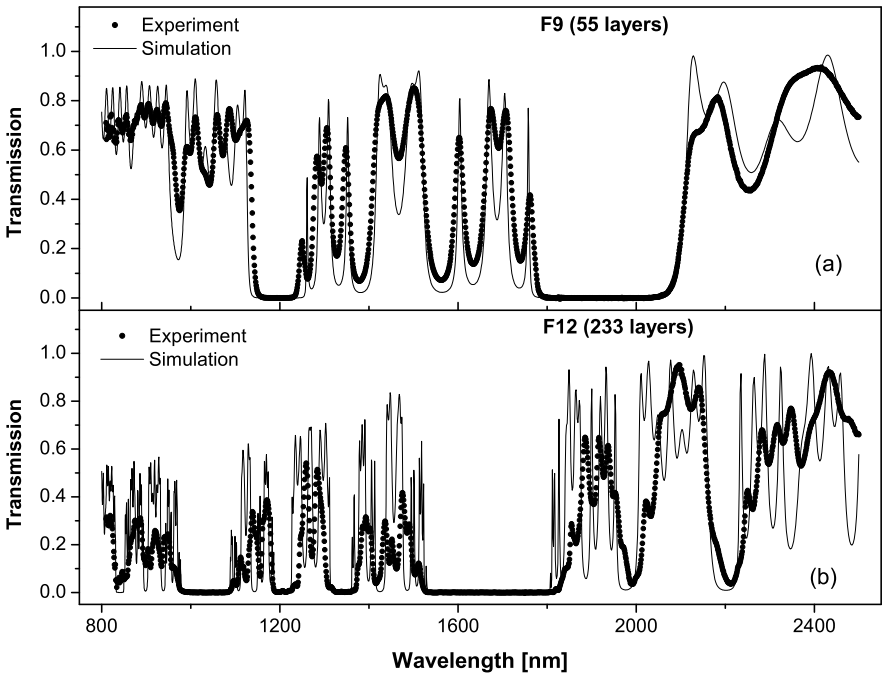

Figure 6.28: Transmission spectra of Fibonacci samples F_9 (a) and F_{12} (b). The solid lines are the results of a transfer-matrix calculation assuming optical path drifts of 1% (for F_9) and 4% (for F_{12}) and optical losses (scattering losses) of $\alpha \sim 120$ cm^{-1}. The dots denote the measured spectra.

Many peculiar and fascinating phenomena, as self-similar wave functions [172], are directly related to the wave propagation in self-similar (fractal) media. Here we focus on spatial field localization (field enhancement) and light localization, which not only characterize finite size periodic structures but have been theoretically predicted also for aperiodic fractal structures such as those realized with the Fibonacci or Cantor generating rule. Field localization and enhancement in quasiperiodic structures are suggesting many possible applications for optical devices such as band-edge lasing, efficient nonlinear filters, bistability, etc.

We performed ultra-fast time-resolved transmission measurement on the band edge regions of the 12^{th} order Fibonacci samples (F_{12}). The band edge is also the region where the periodic-like features (band gap) of the Fibonacci system go over into its disorder properties (critically localized states). Fig. 6.29 shows the detailed transmission

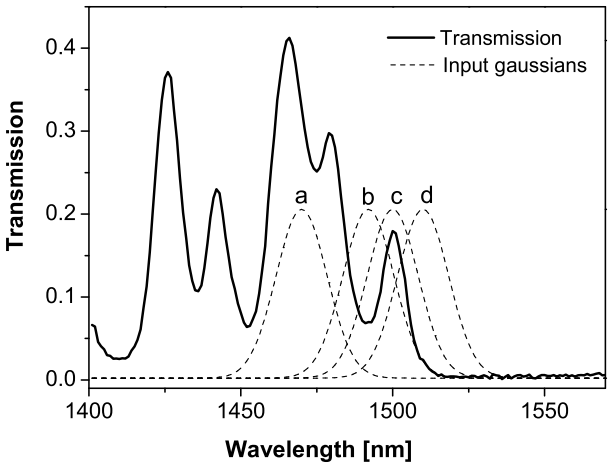

Figure 6.29: The measured transmission spectrum of the sample F_{12} in the laser tuning region (solid line). The Gaussians (dashed lines) represent the spectra of some input pulses (named a, b, c and d)

spectrum of the F_{12} sample together with 4 typical (a-d) spectra of the incoming laser pulses (dotted lines) in the range where the temporal measurements were performed. We have probed the structure at different wavelengths around the band edge region in order to excite the band edge states. The time-resolved transmission of these four pulses (a-d) is shown in Fig. 6.30. The undisturbed pulse (with no sample) is also reported in the plot.

The zero of the time axis in Fig. 6.30 is the time at which the maximum of the unperturbed pulse arrives on the detector. We have corrected for the trivial delay of the pulse due to the additional optical path of the sample. That is, the sample of 44 μm thickness has an optical thickness of 76 μm. (From the refractive indices of the layers we calculate an average effective refractive index of the structure of $n_{eff} \approx 1.88$.) The time offset due to this effect is 99 fs for all pulses that pass through a 12^{th} order Fibonacci sample. We have corrected for this so that the pulse delays, visible for curves (a-d) in Fig. 6.30, are purely due to the internal optical mode structure (internal resonances) inside the sample. Note that by using free-standing porous silicon Fibonacci structures, one avoids large time-offsets due to the silicon substrate.

As the wavelength of the signal is increased, i.e. as we approach the pseudo-band gap, the shape of the transmitted pulses changes. In particular, the pulses are delayed and stretched. In addition, when two states are excited simultaneously, mode beating occurs at a beating frequency given by the frequency separation of the states. In Fig. 6.31, we have plotted the delay of the center of mass of the pulses and the decay time for several measurements in the wavelength range between 1410 and 1530 nm, i.e. the short wavelength edge of the fundamental pseudo-band gap. From the delay time, the group velocity v_g of the wave packet with respect to light velocity v_0 in a medium with effective refractive index of $n_{eff} \approx 1.88$ is deduced and reported in Fig. 6.31c. A maximum group velocity reduction by a factor of three ($v_g/v_0 \approx 0.29$) is found at

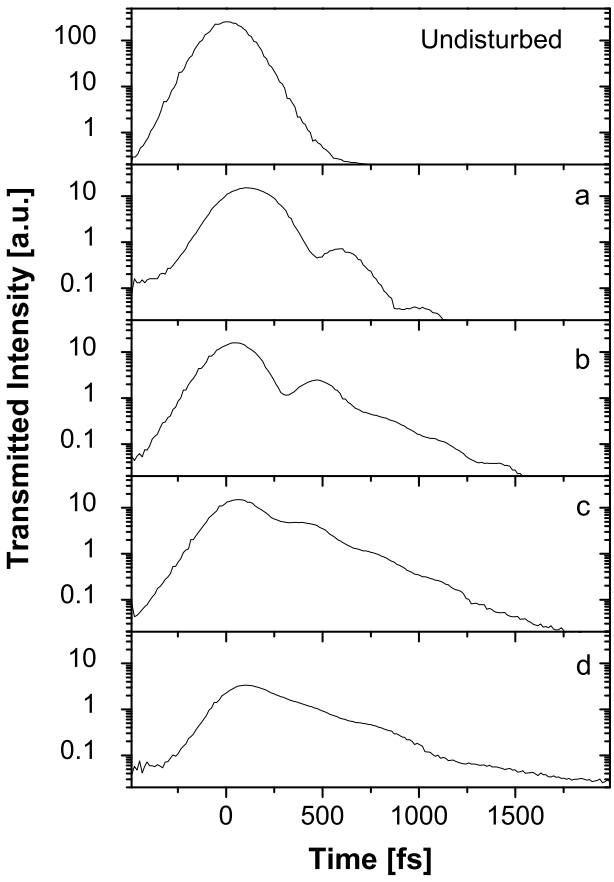

Figure 6.30: Time-resolved signal transmitted trough the F_{12} sample. The undisturbed pulse is shown in the top plot, and plots a, b, c, and d are the transmitted pulses at wavelengths 1470, 1492, 1500, and 1510 nm respectively. The vertical scale is calibrated.

the band edge frequencies. The electric field of the transmitted pulses decays almost exponentially with time. The obtained decay time constants extracted from the raw data are shown in Fig. 6.31d.

Both the delay and the decay times increase as we approach the pseudo-band gap. One expects that slow decays and retarded arrival times should be accompanied by narrow peaks in the transmission spectrum at the edge of the band gap, corresponding to singularities in the density of state. The reason for not observing narrow peaks in transmission (Fig. 6.28) is due to a technical limitation of the method used to obtain the transmission spectra. The transmission spectra were recorded by using a broad source with a large spot of $\gg 1$ mm in diameter on the sample surface (see Fig. 6.19).

In conclusion, the Fibonacci band edge states exhibit mode beating, a sizeable field enhancement, and a group velocity reduction that is 3 times larger than that observed in three-dimensional colloidal photonic crystals of polystyrene. As in the photonic crystal case, the Fibonacci band edge states exhibit band edge resonances which show large delays and strong pulse stretching. We conclude that, at the band

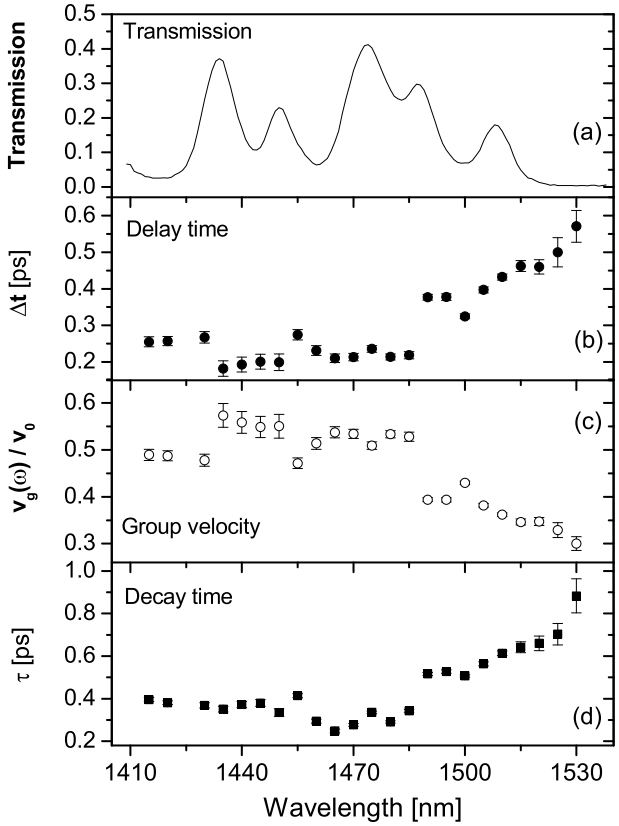

Figure 6.31: (a) Measured transmission spectrum of $F_1 2$. (b) Delay time of the center of mass of the transmitted pulse amplitude with respect to the undisturbed one. (c) Group velocity (as derived from the delay time of the pulse center of mass) with respect to the light velocity in a medium with an effective refractive index equal to the weighted average of the refractive indices of the constituent layers. (d) Decay time of the transmitted signal.

edge, spatially confined Fibonacci states are involved in the quasiperiodicity-induced critical light transport phenomena.

6.8 Conclusions

In conclusion we have investigated light transport in quasi-periodic 1D mesoscopic samples. High resolution static and dynamical experiment can be performed and they can interpreted with a simple and complete transfer matrix theoretical model. We report the first experimental observation of the optical analogue of electronic Bloch oscillations in porous silicon superlattices whose translational invariance is lifted. We have also investigate the light transport in Fibonacci quasi-crystals, which present critical light transport phenomena.

Chapter 7

Conclusions and future perspectives

In this thesis we have presented our recent investigations in mesoscopic optical complex systems. In particular we have focussed on the light transport in the intermediate regime between total order and disorder. This regime is characterized by lower symmetries than in the two extremes, and for, it is harder to model theoretically. We have investigated the effect of reduced symmetries on the transport of light, showing theoretical and experimental evidences of a different and novel behavior.

Multiple scattering of light in ordered nematic liquid crystals can be described with an anisotropic random walk, which induces an anisotropic transport and even anisotropic interference effects. We have observed, for the first time, anisotropic weak localization of light in ordered nematic liquid crystals.

Monte-Carlo simulations of multiple light scattering in an ensemble of anisotropic Rayleigh scatterers shows anisotropic coherent backscattering and a large angle behavior which is very different than the isotropic case, with a non-diffusive behavior.

When a linear variation in the optical constants of a periodic systems is introduced along the propagation direction, the translational symmetry of the photonic crystal is lifted and the Bloch waves become localized. We have predicted and observed the optical counterpart of electronic Bloch oscillations in optical superlattices of porous silicon.

At last we have examined optical quasicrystals, deterministic non-periodic structures, in which translational symmetry is absent. Time-resolved measurements at the Fibonacci band edge states exhibit mode beating, sizeable field enhancement, and a group velocity reduction. We conclude that, at the band edge, spatially confined Fibonacci states are involved in the quasi-periodicity-induced critical light transport phenomena.

Further developments of the research presented in this thesis will be modelling and observing other forms of anisotropic multiple scattering or of anomalous diffusion, as for example light propagation in fractal scattering media. Practical applications of the investigations on anisotropic multiple scattering could be, for instance, in the field of medical imaging and diagnostic for inspection of objects within the human body. In strongly anisotropic random system, the strong localization may be reached or exited just changing the degree of a tunable anisotropy; on the other hand, localization could be approached inside a disordered or lower-symmetrical photonic crystal. If a

gain medium is inserted in the superlattice whose transmission exhibits optical Bloch oscillations, one expects to observe amplification or lasing of the Wannier-Stark states. This would be a laser with a novel mode confinement, within the tilted energy band.

In conclusion, the study of quasi-ordered photonic nano-structures has shown to be extremely interesting, and rich of profitable bridges between the physics of optics and of solid state.

Bibliography

[1] Sebastian Brant *Navicula sive speculum fatuorum*, printed by Joannis Geyler, Argentorati transscriptum XVI die mensis Januarij Anno MDXI, Strassburg Joh. Prüss, (1511).

[2] A.F. Koenderink, L. Bechger, H.P. Schriemer, A. Lagendijk, and W.L. Vos, *Broadband fivefold reduction of vacuum fluctuations probed by dyes in photonic crystals*, Phys. Rev. Lett. **88**, 143903 1-4 (2002).

[3] H. C. van de Hulst, *Multiple Light Scattering* (Dover, New York, 1980).

[4] D. S. Wiersma, P. Bartolini, A. Lagendijk and R. Righini, *Localization of light in a disordered medium* (from the cover) Nature **390**, 671-673 (1997).

[5] P.W. Anderson, *Absence of diffusion in certain random lattices*, Phys. Rev. *109* 1492 (1958); P.W. Anderson, Phil. Mag. B **52**, 505 (1985).

[6] S. John, *Electromagnetic Absorption in a Disordered Medium near a Photon Mobility Edge*, Phys. Rev. Lett. **53**, 2169 (1984).

[7] See for instance: P. Sheng, *Introduction to Wave Scattering, Localization, and Mesoscopic Phenomena* (Academic Press, San Diego, 1995).

[8] Y. Kuga and A. Ishimaru, *Retroreflectance from a dense distribution of spherical particles*, J. Opt. Soc. Am. A **8**, 831 (1984)

[9] M.P. van Albada and A. Lagendijk, *Observation of Weak Localization of Light in a Random Medium*, Phys. Rev. Lett. **55**, 2692 (1985)

[10] P.E. Wolf and G. Maret, *Weak Localization and Coherent Backscattering of Photons in Disordered Media*, Phys. Rev. Lett. **55**, 2696 (1985).

[11] E. Akkermans, P.E. Wolf, and R. Maynard, *Coherent backscattering of light by disordered media: analysis of the peak line shape*, Phys. Rev. Lett. **56**, 1471 (1986).

[12] R. Dalichaouch, J. P. Armstrong, S. Schultz, P. M. Platzman and S. L. McCall, *Microwave localization by two-dimensional random scattering*, Nature **354**, 53 (1991)

[13] A.Z. Genack and N. Garcia, *Observation of photon localization in a three-dimensional disordered system*, Phys. Rev. Lett. **66**, 2064 (1991)

[14] D.S. Wiersma, P. Bartolini, A. Lagendijk, and R. Righini, *Localization of Light in a disordered medium*, Nature **390**, 671 (1997).

[15] N. Garcia and A.Z. Genack, *Crossover to strong intensity correlation for microwave radiation in random media*, Phys. Rev. Lett. **63**, 1678 (1989).

[16] M.P. van Albada, J.F. de Boer, and A. Lagendijk, *Observation of long-range intensity correlation in the transport of coherent light through a random medium*, Phys. Rev. Lett. **64**, 2787 (1990)

[17] P. Sebbah, B. Hu, A. Z. Genack, R. Pnini, and B. Shapiro, *Spatial-Field Correlation: The Building Block of Mesoscopic Fluctuations*, Phys. Rev. Lett. **88**, 123901 (2002).

[18] F. Scheffold and G. Maret, *Universal Conductance Fluctuations of Light*, Phys. Rev. Lett. **81**, 5800 (1998).

[19] A. Blanco *et al*, *Large-scale synthesis of a silicon photonic crystal with a complete three-dimensional bandgap near 1.5 micrometres* Nature, **405** 437 (2000).

[20] See for instance *Photonic Bandgap Materials*, edited by C.M. Soukoulis (Kluwer, Dordrecht, 1996); J.D. Joannopoulos, R.D. Meade, and J.N. Winn, *Photonic Crystals* (Princeton University Press, Princeton, NJ, 1995).

[21] K. Busch and S. John, *Liquid-Crystal Photonic-Band-Gap Materials: The Tunable Electromagnetic Vacuum*, Phys. Rev. Lett. **83**, 967 (1999).

[22] P.G. de Gennes and J. Prost, *The Physics of Liquid Crystals* 2nd edition (Oxford, New York, 1993)

[23] S. Chandrasekhar, *Liquid Crystals* (Cambridge Univ. Press, Cambridge, 1977)

[24] A.Y. Val'kov and V.P. Romanov, Zh. Eksp. Teor. Viz. **82**, 1777 (1982) [Sov. Phys. JETP **56**, 1028 (1983)].

[25] S. Gottardo, S. Cavalieri, O. Yaroshchuk, and D. Wiersma, *Quasi-two-dimensional diffusive random laser action*, Phys. Rev. Lett. in the press (2004).

[26] R. Sapienza, P. Costantino, D. Wiersma, M. Ghulinyan, C. J. Oton, and L. Pavesi, *The Optical Analogue of Electronic Bloch Oscillations*, Phys. Rev. Lett. **91**, 263902 (2003).

[27] D. Levine and P.J. Steinhardt, *Quasicrystals: A New Class of Ordered Structures*, Phys. Rev. Lett. 53, 2477 (1984).

[28] P. A. Thiel and J. M. Dubois, *Quasicrystals: Electrons in a strange sea*, Nature **406**, 570 (2000).

[29] L. Dal Negro, C. J. Oton, Z. Gaburro, L. Pavesi, P. Johnson, A. Lagendijk, R. Righini, M. Colocci, and D. S. Wiersma, *Light Transport through the Band-Edge States of Fibonacci Quasicrystals* Phys. Rev. Lett. **90**, 055501 (2003)

[30] M. Ghulinyan, C. J. Oton, L. Dal Negro, L. Pavesi, R. Sapienza, M. Colocci, and D. Wiersma, *Light pulse propagation in Fibonacci quasicrystals*, Phys. Rev. B, in the press.

[31] Lord Rayleigh, *Phil. Mag.*, **XLIV**,28 (1897), reprinted in his *Scientific Papers*, vol. IV, p. 305.

[32] Gustav Mie, *Contributions to the optics of turbid media, especially colloidal metal suspensions (Beiträge zur Optik trüber Medien, speziell kolloidaler Metallösungen)*. Annalen der Physik, Vierte Folge, Band **25**, No. 3, 377-445 (1908).

[33] J.D.Jackson, *Classical Electrdynamics*, John Wiley & Sons, Second Edition, United States, 1975.

[34] W. Heisenberg, Z. Phys. *Die beobachtbaren Grosen in der Theorie der Elementarteilchen, I und II*, **120**, 513 1943.

[35] R. Carminati, J.J. Sáenz, J.-J. Greffet, and M. Nieto-Vesperinas, *Reciprocity, unitarity, and time-reversal symmetry of the S matric of fields containing evanescent components*, Phys. Rev. A **62**, 012712 (2000).

[36] R.G. Newton, *Scattering Theory of Waves and Particles* McGraw-Hill, New York, 1966, p. 44.

[37] G. Maret and P. E. Wolf, *Multiple light scattering from disordered media. The effect of Brownian motion of scatterers* Z. Phys. B **65**, 409-413 (1987)

[38] M. J. Stephen, *Temporal fluctuations in wave propagation in random media* Phys. Rev. B **37**, 1-5 (1988)

[39] D. J. Pine, D. A. Weitz, P. M. Chaikin, and E. Herbolzheimer, *Diffusing-wave spectroscopy* Phys. Rev. Lett. **60**, 1134- 1137 (1988).

[40] D. Vollhardt, and P. Wölfle, *Diagrammatic, self-consistent treatement of the Anderson localization problem in $d \leq 2$ dimensions* Phys. Rev. B, **22**, 4666 (1980).

[41] A. Schuster, Astrophys. J. **21**, 1 (1905).

[42] E. Amic, J.M. Luck, Th.M. Nieuwenhuizen, *Anisotropic multiple scattering in diffusive media*, J. Phys. A **29**, 4915 (1996).

[43] V.P. Romanov, and A. N. Shalaginov, Opt. Spectrosk. **64**, 774. Group (Springer, Heidelberg), p. 35. (1988).

[44] B.A. v. Tiggelen, *Multiple scattering and localization of light*, Ph.D. thesis, Universiteit van Amsterdam (1992).

[45] G. Labeyrie, E. Vaujour, C. A. Mueller, D. Delande, D. Wilkowski, C. Miniatura and R. Kaiser, *Slow diffusion of light in a cold atomic cloud* Phys. Rev. Lett., **91**, 223904 (2003).

[46] An introduction to electronic weak localization can be found at http://physics1.usc.edu/%7Ebergmann/.

[47] E.Abrahams, P.W.Anderson, D.C.Licciardello and T.V.Ramakrishnan, *Scaling Theory of Localization: Absence of Quantum Diffusion in Two Dimensions*, Phys. Rev. Lett. **42**, 673 (1979)

[48] P.W.Anderson, E.Abrahams and T.V.Ramakrishnan, *Possible Explanation of Nonlinear Conductivity in Thin-Film Metal Wires*, Phys. Rev. Lett. **43**, 718 (1979).

[49] S. Chakravarty and A. Schmid, *Weak localization: The quasiclassical theory of electrons in a random potential*, Phys. Rep. **140** 4, 193-236 (1986).

[50] M. Kaveh, M. Rosenbluh, I. Edrei, and I. Freund , *Weak Localization and Light Scattering from Disordered Solids*, Phys. Rev. Lett. **57**, 2049 (1986)

[51] D.S. Wiersma, M. P. van Albada, B. A. van Tiggelen, and Ad Lagendijk, *Experimental Evidence for Recurrent Multiple Scattering Events of Light in Disordered Media*, Phys. Rev. Lett. **74** 4193 (1995).

[52] G. Labeyrie, F. de Tomasi, J.-C. Bernard, C. A. Müller, C. Miniatura, and R. Kaiser, *Coherent Backscattering of Light by Cold Atoms*, Phys. Rev. Lett. **83**, 5266 (1999)

[53] Y. Bidel, B. Klappauf, J. C. Bernard, D. Delande, G. Labeyrie, C. Miniatura, D. Wilkowski, and R. Kaiser *Coherent Light Transport in a Cold Strontium Cloud*, Phys. Rev. Lett. **88**, 203902 (2002).

[54] I. Freund, M. Rosenbluh, R. Berkovits, and M. Kaveh *Coherent Backscattering of Light in a Quasi-Two-Dimensional System*, Phys. Rev. Lett. **61**, 1214 (1988).

[55] D.S. Wiersma, M.P. van Albada, and A. Lagendijk, *Coherent Backscattering of Light from Amplifying Random Media*, Phys. Rev. Lett. **75**, 1739 (1995).

[56] D.V. Vlasov, L.A. Zubkov, N.V. Orekhova, V.P. Romanov, *Weak localization due to scattering of light in nonoriented liquid crystals*, Pisma Zh. Eksp. Teor. Fiz. **48**, 86 (1988) [JETP Lett. 48, 91 (1988)].

[57] L.V. Kuzmin, V.P. Romanov, and L.A. Zubkov, *Coherent backscattering from anisotropic scatterers*, Phys. Rev. E **54**, 6798 (1996).

[58] J. de Rosny, A. Tourin, and M. Fink, *Coherent Backscattering of an Elastic Wave in a Chaotic Cavity*, Phys. Rev. Lett. **84**, 1693 (2000).

[59] A.F. Koenderink, M. Megens, G. van Soest, W.L. Vos and A. Lagendijk *Enhanced backscattering from photonic crystals*, Phys. Lett. A. **268**, 104-111 (2000).

[60] J. Huang, N. Eradat, M. E. Raikh, and Z. V. Vardeny, A. A. Zakhidov and R. H. Baughman, *Anomalous Coherent Backscattering of Light from Opal Photonic Crystals*, Phys. Rev. Lett. **86**, 4815 (2001).

[61] K. Yu Bliokh, and Yu A. Kravtsov *Observation of sunlight enhanced backscattering from sea bottom near the beach* Waves in Random Media, **14** 479 (2004).

[62] A. Tourin, A. Derode, P. Roux, B. A. van Tiggelen, and M. Fink, *Time-Dependent Coherent Backscattering of Acoustic Waves* Phys. Rev. Lett. **79** 3637, (1997).

[63] E. Larose, L. Margerin, B. A. van Tiggelen, and M. Campillo, *Weak Localization of Seismic Waves*, Phys. Rev. Lett. **93** 048501, (2004).

[64] A. A. Golubentsev, Sov. Phys. JETP **59**, 26 (1984).

[65] F. Erbacher, R. Lenke, and G. Maret, Europhys. Lett. *Multiple Light Scattering in Magneto-Optically Active Media* **21**, 551 (1993).

[66] R. Lenke and G. Maret, *Magnetic Field Effects on Coherent Backscattering of Light*, Eur. Phys. J. B 17, **171** (2000).

[67] R. Lenke, R. Lehner, and G. Maret, *Magnetic-field effects on coherent backscattering of light in case of Mie spheres*, Europhys. Lett. **52**, 620 (2000).

[68] G. Labeyrie, C. Miniatura, C. A. Mller, O. Sigwarth, D. Delande, and R. Kaiser, *Hanle Effect in Coherent Backscattering*, Phys. Rev. Lett. **89**, 163901 (2002).

[69] M. Born and E. Wolf, *Principles of Optics* (Cambridge University Press, 1999).

[70] Eric W. Weisstein. "Green's Function." From MathWorld–A Wolfram Web Resource. http://mathworld.wolfram.com/GreensFunction.htmls

[71] M.C.W. van Rossum and Th.M. Nieuwenhuizen, *Multiple scattering of classical waves: microscopy, mesoscopy and diffusion*, Rev. Mod. Phys. **71**, 313-371 (1999).

[72] C. Cohen-Tannoudji, J. Dupont-Roc, and G. Grynberg. *Processus d'interaction entre photons et atomes*, Inter Editions/Editions du CNRS, 1998.

[73] U. Frisch, *Wave propagation in random media*, part of the book *Probabilistic methods in applied mathematics* A. Bharucha-Reid, ed. (Academic, New York, 1968), pp 75-198.

[74] E. Akkermans and G. Montambuax, *Physique Mesoscopique des electrons et des photons*, EDP Sciences (2004).

[75] O. Sigwarth, G. Labeyrie, T. Jonckheere, D. Delande, R. Kaiser, and C. Miniatura, *Magnetic field enhanced coherence length in cold atomic gases*, Phys. Rev. Lett. **93**, 143906 (2004).

[76] from Cord Mullher's Ph.D. thesis, *Localisation faible de la lumière par un gaz d'atomes froids: rétrodiffusion cohérent et structure quantique interne*, Munchen and Sofia Antiopolis, 2001.

[77] A. Ishimaru, *Wave propagation in Random Media*, Vols 1 & 2 (Academic New York, 1978).

[78] Diederik S. Wiersma, *Light in strongly scattering and amplifying random media*, PhD. thesis, Univ. of Amsterdam, 1995.

[79] A. Lagendijk, R. Vreeker and P. De Vries, *Influence of internal reflection on diffusive transport in strongly scattering media*, Phys. Lett. A **136**, 81 (1989).

[80] M.U. Vera, and D. J. Duriam, Phys. Rev. E, Angular distribution of diffusely transmitted light **53**, 3215 (1996).

[81] D. S. Wiersma, M. P. van Albada, B. A. van Tiggelen, and Ad Lagendijk, *Experimental Evidence for Recurrent Multiple Scattering Events of Light in Disordered Media*, Phys. Rev. Lett. **74**, 4193 (1995).

[82] M. P. van Albada, M.B. van der Mark, and Ad Lagendijk, *Observation of weak localization of light in a finite slab: Anisotropy effects and light path classification*, Phys. Rev. Lett. **58**, 361 (1987).

[83] P.M. Johnson, B.P.J. Bret. J. Gomez-Rivas, J. J. Kelly, and A. Lagendijk, *Anisotropic Diffusion of Lighe in a Strongly Scattering Material*, Phys. Rev. Lett., **89**, 243901, 2002.

[84] B. P. J. Bret and A. Lagendijk, *Anisotropic enhanced backscattering induced by anisotropic diffusion*, Phys. Rev. E, **70**, 036601 (2004).

[85] G. Rikken and B.A. van Tiggelen, *Observation of Magneto-Transverse Light Diffusion*, Nature **381**, 54 (1996).

[86] H. Takakura, A. Yamamoto and A. P. Tsai, *The structure of a decagonal* $Al_{72}Ni_{20}Co_8$ *quasicrystal*, Acta Cryst. **A57**, 576 (2001).

[87] from Olivier Sighwart's Ph.D. thesis, *Localisation faible de la lumière par un gaz d'atomes froids en présence d'un champ magnétique* , Paris, 2004.

[88] M.H. Kao, K.A. Jester, A.G. Yodh, and P.J. Collings *Observation of Light Diffusion and Correlation Transport in Nematic Liquid Crystals* Phys. Rev. Lett. **77**, 2233 (1996).

[89] D.S. Wiersma, A. Muzzi, M. Colocci, and R. Righini, *Time-resolved anisotropic multiple light scattering in nematic liquid crystals*, Phys. Rev. Lett. 83, 4321 (1999).

[90] V.P. Romanov and A.N. Shalaginov, Opt. Spectrosc. **64**, 774 (1988)

[91] H.K. Vithana, L. Asfaw, and D.L. Johnson, *Coherent backscattering of light in a nematic liquid crystal*, Phys. Rev. Lett. **70**, 3561 (1993).

[92] A. Heiderich, R. Maynard, and B.A. van Tiggelen, *Multiple light scattering in ordered nematic liquid crystals*, J. Phys. II (France) 7, 765 (1997).

[93] B. A. van Tiggelen, R. Maynard, and A. Heiderich, *Anisotropic Light Diffusion in Oriented Nematic Liquid Crystals*, Phys. Rev. Lett. **77**, 639 (1996)

[94] R. Sapienza, S. Mujumdar, C. Cheung, A.G. Yodh, D. Wiersma, *Anisotropic Weak Localization of Light*, Phys. Rev. Lett. **92**, 033903 (2004).

[95] G. P. Crawford, and S. Žumer, *Liquid Crystals in Complex Geometries*, cap. 11, Taylor&Francis Ed. (1996).

[96] A review of history of liquid crystals can be found in, for example, P. J. Collings, *Liquid crystals: Natures delicate phase of matter* (Princeton University Press, Princeton, 1990), Ch. 2. 88). 12. O.

[97] S. Singh, *Phase transitions in liquid crystals* Physics Reports **324**, 107-269 (2000).

[98] L. A. Madsen, T. J. Dingemans, M. Nakata, and E.T. Samulski, *Thermotropic Biaxial Nematic Liquid Crystals*, Phys. Rev. Lett. **92**, 145505 (2004).

[99] R. Barberi, F. Ciuchi, G. Lombardo, R. Bartolino, and G. E. Durand, *Time Resolved Experimental Analysis of the Electric Field Induced Biaxial Order Reconstruction in Nematics*, Phys. Rev. Lett. *93*, 137801 (2004).

[100] data taken from *Liquid Crystals On Line*, http://liqcryst.chemie.uni-hamburg.de/

[101] F. C. Frank, *On the theory of liquid crystal*, *Faraday Soc.* **25**, 19 (1958).

[102] P. G. De Gennes and J. Prost, *The Physics of Liquid Crystal*, Oxford University Press, New York (1993).

[103] M. Mitsuishi, S. Ito, M. Yamamotoa, T. Fischer and W. Knoll, *Time-resolved optical waveguide study of the reorientation in a nematic liquid crystal under applied electric field*, J. Appl. Phys. **81**, No. 3, 1135 (1997).

[104] B. v. Tiggelen and H. Stark, *Nematic liquid crystals as a new challenge for radiative transfer*, Rev. Mod. Phys. **72**, 1017 (2000).

[105] M. Liu, *Maxwell equations in nematic liquid crystals*, Phys. Rev. E 50, 2925 (1994).

[106] L.D. Landau, E.M. Lifshitz, and L.P. Piteavskii, *Electromagnetics of Continuous Media* (Pergamon Press, Oxford, 1984).

[107] H. Stark and T. C. Lubensky, *Multiple Light Scattering in Nematic Liquid Crystals* , Phys. Rev. Lett. **77**, 2229 (1996).

[108] B.A. van Tiggelen, A. Heiderich, and R. Maynard *Light Diffusion in Oriented Nematic Liquid Crystals* Mol. Cryst. & Liq. Cryst. **293**, 20 (1997).

[109] A. Lagendijk, B. Vreeker, and P. de Vries, *Influence of internal reflection on diffusive transport in strongly scattering media*, Phys. Lett. A **136**, 81 (1989).

[110] D.S. Wiersma, M.P. van Albada, and A. Lagendijk, *An Accurate Technique to Record the Angular Distribution of Backscattered Light*, Rev. of Sci. Instrum. 66, 5473 (1995).

[111] P.M. Johnson, B.P.J. Bret, J.G. Rivas, J.J. Kelly, and A. Lagendijk, *Anisotropic Diffusion of Light in a Strongly Scattering Material* Phys. Rev. Lett. **89**, 243901 (2002).

[112] G. Labeyrie, D. Delande, C.A. Mller, C. Miniatura, and R. Kaiser, *Coherent backscattering of light by an inhomogeneous cloud of cold atoms*, Phys. Rev. A **67**, 033814 (2003).

[113] F. James, *Monte Carlo theory and practice*, Rep. Prog. Phys, **43**, 1145 (1980).

[114] P. L'Ecuyer, *Maximally Equidistributed Combined Tausworthe Generators*, Mathematics of Computation, **65**, 213 (1996).

[115] H. W. Press et al, *Numerical Recipes in C : The Art of Scientific Computing*, Cambridge University Press (2002).

[116] B.W. Kernighan and D.M. Ritchie, *The C programming language*, second edition, Prentice Hall PTR, (1988).

[117] D. Delande, *Private communication.*

[118] R. Lenke, and G. Maret, *Scattering in polymeric and collodal systems*, edited by W. Brown, Gordon and Breach Science Publisher, Reading, UK (2000).

[119] V. Gopal, S.A. Ramakrishna, A.K. Sood, and N. Kumar, *Photon transport in thin disordered slabs*, Pramana J. Phys., **56**, 6, 2001.

[120] R. Sapienza, D. Delande, and D. Wiersma. *Anisotropic weak localization of light: from isotropic scattering to ordered nematic liquid crystals* Mol. Cryst. Liq. Cryst.(2004) (in the press).

[121] Claudio Oton Ph.D. thesis, *Porous silicon based photonic structures. applications for optical devices and sensors*, Universidad de La Laguna La Laguna, Tenerife 2004.

[122] A. Birner, R. B. Wehrspohn, U M. Gösele, and K. Busch, *Silicon-Based Photonic Crystals*, Adv. Mater. **13**, 377 (2001).

[123] A. Parker, R. Proc. R. Soc. B **265**, 967972 (1998); G. Tayeb, B. Gralak and S. Enoch, *Structural Colors in Nature and Butterfly-Wing Modeling*, Opt. & Phot. News Feb. 2003, 40; P. Vukusic and J. R. Sambles, *Photonic structures in biology Nature* **424**, 852855 (2003).

[124] Only recently rigorous modelling of such natural structures has begun to address some aspects of these complex structures. See, e.g., B. Gralak et al. Opt. Express **9** 567 (2001).

[125] From http://www.physics.usyd.edu.au/ñicolae/seamouse.html 103

[126] W. Gellermann, M. Kohmoto, B. Sutherland, and P.C. Taylor, *Localization of light waves in Fibonacci dielectric multilayers*, Phys. Rev. Lett. 72, 633 (1994).

[127] L. Dal Negro, C. J. Oton, Z. Gaburro, L. Pavesi, P. Johnson, Ad Lagendijk, R. Righini, M. Colocci, and D. S. Wiersma, *Light Transport through the Band-Edge States of Fibonacci Quasicrystals* Phys. Rev. Lett. **90**, 055501 (2003).

[128] E. Yablonovitch, *Inhibited Spontaneous Emission in Solid-State Physics and Electronics*, Phys. Rev. Lett. **58**, 2059 (1987).

[129] S. John, and J. Wang, *Quantum electrodynamics near a photonic band gap: Photon bound states and dressed atoms*, Phys. Rev. Lett. **64**, 2418 (1990). **35**, 265 (1996).

[130] S. John, *Strong localization of photons in certain disordered dielectric superlattices*, Phys. Rev. Lett. **58**, 2486 (1987).

106

[131] E. Lidorikis, M. M. Sigalas, E. N. Economou, and C. M. Soukoulis, *Tight-Binding Parametrization for Photonic Band Gap Materials*, Phys. Rev. Lett. **81**, 1405 (1998).

[132] M. Ghulinyan, C. J. Oton, G. Bonetti, Z. Gaburro and L. Pavesi, *Free-standing porous silicon single and multiple optical cavities*, J. Appl. Phys. **93**, 9724 (2003)

[133] M. Ghulinyan, C. J. Oton, Z. Gaburro, P. Bettotti, and L. Pavesi, *Porous silicon Free-standing coupled microcavities*, Appl. Phys. Lett. **82**, 1550 (2003).

[134] J.B. Pendry, Adv. Phys. **43**, 461 (1994); A. Kavokin, G. Malpuech, A. Di Carlo, P. Lugli, and F. Rossi, *Photonic Bloch oscillations in laterally confined Bragg mirrors*, Phys. Rev. B **61**, 4413 (2000).

[135] F. L. Pedrotti and L. S. Pedrotti, *Introduction to Optics* (Prentice-Hall, 1987).

[136] M. Artoni, G. La Rocca, and F. Bassani, *Resonantly absorbing photonic crystals*, submitted to Phys. Rev. A.

[137] O. Bisi, S. Ossicini and L. Pavesi, *Porous silicon: a quantum sponge structure for silicon based optoelectronic*, Surface Science Reports **264**, 1-126 (2000).

[138] N. W. Ashcroft and N. D. Mermin, *Solid state physics*, 1a Ed., International Thomson Edition, 1976.

[139] F. Bloch, Z. Phys **52** 555, 1928; C. Zener, Proc. R. Soc A **145** 532, 1934.

[140] H.M. James, *Electronic States in Perturbed Periodic Systems* Phys. Rev. **76**, 1611 (1949); G.H. Wannier, *Possibility of a Zener Effect* Phys. Rev. **100**, 1227 (1955).

[141] See e.g. C.F. Hart and D. Emin, *Time evolution of a Bloch electron in a constant electric field* Phys. Rev. B **37**, 6100 (1988); J. Zak, Phys. *Comment on the existence proofs of the Wannier-Stark ladder*, Rev. B **43**, 4519 (1991).

[142] A.G. Chynoweth, G.H. Wannier, R.A. Logan, and D.E. Thomas, *Observation of Stark Splitting of Energy Bands by Means of Tunnelling Transitions*, Phys. Rev. Lett. **5**, 57 (1960).

[143] L. Esaki, and R. Tsu, *Superlattice and negative differential conductivity in semiconductors*, IBM J. Res. Dev. **61**, 16 (1970).

[144] See e.g. J. Feldman, *et al.*, *Optical investigation of Bloch oscillations in a semiconductor superlattice*, Phys. Rev. B **46**, 7252 (1992).

[145] K. Leo, P.H. Bolivar, F. Bruggemann, R. Schwedler, and K. Kohler, *Observation of Bloch oscillations in a semiconductor superlattice* Solid. State Comm. **84**, 943 (1992).

[146] C. Waschke, H. Roskos, R. Schwedler, K. Leo, H. Kurz, and K. Köhler, *Coherent submillimeter-wave emission from Bloch oscillations in a semiconductor superlattice*, Phys. Rev. Lett. **70**, 3319 (1993).

[147] T. Dekorsky, P. Leisching, K. Köhler, and H. Kurz, *Electro-optic detection of Bloch oscillations*, Phys. Rev. B **50**, 8106 (1994).

[148] M. Sudzius, V. G. Lyssenko, F. Loeser, G. Valusis, T. Hasche, K. Leo, M.M. Dignam, K. Koehler, *Bloch Oscillations in Semiconductor Superlattices*, Festkörperprobleme/Advances in Solid State Physics **38**, 225-249 (1999).

[149] M. B. Dahan, E. Peik, J. Reichel, Y. Castin, and C. Salomon, *Bloch Oscillations of Atoms in an Optical Potential*, Phys. Rev. Lett. **76**, 4508 (1996).

[150] O. Morsch, J. H. Mller, M. Cristiani, D. Ciampini, and E. Arimondo, *Bloch Oscillations and Mean-Field Effects of Bose-Einstein Condensates in 1D Optical Lattices*, Phys. Rev. Lett. **87**, 140402 (2001).

[151] G. Monsivais, M. del Castillo-Mussot, and F. Claro, *Stark-ladder resonances in the propagation of electromagnetic waves*, Phys. Rev. Lett. **64**, 1433 (1990).

[152] C.M. de Sterke, J.N. Bright, P. A. Krug, and T. E. Hammon, *Observation of an optical Wannier-Stark ladder*, Phys. Rev. E **57** 2365, 1998.

[153] G. Lenz, I. Talanina, and C.M. de Sterke, *Bloch Oscillations in an Array of Curved Optical Waveguides*, Phys. Rev. Lett **83**, 963 (1999); A. Kavokin, G. Malpuech, A. Di Carlo, P. Lugli, F. Rossi, *Photonic Bloch oscillations in laterally confined Bragg mirrors*, Phys. Rev. B **61**, 4413 (2000).

[154] P. Wilkinson, *Photonic Bloch oscillations and Wannier-Stark ladders in exponentially chirped Bragg gratings*, Phys. Rev. E **65**, 56616 (2002).

[155] T. Pertsch, P. Dannberg, W. Elflein, and A. Bräuer and F. Lederer, *Optical Bloch Oscillations in Temperature Tuned Waveguide Arrays*, Phys. Rev. Lett.**83**, 4752 (1999); R. Morandotti, U. Peschel, U. Peschel, J. S. Aitchison, H. S. Eisenberg and Y. Silberberg, *Experimental Observation of Linear and Nonlinear Optical Bloch Oscillations,* Phys. Rev. Lett **83**, 4756 (1999).

[156] G. Malpuech, A. Kavokin, G. Panzarini and A. Di Carlo, *Theory of photon Bloch oscillations in photonic crystals*, Phys. Rev. B, **63**, 035108 (2001).

[157] C. M. de Sterke, J. N. Bright, P. A. Krug, and T. E. Hammon, *Observation of an optical Wannier-Stark ladder*, Phys. Rev. E **57** 2365, 1998.

[158] G. R. Fleming, *Chemical Applications of Ultrtafst Spectroscopy*, Oxford University Press, New York, 1986.

[159] R. W. Boyd, *Nonlinear Optics*, Academic Press, London, 1992.

[160] M. Holthaus, *Bloch oscillations and Zener breakdown in an optical lattice*, J. Opt. B **2**, 589 (2000).

[161] M. Ghulinyan, C. J. Oton, Z, Gaburro, and L, Pavesi, C, Toninelli and D, Wiersma, *Zener tunnelling of light waves in an optical superlattice*, Phys. Rev. B, in the press, (2004).

[162] D. Shechtman, I. Blech, D. Gratias, J. W. Cahn, *Metallic Phase with Long-Range Orientational Order and No Translational Symmetry*, Phys. Rev. Lett. **53**, 19511953 (1984).

[163] R. Penrose, Bull. Inst. Math. Appl. **10**, 266271 (1974).

[164] R. B. Capaz, B. Koiller, S. L. A. Queiroz, *Gap states and localization properties of one-dimensional Fibonacci quasicrystals*, Phys. Rev. B, **42**, 6402 (1990).

[165] M. Kohmoto, B. Sutherland and K. Iguchi, *Localization of optics: Quasiperiodic media*, Phys. Rev. Lett. **58**, 2436 (1987).

[166] R. Merlin, K. Bajema, R. Clarke, F.Y. Juang, and P.K. Bhattacharya, *Quasiperiodic GaAs-AlAs Heterostructures*, Phys. Rev. Lett. **55**, 1768 (1985).

[167] F. Nori and J. P. Rodriguez, *Acoustic and electronic properties of one-dimensional quasicrystals*, Phys. Rev. B, **34**, 2207 (1986).

[168] W. Gellermann, M. Kohmoto, B. Sutherland, and P.C. Taylor, *Localization of light waves in Fibonacci dielectric multilayers*, Phys. Rev. Lett. **72**, 633 (1994).

[169] T. Hattori, N. Tsurumachi, S. Kawato, and H. Nakatsuka, *Photonic dispersion relation in a one-dimensional quasicrystal*, Phys. Rev. B **50**, 4220 (1994).

[170] C. M. Soukoulis and E. N. Economou, *Localization in One-Dimensional Lattices in the Presence of Incommensurate Potentials*, Phys. Rev. Lett. **48**, 1043 (1982).

[171] T. Fujiwara, M. Kohmoto, and T. Tokihiro, *Multifractal wave functions on a Fibonacci lattice* Phys. Rev. B **40**, 7413 (1989); C.M. Soukoulis and E. N. Economou, *Localization in One-Dimensional Lattices in the Presence of Incommensurate Potentials*, Phys. Rev. Lett. **48**, 1043 (1982).

[172] M. Kohmoto and B. Sutherland , *Critical wave functions and a Cantor-set spectrum of a one-dimensional quasicrystal model*, Phys. Rev. B, **35**, 1020 (1987).

Note

Figure 1: The Ship of Fools Hieronymous Bosch, c. 1490-1500. Oil on wood, 23 x 13" (58 x 33 cm) Musée du Louvre, Paris.

From the first pages, Exlibris: Fools On A Cart And A Boatload Of Fools The fools are setting out for their destination, "the land of fools". They call out *har noch* i.e. "follow us!" and "All aboard, Brothers: it's leaving, it's leaving". The engraving comes from the book *Navicula sive speculum fatuorum* [1] which describes with irony and grotesque images a group of fools of the fifteenth century which free themselves from any social constrain, dress hats with jingle bells and descend the Rhur river on a *navicula*, the boat of fools. Among them, the scientist is present, who, with his folly/science, can be free from the reality, free to follow his dreams and ideals.

Dalle prime pagine, Exlibris: Folli su un Carro e una Barca Carica di Folli. I folli stanno scegliendo la rotta, per la "terra dei folli". Essi chiamano *har noch* cioé "seguiteci!" e "Tutti a bordo, Fratelli: parte, parte!". L'incisione proviene dal libro *Navicula sive speculum fatuorum* [1], nel quale con ironia e toni grotteschi viene rappresentato un gruppo di 'folli' del quindicesimo secolo che si libera da ogni vincolo sociale, veste un cappello a sonagli e discende il Reno su una *navicula*, la nave dei folli. Tra questi folli é presente anche lo scienziato, che con la sua follia/scienza puó liberarsi dalla realtá e seguire i suoi ideali.

Des premières pages, Exlibris : Fous sur un chariot et une cargaison des fous. Les fous choisissent la route pour leur destination, "la terre du fous" ;. Ils hurlent" *har noch* c.-àd. "suivez-nous! " et "Tous à bord, frères: on y va, on y va!". La gravure vient du livre *Navicula sive speculum fatuorum*, le nef des fous [1] qui décrit avec ironie et images grotesques un groupe de fous du quinzième siècle qui se livrent de social contraignez, qui s'habillent avec des chapeaux avec des cloches et qui descendent le fleuve Rhur sur une *navicula*, le bateau des fous. Parmi eux, le scientifique est présent, et avec son folie/science il peut se libérer de la réalité et suivre ses rêves et idéaux.

Acknowledgements Ringraziamenti Remerciements

Al bibliomane, mio padre, anche lui sulla nave dei folli, a mia madre, per il suo affetto incondizionato, a Luca, per la pazienza che ha avuto, nella speranza di incrociare le nostre strade.

I like to think to my thesis and research as a *remix* of past knowledge and experiences. This is, in my opinion, a modern and more appropriate extension of the concept expressed by Isaac Newton with the words "If I have seen further it is by standing on ye shoulders of Giants."[1] Nowadays the inter-exchange of information and people is so dense and essential that the work of my thesis would have not been possible without the help and collaborations with many friends, researchers and scientific institutions. I have not been alone on the shoulders of giants, instead what I have done comes from a collective effort, as a remix of many intuitions, done following my taste and personal point of view. For this I want to thank all the people that contributed to the path that lead me to the doctorate.

Als eerste zou ik Diederik Wiersma willen bedanken, who introduced me to this fascinating research field sharing with me his enthusiasm and passion, and who thought me how to become a physicist. Je remercie chaleureusement Dominique Delande de m'avoir aidé à développer une sensibilité de theoricien, avec largesse d'esprit, et passion raffinée de gourmet.

I thank Maurizio Artoni, il mio secondo-e-mezzo supervisore, for his constant support and friendly advice, per essere stato l'unico to pop in my room at least once a day.

Ringrazio prima di tutto Massimo Inguscio, per avermi accolto al LENS, et je remercie Frank Laloë de m'avoir accueilli au Laboratoire Kastler-Brossel. Inoltre ringrazio Roberto Righini and Marcello Colocci for the friendly supervision and many advice that they gave me in these years. A special thanks also to all the group of Lorenzo Pavesi, Mher Ghulinyan e Claudio Oton, for the many stimulating collaborations. Just looking at few years ago, when I started the path that led me to this doctorate, I want to thank Han Woerdman and Martin van Exter for their patient and precious supervision under my first research project, when they followed and directed my first steps as a physicist. In all these years I gained benefit from exposure to many scientists, among whom I would like to thank for the many stimulating discussions Ad Lagendijk, Bart van Tiggelen, Mike Damzen, Peter Knight and Paolo Villoresi.

Tutta la ricerca qui riportata è stata svolta con i miei compagni di laboratorio, prima di tutto Stefano Gottardo, con il quale ho condiviso molto piacevolmente il mio dottorato e il lab, Sushil Mujumdar e Paola Costantino con la quale ho sgomitato sul tavolo ottico, Costanza Toninelli per le piacevoli discussioni, Nicola Poli l'omniscente, e Francesca, Jacopo, Matteo, Silvia. Ringrazio anche i colleghi dottorandi europei, per il supporto in tutte le nostre avventure internazionali, Massimo, Simona, Margherita e Torsten e tutto il team del LENS.

Je remercie pour le support et l'aide tout le laboratoire Kastler-Brossel, specialement Benoît Grémaud, Thomas Wellens et Olivier Sighwart; je remercie Robert

[1] Newton to Hooke, 5 Feb. 1676.

Khun qui m'as aidè a comprendre la langue des theoriciens.

Scientific advice is not always the most important ingredient for a successful doctorate, many people gave me support, advice and the energy to progress. Je remercie Quiterie, qui avec sa sensibilitè m'as montrè que "comme dans le duel rapporté par I. Calvino qui rassemble les deux moitiés du corps du vicomte, le scientifique et l'artiste fusionneraient, et décèleraient des 'symptômes esthétiques'".

Per il costante supporto, affetto e ospitalità ringrazio Marta, e per avermi sopportato Jason. complexphotonics.org non sarebbe mai nato senza il supporto del primo tra i Lou.agents, Giovanni, con il quale è nata louproject.net. Per fortuna sono ovunque gli attuali abitatori della 111, aperti o chiusoancheladomenica.it. Inoltre non posso dimenticare Martino Trassinelli (also known as Martinelli Trassino), le chef, l'artista e il fisico per la sua amicizia e disponibilità, inoltre Sylvain Gigan, le Mac fanatic, Julien Le Bars, che ora finalmente parla (e recita?) italiano, Giovanni e Beatrice, sempre lì ad appoggiarmi ovunque io fossi, Francesco Intravaia e Marco Romanelli. Reseptc! pour Rex, per i rendering 3D e le serate rubate a Paris. I want to thank also Sumant Oemrawsingh, that even after all that karnemelk is still able to face Kaiser Sose and Erwin Altewischer for its patience in sharing with me his lab in the first physics experiment of our life. Inoltre ricordo Piero e Lara i motardi, che mi hanno iniziato alla passione e alla Hornet e Seeta for all the fun all over Europe, William Irvine, for the many evening of cinema, cucina e fisica, Riccardo e Silvia per l'amicizia e il tempo passato insieme, Patrik per il suo caos d'artista, Daniel dalla bavaria con ardore, Redvin il terrorista, Robert e tutti gli attori dei miei mille traslochi.

Infine un ringraziamento a tutto lo staff tecnico, specialement a Monique Bonnamy e a tutto il personale del LENS e dell'LKB.

Grazie.

Se chiudete la porta a tutti gli errori
anche la verità ne resterà fuori
R. Tagore